2017-09-08

Investigating Structural and Functional Defects in ALS-causing Profilin 1 Variants

Sivakumar Boopathy
University of Massachusetts Medical School

INVESTIGATING STRUCTURAL AND FUNCTIONAL DEFECTS IN ALS-CAUSING PROFILIN 1 VARIANTS

A Dissertation Presented

By

Sivakumar Boopathy

Submitted to the Faculty of the
University of Massachusetts Graduate School of Biomedical Sciences, Worcester
in partial fulfillment of the requirements for the degree of

DOCTOR OF PHILOSOPHY

September 8, 2017

Biochemistry and Molecular Pharmacology

INVESTIGATING STRUCTURAL AND FUNCTIONAL DEFECTS IN ALS-CAUSING PROFILIN 1 VARIANTS

A Dissertation Presented
By

Sivakumar Boopathy

This work was undertaken in the Graduate School of Biomedical Sciences

Biochemistry and Molecular Pharmacology Program

The signature of the Thesis Advisor signifies
validation of Dissertation content

_____

Daryl A. Bosco, Ph.D., Thesis Advisor

The signatures of the Dissertation Defense Committee signify
completion and approval as to style and content of the Dissertation

_____

John E. Landers, Ph.D., Member of Committee

_____

Osman Bilsel, Ph.D., Member of Committee

_____

Zuoshang Xu, M.D., Ph.D., Member of Committee

_____

Thomas D. Pollard, M.D., External Member of Committee

The signature of the Chair of the Committee signifies that the written dissertation
meets the requirements of the Dissertation Committee

_____

Reid Gilmore, Ph.D., Chair of Committee

The signature of the Dean of the Graduate School of Biomedical Sciences
signifies that the student has met all graduation requirements of the School.

_____

Anthony Carruthers, Ph.D.,
Dean of the Graduate School of Biomedical Sciences

September 8, 2017

DEDICATION

To my family

ACKNOWLEDGEMENTS

Dr. Zu Shen, Dr. Tina Nguyen, Peter Trenh and Dr. Lawrence Stern got me (a naïve boy at that time) started on this journey during my first rotation in the Stern Lab, for which I express my heartfelt gratitude to them. I moved on to the Bosco lab for my next rotation which is where I would join later to pursue my thesis research for the next several years. I sincerely thank Dr. Daryl A. Bosco, my thesis advisor, who patiently taught me, guided me, helped me realize my strengths, overcome my weaknesses and shaped me throughout the years to become a scientist I dreamt to be. I am grateful to all the past members of the Bosco lab, Nathan Lemay, Dr. Catherine Douthwright, Dr. Melissa Rotunno, Dr. Reddy Ranjith Kumar Sama, Laura Kaushansky, Dr. Kristin Boggio and Kiera Sapp for providing a lively and friendly environment and for enlightening scientific discussions. Profound thanks are due to Dr. Melissa Rotunno, who also happened to be my rotation mentor, for teaching me scientific skills that would be valuable throughout my graduate career and in the years to come. I extend my gratitude to the present members of the Bosco lab, Dr. Desiree Baron, Dr. Jeanne McKeon, Dr. Heather Yonutas, Maeve Tischbein, Eric Schmidt, Yen-Chen (Nora) Lin, Meenakshi Sundaram Kumar, Salome Funes and Katherine Gall for continuing to maintain a great friendly, scientific environment and for all your help and assistance during experiments and lab meeting discussions. Special thanks to the “Team Profilin 1”,

Dr. Jeanne McKeon, Eric Schmidt and Salome Funes who will carry forward my project.

I thank my rotation mentors, Dr. C. Robert Matthews, Dr. Jill Zitzewitz, Dr. Osman Bilsel and the past and current members of their labs, especially Noah Cohen (who frequently threatened me with beatings to improve my morale), Dr. Can Kayatekin, Dr. Vijay Kumar, Dr. Gangadhara, Dr. Divya Kapoor, Dr. Sagar Kathuria, Dr. Brian Mackness, Dr. Paul Nobrega, Dr. Daniel Lindstrom, Lori Tokarowski, Ornella Bisceglia, Kevin Halloran, Yvonne Chan and Meme Tran. They were our collaborators during my thesis project; most of my experiments were carried out in their labs and I will always remember the long nights I spent collecting data. I thank our collaborators and neighbors, Dr. John Landers, Dr. Claudia Fallini, Dr. Eric Danielson, Dr. Anthony Giampetruzzi, Dr. Eduardo Rodenas, Dr. Kevin Kenna, Pamela Keagle, Monika Chitre, and of course Dr. Chi-Hong Wu, a good friend, scientist, colleague and weekend companion in the lab. I am wholeheartedly grateful to Dr. Robert Brown, Dr. Lawrence Hayward, Dr. Janice Dominov, Dr. Fen-Biao Gao, Dr. Miguel Sena-Esteves, Dr. Helene Tran, Dr. Rodrigo Lopez-Gonzalez, Ozgun Uyan, Pin-Tsun (Justin) Lee, Nicholas Wightman, Cecile Christensen, Dr. Danilo Medinas, Peter Sapp, Kimberly Benoit, Diane McKenna-Yasek, Gabriela Toro, Dr. Gopinath Krishnan, Zachary Kennedy, Dr. Owen Peters, Dr. Jemeen Sreedharan, Dr. Dwijit GuhaSarkar, Havisha Karnam, Leticia Fridman and all the members of the Neurology department and

the Gene Therapy Center, past and present, for providing a cherishing, splendid, sharing and caring atmosphere.

I thank my thesis research advisory committee and dissertation examination committee members, Dr. Reid Gilmore, Dr. John Landers, Dr. Jill Zitzewtiz, Dr. Osman Bilsel and Dr. Zuoshang Xu for valuable discussions and suggestions during progress meetings and Neurology Nexus meetings. I sincerely thank Dr. Thomas Pollard, Yale University, for agreeing to be my external examiner.

Living a lonely life, on the other side of the world far away from your loving family, these difficulties are hard to put in words. It was my father who encouraged me to pursue a career in biomedical sciences and he is the proudest person of all. My family, Mr. Boopathy Gurusamy (father), Mrs. Vasanthakumari Boopathy (mother), Mrs. Suganya Rajaganapathy (sister) and family, and Karthikeyan Boopathy (brother) and family, who all are eagerly waiting for me, you are my greatest strengths. My niece, Gayathri “Pappai” Rajaganapathy, is far younger in age, but continues to give me hope, courage and meaning in my life. I promise, I’ll be back soon.

ABSTRACT

Mutations in profilin 1 (PFN1) cause amyotrophic lateral sclerosis (ALS), a fatal neurodegenerative disease that targets motor neurons. PFN1 is a 15 kDa protein that is best known for its role in actin dynamics. However, little is known about the pathological mechanisms of PFN1 in ALS. In this dissertation, it is demonstrated that certain familial ALS-linked mutations severely destabilize the native conformation of PFN1 *in vitro* and cause accelerated turnover of the PFN1 protein in neuronal cells. This mutation-induced destabilization can account for the high propensity of ALS-linked variants to aggregate and also provides rationale for their reported functional defects in cell-based assays. The source of this destabilization is illuminated by the crystal structures of several PFN1 proteins, revealing an expanded cavity near the protein core of one ALS variant and predicting a non-surface exposed cavity in another. Functional biochemical experiments point to abnormalities in actin filament nucleation and elongation caused by PFN1 mutants. In HeLa cells, PFN1 is essential for the generation of actin-rich filopodia and expression of mutant PFN1 alters filopodia density further supporting a pathogenesis mechanism involving actin cytoskeleton. Taken together, this dissertation infers that the pathogenesis of ALS due to mutations in PFN1 can be mediated at least by two possibly related mechanisms, a destabilization of the native PFN1 structure and an impact on the actin assembly processes.

TABLE OF CONTENTS

LIST OF TABLES

LIST OF FIGURES

Chapter I: Introduction

Chapter II: Structural basis for mutation-induced destabilization of PFN1 in ALS

Chapter III: Investigating defects in actin assembly due to ALS-mutations of PFN1

LIST OF ABBREVIATIONS

AD – Alzheimer's disease
ADP – adenosine 5'-diphosphate
ALS – Amyotrophic lateral sclerosis
AR – androgen receptor
ATP – adenosine 5'-triphosphate
Avg-Abs-DD – average of absolute double difference
CD – circular dichroism
CMTD – Charcot-Marie-Tooth disease
DCTN1 – dynactin subunit 1
DMSO – dimethyl sulfoxide
DNA – deoxyribonucleic acid
DSF – differential scanning fluorimetry
DTT – dithiothreitol
EDTA – ethylenediaminetetraacetic acid
EGTA – ethylene glycol-bis(2-aminoethylether)-N,N,N′,N′-tetraacetic acid
EM – electron microscopy
ER – endoplasmic Reticulum
F-actin – filamentous actin
FALS – familial ALS
FH1 – formin homology 1
FH2 – formin homology 2
FRET – Förster resonance energy transfer
FTD – frontotemporal dementia
FTLD – frontotemporal lobar degeneration
FUS/TLS – fused in sarcoma/translocated in liposarcoma
G-actin – monomeric actin
GAPDH – glyceraldehyde 3-phosphate dehydrogenase
GDP – guanosine 5'-diphosphate
GTP – guanosine 5'-triphosphate
HD – Huntington's disease
HTT – huntingtin
IF – intermediate filament
IPSC – induced pluripotent stem cells
IPTG – isopropyl β-D-thiogalactopyranoside
LTD – long-term depression
LTP – long-term potentiation
MRE – mean residual ellipticity
NF – neurofilament
NMJ – neuromuscular junction
NMR – nuclear magnetic resonance

OPTN – optineurin
PAGE – polyacrylamide gel electrophoresis
PD – Parkinson's disease
PFN1 – profilin 1
PFN2 – profilin 2
PLCγ1 – phospholipase C-γ1
PLP – poly(L-proline)
PQC – protein quality control
PtdIns – phosphatidylinositol
RNA – ribonucleic acid
RNP – ribonuclear proteins
ROCK – rho-associated coiled-coil-containing protein kinase
SALS – sporadic ALS
SBMA – spinobulbar muscular atrophy
SDS – sodium dodecyl sulphate
SMA – spinal muscular atrophy
SMN – survival of motor neuron
SNP – single nucleotide polymorphism
snRNP – small nuclear ribonucleoproteins
SQSTM1 – sequestosome 1
SOD1 – Cu/Zn superoxide dismutase 1
STORM – stochastic optical reconstruction microscopy
TCSPC – time-correlated single photon counting
TDP43 – transactive response DNA-binding protein 43
TIRF – total internal reflection fluorescence
TUBA4A – tubulin α-4A
UBQLN2 – ubiquilin 2
UPR – unfolded protein response
UPS – ubiquitin-proteosome system
VCP – vasolin-containing protein

CHAPTER I – INTRODUCTION

Amyotrophic Lateral Sclerosis

Clinical presentation

Amyotrophic Lateral Sclerosis (ALS) or Lou Gehrig's disease is a progressive and fatal motor neuron disease that occurs during mid-adulthood at about 55 years. This disease is characterized by the death of both upper and lower motor neurons. The upper or corticospinal motor neurons originate from the motor cortex and synapse in the brain stem and spinal cord, from which the lower or bulbar, spinal motor neurons project into skeletal muscles. The common initial symptoms are weakness of the limbs in the case of limb onset, with hyperreflexia, fasciculations and spasticity. As the motor neurons degenerate, the muscles atrophy leading to paralysis, and eventually leading to death 3-5 years post-onset due to respiratory failure. About one-third of the ALS cases are bulbar in nature characterized by difficulty in chewing, swallowing and speech caused by tongue atrophy. The incidence of ALS is 1-2 individuals per 100,000 per year in most countries and the prevalence is about 5 cases per 100,000 people (1,2). Despite all the progress in research, no cure has been found and the drugs approved for treatment, riluzole and edaravone, merely extend survival by a few months (1).

Genetics and pathogenesis

About 10% of ALS cases are inherited dominantly and referred to as familial ALS (FALS). The remaining 90% of cases are sporadic in nature (SALS). Of the

familial cases, 20% are due to mutations in *superoxide dismutase 1* (*SOD1*), which was also the first gene genetically linked to ALS (3). About 25% of FALS cases carry hexanucleotide repeat expansions in the gene *c9orf72*. Mutations in the genes encoding RNA binding proteins fused in sarcoma/translocated in liposarcoma (FUS/TLS) and transactive response DNA-binding protein 43 (TDP43) each account for 5% of FALS cases. Other genes contributing to FALS at varying proportions are *angiogenin* (*ANG*), *vasolin containing protein* (*VCP*), *dynactin subunit 1* (*DCTN1*), *optineurin* (*OPTN*), *ubiquilin 2* (*UBQLN2*), *sequestosome 1* (*SQSTM1*), *profilin 1* (*PFN1*), *hnRNPA1*, *matrin 3*, *tubulin α-4A* (*TUBA4A*), *CHCHD10*, *TBK1* and *NEK1*. (1,2,4). Less frequently, mutations in certain genes such as *SOD1*, *c9orf72*, *TDP43* and *FUS* also account for SALS (2). About 15-20% of the ALS patients display cognitive defects and behavioral changes culminating in dementia. These symptoms correlate with the degeneration of frontal and temporal lobes, a condition commonly seen in frontotemporal dementia (FTD) (1). ALS and FTD are considered two ends of a spectrum of disorders and varying degrees of genetic and symptomatic overlap between the two are often observed (4).

The ALS genes can be classified into three groups based on the primary pathophysiological features – (i) disturbances in protein homeostasis caused by protein stability, misfolding, aggregation and defective degradation of proteins by proteasome and autophagy (*SOD1*, *VCP*, *OPTN*, *SQSTM1, UBQLN2*), (ii) disturbances in RNA metabolism due to defects in RNA splicing, impairment in

nucleocytoplasmic and axonal transport of RNA, deposition of RNA in nuclear foci and cytoplasmic granules (*FUS*, *TDP43*, *c9orf72*, *hnRNPA1*, *ANG* and many other ALS-linked genes encoding RNA binding proteins), (iii) cytoskeletal abnormalities leading to defects in transport of cargo along axons, growth cone elongation. The primary pathways converge on a number of secondary downstream effects such as endoplasmic reticulum (ER) stress, autophagy, proteasome and mitochondrial dysfunction, alterations in dendritic morphology, neuroinflammation and excitotoxicity (1,2,4). While the first two features are well studied in ALS, detailed mechanistic studies of actin-related cytoskeletal defects caused by ALS-mutations in PFN1 are lacking. This dissertation attempts to decipher disease mechanisms caused by ALS mutations in PFN1.

The chemistry and biology of profilins

Profilins

Profilins are a class of molecules involved in actin cytoskeletal modeling, ranging in size from 12-15 kDa. It is present in all eukaryotic cells and several species, including humans, have more than one isoform. Profilins are evolutionarily diverse with respect to their sequence (5). Nevertheless, they are well conserved among mammals (6,7). The structures of profilins studied from different species exhibit high similarity despite low sequence similarity (8). Four profilin isoforms have been identified in humans – PFN1 expressed ubiquitously, the two splice variants PFN2a (major form, here onwards referred to as PFN2) and PFN2b are

expressed in brain and kidney respectively, PFN3 and PFN4 are expressed in kidneys and testes (8,9). The structure of human PFN1, like other profilins, consists of a 7-stranded anti-parallel β-sheet in the center, the N- and C-terminal helices (α1 and α4) on the convex face and two more helices (α2 and α3) and possibly a third single-turn 3_{10}-helix on the concave face of the β-sheet preceding helix α2 (Figure I-1) (10). Oligomerization of PFN1 has been reported previously, but the functional significance of this process needs to be elucidated (11-13). Much of our understanding of human PFN1 is based on studies of profilins from many species and their properties, discussed below and in the following sections, may be applicable to human PFN1 as well.

Profilin was initially isolated as a complex with actin (14) and actin is the best-characterized binding partner to date (15). The actin binding residues on PFN1 can be inferred from the structure of the bovine profilin-β-actin complex. The residues that interact with the barbed face of actin are in helix α3, amino-terminal of helix α4, strands β4, β5 and β6 (16,17) (Figure I-1, II-10). The affinity of profilin for actin is higher for ATP-G-actin over ADP-G-actin and the affinity is higher for G-actin over F-actin (18-20). The dissociation constant (K_d) of human PFN1-G-actin interaction is about 0.3 μM (21).

Profilins can interact with proteins containing poly(L-proline) motifs via the cleft formed by the N- and C-terminal helices (α1 and α4) and the β-sheet (22-26) (Figure I-1, II-10). The poly(L-proline) binding surface is roughly on the opposite side of the actin-binding face and hence profilins can bind both actin and poly(L-

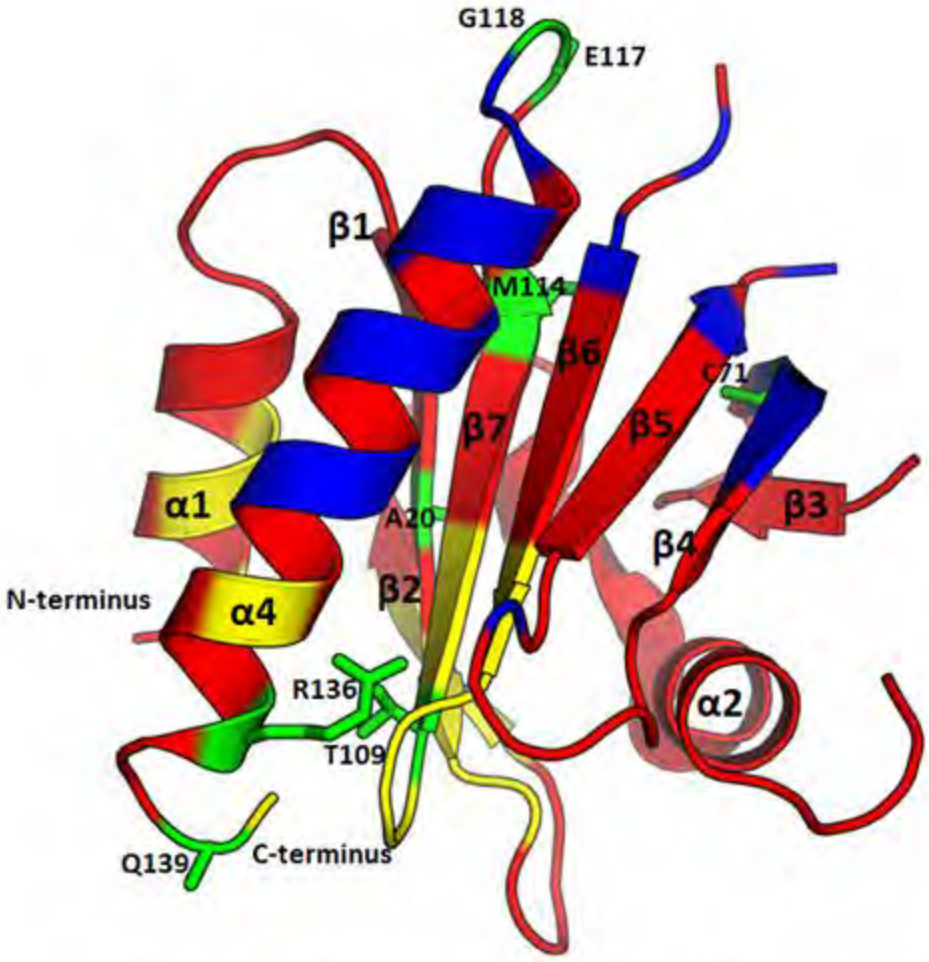
G118
E117
β1
M114
β6
C71
β7
β5
α1
A20
β3
β4
N-terminus
α4
β2
R136
α2
T109
Q139
C-terminus

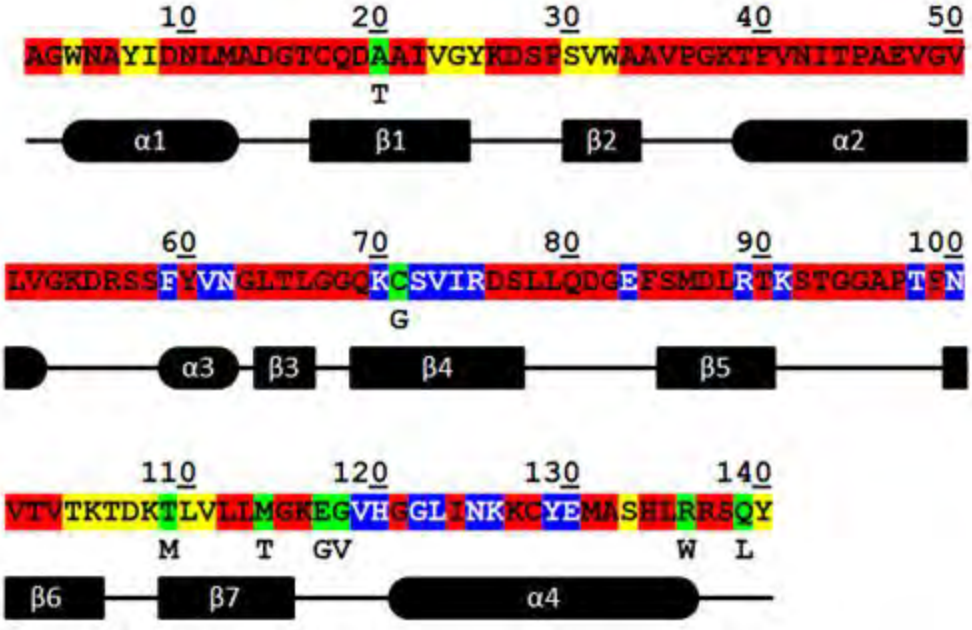
10 20 30 40 50
AGWNAYIDNLMADGTCQDAAIVGYKDSPSVWAAVPGKTFVNITPAEVGV
T
α1 β1 β2 α2
60 70 80 90 100
LVGKDRSSFYVNGLTLGGQKCSVIRDSLLQDGEFSMDLRTKSTGGAPTFN
G
α3 β3 β4 β5
110 120 130 140
VTVTKTDKTLVLLMGKEGVHGGLINKKCYEMASHLRRSQY
M T GV W L
β6 β7 α4

Figure I-1. Structure of human PFN1. The crystal structure (PDB ID code 4X1L) and the amino acid sequence of human PFN1 are shown. The secondary structural elements are mapped below the amino acid sequence. The residues involved in binding to actin and poly(L-proline) are highlighted in blue and yellow respectively. The residues that are mutated in ALS mutations are depicted as green sticks. The residues missing from the structure are 1, 2, 57-62, 92-96. The numbering of the sequence starts from the methionine encoded by the start codon. This numbering scheme for PFN1 adopted throughout this dissertation is different from the published literature in which the alanine following the start methionine is considered the first amino acid in the sequence.

proline) containing proteins simultaneously. Profilin is thought to bind more than 50 proteins via the interaction with poly(L-proline) (9,15). Most notable among those are the cytoskeletal proteins, formins and Ena/VASP. Between 6 and 10 prolines are required for profilin binding, with maximum affinity observed with 10 prolines (27). But in actual proteins, prolines are usually interrupted. It appears that the motif containing multiple prolines has to form a stable type-II helix for a strong interaction with profilin (27). The consensus sequence for this interaction is ZPPX (Z is P, G or A; X is any hydrophobic residue) and hence the binding constant is likely to be different for different poly(L-proline) containing ligands (15).

Phosphatidylinositols (PtdIns) comprise the third class of interacting partners of profilin. Phosphatidylinositol 4,5-bisphosphate (PtdIns(4,5)P_2) is hypothesized to predominantly interact through electrostatic attraction between the negatively charged phosphate group and the basic patch of residues K70, R89, K91, K126 (actin binding side), R136, R137 (poly(L-proline) binding side) of human PFN1 (28-31) (Figure I-1). These residues overlap with both the actin and poly(L-

proline) binding sites of PFN1, and PtdIns(4,5)P_2 has been shown to disrupt profilin-actin and proflin-poly(L-proline) interactions (32-34). Several groups have reported various binding affinities (between 0.1 μM and 1000 μM) depending on whether PtdIns(4,5)P_2 was in sub-micellar, micellar concentrations or part of unilamellar vesicles (29,31,35-38). But phosphatidylinositol 3,4-bisphosphate (PtdIns(3,4)P_2) and phosphatidylinositol 3,4,5-triphosphate (PtdIns(3,4,5)P_3) interact more strongly with human PFN1 than PtdIns(4,5)P_2 (37,39). Interestingly, tryptophan fluorescence and circular dichroism (CD) spectroscopy measurements show that binding to phosphatidylinositols introduces structural changes by increasing α-helical content in PFN1 (39,40). Structures of profilin-phoasphatidylinositols are lacking and are needed to accurately map the binding sites.

Profilins in the test tube

A wealth of information on the role of profilin in actin dynamics have been accumulated mainly through *in vitro* biochemical, fluorimetric and single molecule biophysical methods using fluorescently labeled actin. Actin can spontaneously nucleate and give rise to actin filaments. Once nucleated, the filaments can proceed to elongate bi-directionally, but actin assembly from pointed end is negligible compared to that of barbed end (41) (Figure I-2A). The interaction of profilin with actin serves three main purposes. First, it sequesters monomeric G-actin and prevents its spontaneous nucleation. Increasing concentrations of profilin prevents actin polymerization by inhibiting nucleation and possibly promoting

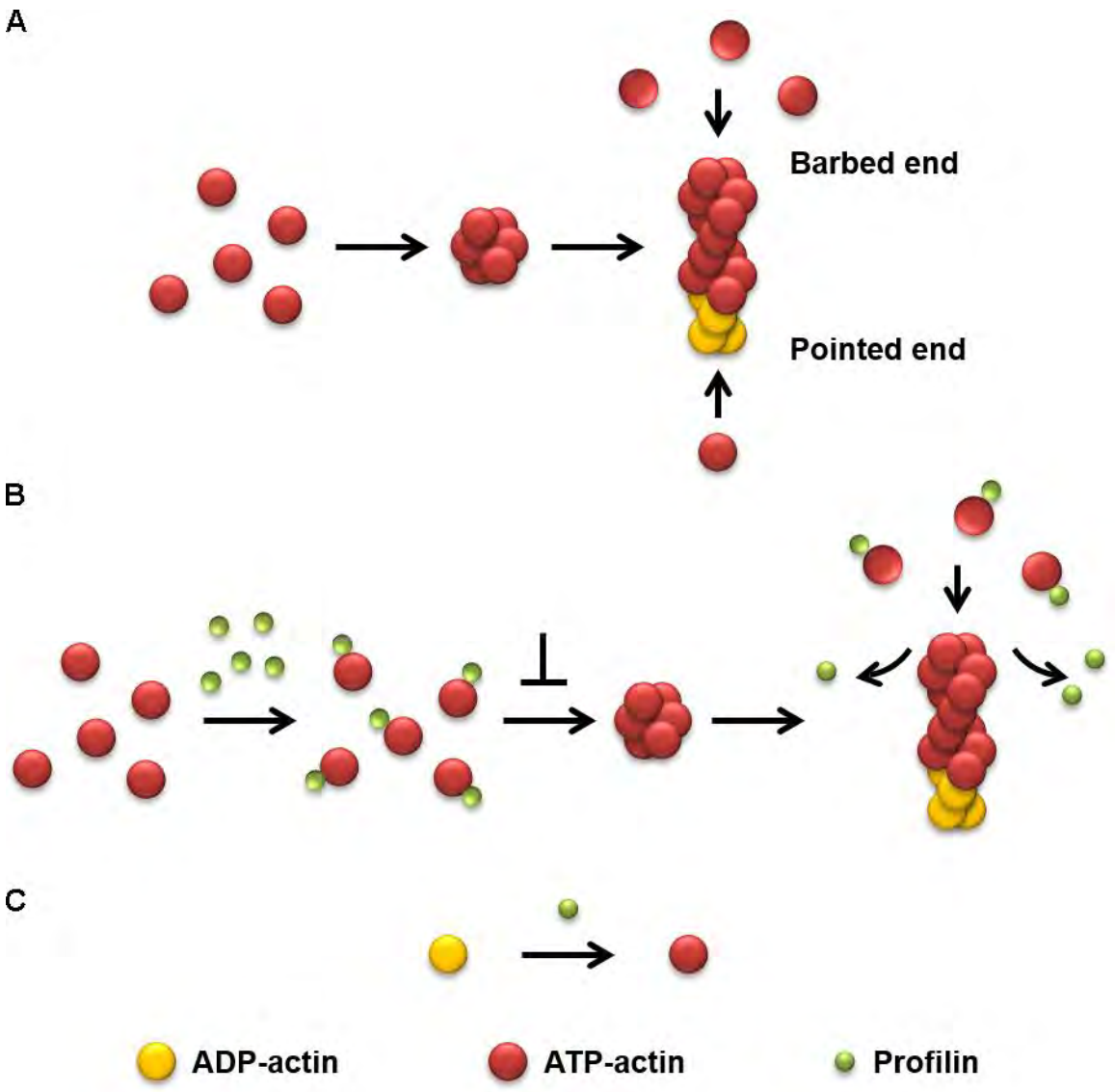

Figure I-2. Functional consequences of profilin-actin binding. (A) Actin has the tendency to spontaneously nucleate under the right ionic conditions when its critical concentration is exceeded. Once a stable actin seed is formed, it can polymerize to produce filaments. The assembly from the barbed end or plus end determines the rate of elongation, since pointed end or minus end assembly is negligible. During the course of the polymerization, the ATP bound to the actin subunits gets hydrolyzed to ADP, favoring recognition by factors such as cofilin. (B) Profilin is one of the actin sequestering proteins that can inhibit nucleation. Once nucleated, polymerization still proceeds, but profilin prohibits pointed end assembly. (C) Profilin can accelerate ADP-ATP exchange on actin thereby maintaining a pool of polymerization-ready actin.

depolymerization from the barbed end (19,42-46) (Figure I-2B). Second, it prohibits subunit addition to the pointed end of filamentous (F) actin (Figure I-2B) due to steric effects (41,43,45). Third, profilins catalyze the exchange of ADP to ATP on monomeric (G) actin, speeding up the process by about 1000 fold thereby effectively "recharging" it for polymerization (15,47,48) (Figure I-2C). The ATP-bound form of actin is polymerization-competent and due to the intrinsic ATPase activity of actin, the bound ATP in F-actin gets hydrolyzed to ADP, which favors recognition by severing factors such as cofilin for recycling G-actin (8,49,50). The presence of PtdIns(4,5)P_2 effectively reduces the ability of profilin to inhibit actin polymerization (29,39).

Three main classes of actin assembly machineries exist – (i) the Arp2/3 complex and its activator WASP nucleate branched actin filaments (51,52), (ii) members of formin family nucleate and elongate unbranched actin filaments (41,53), (iii) Ena/VASP family members elongate unbranched actin filaments (54-56). All three machineries present a free barbed end facilitating actin subunit addition. The feature that ties these machineries to profilin is poly(L-proline). WASP consisting of poly(L-proline) motifs is an interactor of profilin (57). The significance of this interaction in nucleation by Arp2/3 is yet to be established. But the presence of profilin inhibits nucleation by Arp2/3 *in vitro* (58-60). Formins, which function as a homodimer, are a class of proteins characterized by the presence of formin homology (FH1) and formin homology (FH2) domains, in addition to other domains such as those involved in cellular localization and

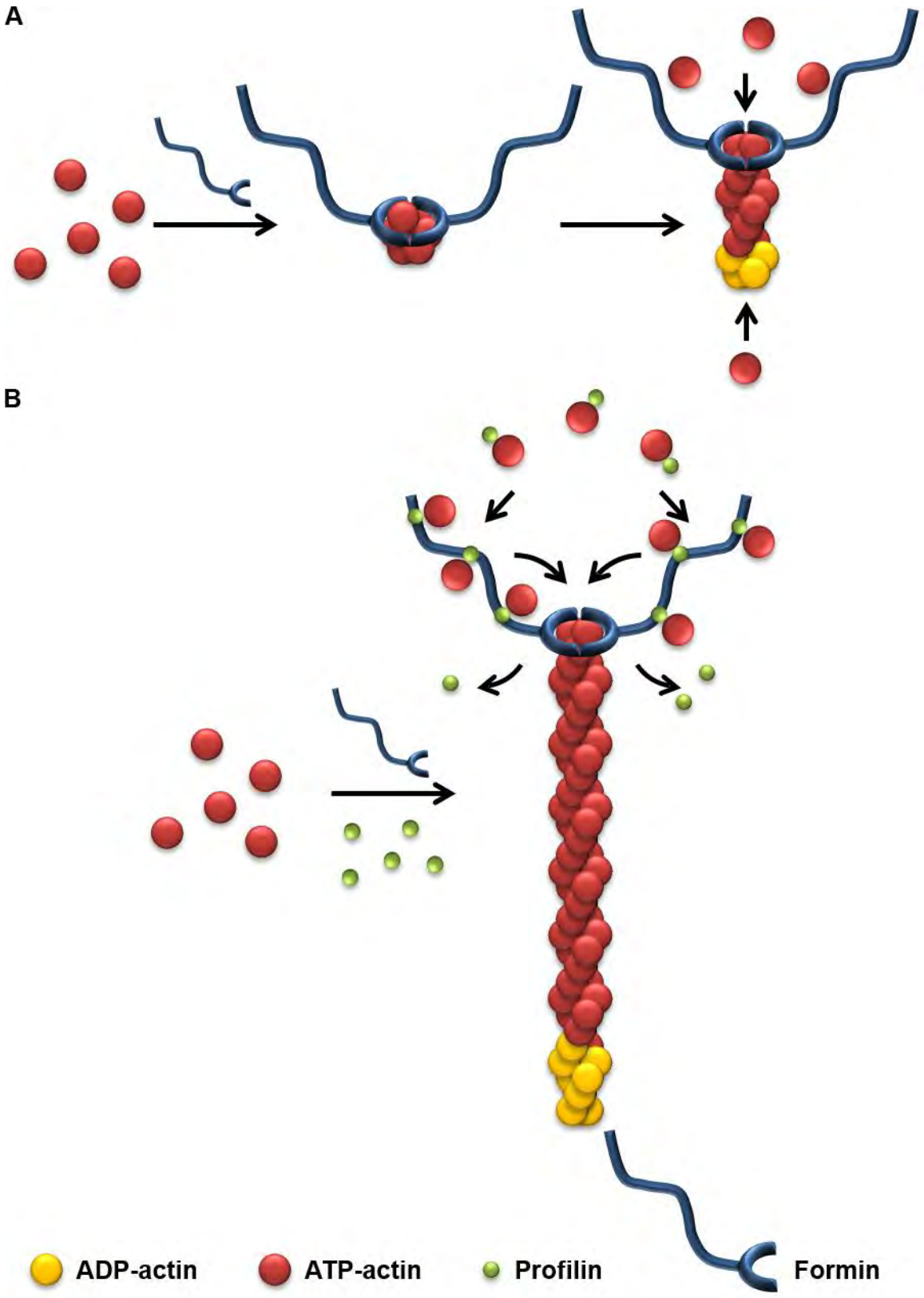
A
B
ADP-actin
ATP-actin
Profilin
Formin

Figure I-3. Nucleation and elongation by formins. (A) Most formins in their functional homodimeric form can nucleate actin filaments via their FH2 domains (depicted as a ring). After nucleation the formin molecule stays attached to the barbed end by exhibiting “helical stair-stepping” motions. (B) The FH1 domain of formins can recruit profilin-actin complexes and deliver them to the growing barbed end. Formins such as mDia1 greatly accelerate filament assembly. The ability of formins to accelerate filament assembly depends on the number of profilin-actin recruiting poly(L-proline) motifs in the FH1 domain. The elongation factor Ena/VASP operates in a similar manner by forming a tetramer.

signaling (41,53,61). The FH2 is the actin nucleating domain that can nucleate actin filaments by binding free actin monomers. Notably, the FH1 domain is rich in poly(L-proline) motifs, the number of which varies depending on the formin. The FH1 domain recruits several profilin-actin complexes which in turn feeds actin subunits to the growing barbed end. The FH2 domain stays attached to the barbed end by a “helical stair-stepping” mechanism (41,53,62-64) (Figure I-3). Formins in general accelerate filament elongation rates to different extents although exceptions do exist (41,53,64,65), and the elongation rate is positively correlated with the number of profilin-binding poly(L-proline) sites in the FH1 domain (66). The Ena/VASP family members exhibit parallelism to formins in their properties. They contain proline-rich motifs between the Ena/VASP homology domains 1 and 2 (EVH1 and EVH2) and when they operate as functional tetramers, they recruit profilin-actin complexes, deliver actin subunits to the barbed end and stay associated to the barbed end by stepping along the growing filaments (54-56,67). The coordinated activities of several factors in addition to actin, profilin and Arp2/3 have been studied using bead motility assays by several groups and demonstrate

the intricate nature of nucleation, assembly, disassembly and turnover of actin filaments (68,69).

Profilins in cells

The cellular concentration of PFN1 is greater than 50 μM, but much lower than actin concentration (15). The major actin sequestration role in some animal cells is performed by thymosin family proteins. In cells, the role of profilin is mainly to maintain a pool of polymerization-ready ATP-actin (9,15). Supporting this view is the fact that microinjecting excess profilin in mammalian cells depolymerizes actin whereas microinjection of profilin-actin complexes favors actin polymerization (70). PFN1 localizes in both the cytoplasm and the nucleus (9,15). PFN1 can also possibly localize to the plasma membrane facilitated by interacting with phosphatidylinositols. This has been shown for yeast profilin (71).

Profilin can act as a signal transducer in at least three ways. Profilin localized to the membrane via PtdIns(4,5)P_2, protects the latter from hydrolysis by phospholipase C-γ1 (PLCγ1) (35,36). Receptor tyrosine kinases, on stimulation, can phosphorylate PLCγ1 which overcomes inhibition by profilin to hydrolyze PtdIns(4,5)P_2. Profilin, released from the breakdown of PtdIns(4,5)P_2, can interact with actin (9,15,35,36). Profilin association with formins can be indirectly linked to its signaling. Diaphanous formins, such as mDia1, exist in an autoinhibited conformation, in which the N-terminal diaphanous inhibitory domain interacts with the C-terminal diaphanous autoregulatory domain (41). On activation by Rho family GTPases, mDia1 is relieved from this autoinhibition, which can then

nucleate actin and recruit profilin-actin for actin polymerization (41). In addition, several phosphorylation sites have been reported on PFN1 (72-75). Notably, phosphorylation of residue S138 occurs downstream of Rho signaling. Some of these modifications regulate binding to actin or poly(L-proline) (76).

There are different kinds of F-actin structures generated by formins, Arp2/3 complex and Ena/VASP. Profilin, by its association with these actin assembly machineries, have been implicated in the formation of F-actin structures associated with stress fibers, cell polarity, centrosome organization, mitotic and meiotic divisions, migration, endocytosis, trafficking and focal adhesions. (9,15). There are about 15 mammalian formins some of which are cell-type specific. In addition to FH1 and FH2, they possess exclusive domains that might help in localization and filament generation in different cellular compartments (41,53,77). Interestingly, the presence of profilin favors assembly of F-actin by formins over Arp2/3 (59,60).

Both actin and mammalian profilins, PFN1 and PFN2, are found in the nucleus. The small size of profilins should enable them to diffuse through the nuclear pores (15). PFN1 has been found in nuclear gems complexed with survival of motor neuron (SMN) (78). SMN interacts with mammalian profilins via its poly(L-proline) motif and is associated with the neurodegenerative disease spinal muscular atrophy (SMA). Further, PFN1 is possibly involved in RNA splicing due to its co-localization with small nuclear ribonuclear proteins (snRNPs) and Cajal bodies (79). Moreover, there is an export factor exportin 6 that transports the

PFN1-actin complex out of the nucleus (80). While the presence of PFN1 in the nucleus is clear, a suitable role for PFN1 in nuclear events needs to be ascertained. Interestingly, actin is believed to participate in a variety of nuclear processes such as chromatin remodeling and transcription (81-83). In addition, formin-2 (FMN2) generated actin filaments in the nucleus participate in DNA repair after drug-induced DNA damage (84). Therefore, if F-actin, formins and PFN1 exist in the nucleus, it is plausible to think of nuclear PFN1 acting to favor polymerization (84-86).

While PFN2 is a brain specific isoform, PFN1 is also found in most neuronal tissues. Both isoforms are present in pre- and post-synaptic compartments, but more so in the latter (87). Both pre-synaptic and post-synaptic proteins that contain poly(L-proline) serve as ligands for profilins in neurons. Examples include (i) gephyrin which is responsible for glycine receptor clustering, (ii) drebrin which is required for dendritic spine morphology, (iii) aczonin is a pre-synaptic scaffold and (iv) delphilin, a formin, is a post-synaptic scaffold that binds glutamate receptor δ2 subunit, indicating that profilins likely contribute to synaptic vesicle cycling, synaptic activity and plasticity (15,88,89). The post-synaptic densities and spines are also enriched in actin filaments suggesting a role for these profilin isoforms in modulating actin dynamics (87). In addition, neuronal stimulation drives both profilin isoforms to dendritic spines (87,90,91).

Profilins in animals

PFN1 is ubiquitously expressed in mammals with the exception of skeletal muscles where the levels are very low (92,93). Homozygous PFN1 knockout in mice is embryonic lethal. The embryos die very early in gestation, as early as two- or four-cell stage, possibly due to failed cleavages (93). This is not surprising in light of the number of binding partners and hence a variety or cellular processes that PFN1 is involved (9,15). PFN1 heterozygous knockout had reduced chances of survival, but the survivors were normal (93).

PFN1 in general acts in the capacity of a pro-migratory and motility factor during development and in adults. Migratory behavior seen during neuronal differentiation, neuritogenesis, and outgrowth of astrocytic processes requires PFN1 (94-98). Whilst PFN1 deletion is embryonic lethal, studies using PFN1 conditional knockout models has aided in understanding the role of PFN1 at the organism level. For example, PFN1 is required for glial cell adhesion and radial migration of cerebellar granule neurons during development. Conditional deletion of PFN1 using nestin-Cre led to cerebellar hypoplasia, disorganized cerebellar cortex layers, Purkinje cell loss and impaired motor coordination (99-102). Deletion of PFN1 in Schwann cells led to impaired lamellipodia formation *in vitro* and radial sorting and myelination *in vivo* (103).

Both PFN1 and PFN2 are found in post-synaptic dendritic spines as well as in pre-synaptic boutons (91,104,105). In addition to exhibiting neuronal subtype specific differential localization with respect to pre- vs. post-synaptic

compartments, PFN1 expression levels vary from one brain region to another (91). Both PFN1 and PFN2 are necessary for the maintenance of dendritic complexity, spine density and morphology (106), the former for spinogenesis and the latter for synaptic function and plasticity (104). Moreover, both PFN1 and PFN2 interact with endocytic components in mouse brains, pointing to their role in synaptic vesicle cycling in the pre-synaptic compartment (92). Surprisingly, conditional knockout of PFN1 in adult forebrain did not affect spine density or structure, synaptic transmission or physiology, suggesting that PFN1 functions can be partly complemented by the PFN2 (107).

On the other hand, PFN2 knockout mice are hyperactive and show increased novelty seeking behavior (105). They impair actin polymerization at synaptosomes under stimulation and increase synaptic vesicle exocytosis. However, loss of PFN2 did not affect neurite outgrowth, long-term potentiation (LTP), long-term depression (LTD), learning and memory further supporting that PFN1 and PFN2 can somewhat complement each other in adult brains (105).

Profilins in diseases

This is the first time disease causing mutations have been identified in PFN1 (7). But PFN1 has been linked to other neurodegenerative conditions such as Huntington's disease (HD) and SMA. Interestingly, huntingtin (HTT) and SMN have both been reported as binding partners of PFN1 (78,108). I will focus on these two neurodegenerative disorders as they are most relevant to this dissertation.

In HTT, the poly(L-proline) motifs occur proximal to the poly-glutamine tract. The levels of both PFN1 and PFN2 were found to be decreased in HD patient brains, cell culture and *Drosophila* models of poly-glutamine disease (108). Contrary to that, Narayanan et al. reported an increase in both PFN1 mRNA and protein levels among other Rho kinase pathway-linked cytoskeletal genes in HD patient brains (109). In cell culture models, expression of mutant HTT enhances PFN1 degradation by the ubiquitin-proteasome system (UPS) and reduces the F/G actin ratio. Exogenous expression of PFN1 restores the F/G actin ratio, mitigates mutant HTT aggregation and toxicity in cell culture models and *Drosophila* (108). Inhibition of HTT aggregation by PFN1 requires its binding to both actin and poly(L-proline) of HTT (75).

The Rho/Rac/Cdc42 family of small GTPases play prominent roles in actin cytoskeletal remodeling (110,111). The diaphanous formins, Arp2/3 and Ena/VASP are all direct or indirect effectors of this family of GTPases (112-114). Rho-associated coiled-coil-containing protein kinases (ROCKs), another downstream effector of RhoA-GTPase, has a number of substrates including myosin light chain, LIM kinases (that phosphorylate cofilin) and profilin (115,116). ROCKs have been considered as therapeutic target for neurological disorders (117,118).

S138 phosphorylation of PFN1 by ROCK1 diminishes its binding to actin and blocks its interaction with HTT (75). ROCK1 inhibition by the drug Y-27632 minimizes poly-glutamine expanded HTT, androgen receptor (AR), ataxin-3,

atrophin-1 aggregation and elevates the activity of UPS and autophagy causing degradation of the poly-glutamine expanded proteins (75,119). PFN1 also has somewhat similar effects in poly-glutamine expanded AR associated with spinobulbar muscular atrophy (SBMA) (75). Another ROCK inhibitor HA-1077 also inhibits profilin phosphorylation *in vivo* and improves retinal defects observed in R6/2 HD mouse model (120). The pathogenic mechanism may involve the interaction of HTT and AR to F-actin (121).

SMA is a motor neuron disease characterized by decreased levels of SMN or loss-of-function mutations in SMN. SMN is essential for mRNA splicing, snRNP transport and neuritogenesis (78,122). Both PFN1 and PFN2 bind to SMN but the latter binds more strongly (78). PFN2 colocalizes with SMN in nuclear gems and growth cones of differentiated PC12 cells in motor neurons (122). PFN1 was also shown to colocalize with gems in HeLa cells (78). Knockdown of both PFN1 and PFN2 in PC12 cells, prevents neurite growth and causes aggregation of SMN in the cytoplasm. Pathogenic mutations in SMN also inhibit neurite outgrowth (123) and diminishes its binding PFN2 (122,123). Knockdown of SMN in PC12 also leads to fewer differentiated cells, short neurites, increased levels of RhoA-GTPase and accumulation of F-actin at the cell periphery. There was an elevated level of PFN2 and its increased association with ROCK (124) possibly resulting in its phosphorylation at S138 (123). The latter was also observed in a severe SMA mouse model (123). In SMA mouse models, there are increased levels of PFN2, decreased plastin 3 (an actin-bundling protein responsible for axon growth) levels

in the brain stem and spinal cord (125) and higher F/G actin ratio (123). Drugs that inhibit RhoA or ROCK including Y-27632, rescued certain neurite outgrowth defects caused by SMN knockdown in PC12 cells (123,124). Further, in U87MG astroglioma cells, SMN knockdown caused decreased migration, loss of stress fibers, reduction in F/G actin ratio, and an increase in PFN1 levels. These cells also show signs of increased RhoA activation and treatment with the ROCK inhibitor Y-27632 restored migration rates of U87MG (126). Taken together, the loss of SMN function point to a dysregulation of PFN2 and to some extent PFN1, and the pathogenesis is probably mediated through RhoA signaling and actin dynamics.

In *Drosophila* the fragile X mental retardation protein (dFMRP) binds and negatively regulates profilin mRNA regulating neurodevelopment (127). In another *Drosophila* study, dFMRP was shown to influence profilin mRNA mobility and transport (128). In *fmr1* knockout mouse, a model of fragile X syndrome, PFN1 levels, but not PFN2, were significantly reduced. Overexpression of PFN1 in *fmr1* knockout mouse rescues the spine phenotypic defects (104).

PFN1 is well studied in the context of cancer proliferation and metastasis where both pro- and anti-migratory roles have been assigned to it (129-131). It is interesting to note that *FUS/TLS*, another ALS-associated gene, was first implicated in cancers as well. In addition, PFN1 is implicated in a variety of disorders such as vascular hypertrophy, diabetic retinopathy and adipose tissue inflammation, which are beyond the scope of this dissertation and are not

discussed (129,132,133). Nevertheless, understanding the role of PFN1 in other diseases can help in our efforts to understand PFN1-ALS pathogenesis.

PFN1 in ALS

ALS-mutations on PFN1 identified till date

Exome sequencing of FALS and SALS patients have resulted in the identification of several mutations in the gene encoding PFN1, namely, C71G, M114T, G118V (7), E117G (7,134), T109M (74), R136W (135), A20T, Q139L (6). The variant E117D was found in Australian SALS patients (136). All the residues that are mutated in ALS are conserved in mammals. The frequency of occurrence of *PFN1* mutations in ALS is similar to those of the other ALS genes, *VCP*, *OPTN*, *UBQLN2* and *SQSTM1* and is estimated to be 1% (2,6). The sites of mutations in PFN1 are indicated in the PFN1 structure shown in Figure I-1.

In addition, several groups reported synonymous mutations when screening for ALS-mutations in PFN1 (137). The most commonly occurring ones are L112L (134,135,138-140) and Q139Q (140). In addition, three novel synonymous mutations, G15G (134), L88L (135), T16T (136) were identified during these screens. Most synonymous mutations have been reported in SNP databases but the allelic frequency in patients needs to be carefully examined to understand their role in ALS.

The genes *c9orf72*, *TDP43* and *FUS* are clearly linked to both ALS and FTD. The only mutation in PFN1 that seems to be associated with FTD is E117G

(74,141,142). It is believed that patients carrying PFN1 mutations represent the ALS-end of the ALS-FTD spectrum of disorders (4,74).

The curious case of E117G

So far, the mutation E117G has been linked to FALS, SALS and FTD. It was also found in controls in several studies (6,7,74,142,143). One study suggested that it is a benign polymorphism (142). But later studies suggest that this mutation occurs at a slightly higher frequency in disease cases compared to controls and is a susceptibility allele (6,74,143). The cellular phenotypes of E117G observed by other groups resemble that of WT (7,144,145), suggesting that it is less pathogenic compared to the other variants.

Progress towards understanding pathogenesis

ALS patients with PFN1 mutations present a predominantly lower motor neuron, spinal onset phenotypes (6,74). At the cellular level, mutations in PFN1, especially C17G, M114T, G118V, A20T cause the protein to aggregate (6,7), although aggregate formation was not observed in *Drosophila* models (7). The mutations cause cytoskeletal abnormalities such as reduced actin binding, defects in axonal growth cone in mouse motor neurons, increased dendritic arborisation and spine density in mouse hippocampal neurons and a reduction in synaptic boutons and F-actin levels at *Drosophila* neuromuscular junction (NMJ) (7,146,147). The mutation T109M does not impair PFN1 binding to actin or affect actin cytoskeleton in HEK293 cells (148).

The ALS-PFN1 variants were linked to RNA metabolism in recent studies. A synthetic lethal screen performed in yeast lacking profilin identified several P-body and stress granule components besides actin-cytoskeletal proteins (144). Under arsenite stress, PFN1 was found in stress granules along with ATXN2, another ALS-associated protein, and the mutants show differences in their association to the stress granules (144). Immunohistochemistry of patient tissues harboring E117G or Q139L mutations show TDP43-positive cytoplasmic inclusions (6,142). In addition, Lewy body pathology was found in the brainstem of one E117G patient (6). This classic TDP43 pathology was confirmed in neuron-like SH-SY5Y cells where it was shown that WT PFN1 interacts with TDP43 and the ALS-mutations cause nuclear depletion, phosphorylation and cytoplasmic aggregation of TDP43 with PFN1 which in turn seeds further TDP43 aggregation (145). Overexpression of mutant PFN1 and TDP43 in Drosophila exacerbates TDP43-induced retinal degeneration in addition to causing cytoplasmic localization of TDP43 in retinal cells (149).

Transgenic mice expressing C71G and G118V have been generated which recapitulate key ALS-phenotypes (150,151). The C71G transgenic mice display late onset, progressive ALS-like motor phenotypes and paralysis in a dose-dependent manner and loss of spinal motor neurons. PFN1 aggregates that stain with ubiquitin were observed in end-stage spinal cord sections. In addition, elevated levels of p62/SQSTM were observed, indicating signs of proteostatic stress. Further, there was reduced expression and disorganized network of

neurofilaments (151). The G118V transgenic mice display reduced amplitude of compound muscle action potential in the hind limb, progressive muscle denervation and loss of ventral horn spinal neurons and NMJs. There was dense nuclear and punctate cytoplasmic skein-like staining of TDP43 and elevated levels of phospho-TDP43 in the end-stage spinal cord sections. The fully symptomatic and end-stage G118V mice showed reduced F/G staining in lumbar spinal cord sections suggesting dysregulation of actin polymerization. Moreover, there was evidence of astrocytosis, microgliosis indicating non-cell autonomous pathways. Other pathological features of the G118V mice include ubiquitinated, insoluble PFN1 aggregates from spinal cord homogenates, axonal degeneration, mitochondrial defects and a reduction in upper motor neurons in the end-stage mice (150). These mouse models will be valuable for researchers in the future to study PFN1-ALS pathogenesis mechanisms.

The burden of misfolded proteins in neurodegeneration

Protein folding

The folding of a protein from a relatively simple primary sequence of amino acids to a biologically functional three-dimensional form is a remarkable process. On the path to acquire a functional native form, a protein encounters less stable intermediate states that can be harmful at times (152). Purely from a chemistry perspective, each state – unfolded, intermediates and folded – have a Gibbs free energy, ΔG°, of formation or folding (also called the thermodynamic or

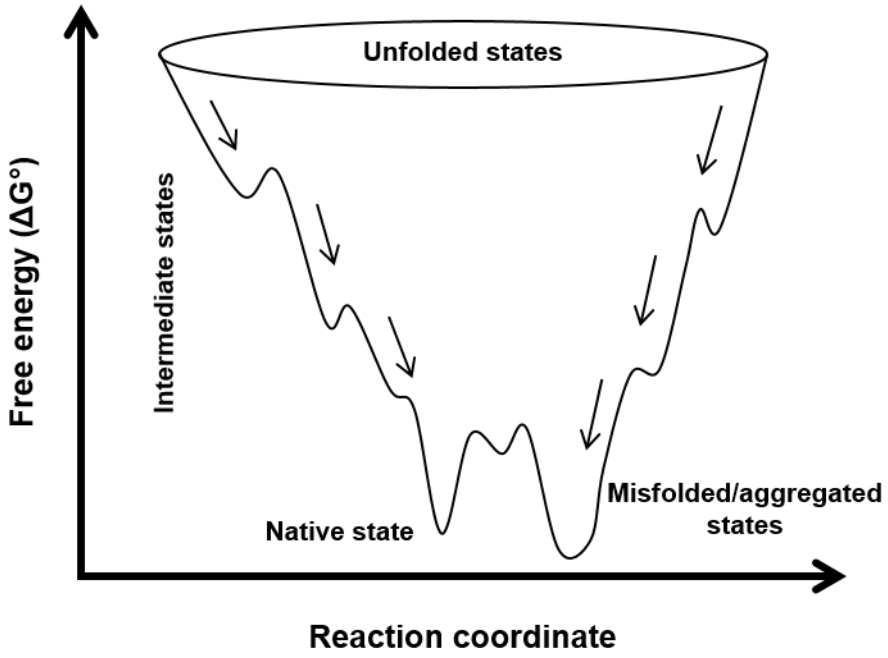

Figure I-4. The protein folding funnel. During the process of folding, the nascent protein chain with high Gibbs free energy samples several states of progressively low free energy until it reaches a native functional form that typically possesses the lowest free energy. But mutations can destabilize or increase the free energy of the native folded state causing them to sample dysfunctional or even toxic misfolded states that have comparable or even lower free energies than the native folded state.

conformational stability) associated with it. The ΔG° is negative in the direction of spontaneity, and a structural state that has the most negative ΔG° (or a high absolute value of ΔG°) is most stable and vice versa (153). A protein samples several states or conformations before it reaches its native state and is often associated with a stable ΔG° value. The process of folding is often intuitively and conveniently represented as a folding funnel (Figure I-4). The protein is "channeled" towards the bottom of the funnel which represents a stable state (154).

In a cell free system, once the protein reaches a stable intermediate state with a certain structure, it can preclude the protein from sampling less stable states. In cells, in addition to this element of spontaneous folding, there are chaperones that assist folding towards the functional state avoiding pitfalls and at the same time reducing the folding time of the protein (154-156). If the free energy gap narrows between a folded protein and a toxic intermediate perhaps due to a destabilizing mutation, then lessons from thermodynamics says that the chances of populating the misfolded intermediate states are higher. Then at equilibrium, a larger fraction of misfolded protein will be present that can become the substrate for an off pathway reaction such as aggregation.

Protein misfolding, aggregation and toxicity

The presence of aggregates of PFN1 mutants in motor neurons puts the topic of protein misfolding in the spotlight. Historically, there has been a heavy emphasis on protein misfolding and aggregation as key mediators of neurodegeneration, most notably the amyloid hypothesis proposed for Alzheimer's disease (AD) (157,158). However, in recent times, new mechanisms underlying neurodegeneration, such as dysregulation of both coding and non-coding RNAs (159-161), started to emerge. Nevertheless, protein misfolding and failure of protein quality control (PQC) mechanisms are actively being studied.

The structure of a protein is crucial for its proper function. Proteins, being dynamic molecules, sample a variety of conformations. When a protein misfolds or adopts a biologically-irrelevant conformation, it can lose its function, aggregate,

or in severe cases it can gain aberrant functions that can be toxic to cells (162,163). There are numerous examples of protein misfolding and aggregation in neurodegeneration – amyloid plaques consisting of amyloid-β (Aβ) fibrils in AD, neurofibrillary tangles consisting of tau in AD and related tauopathies, α-synuclein forming Lewy bodies in Parkinson's disease (PD), poly-glutamine expanded HTT aggregates in HD, prion protein in prion diseases, SOD1 aggregation, cytoplasmic inclusions of TDP43 and FUS, and c9orf72 dipeptides in ALS (162,164-167). Aggregates can be amorphous or structured as in amyloid fibrils (162). A new type of aggregation or inclusion body formation is seen with RNA-binding proteins containing low complexity domains. The aggregation of the disordered low complexity domains of such proteins result in liquid-liquid phase separation whose persistence cause them to become solid-like. Through their RNA recognition motifs these proteins can drag RNAs to the inclusions (168,169).

What causes the toxicity associated with protein misfolding and aggregation? The longstanding question in protein aggregation-mediated neurodegeneration is whether the aggregates are neurotoxic or neuroprotective. It is understood that the toxicity arises from the oligomeric species that are generated during the process of aggregation (162). Oligomers act as seeds for aggregation. These oligomers or the misfolded proteins present hydrophobic groups on their surfaces that can mediate aberrant interactions with cell membranes, receptors, components of endoplasmic reticulum (ER), Golgi and mitochondria, and soluble proteins leading to the drainage of key cellular factors (162). More oligomers can

be generated from fragmentation of aggregates amplifying the toxic effects. Further, these oligomers are capable of prion-like transmission from cell to cell causing aggravation (162). In the case of cytoplasmic inclusions of RNA binding proteins, depletion of RNA and RNA-binding proteins can affect global RNA regulation (170). Understanding the nature of misfolding and aggregate formation is therefore necessary for therapeutic interventions. The advent of new tools such as conformation specific antibodies and structural techniques such as solid-state nuclear magnetic resonance (NMR), cryo-electron microscopy (cryo-EM) is enabling researchers to study protein misfolding and the aberrant nature of aggregates in great detail (171).

Protein quality controls mechanisms

Many proteins have an intrinsic tendency to misfold or aggregate. Naturally, eukaryotic cells have evolved a dedicated and intricate set of machineries to deal with the dissolution of these non-relevant protein species. These protein quality control mechanisms carefully monitor the folding status at every stage during the lifetime of a protein and begin to operate under circumstances of proteostatic stress. At the level of translation, ribosome quality control surveys and degrades nascent chains produced by stalled ribosomes. There are chaperones that help the protein fold in the ER and cytoplasm. Accumulation of misfolded and or aggregated proteins still happen from time to time, but there are mechanisms that recognize misfolded proteins in membranes, cytosol and nucleus and spatially sequester them into different spatial compartments where they can be refolded by

chaperones or degraded by UPS or autophagy. Under conditions of cellular stress such as ER stress, the unfolded protein response (UPR) is initiated, a three-pronged signaling cascade aimed at inhibiting translation, elevating chaperones, evaluating cell health for expression of pro-survival or pro-apoptotic genes. Post-mortem brains of patients with AD, tauopathies, PD, ALS often show signs of oxidative stress, ER stress and UPR (172).

The key issue with the quality control mechanisms is their downgrading with age (162). Research shows age-related (i) increase of oxidative stress, (ii) disturbance in mitochondrial activity, (iii) reduction of chaperone levels, (iv) decline of UPS activity and (v) decreased efficiency of autophagy (162,173-175). With disease causing mutations and other determinants that increase the propensity for misfolding – which happens to be both a cause and an effect of PQC decline – these PQC are over-burdened to the point of a cellular catastrophe (162). Here, I emphasize again the post-mitotic nature of neurons, as there is no chance of recuperation when these quality control mechanisms are compromised. A significant effort, therefore, towards treatment of neurodegenerative diseases has been intervention at the level of protein quality control to minimize build-up of misfolded proteins and is an active area of research (172,176,177).

On account of the presence of PFN1 aggregates in overexpression models (6,7) and the above mentioned implications due to the presence of misfolded proteins and aggregates, it assumes significance to deduce the structural

determinants that leads to its aggregation and potential toxicity. This aspect is explored in detail in Chapter II.

Cytoskeletal defects in neurodegeneration

The neuronal cytoskeleton

Neurons are highly specialized, polarized and asymmetric cells compartmentalized into axons, cell body and dendrites (178). In human motor neurons, axons extend as far as 1 m from the cell body (179), possess complex dendritic branches and synaptic contacts (178). Neurons during development have to constantly seek out cues to form the right synaptic contacts (180). Once post-mitotic, they have to stably maintain axonal structures especially during mechanical stress and at the same time should allow for spatiotemporal changes in synaptic contacts in response to neuronal activity, and repair during injury. This is not possible without the coordinated activity of actin and microtubule cytoskeleton. In short, the neuronal cytoskeleton is significant for proper neuronal function (178,180,181).

The stability and the dynamic nature of microtubules is predominantly determined by post-translational modifications of the tubulin subunits and the hydrolysis-state of bound GTP (178). The axons are composed of stable parallel bundles of microtubules with their plus ends directed away from the cell body towards the axon terminals. Such an orientation aids in bidirectional transport of cargo such as vesicles, RNPs and nutrients by the anterograde kinesin and

retrograde dynein motors (178,181). The axon initial segment close to the cell body consists of a meshwork of actin filaments, probably acting as a filter and sorting cargo for transport along the axons to the distal pre-synaptic terminals (182). Two breakthrough studies described a two-tier organization of actin filaments in axons. The first study, employing high resolution stochastic optical reconstruction microscopy (STORM), identified the presence of periodic adducin-capped F-actin rings connected by spectrins along the axons of hippocampal neurons (183). The presence of these structures was subsequently confirmed in other neuronal cell types (184). These rings appear to be very stable and potentially offer mechanical support to the axons. The second study, using live cell imaging, described dynamic actin trails defined by spurts of rapid formin mediated actin assembly and disassembly along axons that originate from stationary endosomes situated along the axons. They are thought to deliver actin to distal regions of the axons such as the pre-synaptic terminals (185). F-actin is enriched in the form of patches at pre-synaptic boutons and several studies point to a role of these patches in synaptic vesicle clustering, fusion and endocytosis (88,186).

During development, the axonal growth cone regions are rich in both actin and microtubule filaments. The central or C-domain is where the microtubules terminate. Bundles of actin filaments radiate from this region into the peripheral P-domain primarily consisting of F-actin lamellipodia and protruding filopodia that seek out cues from the environment. Between the C- and P-domain is the transition T-domain where contractile actin arcs lie perpendicular to the F-actin bundles. Both

F-actin and microtubules are dynamic in this region allowing for growth cone extension or retraction (178,181).

The dendrites are also comprised of actin and microtubules. The microtubules adopt mixed polarity in the dendrites. The dendritic spines are rich in F-actin and even microtubules have been found to invade these structures. These cytoskeletal assemblies in the spines are modulated and remodeled in response to synaptic activity (187-190). Actin and microtubule dynamics are tightly coupled in both the pre-synaptic and dendritic compartments and there are several factors that mediate the cross-talk and co-ordination between these two (178,181).

Neurofilaments (NF), a type of intermediate filament (IF) found in neurons, are assembled from four proteins NF-H, NF-M, NF-L and α-internexin (adult central nervous system) or peripherin (adult peripheral nervous system). In addition neurons express the Ifs, nestin, vimentin and synemin during development in neurons, but they disappear after maturation. The formation and function of NFs are highly regulated by phosphorylation and glycosylation. Overall NFs act as scaffolds for docking, organizing and regulating synaptic vesicles, endosomes, lysosomes, ER and mitochondria. NFs are present mainly in axons in close co-ordination with microtubules, but are also present in post-synaptic regions. It is required for radial axon growth and stability, modulation of ion channels for proper conduction of electrical impulses along axons. In post-synapses it is involved in dopamine-D1 receptor recycling and synaptic plasticity (LTP in hippocampal neurons). NFs communicate with both microtubule and actin cytoskeleton (191).

A multitude of cytoskeletal proteins have been implicated both directly and indirectly in neurodegeneration. In the rest of this section, I will discuss only key aberrant cytoskeletal features that profoundly dictate disease course.

Microtubule defects

The major cytoskeletal dysfunction associated with neurodegeneration is due to alterations in the stability and dynamics of microtubules which has direct consequences on axonal transport (178). In AD, besides the extracellular amyloid plaques composed of Aβ, aggregates of hyperphosphorylated tau are found in the soma and dendrites where they are referred to as neurofibrillary tangles and neuropil threads respectively (178,192). This pathology is observed in a number of related neurodegenerative conditions collectively termed tauopathies. Certain inherited forms of FTD are due to mutations in tau (192). Tau is a microtubule binding protein and its hyperphosphorylation in diseased states reduces its affinity for microtubules, thereby failing to stabilize microtubules rendering them hyper-dynamic (179,192). However, it has been argued that the effect of tau on microtubules can be limited and that there are also tau-independent mechanisms of microtubule disruption at play (178,179). An example of tau-independent but direct disruption of microtubule function is caused by aberrant regulation of post-translational modifications of tubulin subunits such as acetylation, tyrosination and polyglutamylation and has been observed in several neurodegenerative conditions including AD, PD and HD (178,179,192-195).

The major consequence of alterations of microtubule dynamics such as microtubule destabilization, hyper-dynamicity etc. is the disruption of cargo transport along axons. The Wallerian degeneration or the axon dying back pattern observed in neurodegenerative conditions is characterized by the occurrence of microtubule fragmentation in early stages (179,193). Almost all disease causing mutations in LRRK2, α-synuclein, parkin (PD), SOD1, FUS, TDP43, DCTN1 (ALS), HTT (HD), SMN (SMA) show some form of microtubule abnormalities and axonal transport defects (178,192,196-199). In ALS, disease-causing mutations in SOD1 and FUS cause both anterograde and retrograde transport defects in squid axoplasm assays (200,201). The recently described ALS-causing mutations in TUBA4A alters microtubule dynamics through a dominant-negative mechanism (202). Although axonal microtubule cytoskeleton has been extensively studied, there is evidence for loss of dendritic spines leading to dendritic simplification and decreased synaptic activity (178,179). Significant research efforts have been directed towards developing therapeutics that modulate microtubule cytoskeleton (178).

Actin cytoskeletal defects

Rho-GTPase has been implicated in a number of neurodegenerative diseases (178). The involvement of actin cytoskeleton and Rho/ROCK signaling in HD, SBMA and SMA was discussed earlier in the section “Profilins in diseases”. Actin associated neurite outgrowth defects are frequently reported phenotypes in

neurodegenerative disease models. In ALS, this is observed in SOD1 and TDP43 models (203,204).

Pathological actin structures saturated with cofilin are found in brains of AD patients (205,206). These structures differ from regular F-actin in that they are composed of ADP-actin subunits, cannot be stained with phalloidin and are believed to form in response to energy deficit. The understanding of cofilin-actin rod formation comes from studies in animal and cell culture models of AD and tauopathies where they can be induced by a variety of stimuli such as ATP depletion, oxygen radicals, pro-inflammatory cytokines, Aβ oligomers, cellular prion protein etc. (207-210). An age dependent increase in rods is reported in rat hippocampal neurons (211). A precise pathological mechanism for these structures is not known, but both neuroprotective and neurotoxic roles have been attributed to it. Actin polymerization being an energy-expensive process, cofilin-actin rod formation is thought to freeze actin dynamics during energy stress reallocating ATP for processes that promote survival. On the other hand, these structures are responsible for blocking intracellular transport, loss of synapses and decreased synaptic transmission (205,207,211). Closely related to cofilin-actin rods are actin-rich Hirano bodies found in AD patients and models of AD and tauopathies (212-214). Cofilin-actin rods that contain HTT also form in the nucleus in response to heat shock, and mutant HTT causes persistence of rods (215). Cofilin-actin rods are unreported in ALS. For further information, readers are

encouraged to consult an excellent review article published by Bamburg and Bernstein in the journal Cytoskeleton (207).

The non-neurological muscle disorder relevant to this discussion, intranuclear rod myopathy, are caused by mutations in the skeletal muscle α1-actin (ACTA1). This disease is characterized by intranuclear rod-aggregates of actin and actin-binding proteins. In cell culture models these rods can be mostly stained with phalloidin (unlike cofilin-actin rods). Pathogenic mechanisms include nuclear rod induced changes to RNA polymerase II localization and chromatin organization patterns in addition to disrupted sarcomeric structure (216-219).

Neurofilament defects

Mutations in NF-L cause Charcot-Marie-Tooth disease (CMTD) type 2E and 1F. The mutations affect assembly and transport of NF proteins along axons, reduce axon calibers and impair nerve conduction. Mutations in NF-H and peripherin cause ALS. Mutations in NF-M domain are linked to familial PD and AD. A type of frontotemporal dementia (FTD) called neurofilament inclusion body disease is characterized by the presence of α-internexin in NF protein aggregates. Typically, the pathological feature associated with mutations in NF genes is NF aggregation and failure of NF protein transport along axons leading to axonal dysfunction and degeneration. The NF pathology can also be caused by mutations in other genes such as *HSPB1* in CMTD2F, *gigaxonin* in giant axonal neuropathy, *SOD1* in ALS (191).

Summary

ALS is a debilitating disease leading to paralysis and death. Like most neurodegenerative diseases, ALS is a complicated disease for which no cure has been found despite extensive research following the discovery of the first gene three decades ago. A multitude of interconnected pathways are ascribed to the disease pathogenesis driven by various genes. PFN1 mutations bring forward the case of actin cytoskeletal alterations in ALS. In this dissertation, I look at the two aspects meriting attention and that were also alluded to in this chapter – structural and functional defects of the ALS causing mutations on PFN1. In Chapter II, I try to establish the reasons behind its aggregation in cells. In Chapter III, I attempt to decipher the biochemical implications of mutant PFN1 in actin cytoskeletal assembly. Since structure and function of a protein are interdependent, the functional alterations observed in PFN1 could result directly from the structural defects, and therefore correcting the structure should help correct abnormalities in function.

PREFACE TO CHAPTER II

Dr. Kristin Boggio analyzed the mass spectrograms of purified PFN1 proteins. Noah Cohen provided assistance in fitting the chemical denaturation data. Maeve Tischbein performed the PFN1 turnover experiments in SKNAS cells. Dr. Osman Bilsel helped collect intrinsic tryptophan fluorescence decay data for PFN1. Tania Silvas, Dr. Shivender Shandilya and Dr. Celia Schiffer solved PFN1 crystal structures. Dr. Silvia Jansen and Dr. Bruce Goode performed pyrene-actin polymerization assays. Most of Chapter II, except for Figure II-7, appeared in the following publication,

Boopathy S, Silvas TV, Tischbein M, Jansen S, Shandilya SM, Zitzewitz JA, Landers JE, Goode BL, Schiffer CA, Bosco DA. Structural basis for mutation-induced destabilization of profilin 1 in ALS. Proc Natl Acad Sci U S A. 2015 Jun 30;112(26):7984-9.

CHAPTER II – STRUCTURAL BASIS FOR MUTATION-INDUCED DESTABILIZATION OF PFN1 IN ALS

Introduction

The observation that most ALS-linked PFN1 variants are highly prone to aggregation in mammalian cultured cells suggests that disease-causing mutations induce an altered, or misfolded, conformation within PFN1 (7). Protein misfolding is a hallmark feature of most neurodegenerative diseases, including ALS (220), and can contribute to disease through both gain-of-toxic-function and loss-of-normal-function mechanisms (221).

While ALS-linked mutations were shown to induce PFN1 aggregation, the effect of these mutations on protein stability and structure has not been studied. Because the impact of disease-causing mutations on protein stability varies from protein to protein (222-224), these parameters must be determined empirically. Here, we demonstrate that certain familial ALS-linked mutations severely destabilize PFN1 *in vitro* and cause faster turnover of the protein in neuronal cells. To gain insight into the source of this mutation-induced instability, the three-dimensional crystal structures for three PFN1 proteins, including the WT protein, were solved by X-ray crystallography. We discovered that the M114T mutation created a cleft that extended into the interior of PFN1. Further, we predict that the most severely destabilizing C71G mutation also creates a cavity near the core of the PFN1 protein, proximal to the cleft formed by M114T. Experimental mutations

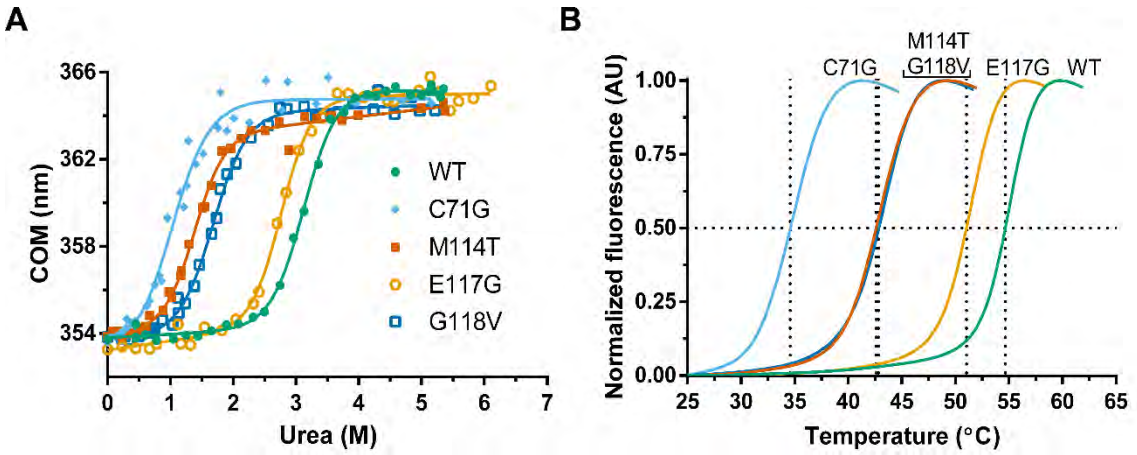

Figure II-1. ALS-linked mutations destabilize PFN1. Chemical and thermal denaturation studies reveal that ALS-linked variants C71G, M114T, and G118V, but not E117G, are severely destabilized relative to PFN1 WT. (A) Equilibrium unfolding curves for PFN1 WT and ALS-linked variants generated by measuring the intrinsic tryptophan fluorescence of the indicated protein equilibrated in increasing concentrations of urea. Data were processed to obtain the center of mass (COM) of the emission spectrum and then fit to a two-state model for protein folding. The resulting fits are displayed as solid lines. The corresponding thermodynamic parameters obtained from the fitted data are shown in Table II-1. (B) Thermal denaturation profiles of PFN1 proteins measured by SYPRO Orange fluorescence as a function of increasing temperature were used to determine the apparent T_m, which is the temperature corresponding to 0.50 fluorescence signal as denoted by the intersection of the dashed lines for each curve.

that create enlarged pockets or cavities are known to exert a destabilizing effect on the native conformation of the protein (225), and there are several examples of mutation-induced cavity formation occurring in nature and disease (226,227). Interestingly, the variant predicted to be the least pathogenic according to recent genetics studies, E117G, was relatively stable and closely resembled the WT protein in every assessment performed herein (7,143). These data implicate a

destabilized form of PFN1 in ALS pathogenesis and call for therapeutic strategies that can stabilize mutant PFN1.

Results

ALS-linked mutations destabilize PFN1 in vitro

To investigate the effect of ALS-linked mutations on the stability of PFN1, PFN1 proteins were expressed and purified from *Escherichia coli* (*E. coli*) and subjected to chemical and thermal denaturation analyses. A novel purification protocol that includes sequential cation-exchange and gel filtration chromatography steps was developed here and applied to all PFN1 variants (see Appendix I). PFN1 C71G was found to be highly prone to aggregation in *E. coli*, consistent with observations that this variant exhibited particularly low solubility in mammalian cells (7), and therefore was isolated from inclusion bodies (see Appendix I). The biochemical properties of PFN1 C71G purified from inclusion bodies are indistinguishable from PFN1 C71G purified from the soluble lysate of *E. coli* as determined by several assays (Figure AI-4), providing confidence that PFN1 proteins purified by these two methods can be directly compared.

To examine the stability of PFN1 proteins, fluorescence from tryptophans (W4 and W32) in PFN1 WT and ALS-linked variants was measured as a function of increasing urea concentration (Figure II-1A). To ensure reversibility, the reciprocal analysis was also performed, where denatured PFN1 proteins in urea were refolded upon dilution with buffer (Figure II-2A-E). Only one transition was

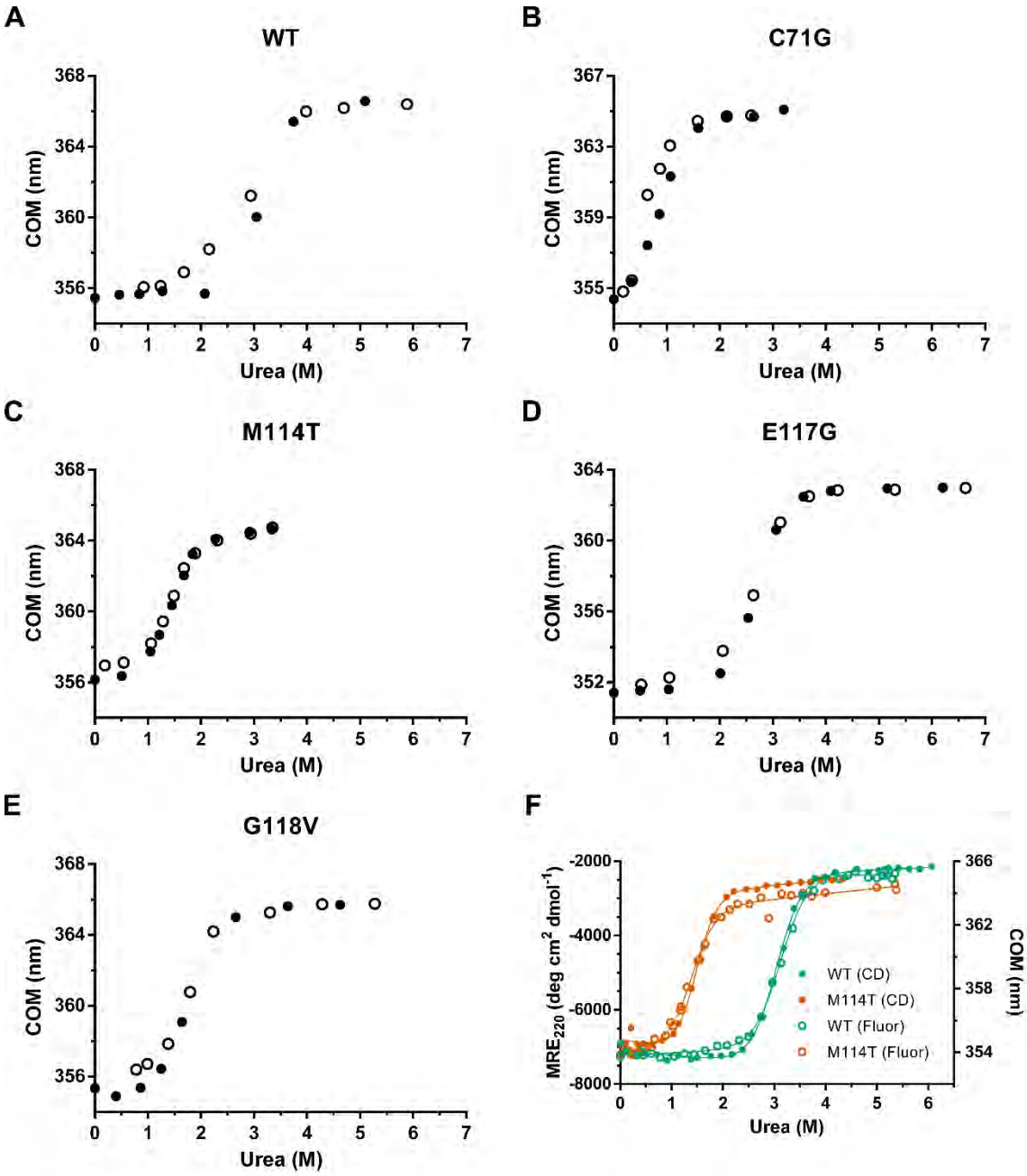
A
WT
COM (nm)
Urea (M)
B
C71G
COM (nm)
Urea (M)
C
M114T
COM (nm)
Urea (M)
D
E117G
COM (nm)
Urea (M)
E
G118V
COM (nm)
Urea (M)
F
MRE220 (deg cm2 dmol-1)
COM (nm)
Urea (M)
WT (CD)
M114T (CD)
WT (Fluor)
M114T (Fluor)

Figure II-2. All PFN1 variants unfold by a two-state process. (A–E) PFN1 variants denatured in urea were refolded by diluting the urea. The final concentration of PFN1 in each sample was 10 μM and tryptophan fluorescence was used to monitor folding. The equilibrium transition regions overlay closely for the unfolding and refolding curves, indicating that the unfolding reaction is reversible. Filled and open circles represent unfolding and refolding, respectively. (F) The two-state unfolding of PFN1 observed by intrinsic fluorescence (data from Figure II-1A; Fluor) was verified by CD measurements for PFN1 WT and M114T. The concentration of protein used was 2 μM and 10 μM for tryptophan fluorescence and CD measurements, respectively. The y axis on the left is the mean residue ellipticity at 220 nm (MRE_{220}) obtained from CD experiments, whereas the y axis on the right reflects the change in the COM (as shown in Figure II-1A). The thermodynamic parameters obtained by fitting the CD data agree well with those obtained from the fluorescence data (Table II-1) and are as follows: for WT $\Delta G°$ = 7.16 ± 0.11 kcal·mol^{-1}, m = 2.36 ± 0.04 kcal·mol^{-1}·M^{-1}, C_m = 3.03 ± 0.07 M; for M114T $\Delta G°$ = 4.35 ± 0.10 kcal·mol^{-1}, m = 2.95 ± 0.06 kcal·mol^{-1}·M^{-1}, C_m = 1.47 ± 0.05 M.

observed between the folded or native (N) and unfolded (U) states for all PFN1 proteins, indicative of a two-state (N⇆U) unfolding mechanism. This two-state unfolding model was further substantiated with an unfolding study of two PFN1 proteins (WT and M114T) using circular dichroism (CD) spectroscopy (Figure II-2F). The following thermodynamic parameters were determined by fitting the fluorescence data to a two-state folding model: apparent $\Delta G°$, the free energy of folding; m, the denaturant dependence of $\Delta G°$; and C_m, the midpoint of the unfolding transition (Table II-1). Both $\Delta G°$ and C_m were reduced for ALS-linked variants relative to PFN1 WT, particularly for the PFN1 variants C71G, M114T and G118V, indicating these variants are severely destabilized compared to PFN1 WT (Figure II-1A and Table II-1). Differential scanning fluorimetry (DSF) with SYPRO Orange, a fluorescent indicator of hydrophobic regions exposed upon protein

Table II-1. Summary of experimental stability and binding measurements for PFN1 variants.

Variant	Equilibrium unfolding (N⇆U)[a]			Melting temperature, Tm (°C)[b]		Binding to poly-L-proline[b], K_d (μM)[c]
	ΔG° (kcal mol^{-1})	m (kcal mol^{-1} M^{-1})	C_m (M)	Protein alone	+ 4 mM proline	
WT	7.04 ± 0.49	2.25 ± 0.16	3.13 ± 0.31	54.68 ± 0.04	57.25 ± 0.03	463 ± 26
C71G	1.89 ± 0.70	1.95 ± 0.40	0.97 ± 0.41	34.60 ± 0.03	39.96 ± 0.03	687 ± 77
M114T	3.51 ± 0.40	2.51 ± 0.24	1.40 ± 0.21	42.62 ± 0.03	46.52 ± 0.02	572 ± 23
E117G	6.90 ± 0.74	2.49 ± 0.26	2.77 ± 0.42	51.05 ± 0.04	53.78 ± 0.03	407 ± 27
G118V	3.70 ± 0.44	2.20 ± 0.23	1.68 ± 0.26	42.84 ± 0.04	46.92 ± 0.04	397 ± 40

[a]Errors are shown as SD.
[b]Errors are shown as SEM.
[c]K_d values are reported in terms of proline residues.

unfolding, was employed next to determine the apparent melting temperature, T_m, for all PFN1 proteins used in this study (228). Consistent with the chemical denaturation results, all ALS-linked variants except E117G exhibited a T_m that was at least 10 °C lower than WT (Figure II-1B, Table II-1). Based on the denaturation studies, C71G emerges as the most destabilizing mutation in the context of PFN1, whereas the E117G mutation has a relatively modest impact on PFN1 stability.

ALS-linked PFN1 exhibits faster turnover in a neuronal cell line

The turnover rate for proteins with destabilizing mutations is often faster relative to their wild-type counterparts, generally because destabilized proteins are misfolded and targeted for degradation by the cellular quality control machinery (229). To determine whether the results of our *in vitro* denaturation studies extend to a cellular environment, V5-tagged PFN1 variants were transiently transfected into human neuronal SKNAS cells, and PFN1 turnover was assessed by tracking

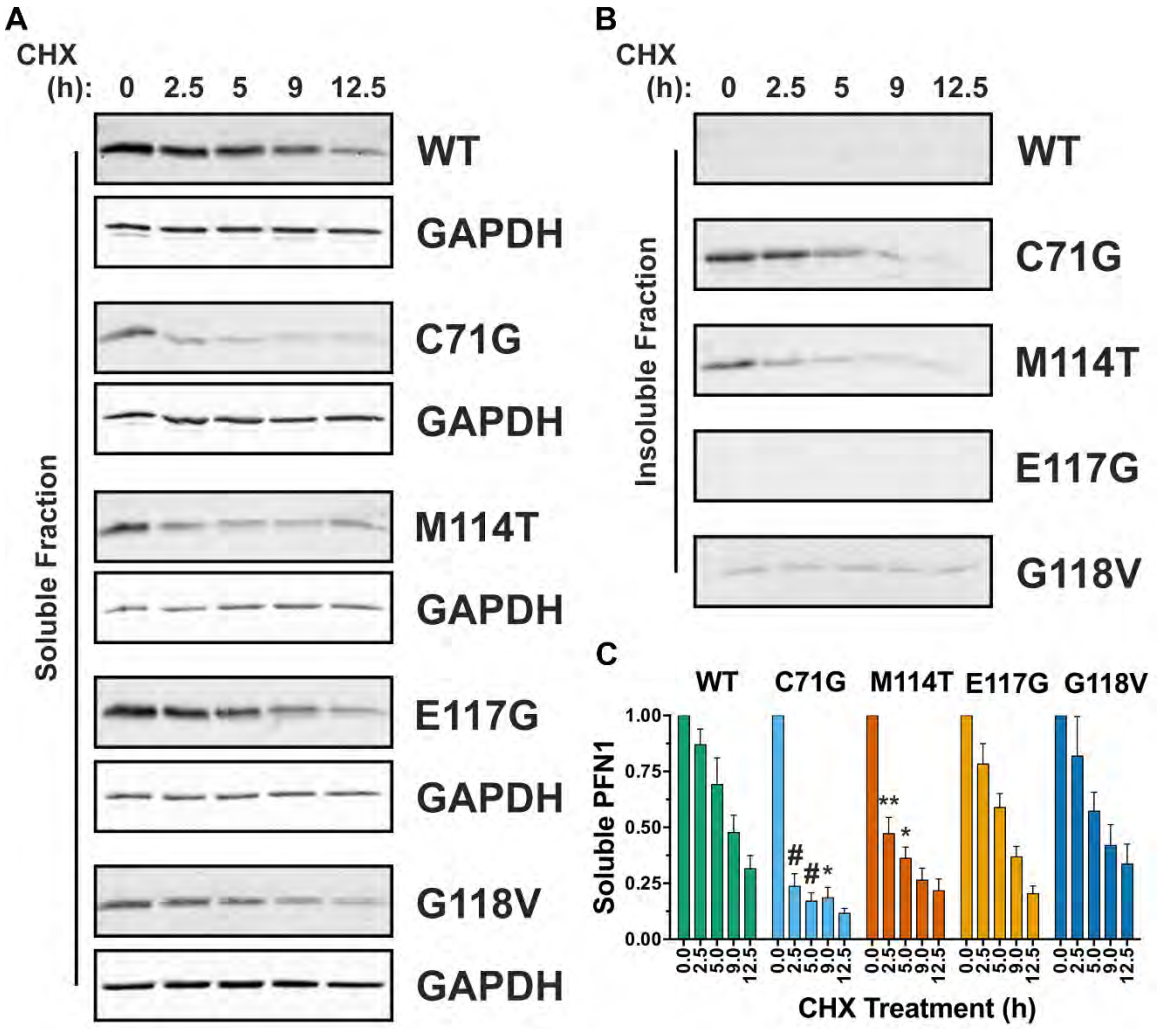

Figure II-3. ALS-linked PFN1 variants exhibit faster turnover in a neuronal cell line. SKNAS cells transiently transfected with V5-PFN1 constructs were treated with cycloheximide (CHX) for up to 12.5 h, during which time lysates were collected and probed by Western analysis with a V5-specific antibody to assess the rate of PFN1 turnover in cells. (A and B) A representative Western blot analysis of soluble and insoluble fractions from cell lysates demonstrates a decrease in V5-PFN1 protein with time. GAPDH serves a loading control for the soluble fraction. (C) Densitometry analysis of (A) reveals that the turnover of PFN1 C71G and M114T is significantly faster than that of PFN1 WT. Statistical significance was determined using a two-way ANOVA followed by a Tukey's post hoc analysis (*P < 0.05, **P < 0.01, #P < 0.0001). Error bars represent SEM. WT and E117G, n = 3; G118V, M114T and C71G, n = 4 independent experiments.

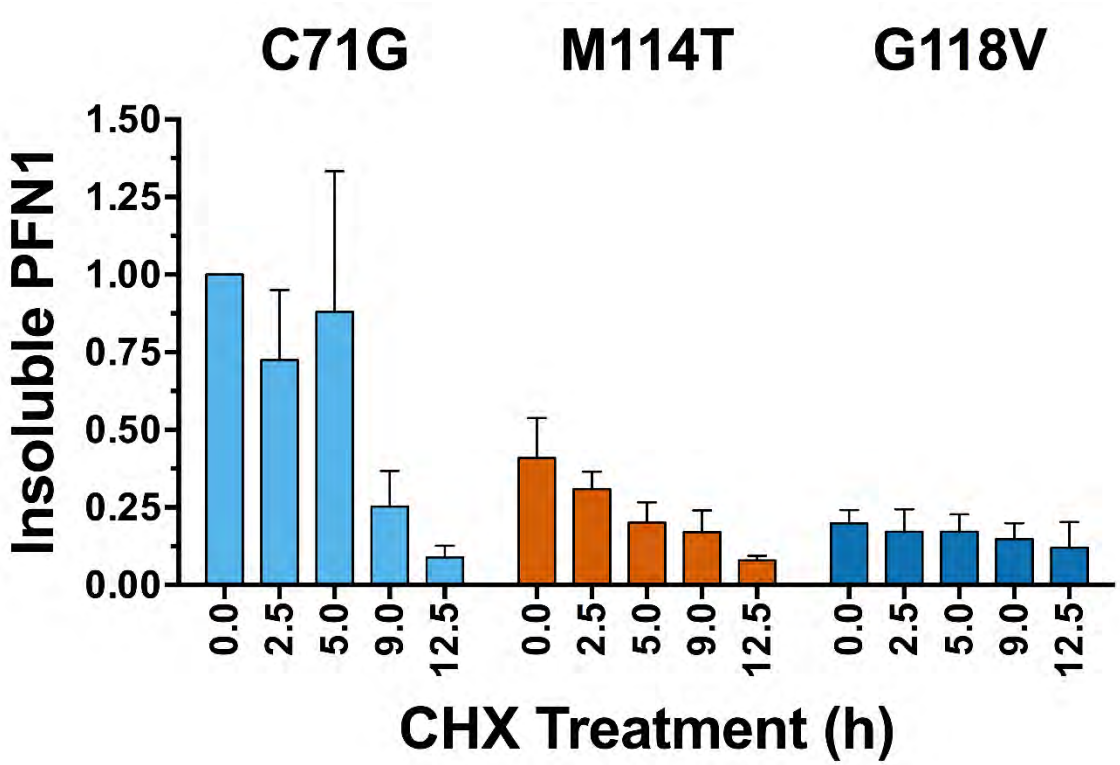

Figure II-4. The turnover of insoluble PFN1 in SKNAS cells. The experiment was carried out as described in Figure II-3, and a representative Western blot analysis of the insoluble fraction is shown in Figure II-3B. The data above reflect the densitometry results from an average of n = 2 (M114T) or n = 3 (C71G and G118V) independent experiments and error bars represent SEM. Each sample was normalized to the PFN1 C71G band corresponding to "time 0." The turnover of C71G within the insoluble fraction was slower relative to C71G within the soluble fraction (compare this graph to that in Figure II-3C). There was relatively less M114T and G118V in the insoluble fraction compared with C71G, and the small fraction of insoluble G118V persisted throughout the experimental time course.

V5-PFN1 protein expression over a 12.5 h time course in the presence of cycloheximide. At the start of the experiment (t = 0 of the cycloheximide time course), all V5-tagged PFN1 variants were expressed at similar levels except that V5-PFN1 C71G, M114T and G118V partitioned into the insoluble fraction (Figure

II-3A and B) as reported previously (7). The turnover of both PFN1 C71G and M114T occurred significantly faster than PFN1 WT. As early as 2.5 h, the majority of PFN1 C71G and M114T within the soluble fraction had already degraded (Figure II-3A and C). This decrease in soluble PFN1 content was not simply due to further PFN1 aggregation, which could confound our analysis, as evidenced by the concomitant clearance of PFN1 from the insoluble fraction at the early time points of cycloheximide exposure (Figure II-3B). The faster turnover of PFN1 C71G and M114T in cells closely correlates with their reduced stabilities *in vitro*, confirming the destabilizing effect of the C71G and M114T mutations. We note that the turnover of PFN1 C71G was faster in the soluble fraction compared to the insoluble fraction (Figure II-4), likely because clearance of insoluble cellular aggregates by the quality control machinery is less efficient compared to the turnover of smaller, soluble species (230). Although PFN1 G118V was destabilized to a similar degree as M114T *in vitro*, the turnover of this variant within the soluble fraction appeared slower in cells (Figure II-3C), which may reflect a stabilizing effect of other proteins and/or factors that interact with PFN1 in the cellular milieu (15), or that this variant is not properly handled by the quality control machinery in the cell. In fact, we detected a low level of insoluble PFN1 G118V that persisted throughout the 12.5 h time course (Figure II-3B and Figure II-4).

ALS-linked mutations induce a misfolded conformation within PFN1

We reasoned that ALS-linked variants must undergo some degree of structural or conformational change to account for their destabilization. However,

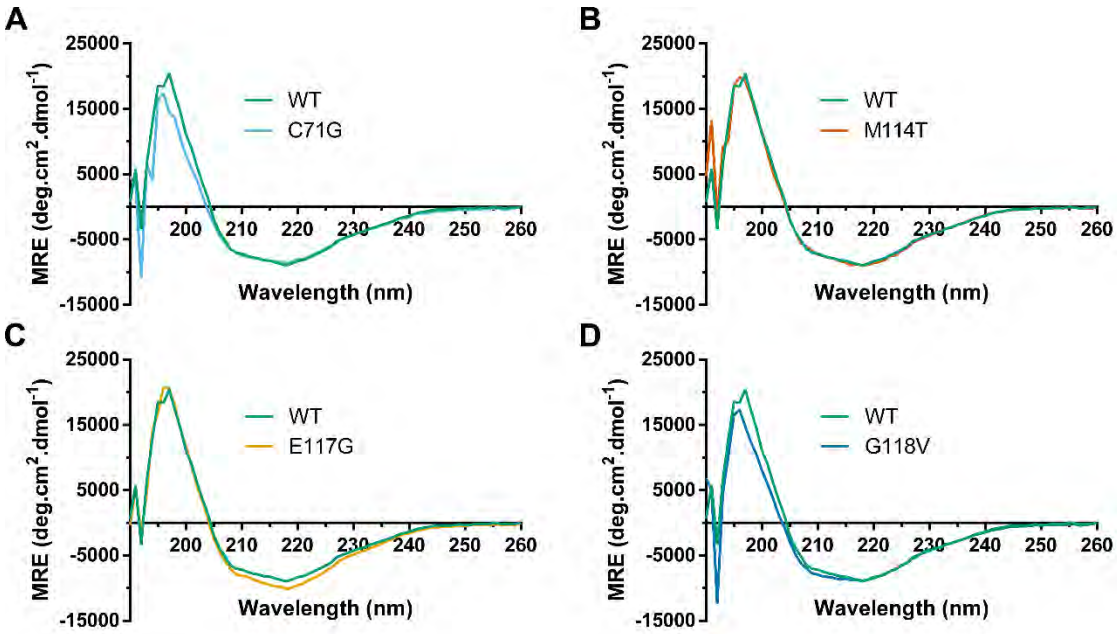

Figure II-5. ALS-linked PFN1 variants retain the same secondary structure as PFN1 WT. (A–D) Far UV CD spectra for the indicated PFN1 variant (10 μM) overlaid with CD spectrum for PFN1 WT (10 μM).

ALS-causing mutations did not perturb the secondary structural elements of PFN1 as determined by circular dichroism (CD) spectroscopy (Figure II-5) and the fact that similar m values were determined for all PFN1 variants by the urea denaturation analysis suggested these proteins adopt similar tertiary structures as well (Table II-1) (231). To probe further for potential structural differences between PFN1 WT and ALS-linked variants, these proteins were subjected to native gel electrophoresis, a biochemical technique capable of detecting conformational differences between misfolded variants and their wild-type counterparts (232). PFN1 WT and E117G migrated predominately as single, distinct bands with similar mobility, whereas multiple bands of slower mobility were observed for PFN1

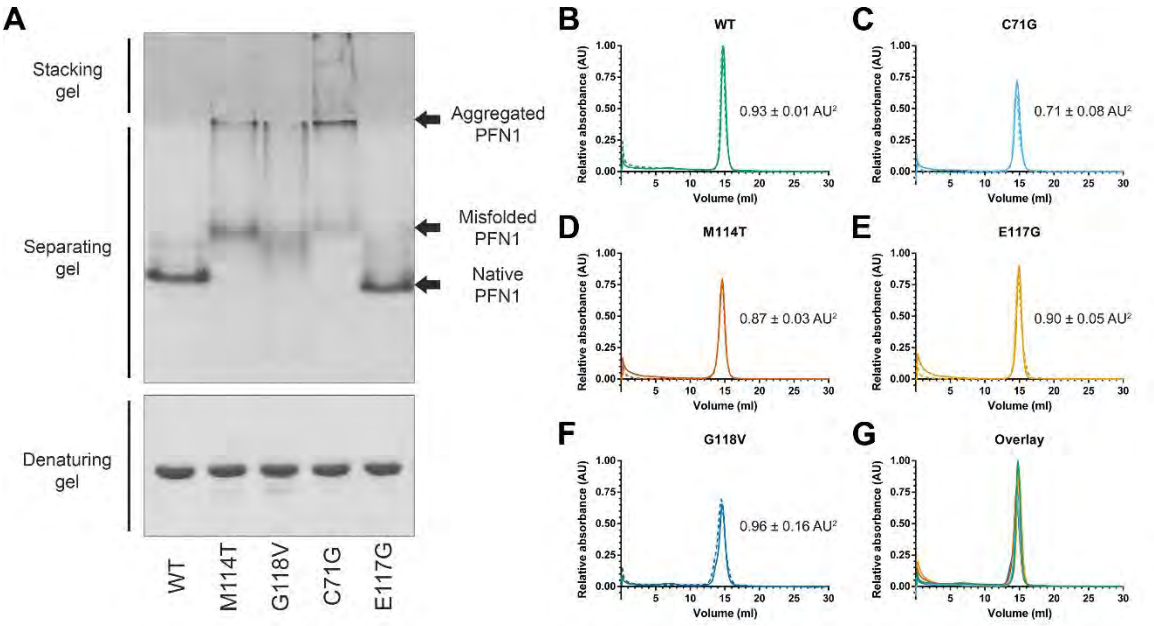

Figure II-6. Analysis of PFN1 proteins by native page and analytical size-exclusion chromatography. (A) PFN1 proteins (10 µg) were subjected to native (top) or denaturing (bottom) gel electrophoresis and detected with Coomassie Brilliant Blue stain. The mobility of native PFN1 WT is indicated. PFN1 E117G migrates with a slightly faster mobility than PFN1 WT owing to the addition of a negatively charged amino acid. Misfolded ALS-linked PFN1 variants migrate with slower mobility and form aggregated species that are retained in the stacking gel. This gel is representative of n = 2 experiments using proteins from different purification preparations. (B–F) The indicated PFN1 protein (40 µg) was subjected to analytical size-exclusion chromatography using a Superdex 75 column. A single peak corresponding to the expected elution volume (~15 ml) for monomeric PFN1 was detected for all PFN1 proteins. The experiments were carried out in duplicate for each variant, indicated by solid (n = 1 experiment) and dashed (n = 2 experiment) lines. The average relative peak area ± the SD is indicated to the right of each curve. Despite equal sample loading, the peak area of PFN1 C71G and M114T is lower than that of WT (within error), consistent with a reduced level of soluble protein for these ALS-linked variants. (G) An overlay of B–F for the n = 1 experiment demonstrates a similar elution profile for all PFN1 proteins.

variants C71G, M114T and G118V (Figure II-6A). The slower mobility bands likely reflect the larger hydrodynamic volume due to partial unfolding of these variants.

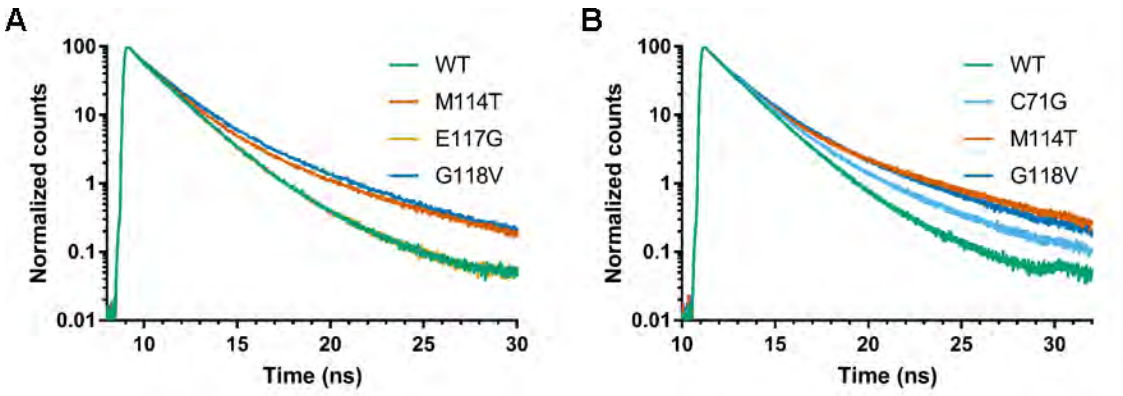

Figure II-7. The PFN1 mutants exhibit relatively slower tryptophan fluorescence decay. PFN1 proteins (4 μM) were excited with vertically polarized light at 295 nm and the horizontal and vertical emission at 350 nm were measured over time. Figures show the total fluorescence decay plots of (A) WT, M114T, E117G and G118V and (B) WT, C71G, M114T and G118V. The decay profiles of WT and E117G were similar, but the mutants C71G, M114T and G118V decayed relatively slowly compared to WT and E117G. This figure was not part of the original publication.

In addition, PFN1 C71G, M114T and G118V produced relatively large molecular-weight species that were retained in the stacking gel and unable to electrophorese through the separating native gel, but were resolublized under conditions employed for the denaturing gel (Figure II-6A). Analytical size exclusion chromatography revealed that all PFN1 proteins eluted as expected for soluble, monomeric PFN1 (Figure II-6B-G). However, despite equal loading of PFN1 proteins onto the analytical size exclusion column, the peak area corresponding to soluble monomer PFN1 is reduced for ALS-linked variants, particularly for the most aggregation prone variant C71G. These data are consistent with a loss of soluble monomer PFN1 in the form of insoluble species that cannot pass through the analytical size exclusion column filter. In addition, measurements of tryptophan

Table II-2. Crystallographic and refinement statistics of human PFN1 structures.

	WT	E117G	M114T
Resolution (Å)	2.160	2.170	2.230
Space group	C121	C121	P6
a (Å)	74.26	73.65	81.69
b (Å)	31.84	31.71	81.69
c (Å)	61.02	60.54	65.35
A	90°	90°	90°
B	122.66°	122.03°	90°
Γ	90°	90°	120°
Z	1	1	2
R_{merge} (%) linear	0.075	0.036	0.147
I/sigma	13.3	12.2	12.4
Completeness (%)	99.28	99.49	99.58
Total no. of reflections	20783	16453	76801
No. of unique reflections	6416	6422	12156
R_{factor} (%)	0.2159	0.1965	0.1952
R_{free} (%)	0.2469	0.2139	0.2383
RMSD in: Bond lengths (Å)	0.002	0.003	0.003
RMS Angle (°)	0.62	0.67	0.61
Temperature (°C)	-80	-80	-80
Residues Missing: Chain A	1, 2, 57-62, 92-96	1, 2, 59-62, 81,82, 93-95, 140	1, 93-97
Chain B	---	---	1, 13, 91-97
PDB ID	4X1L	4X1M	4X25

fluorescence decay revealed that the variants C71G, M114T and G118V exhibited a slower decay relative to WT and E117G whose decay profiles were similar, further pointing to the existence of a misfolded conformation among the ALS-PFN1 variants (Figure II-7).

A source of mutation-induced destabilization revealed by X-ray crystallography of PFN1

Crystal structures of PFN1 proteins were determined in order to identify regions within mutant PFN1 that are conformationally distinct from PFN1 WT at atomic resolution. PFN1 WT, E117G and M114T produced crystals that diffracted at relatively high resolution (~2.2 Å; Table II-2). The three-dimensional structure of human PFN1 WT agrees well with previously determined structures (25,67,233). PFN1 WT and E117G crystallized in the same space group, C121, whereas M114T crystallized in the P6 space group, with two molecules (designated as chains A and B) in the asymmetric unit (Table II-2).

Residues 22–36, 46–52, 101–105, 112–120 and 125–128 within PFN1 were used for Cα superimposition of the four molecules (PFN1 WT, M114T chains A and B, and E117G). In agreement with the biochemical analyses described above (Table II-1 and Figure II-5), the secondary and tertiary structures of all three PFN1 proteins, including chains A and B of M114T, are highly similar (Figure II-8). Although the space groups for PFN1 WT and M114T crystals were different, we calculated the double difference plots between these and the other PFN1 structures to get a sense for structural perturbations potentially induced by the

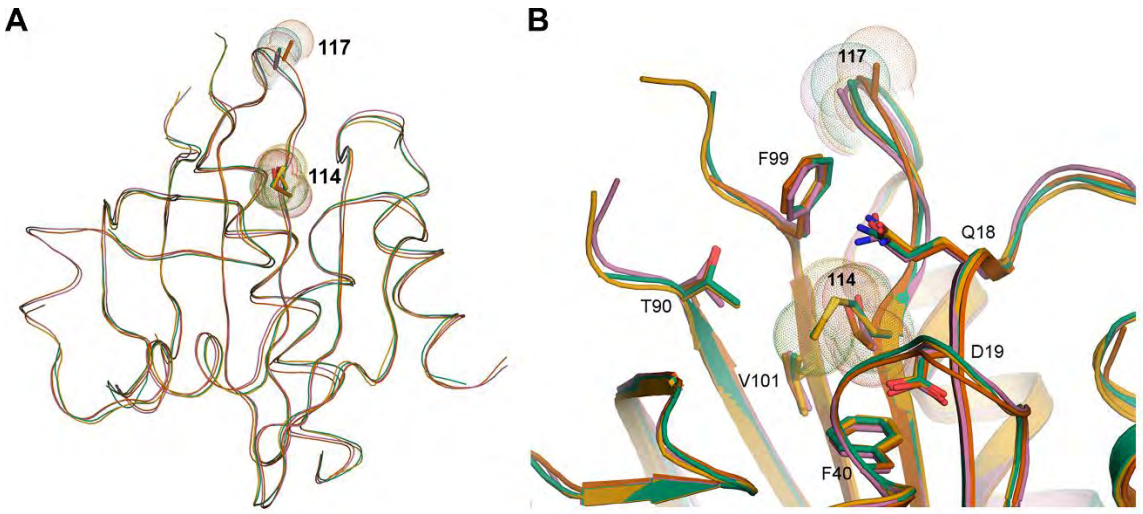

Figure II-8. Superimposition of the crystal structures for PFN1 WT, E117G, and M114T. (A and B) The secondary and tertiary structures for PFN1 WT (green), E117G (mustard), M114T chain A (pink), and B (red) are highly superimposable. For each structure, sticks and spheres denote the side chains and van der Waals radii, respectively, for residues at position 114 and 117. Residue 117 is located within a solvent-exposed flexible loop that has no discernible secondary structure, whereas Met114 is located within a β-sheet toward the interior of the protein. (B) A zoomed cartoon representation showing residues within 4 Å of residue 114. The side chains of these residues are indicated as sticks with nitrogen, oxygen, and sulfur atoms indicated in blue, red, and yellow, respectively. The van der Waals radii of the atoms comprising residue 114 are reduced upon mutation of methionine (green and mustard structures) to threonine (red and pink structures).

ALS-linked mutations. Double difference plots were constructed by calculating the distances between all of the Cα atoms in PFN1 WT and an ALS-linked variant separately, and then plotting the difference of the difference between PFN1 structures as described previously (234). Virtually no structural deviations were observed between PFN1 WT and E117G, whereas moderate differences were detected between WT and M114T (Figure II-9).

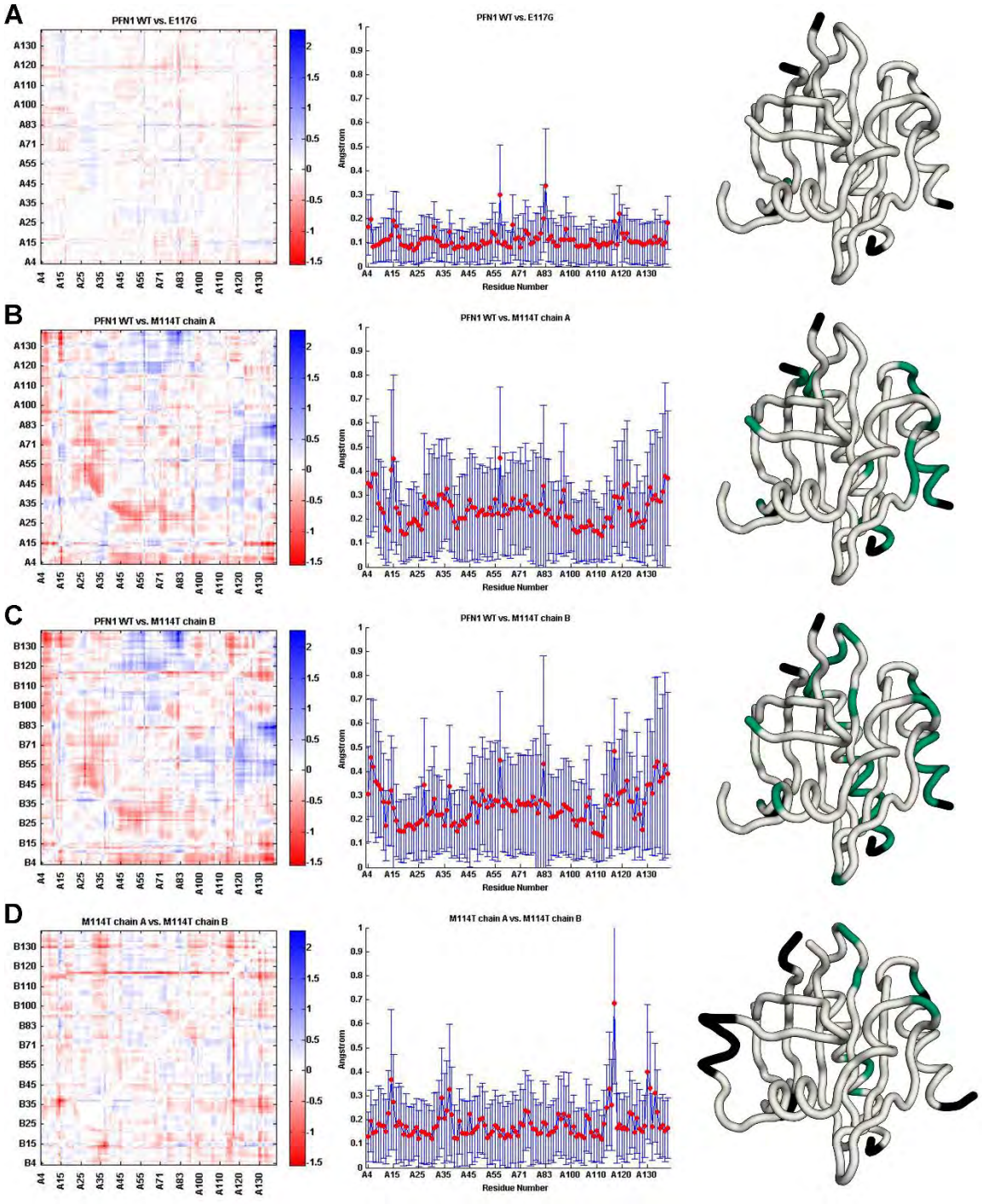
A
PFN1 WT vs. E117G
PFN1 WT vs. E117G
Angstrom
Residue Number
B
PFN1 WT vs. M114T chain A
PFN1 WT vs. M114T chain A
Angstrom
Residue Number
C
PFN1 WT vs. M114T chain B
PFN1 WT vs. M114T chain B
Angstrom
Residue Number
D
M114T chain A vs. M114T chain B
M114T chain A vs. M114T chain B
Angstrom
Residue Number

Figure II-9. Structural changes induced by the M114T mutation revealed in double difference plots. Double difference plots (left) of WT vs. E117G (A), WT vs. M114T chain A (B), WT vs. M114T chain B (C), and M114T chains A vs. B (D). The Avg-Abs-DD values are plotted as a function of residue number for each structural comparison (middle); these plots provide an indication for residues that undergo a structural change between the proteins that are being compared. Residues with Avg-Abs-DD values of 0.3 Å or greater are plotted onto the structure (right) of PFN1 WT (A–C) and PFN1 M114T chain A (D) in green. Residues not used in this analysis are colored black.

Next we sought to determine whether these moderate structural changes between PFN1 WT and M114T mapped to regions involved in PFN1 function, namely to residues that make contact with actin (17,31,47,57,235-238) or poly(L-proline) (22,25,67,235,239). The ternary complex comprised of PFN1 WT, actin and the poly(L-proline) peptide derived from vasodilator-stimulated phosphoprotein (VASP) (67) (PDB ID: 2PAV) is shown in Figure II-10. Residues with the highest (0.3 Å or greater) average of absolute double difference (Avg-Abs-DD) values between PFN1 WT and M114T chain B (Figure II-9C) were mapped onto PFN1 WT (Figure II-11). PFN1 M114T chain B was used for this and all subsequent structural comparisons because chain B had lower B-factors compared to chain A (Figure II-12). Indeed, several PFN1 residues that reportedly make contacts with actin (V119, H120, G122, K126) and poly(L-proline) (W4, Y7, H134, S138) also have relatively high Avg-Abs-DD values (Figure II-11).

To assess whether these mutation-induced structural changes are sufficient to alter the normal binding interactions of PFN1, we first monitored changes in the intrinsic tryptophan fluorescence of PFN1 as a function of poly(L-proline) peptide

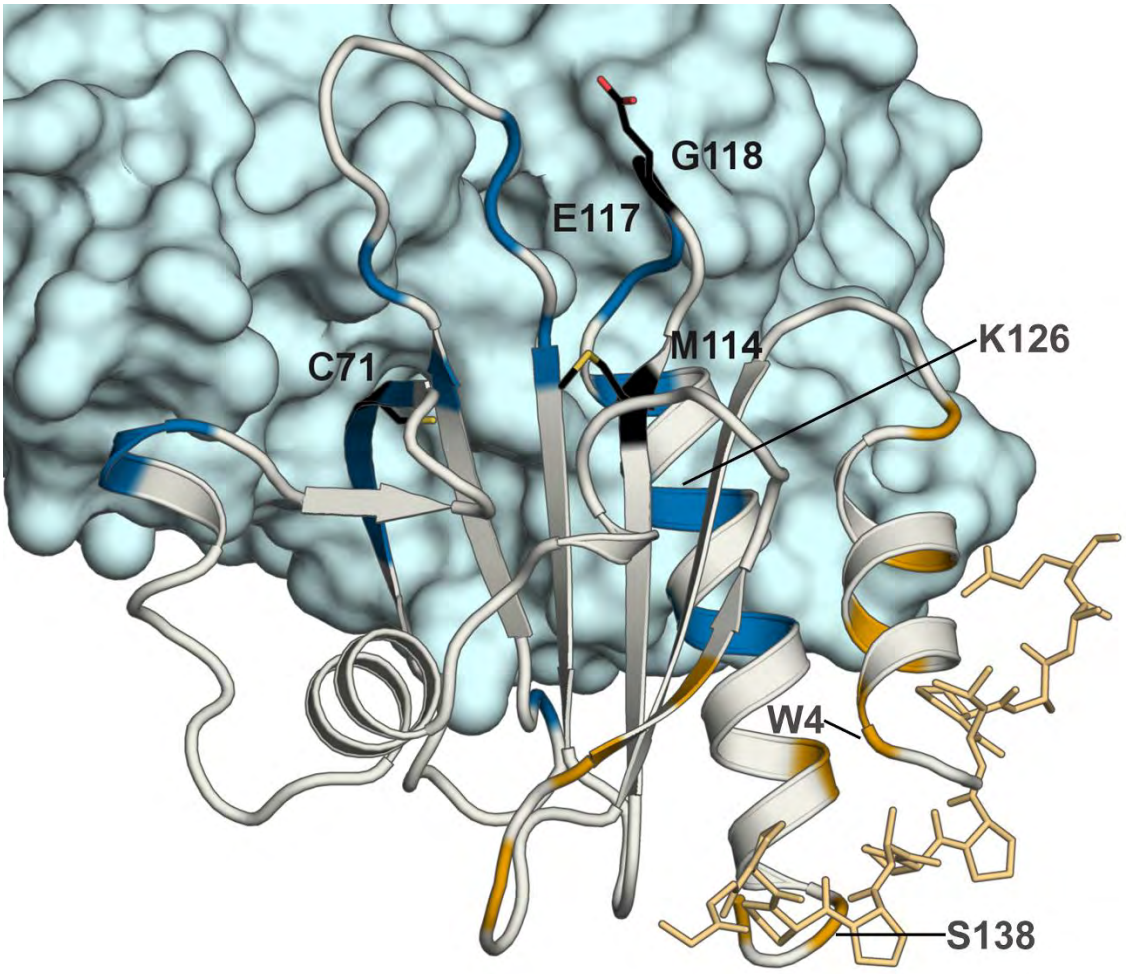

Figure II-10. Structure of actin–PFN1–VASP peptide ternary complex with the actin and poly(L-proline) binding residues mapped on PFN1. The X-ray structure of the PFN1 WT (gray)–actin (blue)–poly(L-proline) peptide (gold) complex (PDB ID code 2PAV) is shown. Residues reportedly involved in actin binding (V61, K70, S72, V73, I74, R75, E83, R89, K91, P97, T98, N100, V119, H120, G122, N125, K126, Y129, and E130) and poly(L-proline) binding (W4, Y7, N10, A13, S28, S30, W32, H134, S138, and Y140) are highlighted in blue and gold, respectively. The sites of ALS-linked mutations investigated in this study are highlighted and labeled in black with side chains displayed as black sticks. Residues involved in actin or poly(L-proline) binding that also exhibit Avg-Abs-DD values of 0.3 Å or greater between PFN1 WT and M114T chain B (W4, K126, and S138) are labeled in black (the remaining residues that fulfill this criteria are shown in Figure II-11).

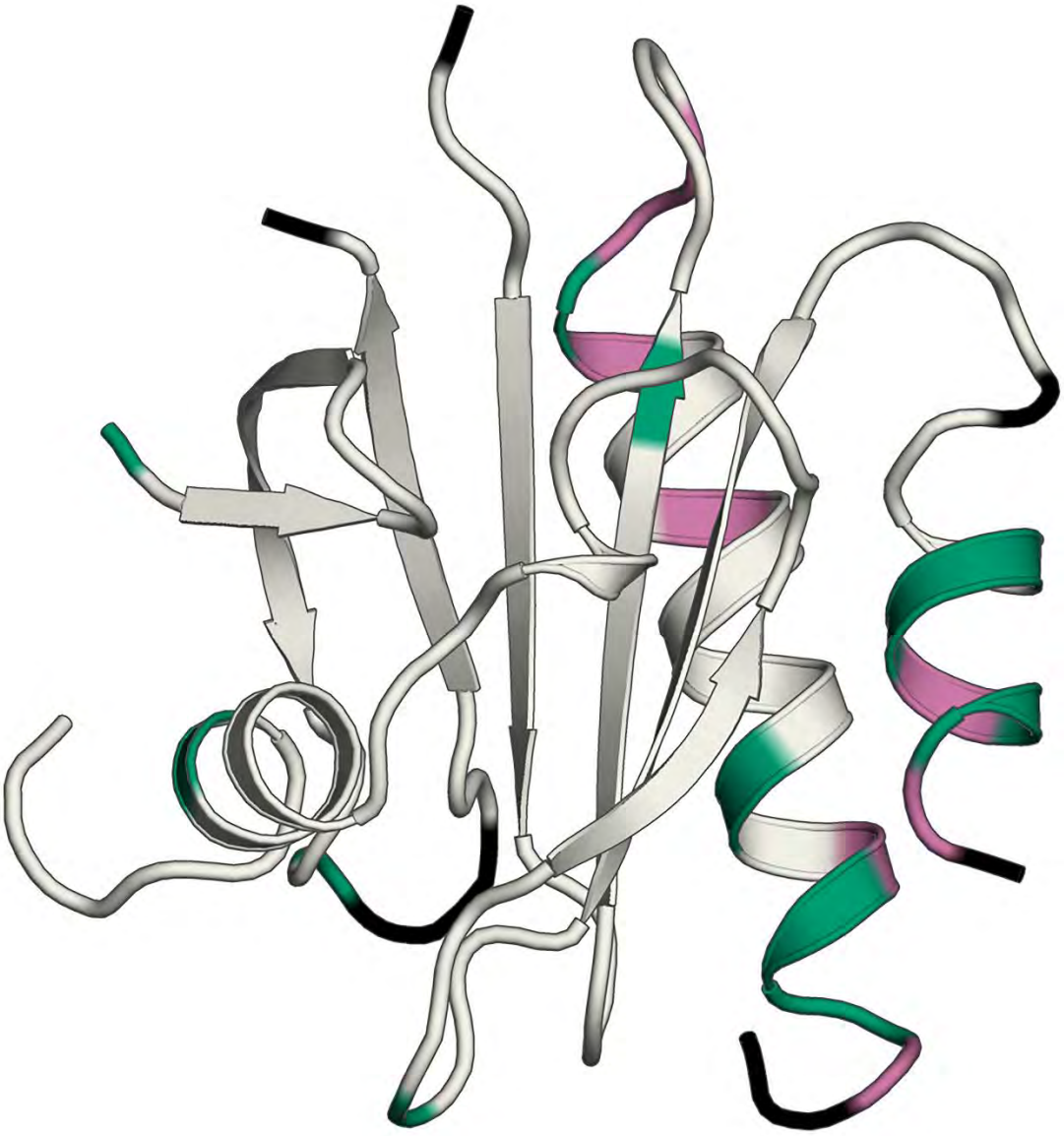

Figure II-11. Actin and poly(L-proline) binding residues exhibit relatively high double difference values. Residues that have Avg-Abs-DD values of 0.3 Å or greater that are also engaged in actin binding (V119, H120, G122, and K126) or poly-Pro binding (W4, Y7, H134, and S138) are mapped onto the structure of PFN1 WT in magenta. All other residues with Avg-Abs-DD values of 0.3 Å or greater are highlighted in green. Residues with Avg-Abs-DD values between chain A and chain B of M114T 0.3 Å or greater (Figure II-9D) were excluded from this analysis. Residues not used in this analysis are colored black.

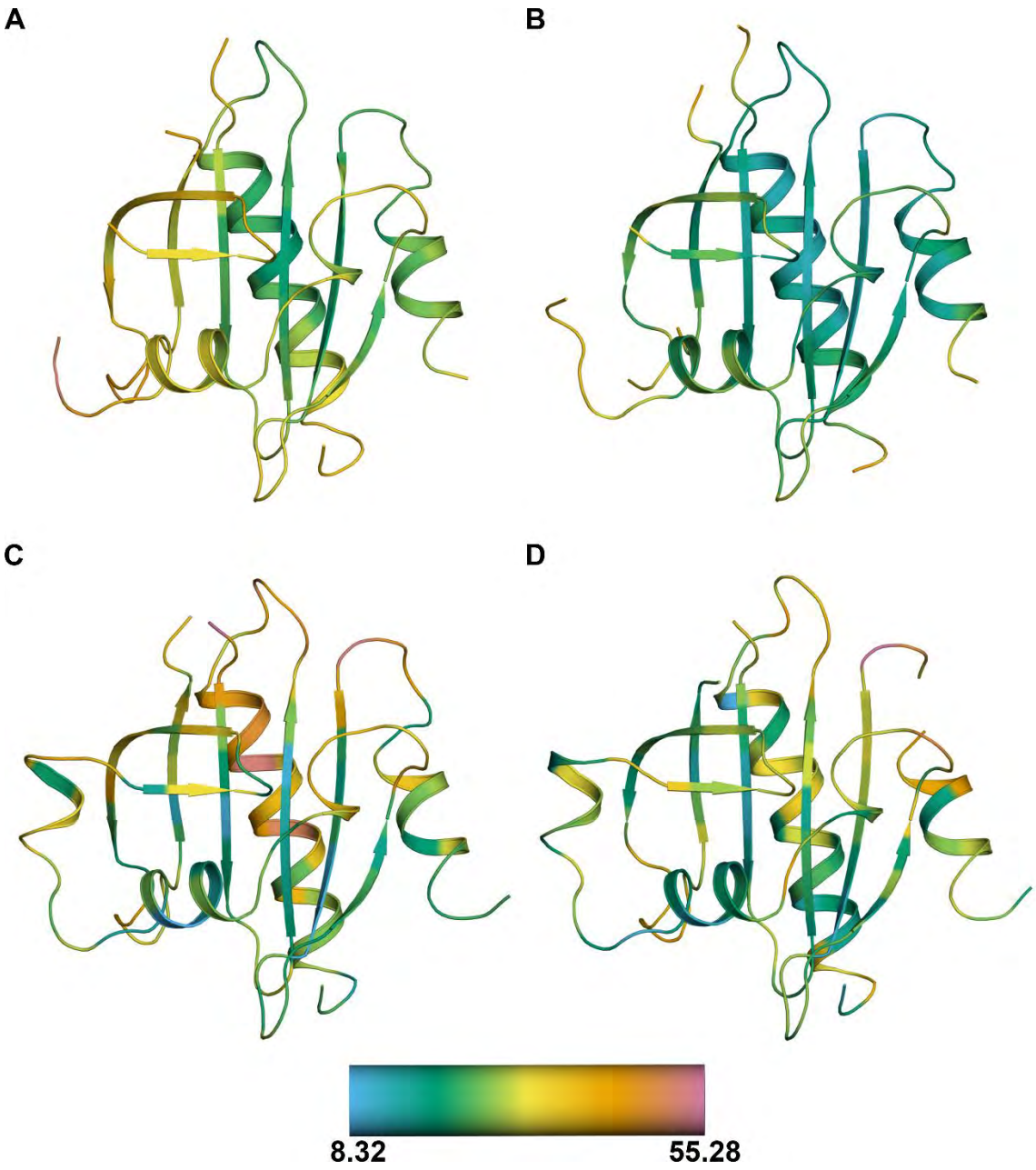

Figure II-12. The calculated α-carbon B factors for all PFN1 structures. Cartoon representations of WT (A), E117G (B), and M114T chains A (C) and B (D). Residues are colored according to the α-carbon B factors using the scale shown at the bottom. The average α-carbon B factor for WT, E117G, and M114T chains A and B structures are 30.52, 22.94, 29.47, and 27.33, respectively. Because the average B factor is higher for M114T chain A, M114T chain B was used for structural analyses unless otherwise noted.

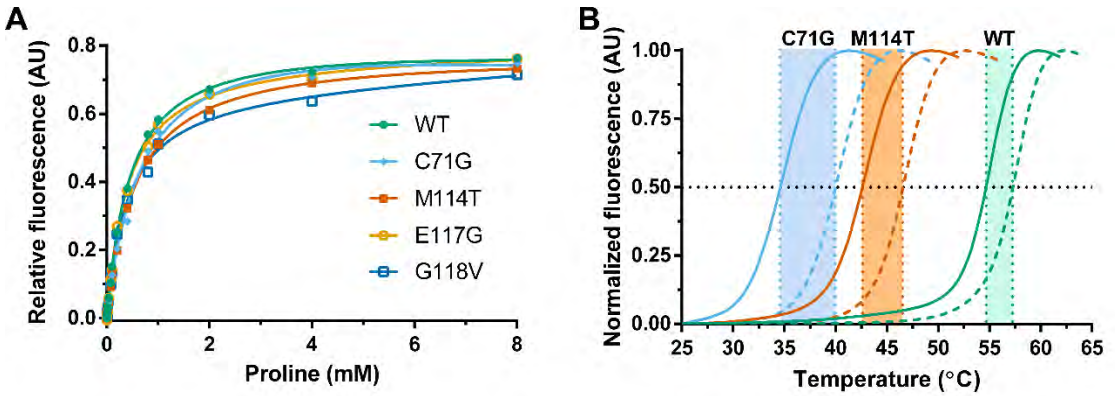

Figure II-13. ALS-linked PFN1 variants retain the ability to bind poly(L-proline). (A) Binding of PFN1 to the poly(L-proline) peptide was monitored by measuring the intrinsic tryptophan fluorescence of the indicated PFN1 protein as a function of increasing peptide concentration. The data points were fit using a one-site total binding model in GraphPad Prism and the apparent dissociation constants (K_d) obtained from the fit are shown in Table II-1. Note that the concentration of the peptide is reported in terms of [proline] because the peptide stock is supplied as a mixture of poly(L-proline) species (see Materials and Methods). (B) DSF was performed as described in Figure II-1B in the presence (dashed lines) and absence (solid lines) of 4 mM proline. The presence of proline increases the T_m for all PFN1 proteins used in this study (Table II-1), as illustrated here for WT, C71G, and M114T.

concentration (Figure II-13A). Our results revealed that the effect of ALS-linked mutations on the PFN1-poly(L-proline) interaction was modest, as the apparent dissociation constants (K_d) were within 2-fold for all PFN1 proteins in this study (Table II-1). In fact, excess concentrations of poly(L-proline) effectively stabilized all PFN1 proteins as determined by DSF, with the largest increase in T_m observed upon poly(L-proline) peptide binding to C71G (Figure II-13B and Table II-1). Next, we measured the binding capacity of our PFN1 proteins for G-actin by comparing their concentration-dependent abilities to suppress spontaneous polymerization of pyrenyliodoacetamide-labeled actin monomers (240). This assay is based on the

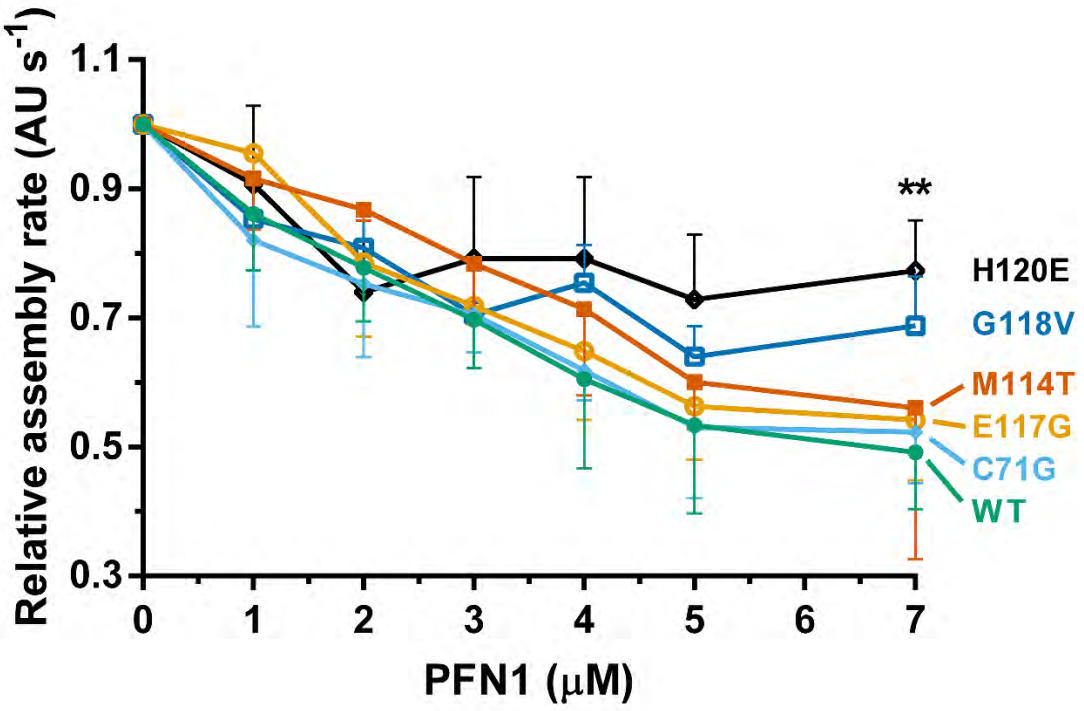

Figure II-14. The binding of PFN1 proteins to G-actin. Polymerization of monomeric rabbit muscle actin (3 μM, 5% pyrene-labeled) was monitored in the presence of increasing concentrations of WT or ALS-linked PFN1 variants and used to derive relative rates of polymerization (n = 3). The variant H120E, which is impaired in binding to actin, fails to suppress spontaneous actin polymerization as effectively as WT PFN1. Although G118V is relatively weak in suppressing actin polymerization, the data did not reach statistical significance. Statistical significance was determined using a two-way ANOVA followed by a Tukey's post hoc analysis. **P ≤ 0.01 for WT vs. H120E at 7 μM concentration. No other significant comparisons with WT were obtained. Other significant comparisons included C71G vs. H120E and E117G vs. H120E (P ≤ 0.05) at 7 μM concentration. Error bars represent SD.

fact that PFN1 binds G-actin and inhibits actin nucleation in the absence of formins (Figure I-2B) (240). As expected, increasing concentrations of recombinant PFN1 WT reduced the rate of actin polymerization, whereas the H120E variant that exhibits impaired binding to actin failed to suppress actin polymerization to the

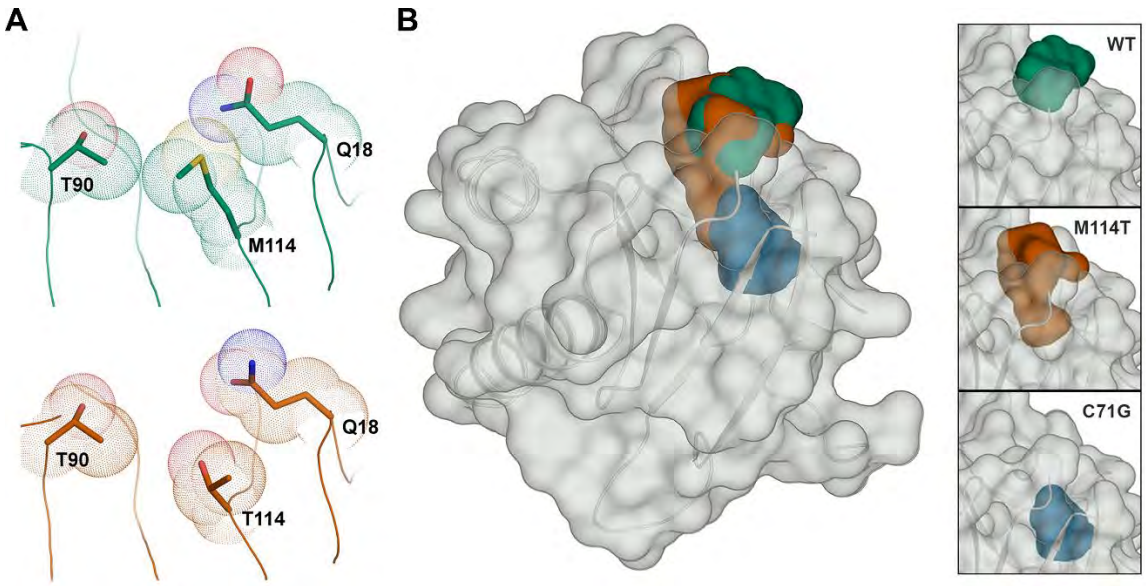

Figure II-15. The M114T mutation causes a surface-exposed pocket to expand into the core of the PFN1 protein. (A) Residues are depicted as described in Figure II-8. The van der Waals radii of residues 90, 114, and 18 are in contact in the PFN1 WT structure (Top). These contacts are reduced by the M114T mutation (Bottom) owing to the smaller size of threonine, leading to an enlargement of the surface-exposed pocket. (B) PFN1 WT is shown with a transparent surface and the secondary structure is shown in cartoon representation. The surface pocket volume for PFN1 WT (green) and the cleft volume for PFN1 M114T chain B (red-brown) are depicted as opaque surfaces and were generated using SiteMap. The predicted cavity (blue) for PFN1 C71G (generated using PyMOL) overlays with the M114T void, and unlike the WT and M114T volumes, is not surface-exposed. The insets (Right) show the aforementioned voids for WT (Top), M114T chain B (Middle), and C71G (Bottom).

same extent (Figure II-14). Of the four ALS-linked variants, only G118V was defective in suppressing actin polymerization, which was most apparent at the highest concentration of PFN1 used in this assay, although this effect did not reach statistical significance (Figure II-14). These data argue against a general

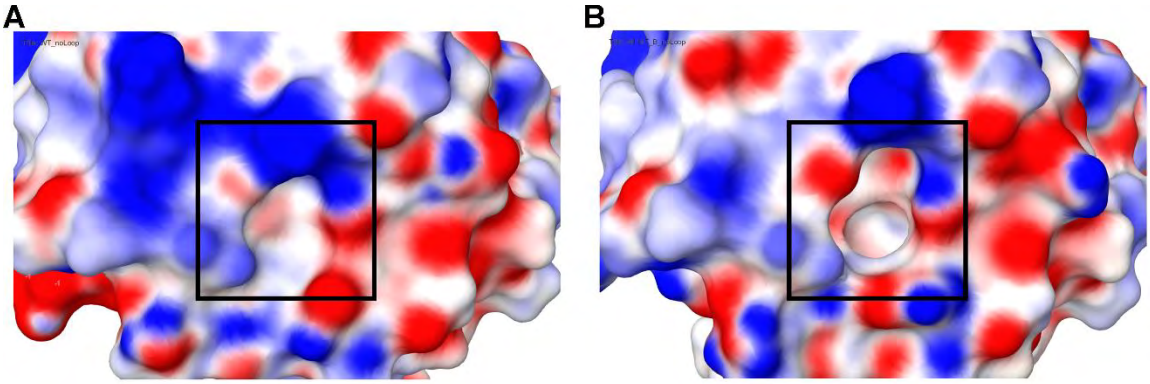

Figure II-16. Electrostatic surface potential (ESP) of PFN1 WT and PFN1 M114T. A comparison of the ESP for PFN1 WT (A) and M114T (B) around the surface pocket (for WT) and cleft (for M114T) shown in Figure II-15. Comparison of the ESP was calculated using Maestro (Schrödinger, LLC). The Red_White_Blue color scheme was used to depict the ESP of both surfaces, where red denotes negative, blue denotes positive, and white denotes neutral ESP. The minimum and maximum values are −0.12 and 0.12, respectively. The cleft (boxed region in B) formed by M114T exposes a deeper pocket comprised of hydrophobic residues that would otherwise be buried beneath the surface-exposed pocket (boxed region in A) in PFN1 WT.

mechanism for PFN1-mediated ALS pathogenesis that involves impaired direct-binding between PFN1 and either poly(L-proline) or actin.

Importantly, the X-ray crystal structures reveal a possible mechanism by which ALS-linked mutations destabilize PFN1. Residues Thr90, Met114 and Gln18 contribute to the formation of a surface exposed pocket that was detected using SiteMap (Figure II-15). Mutation of methionine to threonine at position 114 increased the size of this pocket, thereby forming a cleft, because the residues nearby failed to rearrange and compensate for the loss of van der Waals contacts (Figure II-15B). This cleft is expected to exert a destabilizing effect on the native conformation of PFN1 due to this loss of van der Waals contacts and the reduced

hydrophobicity of the threonine side chain relative to that of methionine (225). Moreover, hydrophobic residues that are otherwise buried in the PFN1 WT structure were exposed by the cleft in the PFN1 M114T structure (Figure II-15 and Figure II-16). In order to investigate the potential impact of the C71G mutation on PFN1 structure, the cysteine side-chain of residue 71 was removed to mimic a glycine amino acid in the PFN1 WT structure using PyMOL. Interestingly, this mutation is predicted to form a void in the core of the protein that partially overlaps with the cleft observed in the PFN1 M114T crystal structure (Figure II-15B). Analysis using PyMOL and SiteMap suggest that, unlike the solvent accessible WT and the M114T pocket, the proposed C71G void is buried within the core of the protein. Solvent inaccessible voids have a more destabilizing effect than solvent exposed cavities (225,241), providing an explanation for why the C71G mutation is more destabilizing than M114T (Figure II-1).

Discussion

Here we show that ALS-linked mutations severely destabilize (Figure II-1) and alter the native protein conformation (Figure II-8) of PFN1. Changes in protein stability due to disease-causing mutations, whether these mutations stabilize or destabilize the protein, are thought to play a pivotal role in various disease mechanisms (227). In the context of ALS, disease-linked mutations destabilize Cu,Zn-superoxide dismutase (SOD1) (223), but instead hyper-stabilize TAR DNA-binding protein 43 (TDP-43) (222,224,242). These findings underscore the

importance of defining the toxic properties of disease-linked proteins, thereby directing the rational design of therapeutic strategies against those offending proteins (220).

Our X-ray crystal structures of PFN1 proteins illuminate a probable source of mutation-induced destabilization. An enlarged surface pocket, or void, forms as a result of the M114T mutation (Figure II-15). The destabilizing effect of similar voids has been demonstrated using a systematic site-directed mutagenesis approach with lysozyme, and is thought to arise from a loss of hydrophobic interactions (225,241). Examples of mutation-induced cavity formation and destabilization have also been observed in nature (227). Interestingly, modeling the removal of the cysteine side-chain at position 71 creates an internal cavity that is predicted to partially overlap the cleft formed by M114T, raising the intriguing possibility that both mutations destabilize PFN1 through a common mechanism that involves the loss of hydrophobic and van der Waals contacts within the same region of PFN1 (Figure II-15). Because G118V is located within a solvent exposed flexible loop, it is difficult to predict whether this mutation propagates structural changes to the same region affected by M114T. We note that the phi and psi angles for Gly118 are in a region of the Ramachandran plot that are generally disallowed for a valine residue, and therefore we speculate that the G118V mutation also induces a conformational change within PFN1 that allows valine to adapt dihedral angles that are energetically more favorable.

Our study also provides insight into the relative pathogenicity of ALS-linked PFN1 variants. The pathogenicity of the E117G variant was called into question after it had been detected in the control population (7,141-143). Moreover, this variant exhibited mild phenotypes compared to other ALS-linked PFN1 variants in cell-based functional experiments (7,144). Here, the E117G mutation had only a modest effect on the stability and structure of PFN1 (Table II-1 and Figure II-9), supporting the view that E117G is a risk factor for disease rather than overtly pathogenic (6,143). Further, the E117G mutation was detected in sporadic ALS and frontotemporal lobar degeneration cases (134,136,141-143), consistent with the idea that environmental factors and/or genetic modifiers contribute to PFN1 E117G toxicity. In fact, proteasome inhibition triggered the aggregation of PFN1 E117G (7), suggesting that cellular stress may exacerbate PFN1 misfolding and dysfunction *in vivo*.

Although the mechanism of PFN1 in ALS has yet to be fully elucidated, the destabilized mutant-PFN1 species identified here can serve as an upstream trigger for either loss-of-function or gain-of-toxic-function mechanisms. Several investigations from cell-based experiments support a loss-of-function mechanism for ALS-linked PFN1 variants with respect to actin binding (7), actin dynamics (7) and stress granule assembly (144). For example, PFN1 variants immunoprecipitated less actin from mammalian cells compared to PFN1 WT (7). Our *in vitro* results suggest this is unlikely due to a general defect in the inherent ability of mutant PFN1 to directly bind actin (Figure II-14), but may be the

consequence of mutant PFN1 being sequestered away from actin and/or engaged in other aberrant interactions within the cell. Moreover, ALS-linked mutations do not simply abrogate the direct-binding interaction between PFN1 and the poly(L-proline) motif (Figure II-13A) that is present in many biological PFN1 ligands. These data, however, do not rule out the possibility that mutation-induced misfolding and destabilization culminate in defective actin homeostasis *in vivo*. PFN1 plays a complex role in actin homeostasis, requiring coordinated interactions between PFN1 and many other cellular factors that ultimately dictate the fate of different actin networks within the cell (59).

The misfolding of PFN1 variants may also induce gain-of-toxic-functions and interactions, the latter via aberrant protein-protein interactions through exposed hydrophobic patches, such as those detected for PFN1 M114T (Figure II-16). Further, the aggregation of PFN1 variants can potentially sequester other vital proteins, including those with poly(L-proline) binding motifs (15), culminating in compromised actin and/or cellular homeostasis (221).

Although the downstream effect of ALS-linked PFN1 on actin dynamics and other cellular processes have not been elucidated, our data identify misfolded and destabilized PFN1 as a potential upstream trigger of the adverse events that culminate in ALS, opening new avenues for therapeutic advancement in ALS. One potential direction is the development of pharmacological chaperones (229). For example, small molecules that fill the void formed by the M114T mutation are expected to stabilize the protein (241). Our data with poly(L-proline) (Figure II-13B)

suggest that small-molecules binding to other regions of PFN1 could also stabilize the protein. We posit that stabilizing mutant PFN1 will restore the normal structure and function of the protein, thereby preventing the pathogenic cascade leading to ALS.

Materials and Methods

Recombinant PFN1 cloning, expression and purification

A pET vector containing human PFN1 flanked by NdeI and EcoRI restriction sites was kindly provided by Dr. Bruce Goode (Brandeis University). The mutant PFN1 DNA (7) was amplified using primers 5'- GGACCATATGGCCGGGTGGAAC -3' and 5'- GCCTGAATTCTCAGTACTGGGAACGC -3' and ligated into the pET vector using NdeI and EcoRI restriction sites. Please see Appendix I for information on PFN1 expression and purification.

Equilibrium unfolding experiments

For equilibrium unfolding experiments using tryptophan fluorescence, solutions of increasing urea concentration were prepared from a concentrated stock-solution of 10.546 M urea in phosphate buffered saline (PBS) using a Hamilton Microlab 500 titrator. PFN1 was mixed into the urea solutions to a final concentration of 2 μM with 1 mM tris(2-carboxyethyl)phosphine (TCEP) and the samples were equilibrated for 15–30 min. The intrinsic tryptophan fluorescence of PFN1 was measured at 25 °C with a T-format Horiba Fluorolog fluorimeter using an excitation wavelength of 295 nm. Three emission spectra (310 nm to 450 nm)

were collected for each sample and averaged. The concentration of the urea in each sample was measured using an Abbe refractometer after data acquisition. Data were processed to obtain the center-of-mass (COM) of the emission spectrum. The COM was fit to a two-state transition model as previously described and the thermodynamic parameters, apparent ΔG° (the free energy of folding), m (the denaturant dependence of ΔG°) and C_m (the midpoint of the unfolding transition) were determined with the program Savuka (243,244). Because the quantum yield of the native and unfolded states were within a factor of 2, the use of COM analysis is justified. We explicitly checked this by a rigorous global analysis using singular value decomposition and showed that the fit of the urea dependence basis vector gave thermodynamic parameters that were within the error of the COM and circular dichroism (CD) spectroscopy analyses, and no indications of non-two-state behavior. For equilibrium unfolding experiments using CD spectroscopy, PFN1 (10 μM) was equilibrated in various concentrations of urea as described above and CD spectra were acquired from 215 nm to 260 nm using a Jasco J-810 spectropolarimeter. Three spectra were averaged and the mean residual ellipticity (MRE) at 220 nm was plotted as a function of urea concentration and fit to a two-state equilibrium unfolding model.

For protein refolding experiments, a concentrated stock of PFN1 (100-250 μM) denatured in urea (4-8.5 M) was diluted in urea/PBS to obtain a series of samples with decreasing concentrations of urea, 10 μM PFN1 and 1 mM TCEP.

Samples were equilibrated for 30 min prior to acquisition of fluorescence emission spectra as described above.

Differential scanning fluorimetry

Samples containing WT or mutant PFN1 (20 μM) in PBS with 20x SYPRO Orange (Invitrogen, S6651) were pipetted in quadruplicate into a 384 well plate (BioRAD, HSR4805) and subjected to heat denaturation using a Bio-RadCFX384 Touch™ Real-Time PCR Detection System. The temperature was increased from 25 °C to 100 °C in 0.3 °C increments and at each increment fluorescent intensities were acquired using HEX detector (excitation 515–535 nm, emission 560–580 nm). PFN1 proteins were analyzed alone and in the presence of the poly(L-proline) peptide (MW 1,000–10,000, Sigma, P2254). Because this peptide was supplied from the manufacturer as a mixture of poly(L-proline) species, the concentration is reported here in units of proline (MW 115.13 g mol^{-1}). For experiments with the poly(L-proline) peptide, PFN1 was prepared with 4 mM proline. The fluorescence intensities for the four replicates were averaged, normalized to the maximum fluorescence intensity and plotted as a function of temperature to obtain melting curves, which were fit with a sigmoidal function in GraphPad Prism to determine the midpoint of transition or the apparent melting temperature (T_m).

Measuring PFN1 turnover in cells

Human SKNAS cells were cultured in Dulbecco's minimal essential medium (Gibco, 11965) containing 10% (vol/vol) fetal bovine serum (Sigma-Aldrich, F4135) and 1% (wt/vol) penicillin and streptomycin (Gibco, 10378) under standard culture

conditions (37 °C, 5% CO2/95% air). SKNAS cells were transiently transfected with 0.5 µg of V5-PFN1 plasmids (7) in 24-well plates using 1.75 µl NeuroMag (OZ Biosciences, NM50500) diluted in Opti-MEM (Invitrogen, 38915). After 12 h of V5-PFN1 expression, translation was inhibited with 30 µg ml^{-1} cycloheximide (Sigma Aldrich, C7698). Cells were lysed at specific time points during a 12.5 h time course following cycloheximide addition using RIPA buffer (Boston BioProducts, BP-115-500) supplemented with protease inhibitors (Roche, 11836170001), and centrifuged at 13,500 rpm (19,357 x g) for 15 min, after which the supernatant (containing soluble PFN1) was collected. The remaining pellet (containing insoluble PFN1) was washed once with RIPA lysis buffer, centrifuged again, and resolubilized with 8 M urea in volumes equal to their soluble counterparts. The protein concentration of soluble fractions was determined using a bicinchoninic acid assay (Thermo Scientific Pierce, 23227). Samples were processed and subjected to western blot and densitometry analyses essentially as described (232). Western blots were probed using V5-specific (1:1,000 Invitrogen, R96025) and GAPDH-specific (1:20,000 Sigma, G9545) antibodies. Bands corresponding to soluble V5-PFN1 were normalized to the loading control, GAPDH, and then to the band corresponding to cycloheximide treatment for ‘0 h’ for each protein. For each biological replicate, visible bands corresponding to insoluble V5-PFN1 were normalized to their respective ‘0 h’ PFN1 C71G band. Statistical significance was determined using a two-way ANOVA followed by Tukey’s post-hoc analysis.

Circular dichroism spectroscopy

Circular dichroism (CD) spectra of WT PFN1 or mutants (10 μM in PBS) were acquired from 190 nm to 260 nm at a scan speed of 2 seconds per wavelength with a 1 mm cuvette at 25 °C using a AVIV Biomedical circular dichroism spectrometer model 400. Data reflect an average of five scans that were blank subtracted. The resulting ellipticity curves were transformed to mean residue ellipticity as described (152).

Acidic native PAGE

The method for acidic native PAGE analysis of basic proteins described by the Mario Lebendiker laboratory (http://wolfson.huji.ac.il/purification/) was used. Briefly, 29:1 acrylamide-bisacrylamide (Fisher Scientific BP1408-1) native gels were cast with 7.5% (wt/vol) polyacrylamide in the resolving gel, pH 4.3, and 3% (wt/vol) polyacrylamide in the stacking gel, pH 6.8. The gel sample containing WT or mutant PFN1 (0.8 μg μl^{-1}) was prepared under native conditions using ice-cold acetate-KOH pH 6.8, 10% (vol/vol) glycerol with 0.025% (wt/vol) of methylene blue. PFN1 proteins (10 μg) were loaded onto the gel and subjected to reversed polarity electrophoresis under ice-cold conditions for 2 h at 100 V. The protein bands were visualized with Coomassie Brilliant Blue as described above for denaturing gels.

Analytical size exclusion chromatography

WT or mutant PFN1 (50 μl of PFN1 at 0.8 μg μl^{-1}) were subjected to analytical size exclusion chromatography at 4 °C using a Superdex 75 column (GE Healthcare, 17-5174-01) equilibrated with PBS and a flow rate of 0.5 ml min^{-1}. For

each trial (n = 2), elution profiles were acquired using absorbance at 280 nm and normalized to the peak value of WT PFN1. The area under peak was calculated using GraphPad Prism.

Fluorescence decay measurements

The time resolved data were collected using a Becker and Hickl based custom time-correlated single photon counting (TCSPC) equipment (245,246). G-factor was measured using 5 μM N-Acetyl-L-tryptophanamide. The total intensity was calculated using the formula, $I_{VV} + 2GI_{VH}$ where I_{VV} is the vertical emission and I_{VH} is the horizontal emission. A python class for reading the TCSPC generated .sdt files can be found in Appendix II.

Protein crystallization and X-ray structural determination

PFN1 crystals were grown by hanging drop vapor diffusion after mixing the PFN1 protein with a 1:1 ratio of reservoir solution at 25 °C for WT and E117G and at 18 °C for M114T. Reservoir solution for WT contained 50 mM KH_2PO_4, 36% (wt/vol) PEG 8,000 and 100 mM MES pH 6.0. Reservoir solution for E117G contained 50 mM KH_2PO_4, 41% (wt/vol) PEG 8,000 and 100 mM MES pH 6.0. Reservoir solution for M114T contained 750 mM sodium citrate, 200 mM NaCl and 100 mM tris pH 7.5.

E117G crystals where soaked in cryo-protectant composed of 25% (vol/vol) ethylene glycol, 75% (vol/vol) reservoir solution and M114T crystals were passed through mineral oil before mounting for data collection. Diffraction data were collected using a Rigaku 007 MicroMax HF rotating anode X ray generator, under

a nitrogen cryostream at 100 K (Oxford Cryosystems), on a Saturn944+ CCD detector.

The data were reduced using Xia2 (247) (running XDS (248)) for WT and M114T and HKL2000 (HKL Research) for E117G. All three structures were solved via molecular replacement with Phaser (249) using the profilin structure PDB ID: 1FIK (233) as the starting model followed by multiple rounds of manual model building performed with Coot (250). WT was refined with PHENIX (251) and E117G with REFMAC5 (252) using standard refinement protocols. M114T was refined with PHENIX using twin refinement with the twin law {h,-h-k,l} applied through refinement, because the data was highly twinned with a twin fraction estimated to be 0.48.

Structural analysis

SiteMap (Schrödinger, LLC) was used to identify and evaluate the mutation-site cavity volumes. Figures were generated using PyMOL (Schrödinger, LLC).

Poly(L-proline) peptide binding experiments

The intrinsic tryptophan fluorescence of WT or ALS-PFN1 (2 μM) as a function of increasing concentrations of the poly(L-proline) peptide described above at 25 °C was used to measure binding of PFN1 to poly(L-proline) as previously described (21). The samples were excited at 295 nm and three emission spectra between 310 nm and 450 nm were collected for each sample and averaged. The fluorescence emission intensity at 323 nm was base-line corrected,

normalized, plotted as a function of poly(L-proline), and fit to a one-site total binding model in GraphPad Prism to yield apparent K_d values.

Inhibition of spontaneous actin assembly

Gel-filtered monomeric rabbit muscle actin (3 μM, 5% pyrene labeled) was converted to Mg-ATP-actin immediately before use in each reaction and mixed with 7 μl of different concentrations of PFN1 WT, PFN1 mutants or control buffer and 3 μl of 20x initiation mix (40 mM $MgCl_2$, 10 mM ATP, 1 M KCl) in 60 μl reactions. Actin polymerization was monitored over time at 365 nm excitation and 407 nm emission in a PTI fluorometer at 25 °C. Average relative rates of actin polymerization (n = 3) were determined based on the slopes of the assembly curves during the first 500 seconds of each reaction and plotted against increasing concentrations of PFN1 (mutants). Statistical significance was determined using a two-way ANOVA followed by Tukey's post-hoc analysis.

PREFACE TO CHAPTER III

The single molecule experiments were performed in the laboratory of Dr. Bruce Goode (Brandeis University) in part by Dr. Jessica Henty-Ridilla and myself. Unlabeled and labeled actin, and mDia1 used in single molecule experiments were purified by personnel in the laboratory of Dr. Bruce Goode (Brandeis University). The stable HeLa lines described in the experiments were generated by Dr. Jeanne McKeon. Western blotting experiments were performed with assistance from Dr. Jeanne McKeon and Katherine Gall. The artificial 3'-UTR PFN1-miRNAs were designed by Dr. Miguel Sena-Esteves and cloned by Sneha Suresh. Lentiviral vectors were prepared and titered by Katherine Gall. The construct EGFP*-mDia1-FH1-mDia2-FH2-C was cloned by Sneha Suresh. Live cell imaging experiments were performed with assistance from Dr. Claudia Fallini. Statistical analyses on datasets were performed with assistance from Dr. Jeanne McKeon.

CHAPTER III – INVESTIGATING DEFECTS IN ACTIN ASSEMBLY DUE TO ALS-MUTATIONS IN PFN1

Introduction

Abnormal binding of ALS-variants of PFN1 to either actin or poly(L-proline) containing proteins such as formins, Ena/VASP (9,15) can have a disastrous effects on actin dynamics. The ALS-PFN1 mutations C71G, M114T, E117G and G118V are close to the actin-binding interface whereas the mutations T109M, R136W and Q139L occur near the poly(L-proline) binding surface of PFN1 (Figures I-1 and II-10). Moreover, the cavity introduced by the mutation M114T and possibly C71G (Figures II-15 and II-16) is proximal to the actin-binding interface. Although published results point to defects in neuronal actin cytoskeleton (7,146,147), the *in vitro* experiments described in Chapter II did not point to major differences in binding to poly(L-proline) or actin (Figures II-13A and II-14). More importantly, our experiments showed that the binding of PFN1 to actin is not completely impaired as suggested previously (7). There is a need for reconciliation of these contrasting results. The pyrene-actin polymerization assays and poly(L-proline) binding experiments are inadequate and have certain shortcomings. For example, the former is not a direct actin-binding experiment that provides dissociation constants, and the latter involved poly(L-proline) peptides rather than an intact full-length protein. In addition, the actin polymerization assays are bulk fluorimetric assays that do not provide any information on the individual filaments.

Furthermore, *in vivo*, there are a number of actin cytoskeletal factors involved in nucleation, elongation, capping, severing and depolymerization that act in a concerted manner (253). So truly, the functional assays described in Chapter II fall short of simulating a situation where multiple interactions of PFN1 occur simultaneously and in different contexts as in a cellular environment.

To address the above shortcomings, we considered certain processes discussed in Chapter I where PFN1 could be a key player, (i) the process of actin assembly, involving actin nucleation and elongation, (ii) actin disassembly from the barbed end, (iii) the exchange reaction of ADP- to ATP-actin catalyzed by profilins, (iv) the interaction of profilins with phosphatidylinositols and its connection to cellular signaling, and (v) the putative post-translational modifications of PFN1. We decided to exclusively study the effect of ALS-PFN1 on actin nucleation and elongation events, for which we focused entirely on the “minimal” system consisting of actin, PFN1 (WT or ALS-variants) and the constitutively active formins mDia1-FH1-FH2-C or mDia2-FH1-FH2-C (254,255) (Figure III-1). A combination of single molecule techniques and cell biology experiments were used in this study to observe individual filaments and the formin-nucleated filopodial actin structures (256,257), respectively. By this way we were able to (i) study the behavior of individual or a bundle of actin filaments (254,258) which possesses advantages over the bulk pyrene-actin polymerization assays and (ii) at the same time partly address the complex nature of actin assembly processes by observing

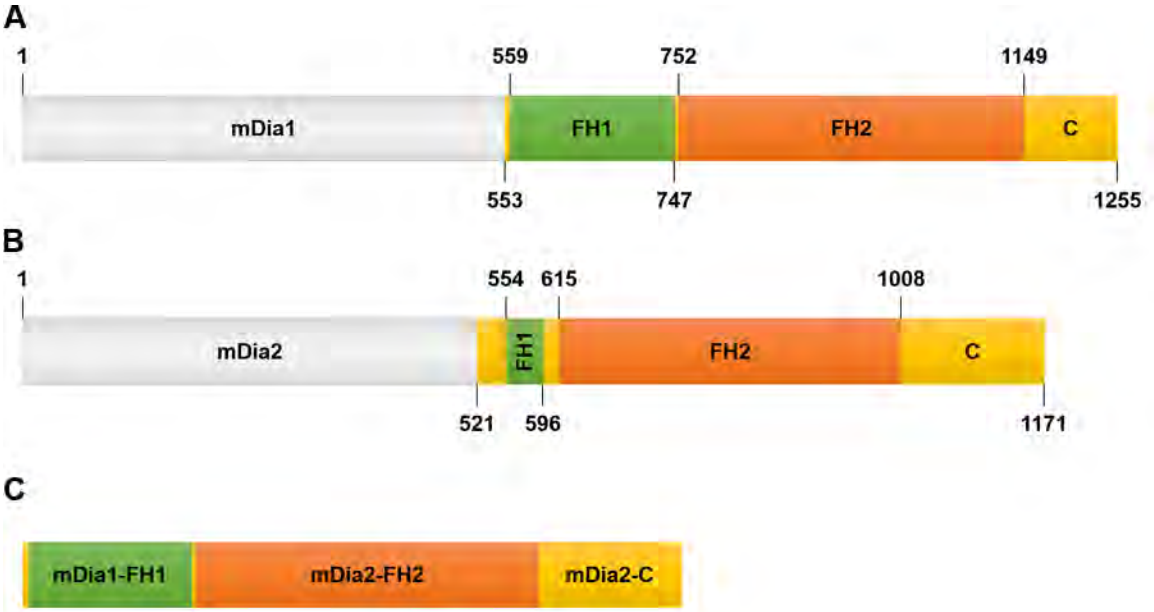

Figure III-1. Constitutively active formin constructs used in experiments. (A) mDia1-FH1-FH2-C (553-1255). (B) mDia2-FH1-FH2-C (521-1171). (C) mDia1-FH1-mDia2-FH2-C (553-747 of mDia1 and 615-1171 of mDia2). For the fixed and live cell imaging experiments, mDia2-FH1-FH2-C and mDia1-FH1-mDia2-FH2-C fused to EGFP* was used (see Materials and Methods).

reactions that involve a simultaneous interplay of PFN1-actin, PFN1-formin and actin-formin, and formin-PFN1-actin complexes *in vitro* and in cells.

Here, we demonstrate that the ALS-variants of PFN1 affect both nucleation and elongation rates *in vitro*. In HeLa cells, PFN1 is necessary for filopodia generation by mDia2-FH1-FH2-C and the variant M114T increases filopodia density. Our studies show that mutant PFN1 causes defects in actin assembly which may be difficult to deduce from simple binding experiments alone.

Results

Abnormalities in actin nucleation and elongation with ALS-PFN1

Using *in vitro* single molecule techniques, the effects of WT or ALS-PFN1 on actin nucleation and elongation in the presence or absence of the formin mDia1 were investigated. This approach provides information at the individual filament resolution and by tracking the filament growth over time the elongation rates can be computed (Figure III-2). We chose mDia1 for these experiments as it is well characterized *in vitro*, contains several poly(L-proline) motifs in its FH1 domain and is capable of vastly accelerating actin filament elongation in its functional dimeric form (41,255,259). To avoid confounding factors that might arise due to autoinhibition observed in full-length mDia1 (41), we utilized the constitutively active form of mDia1, hereby referred to as mDia1-FH1-FH2-C, consisting of the nucleating FH2 and the proline rich FH1 domain (Figure III-1A).

First, we studied the effect of WT and ALS-PFN1 on actin nucleation in the absence of mDia1-FH1-FH2-C using total internal reflection fluorescence (TIRF) microscopy (schematics in Figure I-2A and B). The number of filaments 1000 s after the start of the reaction were counted as a measure of nucleation. The control reaction containing 1 μM actin alone contained about 156 ± 5 filaments per 100 μm^2. In the presence of 1 μM WT PFN1, there were 86 ± 3 filaments per 100 μm^2, and this decreases with increasing concentration of WT PFN1 as expected. Interestingly, at 1 μM concentration, we observed a significant decrease in the number of filaments with M114T (37 ± 2 per 100 μm^2) and significant increase with

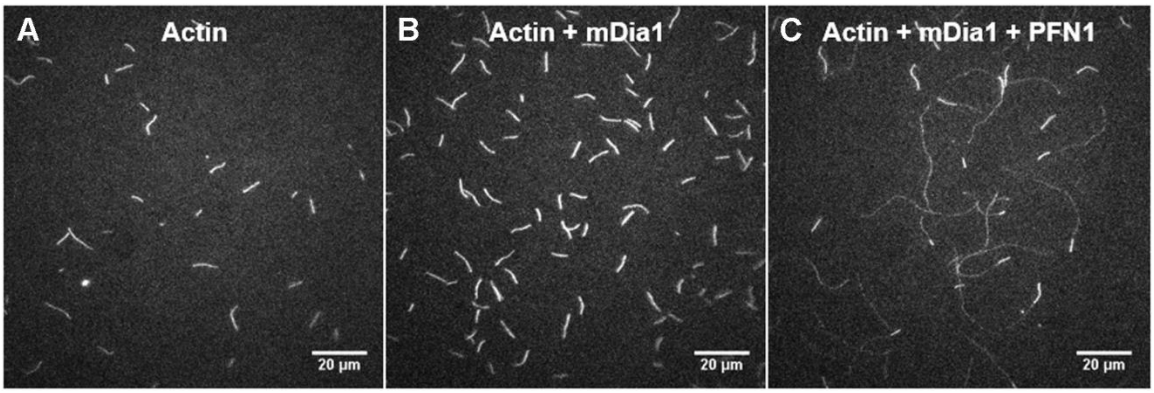

Figure III-2. Actin filaments observed using total internal reflection fluorescence (TIRF) microscopy. (A) 0.5 µM actin (10% Oregon Green labeled, 0.2% biotin-labeled). (B) 0.5 µM actin and 50 pM mDia1-FH1-FH2-C. The increased number of filaments observed is due to the nucleating activity of mDia1-FH1-FH2-C. (C) 0.5 µM actin, 50 pM mDia1-FH1-FH2-C and 3 µM WT PFN1. The filaments elongated by mDia1-FH1-FH2-C appear faint because PFN1 binds unlabeled actin with higher affinity and hence the unlabeled actin is favorably added to the growing barbed end by the FH1 domain. For the same reason, the spontaneously nucleated filaments are bright as the unbound labeled actin can be readily added to these filaments.

G118V (175 ± 7 per 100 µm^2). Increasing the concentrations of both M114T and G118V reduced the number of filaments, but with M114T the number of filaments were lower than WT at all the concentrations tested (Figure III-3A).

Next the effect of WT and ALS-PFN1 on actin nucleation was evaluated in the presence of 100 pM mDia1-FH1-FH2-C (schematics in Figure I-3). After 250 s, no difference was observed in the number of filaments between the control reaction lacking PFN1 (45 ± 2 per 100 µm^2) and the reaction containing 5 µM WT PFN1. However, the filament count was much higher when 5 µM M114T was present in the reaction (196 ± 8 per 100 µm^2 with M114T vs. 51 ± 2 per 100 µm^2 with WT). This was in contrast to the behavior of M114T compared to WT in the

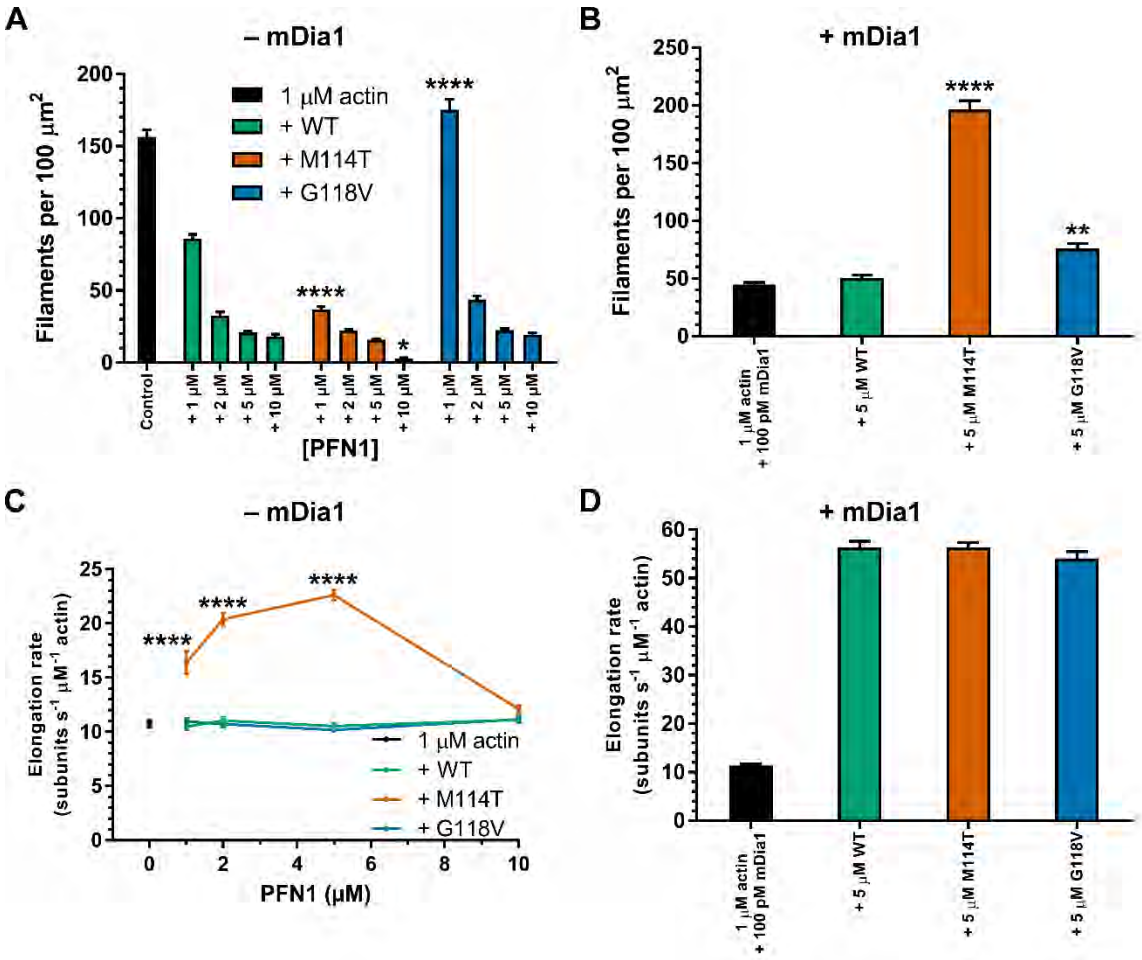

Figure III-3. Actin nucleation and elongation in the presence of WT or ALS-PFN1. (A) Number of spontaneously nucleated filaments (absence of mDia1-FH1-FH2-C) after 1000 s from the start of the reaction. Reactions contained 1 μM actin (10% Oregon Green labeled) alone or along with varying concentrations of PFN1 variants. (B) Number of filaments generated in the presence of mDia1-FH1-FH2-C after 250 s from the start of the reaction. Reactions contained 1 μM actin and 100 pM mDia1-FH1-FH2-C alone or with 5 μM of PFN1 variants. (C) Elongation rates of spontaneously nucleated filaments in (A) as a function of PFN1 concentration. (D) Elongation rates of mDia1-FH1-FH2-C nucleated filaments in (B). In (A) and (B) filaments were counted from 6 reactions and averaged. In (C) and (D) elongation rates of 60 filaments from 6 reactions were averaged. Statistical significance was determined using a one-way ANOVA followed by a Tukey's post hoc analysis. All comparisons are with respect to the corresponding WT PFN1 condition (*P < 0.05, **P < 0.01, ****P < 0.0001). Error bars represent SEM.

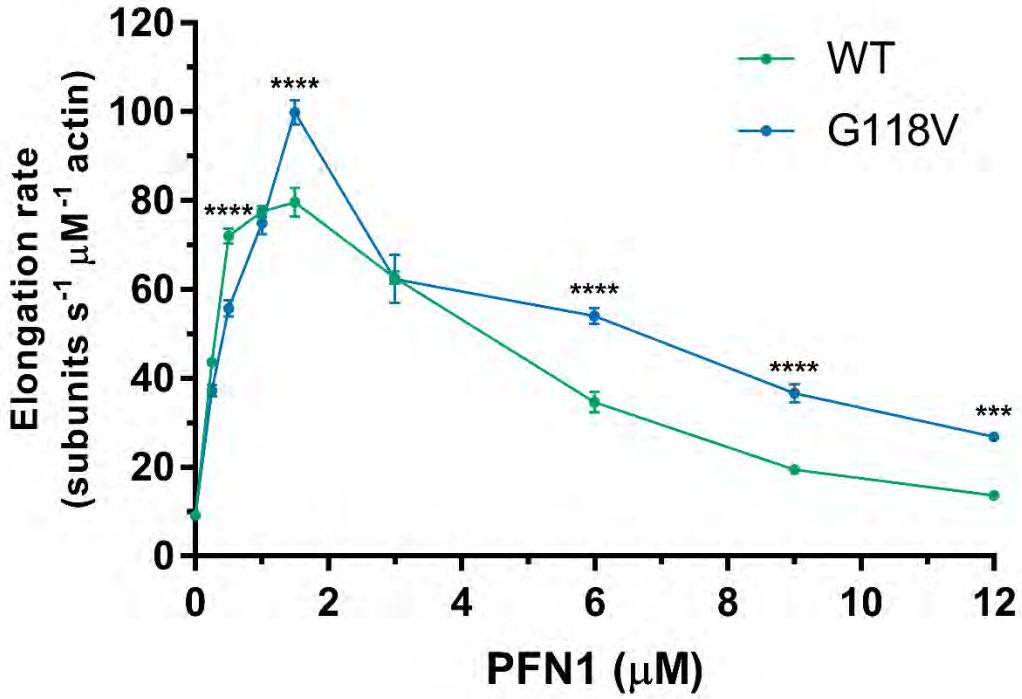

Figure III-4. mDia1-generated filament elongation rates as a function of PFN1 concentration. Reactions contained 0.5 µM actin (10% Oregon Green labeled), 50 pM mDia1-FH1-FH2-C and varying concentrations of PFN1 WT or G118V. Differences in elongation rates of filaments generated by mDia1-FH1-FH2-C between WT and G118V were apparent at concentrations of PFN1 above 3 µM. For each condition, between 8 and 16 mDia1-generated filaments were analyzed from 3-4 reactions. Statistical significance was determined using a one-way ANOVA followed by a Tukey's post hoc analysis (***P = 0.0002, ****P < 0.0001). Error bars represent SEM.

absence of mDia1-FH1-FH2-C. G118V (76 ± 4 per 100 µm^2) also had a higher filament count compared to WT (Figure III-3B).

Actin, at 1 µM, exhibited an elongation rate of about 11 subunits s^{-1} µM^{-1} actin (Figure III-3C). This is in agreement with published data from other research groups (255,259). Actin displayed similar elongation rates with varying concentrations of WT and G118V PFN1. Interestingly, M114T shows significantly

higher elongation rates for three out of the four concentrations tested (Figure III-3C). In the presence of 100 pM mDia1 and at a fixed PFN1 concentration of 5 μM, no differences in elongation rates were observed among the variants (Figure III-3D). With 0.5 μM actin, 50 pM mDia1 and varying concentrations of PFN1, we observed the biphasic behavior of the elongation rates as described previously (255). But the elongation rates of mDia1-generated actin filaments were higher in the presence of G118V for most PFN1 concentrations tested (Figure III-4). Collectively, our data suggest that differences in actin nucleation and elongation between WT and ALS-PFN1 are dependent on the PFN1 variant in question and the relative concentrations of actin, PFN1 and mDia1-FH1-FH2-C.

Tools for studying actin assembly in cells

We decided to investigate if the *in vitro* observations in actin nucleation and elongation can be recapitulated in a more complex yet physiological cellular milieu with all the other cytoskeletal proteins present. Several factors had to be considered while studying the role of WT or ALS-PFN1 on nucleation and elongation. First, the filament elongation rates display a biphasic behavior with respect to profilin concentration (255). Hence, it is absolutely critical to have similar expression levels of exogenous WT or ALS-PFN1. To address this issue, we generated several stable HeLa lines that express PFN1 shRNA, WT or ALS-variants of PFN1 at near endogenous levels under doxycycline induction (Figure III-5). Second, since mammalian cells express about 15 different formins (77), it would be impossible to make observations on nucleation and elongation in the

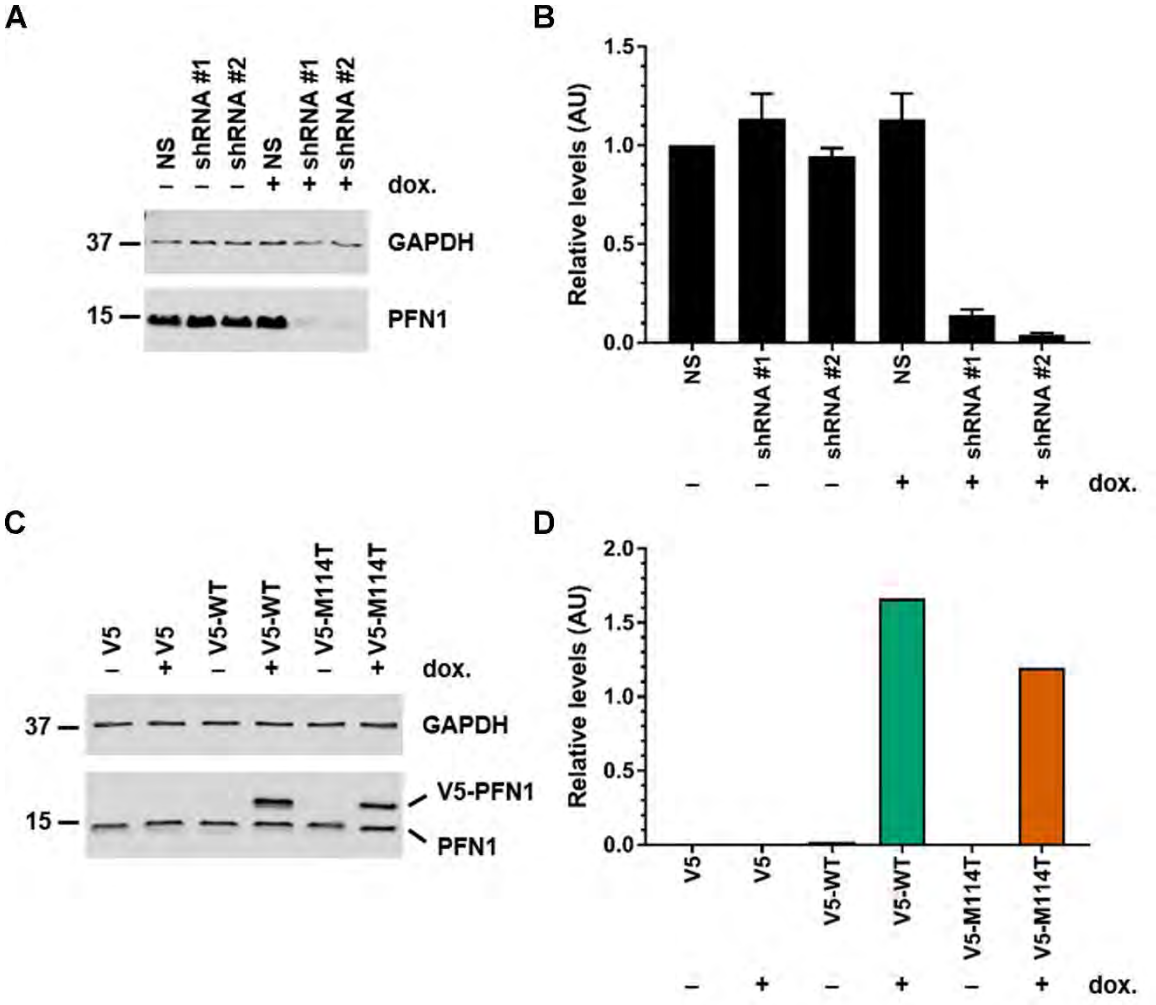

Figure III-5. Characterization of generated HeLa cell lines. (A) Western blotting of lysates prepared from HeLa cell lines uninduced or induced with 1 µg ml^{-1} doxycyline (dox.) for 96 h to express non-silencing (NS) shRNA, PFN1 shRNA #1 or PFN1 shRNA #2. (B) Quantification of PFN1 levels relative to GAPDH from n = 3 experiments by densitometry. A knockdown efficiency of 90% or above was observed for the two PFN1 shRNAs. (C) Western blotting of lysates prepared from HeLa cell lines uninduced or induced with 1 µg ml^{-1} to express V5, V5-WT or V5-M114T. (D) Quantification of V5-PFN1 levels relative to endogenous PFN1 from n = 1 experiment by densitometry. The V5-PFN1 levels were within two-fold of endogenous PFN1 levels.

absence of formins, as this would entail knocking down or downregulating all the members. Thus, the only processes that can be reliably studied are nucleation and

elongation in the presence of formin. Third, the experiments should allow the visualization of near individual filaments. Direct actin markers such as GFP-actin, lifeact-GFP and phalloidin-derivatives enable one to observe F-actin, but have been shown to interfere with actin dynamics in live cells (260-265). Hence, we adopted an indirect approach to track individual filaments specifically nucleated by formins by utilizing the fact that each filament has a single functional formin homodimer attached to its growing barbed end (41). Previously described EGFP-mDia1-generated filaments in the cytoplasm of *Xenopus laevis* oocytes required sparse labeling coupled with speckle microscopy to avoid background fluorescence (266). We used the constitutively active mDia2 (mDia2-FH1-FH2-C) which generates filopodia and that allows us to easily visualize actin filaments using conventional wide-field microscopy (254). The FH1 domain of mDia2 contain fewer PFN1-binding poly(L-proline) stretches than that of mDia1. To address whether the number of PFN1-binding sites in the FH1 domain influences actin nucleation and elongation, we generated a chimeric construct containing the FH1 domain of mDia1 and FH2 domain of mDia2 (mDia1-FH1-mDia2-FH2-C) (see Materials and Methods).

Initially, naïve HeLa cells were transiently transfected with EGFP*-mDia2-FH1-FH2-C. As expected, mDia2 gave rise to filopodia that can be distinctly identified by the presence of mDia2 molecules at its tip (Figure III-6). Surprisingly, extremely low levels of the constitutively active mDia2 are sufficient to produce filopodia. A fraction of mDia2 (and mDia1) expressing cells produced ring like

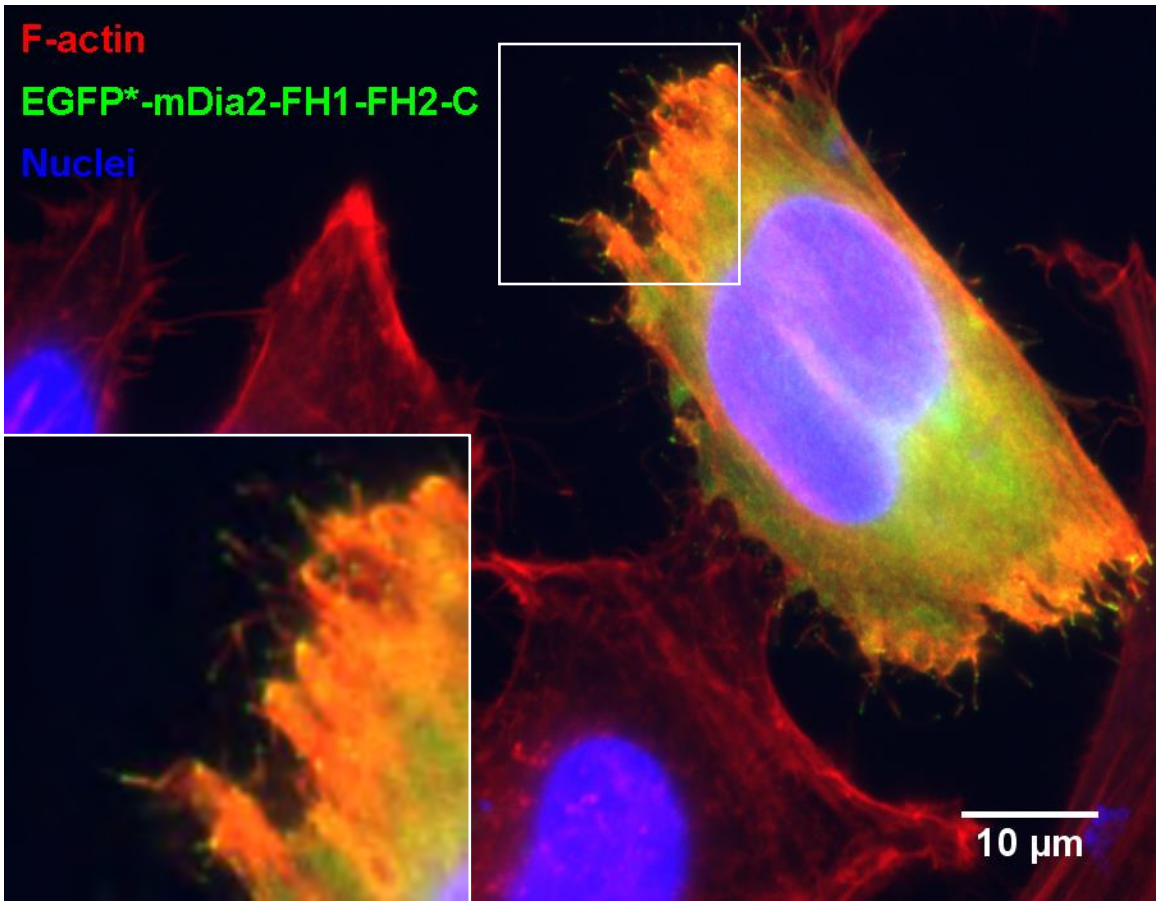

Figure III-6. The formin mDia2 in its constitutively active form nucleates filopodia. Naïve HeLa cells transiently transfected with EGFP*-mDia2-FH1-FH2-C, fixed and stained with phalloidin (red), anti-GFP antibody (green) and DAPI (blue). The region inside the square is enlarged in the inset. The filpodia nucleated by mDia2 can be distinctly seen by the presence of mDia2 molecules at its tip.

structures (data not shown), which were concluded as focal adhesions based on similar observations by other groups (267-269). Low level expression of mDia2-FH1-FH2-C is critical for two reasons. One, high expression levels can lead to toxicity, likely due to the constitutively active nature of this construct. The cells sometimes adopt fusiform morphology with elongated nuclei as reported by others for mDia1 (268,269). In extreme cases, the cells adopt abnormal shapes possibly

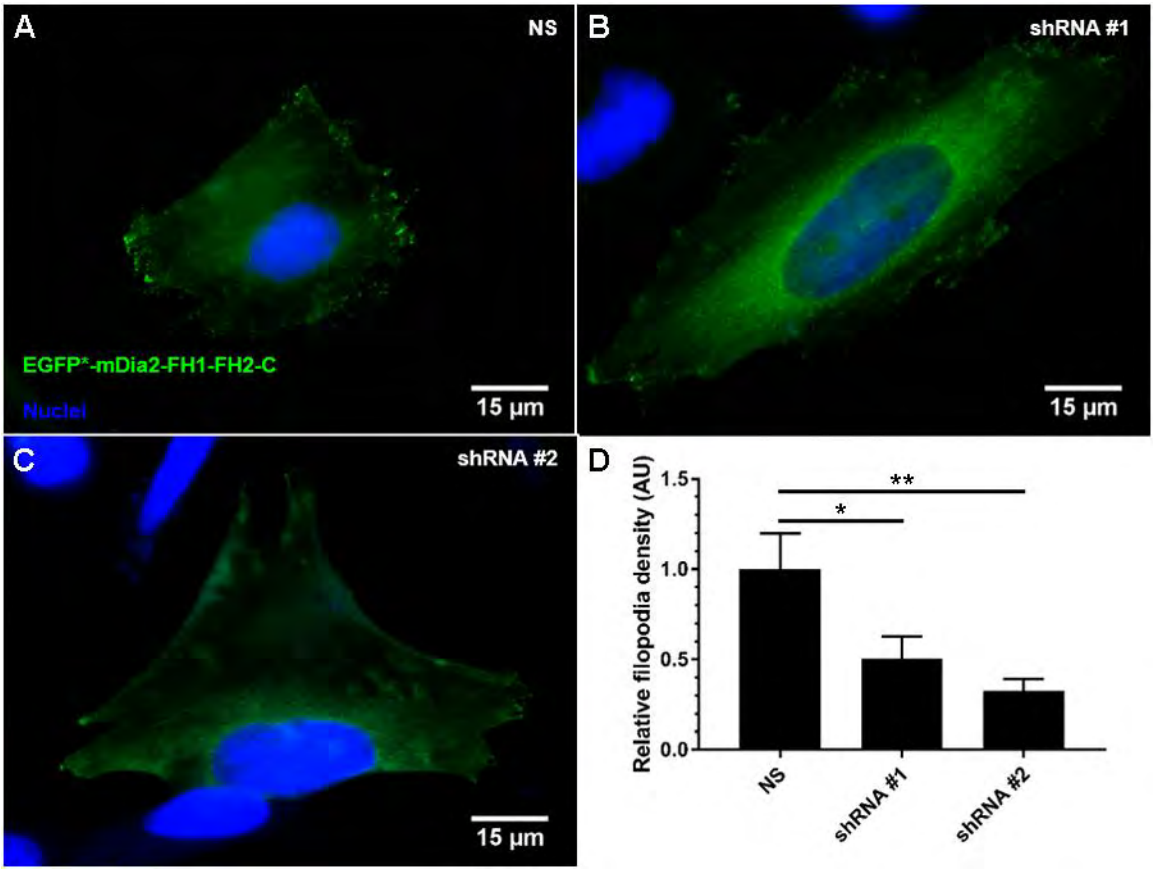

Figure III-7. PFN1 is required for filopodia formation. HeLa cell lines were induced with doxycyline for 96 h to express non-silencing (NS) shRNA (A), PFN1 shRNA #1 (B) or PFN1 shRNA #2 (C), transiently transfected with EGFP*-mDia2-FH1-FH2-C after 72 h of knockdown, fixed and stained with anti-GFP antibody and DAPI. (D) The relative filopodia density from n = 1 experiment was analyzed (18, 21 and 23 cells for NS, shRNA #1 and shRNA #2, respectively) and plotted. The filopodia density was significantly reduced upon PFN1 knockdown. Statistical significance was determined using a one-way ANOVA followed by a Tukey's post hoc analysis (*P < 0.05, **P < 0.01). Error bars represent SEM.

as a result of failed cell division. Two, actin nucleation is directly correlated with the amount of formin. Hence, care was taken to have very low but similar mDia2 expression levels (see Materials and Methods) to obtain meaningful data that can be compared across different cell lines and experiments.

Loss of PFN1 leads to a reduction in formin-generated filopodia

To investigate the effect of loss of PFN1 on filopodia formation, EGFP* tagged mDia2-FH1-FH2-C or mDia1-FH1-mDia2-FH2-C was expressed in cells with inducible PFN1 knockdown (Figure III-5A and B). Robust filopodia formation was observed in the control cell line expressing non-silencing shRNA (Figure III-7A). In contrast, the lines expressing PFN1 shRNA #1 and shRNA #2 displayed significant reductions in filopodia density (Figure III-7B, C and D). As additional controls, we measured the filopodia density under uninduced conditions. Surprisingly, we saw a reduction in filopodia density in the HeLa shRNA #2 line in the absence of induction (Figure III-8C). On assessment by Western blotting, about 50% reduction in PFN1 levels were observed in this line (Figure III-8A and B). This happens only under transfection conditions, as the untransfected and uninduced cell lines had similar PFN1 expression levels (Figure III-5A and B). In fact, the filopodia density correlated strongly with PFN1 levels (Figure III-8D). We reasoned that the process of transfection somehow causes a deregulation of shRNA expression that should be under doxycycline control.

To measure the rates of filopodia growth, the transfected cells were subjected to live cell imaging (Figure III-9). Under PFN1 knockdown, it was difficult to identify transfected cells that contained filopodia, further confirming our fixed cell immunofluorescence experiments described above. On qualitative inspection, the fewer filopodia observed under PFN1 knockdown had rates indistinguishable from that of the non-silencing control (data not shown). Additional experiments need to

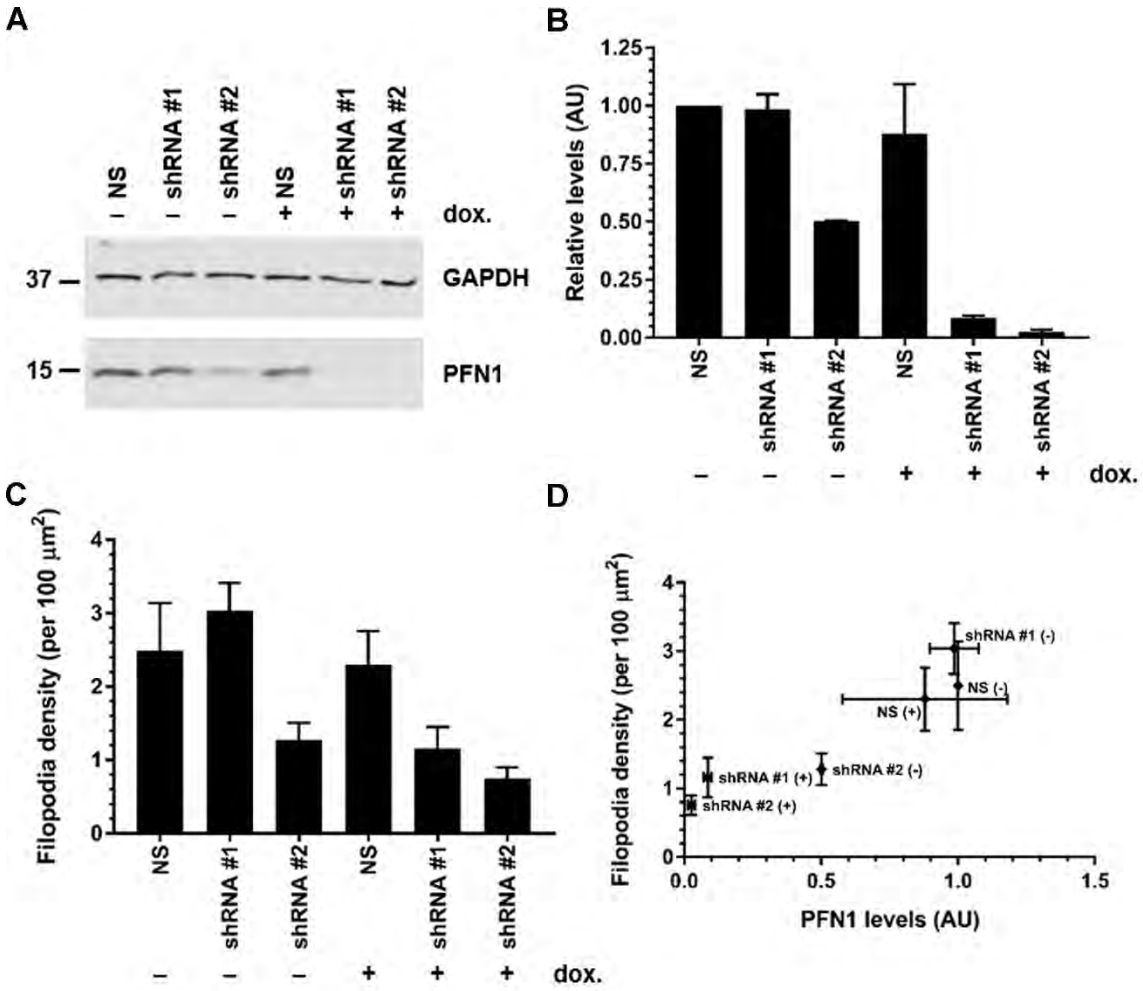

Figure III-8. Transfection deregulates doxycycline control in the PFN1 shRNA #2 HeLa line. (A) Western blotting of lysates prepared from HeLa cell lines uninduced or induced with 1 μg ml^{-1} doxycyline (dox.) for 96 h to express non-silencing (NS) shRNA, PFN1 shRNA #1 or PFN1 shRNA #2 and transiently transfected with EGFP*-mDia2-FH1-FH2-C after 72 h from the start of the experiment. (B) Quantification of PFN1 levels relative to GAPDH from n = 2 experiments by densitometry. The PFN1 levels were similar in the absence of transfection under uninduced conditions (Figure III-5A and B), but transfection with EGFP*-mDia2-FH1-FH2-C caused about 50% reduction in PFN1 level in the HeLa shRNA #2 line even in the absence of induction. (C) The filopodia density in the HeLa shRNA #2 under uninduced condition was reduced as a consequence of the low PFN1 level in that condition. (D) A correlation was observed between the filopodia density and PFN1 levels (+ and – represent induction and non-induction respectively). Errors bar represent SEM.

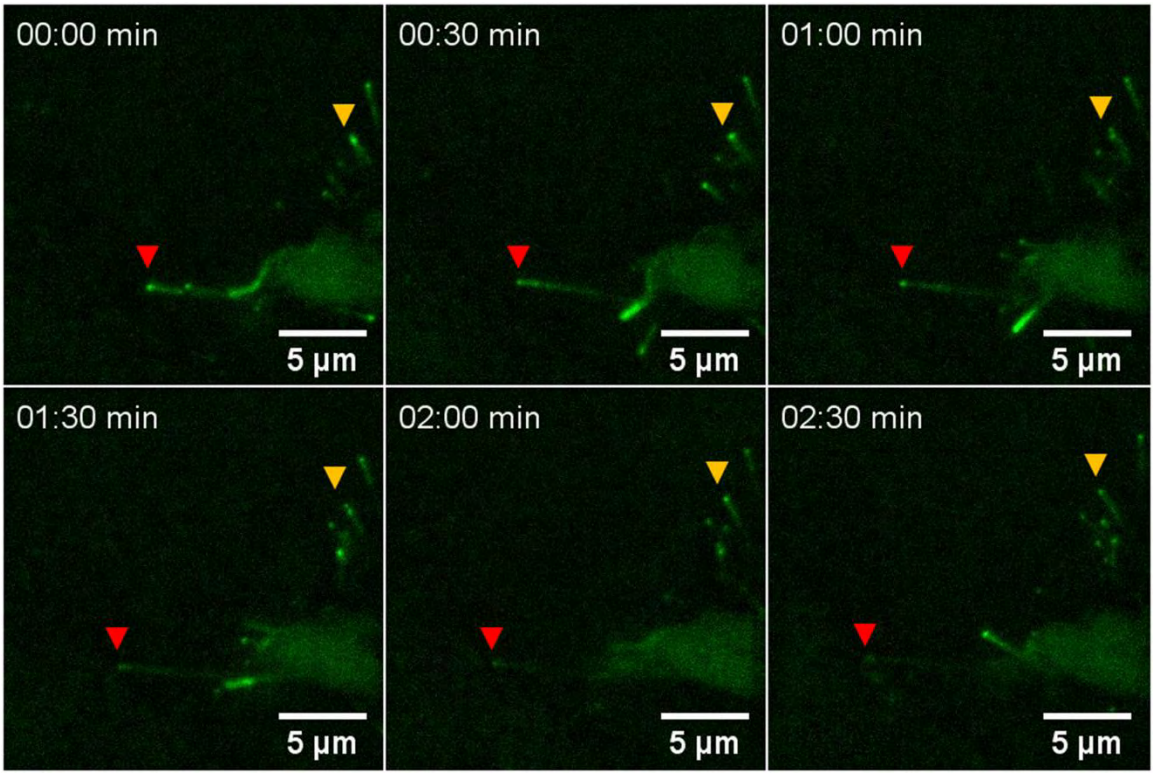

Figure III-9. Live imaging of filopodia growth. An example of a time series of images showing the elongation of filopodia. In this case, HeLa cells were induced for expression of non-silencing shRNA for about 90 h, transfected with EGFP*-mDia2-FH1-FH2-C after 72 h of expression. Images were acquired every 2 s for 3 minutes. Arrowheads point to growing filopodia.

be performed under the knockdown conditions to reliably measure potential differences in elongation rates as a function of PFN1 expression.

M114T PFN1 causes a modest increase in formin-generated filopodia

Next, we tested the impact of the ALS-PFN1 variant M114T on filopodial phenotypes. Expression of V5 tag alone for 48 h did not affect filopodia formation. Expression of V5-WT over endogenous WT produced filopodia to the same extent as V5 tag alone. We reasoned this to be due to the controlled expression of V5-PFN1 close to endogenous levels. Expression of V5-M114T for 48 h over the

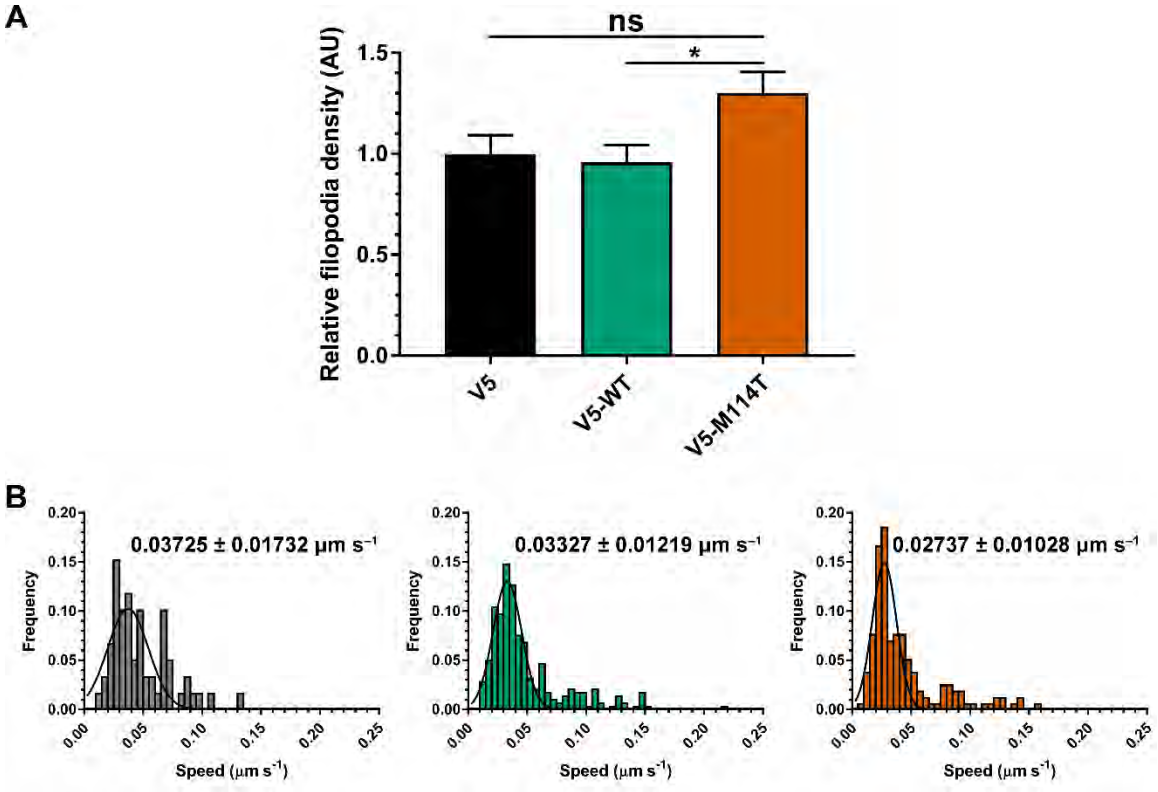

Figure III-10. M114T PFN1 causes modest increase in fliopodia density but does not alter filopodia growth rates. (A) HeLa cell lines were induced with doxycyline for 48 h to express V5, V5-WT or V5-M114T, transiently transfected with EGFP*-mDia2-FH1-FH2-C after 24 h of expression, fixed and stained with anti-GFP antibody for quantification and analysis. The relative filopodia density from n = 1 experiment was analyzed (29, 29 and 30 cells for V5, V5-WT and V5-M114T respectively) and plotted. The filopodia density was higher for V5-M114T compared to V5-WT or V5. Statistical significance was determined using a one-way ANOVA followed by a Tukey's post hoc analysis (*P < 0.05, ns – non significant). Error bars represent SEM. (B) HeLa cells lines were induced and transfected as in (A) and imaged live. The apparent speed (root mean square) of filopodia growth was similar across all three conditions. Errors represent SD from the Gaussian fit.

endogenous WT produced a modest increase in filopodia density compared to V5-WT (Figure III-10A). Expression of V5, V5-WT or V5-M114T did not affect the filopodia elongation rates (Figure III-10B). To test if the exogenously expressed WT or ALS V5-PFN1 can rescue the filopodia density phenotype observed under

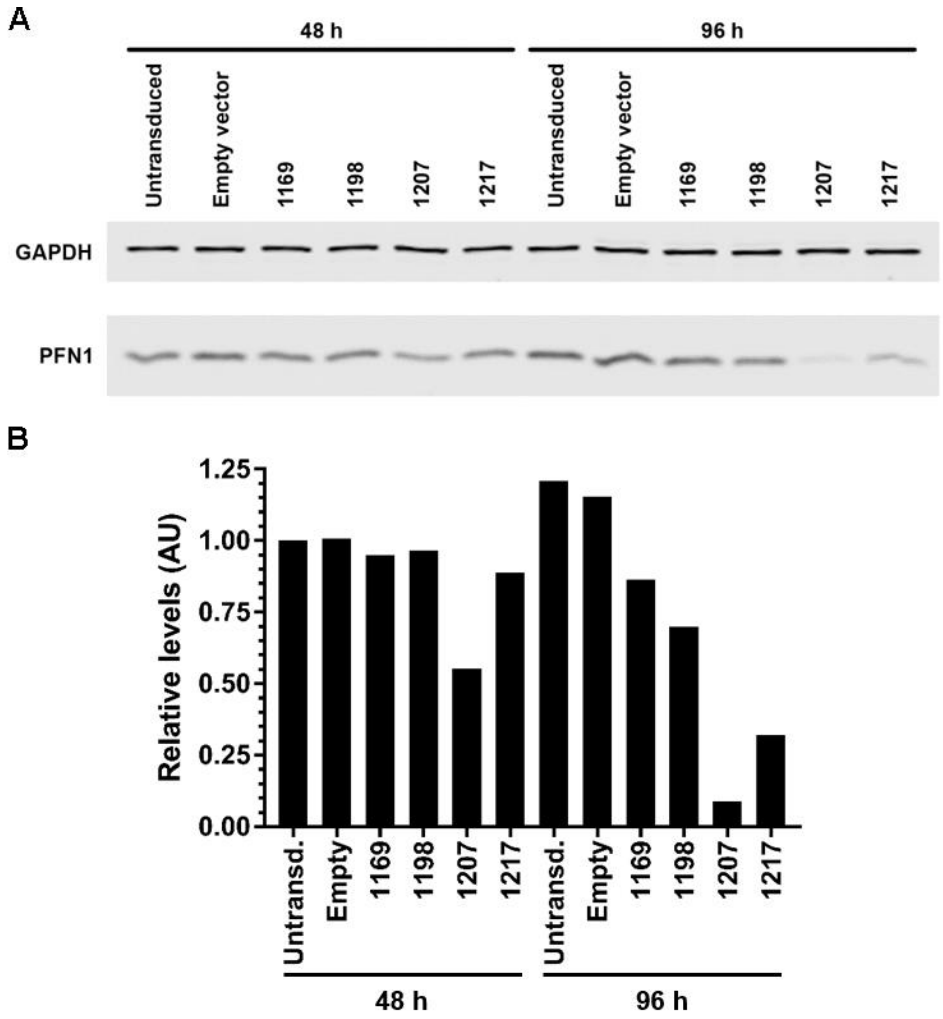

Figure III-11. Characterization of 3'-UTR PFN1-miRNAs. (A) Western blotting of lysates prepared from HEK293T cells transduced for 48 h or 96 h with empty CSCGW2.tdT vector or the four 3'-UTR PFN1-miRNAs (see Materials and Methods). (B) Quantification of PFN1 levels relative to GAPDH from n = 1 experiment by densitometry. A robust knockdown was observed with the 3'-UTR PFN1-miRNA-1207 at 96 h.

endogenous PFN1 loss, we cloned four artificial 3'-UTR PFN1-miRNAs under the control of U6 promoter into the CSCGW2.tdT lentiviral backbone (see Materials and Methods and Appendix V). These 3'-UTR PFN1-miRNAs are expected to specifically knockdown endogenous PFN1 while not affecting the exogenous V5-

PFN1. Of the four 3'-UTR PFN1-miRNAs tested, miR-1207 was able to robustly knockdown endogenous PFN1 in HEK293T cells (Figure III-11). The next steps would entail knocking down the endogenous PFN1, simultaneously expressing V5-PFN1 and assessing the rescue of filopodia density phenotype.

Discussion

In the single molecule experiments, a reduction in the number of filaments for M114T in the absence of mDia1 (Figure III-3A) suggests that M114T might exhibit a tighter binding to actin thereby inhibit actin nucleation. In the presence of mDia1, unexpectedly, there is an increase in the number of filaments compared to WT (Figure III-3B). While there is no clear explanation of the mechanism, we reason that in the presence of mDia1 the FH1 domain can efficiently deliver high affinity M114T-actin complexes to FH2 sites for nucleation. The other possibility is that binding of M114T to formin affects the interaction of M114T with actin. This was demonstrated using PFN2; PFN2, upon binding SMN, partially failed to suppress spontaneous actin polymerization (122). The number of filaments in the presence of G118V was higher than WT without mDia1 (Figure III-3A) implying a weaker affinity for actin which supports our pyrene-actin polymerization assays (Figure II-14). However, it is unclear why an increase in filament number is seen with G118V in the presence of mDia1. Interestingly, the elongation rates of spontaneously generated actin filaments in the presence of M114T is significantly higher (Figure III-3C). It must be that the M114T PFN1 has an otherwise

undescribed manner of interaction with F-actin. Profilin has transient interactions with the filament barbed end (19,42-46). Further studies are needed in order to verify if this profilin-F-actin interaction influences the filament elongation rate. The second possibility is that M114T has enhanced ability to maintain actin in the ATP-charged state. Our experiments explain why the polymerization status of M114T in the fluorimetric assays was indistinguishable from WT (Figure II-14). Although there is a reduction in filament number with M114T, this is compensated by an increase in F-actin elongation rates effectively resulting in a polymer mass similar to WT.

The elongation rates of mDia1-generated filaments were elevated for G118V at higher PFN1 concentrations (Figure III-4). It is quite possible that the relative equilibrium levels of PFN1-actin, PFN1-formin, actin-formin, PFN1-actin-formin can determine filament nucleation and elongation rates. Therefore, the relative concentrations of actin, PFN1 and formin assumes significance and necessitates careful study of these processes in future. Taken together, we speculate that M114T and G118V, both affect actin polymerization but by different mechanisms.

In this study, we adapted certain published methods (254,266) to study the role of WT and ALS-PFN1 in actin nucleation and elongation rates. While mDia1 exhibits faster elongation rates *in vitro* than mDia2 (255), it requires high resolution microscopy to observe these molecules in cells. On the other hand, mDia2-generated filopodia are much easier to visualize (254). In addition, the actin

nucleating FH2 domains of these two formins share about 76% sequence similarity (and 59% sequence identity). Hence, we made a compromise by using mDia2 to improve detection but at the cost of elongation speed.

In our experiments in HeLa cells, loss of PFN1 led to a reduction in filopodia density. This could reflect unproductive nucleation or elongation due to (i) lack of ATP-charged actin normally produced by profilin, (ii) unloaded poly(L-proline) motifs in the FH1 domain of mDia2-FH1-FH2-C, (iii) sequestering of excess free actin (normally bound to PFN1) by factors such as thymosins, resulting in nucleation inhibition. All these unfavorable polymerization conditions can result in a net depolymerization. It is also likely that the effective nucleation by formin requires PFN1 – the FH1 may help increase local concentration of profilin-actin that can be subsequently captured by the FH2 domain for nucleation. Interestingly, recent studies show that the loss of profilin leads to a reallocation of actin from formins to Arp2/3 machinery (59,60). Expression of V5-M114T causes a small increase in filopodia density (Figure III-10), which agrees with our biochemical data, further supporting that M114T enhances formin nucleation.

Although differences in filopodia density were observed, elongation rates of filopodia were similar under M114T PFN1 expression (Figure III-10B). *In vitro*, differences in elongation rates between WT and G118V started to emerge only at higher PFN1 concentrations (Figure III-4). The concentration of PFN1 in cells is estimated to be greater than 50 μM (15), but the local concentration of PFN1 can be different depending on the cellular location. Concentrations of PFN1 (and actin)

in the neighborhood of actin polymerization are likely to determine rates. So, it is possible that the filament elongation rates generated by the same formin can be different depending on the cellular location. The average filopodia elongation rate in our experiments was about 0.03 μm s^{-1} (Figure III-10B), which was very slow compared to mDia1 (266). Nevertheless, this is in agreement with recent studies of actin velocities in motor neuron growth cones (270) and the similar average filopodia length in *Drosophila* NMJs expressing different PFN1 variants (147). There could be a number of reasons for relatively slower elongation rate observed with mDia2 – the amount of PFN1 localized in the vicinity of filopodia is much lower, fewer poly(L-proline) motifs in the FH1 of mDia2, the membrane provides a resistance and has to be remodeled to allow filaments to push and protrude out of the membrane. Therefore, it is necessary to carefully examine different formins capable of generating filaments in different areas of the cell, possibly at different rates, and identify the actin structures that behave abnormally under mutant PFN1.

It is known that the elongation rates are directly correlated with the number of profilin-binding poly(L-proline) motifs in the FH1 domain of formins (66). This prompted us to test the hypothesis that increasing the number of poly(L-proline) motifs in FH1 might amplify certain cellular phenotypic differences caused by mutant PFN1, which would otherwise be undetectable due to inherent noise in experimental measurements. Hence, by fusing the FH1 of mDia1 to the FH2 of mDia2, we expect to see higher filopodia elongation rates, and any differences between WT and mutants will become visible. This chimeric mDia1-FH1-mDia2-

FH2 also gave rise to filopodia (data not shown). It will be interesting to see if the increase in profilin-binding sites in FH1 also influences nucleation and rescues filopodia density upon PFN1 reduction.

To summarize, differences in nucleation and elongation are observed with ALS-PFN1 both *in vitro* and in cells. To explain the mechanism, comprehensive kinetic and equilibrium binding studies of both the binary (actin-PFN1, formin-PFN1) (see Appendix III) and the ternary complexes (actin-PFN1-formin) have to be performed. In addition, rescue experiments in cells with endogenous PFN1 knocked down will help to unambiguously determine if ALS-PFN1 variants act by a loss-of-function or gain-of-function mechanisms. Our results already suggest that M114T or G118V is unlikely to cause a loss-of-function in PFN1. They can both bind actin and likely formins, and both enhance nucleation relative to WT, in the presence of the formins and therefore act via a gain-of-function mechanism. We did not include the variant C71G in our studies as this variant is aggregation prone and could have confounded our results. This variant was highly unstable as demonstrated by its unfolding below the body temperature of 37 °C (Figure II-1B). But we predict that under near endogenous expression levels and in the absence of endogenous WT, C71G should fail to induce filopodia. Therefore, C71G can act via a loss-of-function mechanism with respect to actin assembly. Nevertheless, it needs to be tested if C71G can contribute to defective actin assembly. While the study was focused predominantly on the impact of ALS-PFN1 on actin assembly, there are other important aspects of actin dynamics such as actin disassembly, the

role of PFN1 in ADP-ATP exchange on actin, binding to phosphatidylinositols and Rho GTPase signaling that need to be investigated. The use of super-resolution microscopy, such as STORM, is also advocated to study neuronal actin cytoskeletal structures in the future.

Materials and Methods

Plasmids, lentiviruses and cloning

The pEGFP*-C1-mDia2-FH1-FH2-C plasmid was kindly provided by Dr. Henry Higgs (Dartmouth College). The EGFP protein contains the mutation A206K that prevents its dimerization (254,271). Hence, the protein product is referred to as EGFP*-mDia2-FH1-FH2-C throughout this chapter. To construct the chimeric plasmid pEGFP*-C1-mDia1-FH1-mDia2-FH2-C, two PCR reactions were carried out to generate the mDia1-FH1 domain (amino acids 553 to 745 of full length mDia1) and the other large linear fragment consisting of the backbone pEGFP*-C1 and mDia2-FH2-C (amino acids 609 to 1171 of full length mDia2). The primers 5'-GAGCTGTACAAGTCCGGACTCAGATC-3', 5'-GGTTTCAAACCAAATGGCAGAACTGGGGCCGCAGGAA-3' for the former and 5'-TTCCTGCGGCCCCAGTTCTGCCATTTGGTTTGAAACC-3', 5'-GATCTGAGTCCGGACTTGTACAGCTC-3' for the latter were designed to introduce appropriate overlaps between the fragments for subsequent cloning using NEBuilder® HiFi DNA Assembly Cloning Kit (NEB E5520S).

Artificial 3'-UTR PFN1-miRNAs, miR-1169, miR-1198, miR-1207, miR-1217, targeting the 3' non-coding region of the human PFN1 gene were designed by Dr. Miguel Sena-Esteves. G-blocks were synthesized (IDT) (miR-1171 could not be synthesized due to technical difficulties) and cloned into the lentiviral CSCGW2.tdT background using the NEBuilder® HiFi DNA Assembly Cloning Kit. The CSCGW2.tdT differs from the CSCGW2 vector by the presence of tdTomato reporter in place of EGFP. To generate the CSCGW2.tdT plasmid, the EGFP sequence in the CSCGW2 vector was replaced with the tdTomato sequence using the restriction sites NheI and XhoI. The primers 5'-GAGAGCTAGCGCTACCGGTCGCCACCATGGTGAGCAAGGGCGAGGAGGT-3', 5'-GAGACTCGAGATCCTACTACTTGTACAGCTCGTCCATGCCGTACAG-3' were used in a PCR reaction to generate the tdTomato insert flanked by the restriction sites from the plasmid pGW1-tdTomato (provided by Dr. John Landers) as the template. This was done so as to use it along with the pEGFP*-mDia2-FH1-FH2-C plasmid. Lentiviruses were generated in HEK293T cells using VSVG and CMVdR8.91 packaging plasmids.

Protein purification

PFN1 proteins were purified as described in Appendix I. Rabbit muscle actin and mDia1-FH1-FH2-C proteins used in single molecule experiments were purified as previously described (259).

Single molecule experiments

The single molecule experiments were done as described previously (272). The experiments used rabbit muscle actin, recombinant WT or ALS-PFN1 variants. To visualize actin filaments, actin labeled at Cys374 with the fluorophore Oregon Green (272) was employed and imaged using a Nikon total internal reflection fluorescence microscopy.

Cell culture

HeLa and HEK293T cells were cultured in Dulbecco's minimal essential medium (Gibco, 11965) containing 10% (vol/vol) fetal bovine serum (Sigma-Aldrich, F-6178) and 1% (wt/vol) penicillin and streptomycin (Gibco, 10378) under standard culture conditions (37 °C, 5% CO2/95% air).

Stable HeLa cell lines used in the fixed and live cell imaging experiments were generated by Dr. Jeanne McKeon. HeLa cell lines expressing doxycycline inducible non-silencing shRNA, PFN1 shRNA #1, PFN1 shRNA #2 (Dharmacon RHS4743) were made using lentiviral transduction and subsequent selection and maintenance using puromycin. Stable lines with inducible expression of V5, V5-WT or V5-ALS-PFN1 were generated in HeLa cells stably expressing tetracycline repressor (Addgene, 17492) using lentiviral transduction followed by puromycin selection. The V5-PFN1 used to generate these lines were cloned into the pLenti-CMV-TO-Puro backbone. To induce knockdown or expression of exogenous PFN1, fresh doxycycline at 1 μg ml^{-1} final concentration was added to the stable lines. PFN1 knockdown was induced for approximately 96 h and formin

transfections were carried out at 72 h time point using Lipofectamine 2000 (Invitrogen, 11668-019). Exogenous PFN1 was induced for 48 h with transfections at 24 h time point.

Viral transductions of CSCGW2.tdT-3'-UTR-PFN1-miRNAs in HEK293T cells were carried out on a 6-well plate. 225 µl of low titer virus (~10^7) were added on two consecutive days and the levels of PFN1 were assessed by western blotting at 48 h and 96 h from the first round of transduction.

Western blotting

Cells were lysed using RIPA buffer (Boston BioProducts, BP-115-500) containing protease inhibitors (Roche, 11873580001), clarified by centrifugation in a table-top centrifuge at 13,000 rpm for 15 minutes at 4 °C. The protein concentration of soluble fractions was determined using a bicinchoninic acid assay (Thermo Scientific Pierce, 23227). Western blotting experiments were done as previously described (232,273). Endogenous PFN1 and exogenous V5-PFN1 were detected using anti-PFN1 (1:1,000, Sigma-Aldrich, P7749-200UL) and anti-V5 antibody (1:1,000, Invitrogen, R96025) respectively. GAPDH, detected using anti-GAPDH (1:20,000, Sigma-Aldrich, G9545) was used as a loading control.

Measurement of filopodia densities

Stable HeLa cells, plated in 24 well plate, were transiently transfected with 100-150 ng of pEGFP*-C1-mDia2-FH1-FH2-C for 24 h using Lipofectamine 2000 (Invitrogen, 11668-019) at 1 µl per 500 ng of plasmid. The cells were fixed in 4% paraformaldehyde, blocked with DPBS (CellGro, 21-031-CV) containing 4%

normal goat serum (Jackson ImmunoResearch, 005-000-121) and 0.1% Triton™ X-100 (Sigma-Aldrich, T9284). The antibodies were diluted in DPBS containing 2% normal goat serum and 0.1% Triton X-100. The cells were incubated with Alexa Fluor 488 conjugated anti-GFP antibody (1:2,000, Invitrogen A-21311) for 1 hour at room temperature, followed by incubation with Alexa Fluor™ 647 phalloidin (1:40 to 1:25, Thermo Fisher Scientific, A22287) for 30 min and DAPI for 15 min. To stain V5-PFN1 in the V5-PFN1 lines, the cells were incubated with anti-V5 antibody (1 h, 1:2,000, Invitrogen, R960-25) and Cy5-conjugated secondary antibody (1 h, 1:2,000, Jackson ImmunoResearch, 715-175-151) prior to incubation with anti-GFP antibody. The coverslips were mounted on microscope slides (Globe Scientific, 1380-20) using ProLong® Gold Antifade Mountant (Invitrogen, P36930). The coverslips were blinded before mounting for an unbiased image acquisition and analysis.

Using a 100x objective, Z-stack images at 0.2 µm spacing were collected using Leica DMI600 B microscope. Images were acquired from cells that had similar levels of low EGFP*-formin expression. Maximum projection images were processed using a Gaussian filter, and thresholded EGFP*-formin particles were counted using the automated particle counting feature in FIJI (ImageJ). The filopodia density was calculated as the number of EGFP*-formin particles per 100 μm^2 and normalized against the control condition (shRNA NS or V5). A macro for carrying out the above process is described in Appendix IV. Graphing and statistics were performed using GraphPad Prism.

Measurement of filopodia elongation rates

For live cell imaging, 50,000 cells were plated on 6 cm glass bottomed plates pre-coated with poly-D-lysine (MatTek, P35GC-1.5-14-C) and transfected with 250 ng of plasmid using Lipofectamine 2000 (2 µl per 1 µg of plasmid) (Invitrogen, 11668-019) for about 16 h. Images were acquired every 2 seconds for 3 minutes (60x objective and an added 1.5x magnifier) using a Nikon Eclipse Ti microscope equipped with a temperature and CO_2 controlled chamber. The filopodia growth trajectories were obtained using the TrackMate plugin in FIJI. The Laplacian of Gaussian detector with an estimated blob diameter of 0.5 µm and a threshold value of 10 was applied to detect the particles in each frame. For tracking, the linear alignment program (LAP) linking was used with 1 µm as the maximum frame to frame linking distance. Tracks extending less than 20 seconds were discarded. The tracks and the co-ordinates of the mDia2 particles at each time point were exported to an .xml file which was subsequently read in MATLAB using the function written by Tarantino et al. (274). The filopodia in the live cells display a variety of motions, but to obtain meaningful elongation rates, only those filopodia growing in straight line had to be analyzed. The tracks generated by randomly diffusing, non-filopodia generating mDia2 molecules and the filopodial “swinging” due to non-attachment to the substrate (coverslip) had to be excluded. Two different approaches were used to identify filopodia tracks that exhibit growth in a near straight line, which is essential for obtaining elongation rates. The first method, qualitative in nature, involves plotting the bivariate distributions of effective

speed (y-axis) vs. the root mean square (RMS) speed (x-axis) as a heat map. The data points along the line y = x, represent the velocities of mDia2 particles moving in a near straight line. The second method involves autocorrelation of the position (or velocity) vectors over time within a track. This is similar to the analysis described previously (274,275) but instead of applying the analysis to the ensemble tracks, it can be applied to each individual track. If the mDia2 particles move in a straight line, the corresponding track exhibits high position or velocity autocorrelation in time. This method was used to analyze the data presented in Figure III-11. Appendix IV lists the MATAB functions written for this analysis.

CHAPTER IV – DISCUSSION

Complexity of ALS

ALS is one of the several complex neurodegenerative diseases for which a cure is still elusive (1). The fact that a majority of the people are afflicted sporadically, makes neurodegenerative diseases like ALS extremely difficult to study. The knowledge accumulated over the past three decades stems mainly from the study of familial mutations, and has nevertheless helped gain tremendous knowledge on disease pathogenesis (2,4). Mutations in SOD1 were first linked to ALS in 1993 (3). The mutations such as A4V, G93A and G85R caused SOD1 to be aggregation prone and therefore, the initial focus was on protein misfolding and aggregation as in many other neurodegenerative diseases. However, the subsequent identification of several functionally distinct genes implicates a disease course that involves multiple pathogenesis mechanisms leading to multiple failures, culminating in the death of the motor neurons (2,167,276). Many of these pathways are interconnected, and so if one is “hit” there could arise a domino effect harming other pathways, but somehow, all pathways eventually converge causing neuronal loss.

It has been puzzling that most ALS-linked genes are expressed ubiquitously, yet motor neurons are particularly susceptible. This selective death of neuronal subtypes is also observed in other neurodegenerative diseases such as AD, PD and HD (277-279). The key is to answer the critical question – what

makes specific neuronal subtypes susceptible? What is it about these neuronal subtypes that makes them very different from other cell types and why are they susceptible compared to other cell populations? One possible answer that we already saw in Chapter I, is the extremely complex morphology of neurons with axons sometimes extending up to one meter and the extensive dendritic branching. The second feature is their post-mitotic nature. The features that make them distinct and special also make them susceptible to disease-causing insults, therefore neuronal quality control mechanisms have to be at their peak capability to protect them from mutations, cellular stresses and toxicity. It has been widely believed that with age, the general health keeping measures such as proteasome, UPR, autophagy etc. deteriorate in their performances (162,163,172,280). Under situations of a “second-hit” such as a mutation in a crucial gene, the recovery of these neurons is not guaranteed, because they are post-mitotic and cannot divide to create new populations.

The major factor responsible for developing and preserving the overall neuronal morphology, yet allowing for changes during neuronal activity, is the cytoskeletal system comprised of microtubules, actin filaments and neurofilaments. Compromise of the neuronal cytoskeleton during neurodegeneration-mediated death of neurons cannot be ignored. While microtubule cytoskeletal defects have been studied extensively (192,195), research focusing on actin cytoskeletal defects has gained significance. For example, the formation of cofilin-actin rods and Hirano bodies has been reported

in AD patients but little is known about these abnormal structures (207,209). These structures have not been reported in ALS nevertheless. There is evidence for actin dysregulation in HD, SBMA and SMA which was discussed in Chapter I. The discovery of mutations in actual cytoskeletal proteins, such as DCTN1, PFN1 and more recently, TUBA4A brings the cytoskeletal picture to the forefront. Even though there have been suggestions that pathogenic mechanisms can be mediated through PFN1 in HD and SMA (75,78,108,109,122,123), this is the first time disease causing mutations in PFN1 have been identified. Studying how PFN1 mutations cause ALS may provide insights into the role of PFN1 in HD and SMA, and actin dysregulation in neurodegeneration in general.

The foremost question to address, when discussing implications of ALS-PFN1 mutations is whether the mutations act through a loss-of-function or gain-of-function mechanisms. PFN1 homozygous knockout mice are embryonic lethal suggesting PFN1 is required for development (93). Heterozygous PFN1 knockout mice have reduced chances of survival but nevertheless develop normally (93). PFN1 conditional knockout in nervous tissues of mice do not present overt phenotypes (99-103,107) with respect to actin. ALS caused by mutations in PFN1 is dominantly inherited (6,7). Hence, broadly it can be said that PFN1 mutations act through gain-of-function mechanisms. But do the gain-of-function mechanisms act through structural destabilization of PFN1, functional defects or a combination of different mechanisms? We can hypothesize that the structural destabilization of PFN1 due to mutations can lead to protein misfolding or aggregation that can

acquire toxicity due to aberrant interactions with other proteins. At the functional level, however, the terms loss-of-function and gain-of-function are somewhat difficult to delineate. For example, a loss of PFN1 may not simply imply a loss of actin polymerization. As already discussed, PFN1 affects nucleation and elongation both of which depend on PFN1 levels. In our experimental paradigm, the interactions of PFN1 with actin, formin or both determine how actin polymerization proceeds. The ALS-mutations can affect these interactions triggering an “aberrant” polymerization which would normally be absent in the PFN1 heterozygous knockout mouse. Hence the term, “dominant gain-of-function of PFN1” in genetics may translate to an “aberrant actin polymerization” or “actin cytoskeletal dysregulation” at the biochemical level that can lead to toxicity. It is also possible that the ALS-variants of PFN1 studied in our experiments can gain toxic functions by an altogether different mechanism, not involving actin cytoskeleton or more than just one mechanism. In the rest of this chapter, I expand on the two potential pathogenic mechanisms described in this dissertation – structural destabilization and defects in actin cytoskeleton – and suggest future directions.

Structural complications and beyond

The seminal study describing the presence of insoluble aggregates colocalizing with ubiquitin in motor neurons (7) prompted us to study the biophysical characteristics of PFN1 mutants. The variants that were described in

the original study, C71G, M114T and G118V were all destabilized (Figures II-1 and II-3). Our data for the most part were supported by equilibrium and kinetic studies by Chiti and colleagues (281). However, there were certain differences – C71G in their studies had a conformational stability similar to WT, and the CD spectrums revealed structural differences compared to WT. Further, they report a correlation between aggregation propensities of PFN1 variants and structural changes observed in native state but not conformational stabilities; the lack of correlation was mainly due to C71G exhibiting near WT conformational stability in their experiments (281). The differences could arise due to the protocol employed to purify PFN1. While we developed a novel method for purifying PFN1, Chiti and colleagues used the poly(L-proline) affinity chromatography eluting bound PFN1 with 8 M urea (281,282). It is interesting to note that from these two studies that C71G can adopt different conformational states further supporting protein misfolding as a causative factor in PFN1-ALS. In addition, Chiti and colleagues characterized the ALS variants A20T, T109M and Q139L identified in subsequent genetic screens. T109M and Q139L had similar conformational stabilities as WT, but A20T had a stability similar to that of G118V. The overall aggregation propensities of the PFN1 mutants according to their studies were WT ~ E117G, Q139L < A20T, G118V < M114T < C71G, T109M and that they are correlated with structural changes in the native state as opposed to conformational stability (281,283). Here again, in their studies T109M purified using poly(L-proline) affinity chromatography had a high aggregation propensity despite a conformational

stability similar to WT. It will be interesting to see if T109M purified using our novel purification protocol has a lower conformational stability. In cells, the mutants form visible aggregates when overexpressed (7). As ALS-mutations in PFN1 are rare, verifying the presence of aggregates in brain and spinal cord autopsy tissues has been difficult. Immunohistochemistry of patient derived tissues harboring E117G or Q139L mutations did not contain PFN1-positive inclusions, although TDP43-positive cytoplasmic inclusions were observed (6,142). Under near endogenous expression levels in HeLa cells, no visible ALS-PFN1 aggregates were seen (Dr. Jeanne McKeon in Bosco lab, unpublished results), although the presence of toxic PFN1 oligomers cannot be ruled out. Further, the insoluble PFN1 that forms gets cleared eventually (Figure II-3). Importantly, the studies should be conducted in aging neurons at physiological expression levels as ALS is an adult-onset disorder affecting specific neuronal subtypes. It is interesting to note that all PFN1 variants when aggregated cause an increase in thioflavin-T fluorescence suggesting the aggregates have cross β-sheet structure (281). Analysis of the time course of WT PFN1 aggregation by transmission electron microscopy revealed the formation of 13 nm curvilinear fibrils after 4 days that increase in length and eventually form straight fibrils that associate to form larger bundles (281). The presence of structured aggregates and the fact that PFN1 and the neuronal isoform PFN2 have highly similar structures, raises the possibility that mutant PFN1, in addition to recruiting WT PFN1, can also recruit PFN2 thereby leading to loss of key neuronal functions mediated by PFN2. In light of these observations, it will be informative to

conduct studies in motor neurons harvested from PFN1 ALS-mouse models (150,151) or derived from induced pluripotent stem cell (IPSC) models to see if the above predictions are true. It is also important to look for signatures of proteostatic stress and if the PQC mechanisms are overburdened. Acquiring all this knowledge will assist us in designing therapies that can target misfolded PFN1 and aggregates. The DSF method described in Chapter II was performed in a 384-well plate. This provides an opportunity to design high-throughput screens to probe for chemical or biological ligands that can enhance the stability of mutants as a therapeutic intervention (229).

X-ray crystallography is a valuable tool to study protein structures. In the X-ray crystallographic studies, M114T crystallized in a different space group than WT or E117G (Table II-2). The extended cleft observed in M114T (Figures II-15 and II-16) is unlikely due to normal thermal motions present in PFN1 for several reasons. The residue Met114 resides in the interior of a protein and is mutated to a relatively small threonine residue (Figures I-1, II-15). The variant M114T had to be crystallized under different conditions (see Chapter II Materials and Methods) which already suggested existence of structural perturbations. Further, the extended cleft was not present in WT PFN1 upon inspection of the ensemble WT PFN1 structures solved by NMR (10,284). While a non-surface exposed cavity is predicted for C71G using similar arguments, it would be important to verify its presence by actually solving structures. The ALS-mutations A20T, T109M and R136M also occur in secondary structural elements in the interior of the protein

(Figure I-1) and it is important to investigate if these mutations also introduce clefts or cavities in the hydrophobic core of PFN1. Even though X-ray crystallography allowed us to capture M114T in an aberrant conformation, it usually reports a static protein structure. It is therefore essential to perform experiments that report on the dynamics of WT and ALS-PFN1 to thoroughly understand the structural perturbations present in the mutants that lead to destabilization and aggregation. The variant G118V will be particularly interesting, as the residue G118 is surface exposed, but is still destabilized. Since PFN1 is small, it is amenable to be studied by NMR. Hydrogen-deuterium exchange coupled to NMR or mass-spectrometry will further complement these studies and will aid us in structure-based drug design. Understanding the structural and conformational dynamics may also enable us to understand some of the complex behaviors exhibited by M114T in actin assembly (Figure III-3).

Comprehending the role of actin in ALS

Experiments of increasing complexity were designed to study the fundamental actin processes of nucleation and elongation, i.e. we began with experiments that reported on binding of PFN1 to its ligands (Chapter II), proceeded to functional biochemical experiments, and then to mammalian cells for recapitulation of key phenotypes (Chapter III). In the actin polymerization and poly(L-proline) binding experiments, there was no evidence for impaired binding of PFN1 to poly(L-proline) or actin (Figures II-13 and II-14). Further *in vitro*, mutant

PFN1 participates in mDia1-mediated actin filament assembly (Figures III-3 and III-4). Hence, it is important to emphasize that the mutations simply do not abrogate the binding of PFN1 to actin as previously suggested (7,129). But anomalies in actin filaments were observed in the presence of mutant PFN1 in neurons (7,146,147), in HeLa cells under conditions where the exogenous PFN1 expression levels were comparable to endogenous PFN1 (Figure III-10), and *in vitro* single molecule experiments (Figures III-3 and III-4). The data presented in Chapter III do not provide mechanistic details, and several experiments need repetition to ensure data reproducibility. Even though actin is highly conserved, the use of non-muscle actin such as β- and γ-actin over the rabbit muscle α-actin is encouraged. The other ALS-PFN1 mutants – T109M, R136W, A20T and Q139L – also need to be examined using the biochemical and cell culture assays. Additionally, it needs to be tested if these mutants behave in a dominant manner in the experiments.

Determining the kinetic and equilibrium parameters of binding of PFN1 to G-actin, F-actin and mDia1 will be crucial to explain the differences observed in actin nucleation and elongation with mutant PFN1. An approach for measuring equilibrium dissociation constants is described in Appendix III. The increase in actin elongation rates observed with M114T presents an enigma (Figure III-3C). Therefore, equilibrium and kinetic binding studies to both G- and F-actin are needed to explain the differences observed with mutant PFN1. Our attempts at measuring equilibrium dissociation constants using fluorescence anisotropy were

not successful and need further optimization (see Appendix III). An alternative to fluorescence spectroscopy is fluorescence correlation spectroscopy or biolayer interferometry from which kinetic as well as equilibrium parameters can be obtained (285).

It is important to note that the binding to one ligand can have allosteric effects or alter the interaction with another. We presented evidence for altered structural features in the vicinity of the two tryptophan residues measured by their increased lifetimes, even though these residues were distal to site of mutations (Figure II-7). Bovine PFN1 has been co-crystallized with actin in two different conformations partly explaining how the nucleotide exchange on actin is facilitated (17,236,286,287). Moreover, Sharma et al. showed that SMN binding to PFN2 through its poly(L-proline) motifs affects the ability of PFN2 to suppress spontaneous actin polymerization (122). Thus, the binding of PFN1 to poly(L-proline) containing ligands such as mDia1 can modulate the affinity of PFN1 towards actin. Therefore, ternary complexes of actin, PFN1 and poly(L-proline) ligands such as mDia1 and their binding kinetics deserve attention. Investigating their structure and conformations will be useful to deduce their mode of operation. With the recent technological achievements in cryo-EM and the growing optimism about solving structures of molecules and complexes below 100 kDa, it should be possible to capture the conformational dynamics of PFN1-actin, PFN1-mDia1 and mDia1-PFN1-actin.

The experiments described in Chapter III focused on only a small aspect of actin dynamics – actin nucleation and elongation in the absence or presence of the formins mDia1 and mDia2. A lot of questions still remain unanswered. Do the mutations affect the ability of PFN1 to catalyze ADP-ATP exchange on actin (Figure I-2C)? If so, does mDia1 cause allosteric effects on this catalytic activity? Can these be used to explain the altered filament nucleation and elongation rates observed with the ALS variants? Is binding to phosphatidylinositols impacted by the mutations? Aβ oligomers disrupt PtdIns(4,5)P_2 metabolism in primary cortical neurons and this is linked to its synaptic dysfunction (288). Can the ALS-PFN1 variants act in a similar manner? Virtually, there is no information regarding ALS-linked PFN1 and PtdIns(4,5)P_2 metabolism. Do the ALS-PFN1 variants contain aberrant post-translational modifications? Does manipulating Rho/Rac/Cdc42 signaling reverse some of the phenotypes observed in cells and mouse models (117,118)? Moreover, there is the other side of actin dynamics, actin disassembly, turnover and treadmilling that involves coordination between severing factors such as cofilin and PFN1 (49). Once mechanistic details on the actin abnormalities due to mutant PFN1 are available, the attention should be placed on higher order cellular actin structures. In particular, the emphasis should be on filaments generated by neuronal formins (such as delphilin), in addition to the other two key actin assembly machineries Arp2/3 and Eva/VASP which were not investigated in this thesis. Some of the neuronal actin structures that deserve close examination are, (i) the axon initial segment, (ii) the F-actin rings along axons, (iii) the formin-

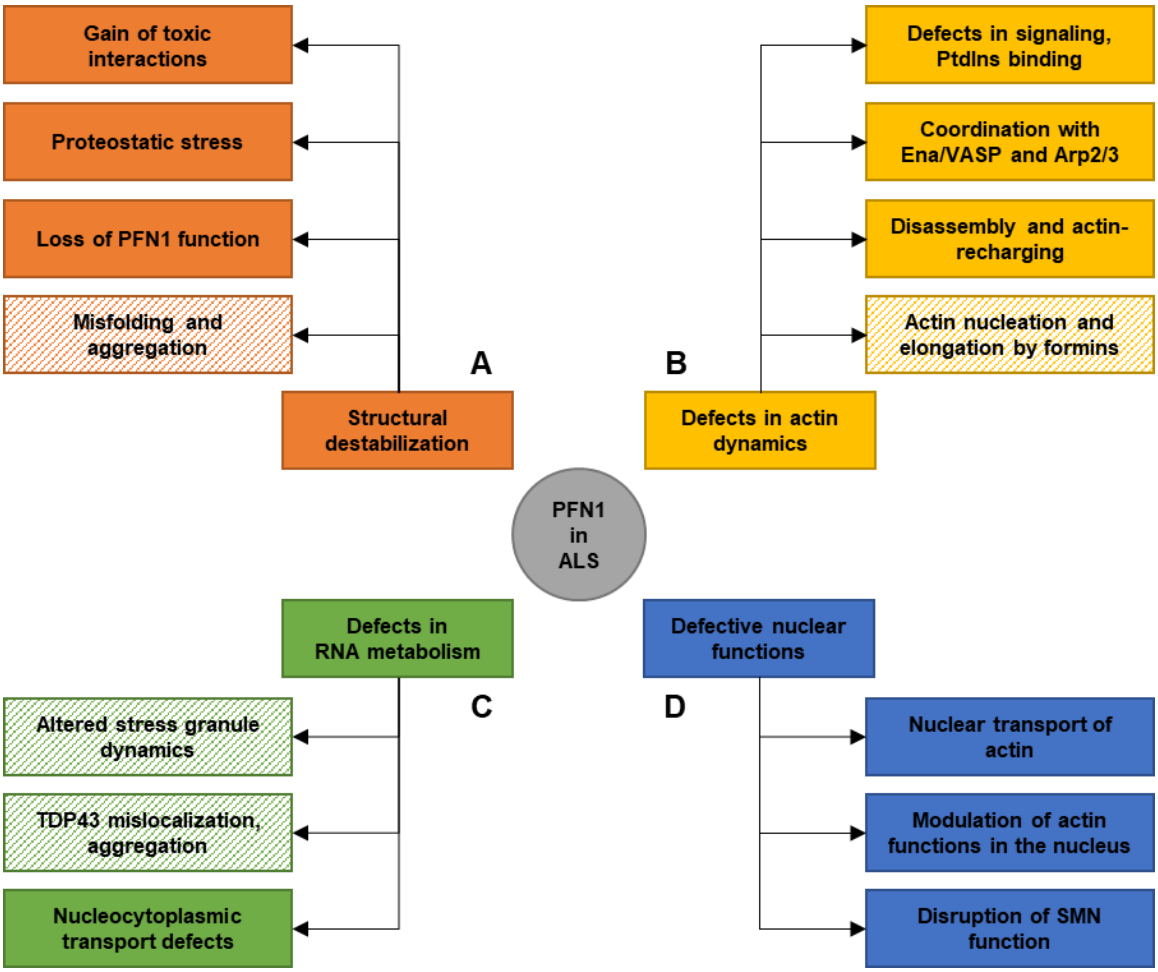

generated dynamic F-actin trails in axons, (iv) the synaptic vesicle cycle, (v) the dendritic spine plasticity and (vi) the actin-microtubule-neurofilament cross-talk and co-ordination. Non-cell autonomous effects partly drive ALS pathogenesis. Hence, the role of PFN1 in glial cells such as myelination (103) also merits attention. Super-resolution microscopy, such as STORM, can prove valuable for studying both neuronal and non-neuronal cellular cytoskeletal structures.

A noteworthy point is that the ubiquitously expressed PFN1 is mutated in ALS whereas the neuronal isoform PFN2 is not. Both isoforms are structurally and functionally similar albeit differences in affinities towards actin (43) as well as

Figure IV-1. A proposed mechanistic model for PFN1 in ALS pathogenesis. (A) ALS-mutations destabilize PFN1 structure which can cause the protein to misfold and aggregate, depleting functional PFN1 and at the same time burdening the protein quality control mechanisms leading to proteostatic stress. Further, the aggregates could recruit key cellular proteins thereby acquiring toxic properties. (B) Data presented in this dissertation point to an anomaly in actin nucleation and elongation caused by PFN1 mutants. Examples of other actin-related processes where mutant PFN1 could interfere are actin disassembly and recycling, actin assembly by Ena/VASP and Arp2/3, aberrant Rho/Rac/Cdc42 cytoskeletal signaling that could be mediated through PFN1-PtdIns interactions or PFN1 post-translational modifications. (C) ALS-PFN1 can disturb RNA metabolism by altering stress granule dynamics and by causing TDP43 mislocalization and aggregation. The presence of PFN1 aggregates can also interfere with nucleocytoplasmic transport of RNA and proteins. (D) ALS-mutations in PFN1 can impact actin nuclear transport, alter nuclear functions of actin such as chromatin remodeling, transcription and DNA repair. It can also associate with nuclear PFN1 ligands such as SMN and disrupt its function. The proposed features for which evidence currently exists are depicted in striped boxes.

different poly(L-proline) containing protein interaction partners (15,92). It will be important to see how the combination of PFN1 and PFN2 can contribute to actin dynamics. It is not difficult to envision actin polymerization by a formin that can recruit both PFN1-actin and PFN2-actin complexes. I alluded to the possibility of co-aggregation of PFN1 and PFN2 earlier. In a similar manner, does mutant PFN1 mimic and acquire the properties or polarize the activity of PFN2 thereby interfering with PFN2? The HeLa cells used in Chapter III do not express PFN2, so neuronal cells should be used to test the above hypothesis.

A pathogenesis mechanism closely associated with DNA/RNA metabolism is possible. Disturbances in RNA metabolism and nucleocytoplasmic transport are emerging themes in neurodegeneration. Aggregation of TDP43 and mutant HTT

in the cytoplasm interferes with the nucleocytoplasmic transport of RNA and proteins (289). The repeat expanded c9orf72 RNA also disrupts nucleocytoplasmic transport by direct binding to RanGAP1 causing its mislocalization and disrupting RAN gradient (290). ALS-PFN1 alters stress granule dynamics (144) and causes mislocalization and aggregation of TDP43 (145,149). More studies are necessary to determine if TDP43 mislocalization is caused by aggregates or oligomers of PFN1 in the cytoplasm and whether these aggregates disrupt nucleocytoplasmic transport of RNA and proteins in general. Moreover, actin has under-appreciated roles in the nucleus. Actin is involved in transcription, chromatin remodeling and DNA repair in the nucleus (81-84). It is not uncommon for poly(L-proline) containing proteins to exist in the nucleus. However, it is not known whether PFN1 binds these proteins with functional implications and effects nuclear actin functions. Genetic screens and proteomics approaches will enable us to identify hitherto unknown binding partners that can offer insights into DNA and RNA processing roles of PFN1 as well as connections to other biochemical pathways in general.

Finally, on a less relevant yet peculiar note, plant profilins are major allergens for humans (291,292). It is not known if human PFN1 can trigger inflammation. Intriguingly, extracellular F-actin can trigger inflammatory response and autoimmunity (293). Hence, there is a remote possibility that the mutations on PFN1 somehow trigger autoimmune reaction towards the motor neurons. This theory is purely speculative at this juncture and has to be tested.

Concluding remarks

A mechanistic model is proposed comprising of (but not limited to) four features for PFN1-ALS pathogenesis, based on what is known from our studies and other research groups as well as the conjectures drawn in this dissertation (Figure IV-1). I discussed two possible ways through which PFN1 pathogenesis can be mediated. First, ALS-mutations destabilize PFN1 structurally. This could lead to misfolding and aggregation of PFN1 causing a functional loss. Further the misfolded PFN1 and the fibrillar aggregates can also recruit important cellular factors such as PFN2 gaining aberrant and toxic functions (Figure IV-1A). Second, evidence was presented for certain irregularities in actin nucleation and elongation which need to be thoroughly examined. In addition, PFN1 involvement in actin-cytoskeletal processes discussed earlier such as actin disassembly, nucleation by Arp2/3, elongation by Ena/VASP, Rho signaling, cross-talk with microtubules also need to be investigated (Figure IV-1B). At the time of writing this dissertation, the role of PFN1 in RNA metabolism with respect to ALS was shown by other groups. Notably PFN1 associates with stress granules and the ALS-mutations affect stress granule dynamics. In addition, the mutations induce classic TDP43 pathology (Figure IV-1C). We also speculate about a few other mechanisms including the roles of PFN1 in the nucleus that can be impacted by the mutations such as nuclear transport of actin and its role in chromatin remodeling, transcription and DNA repair (Figure IV-1D). Not all ALS-PFN1 variants are expected to follow the same pathogenesis pathways, and a combination of multiple mechanisms is also

possible. Future work *in vitro*, in neuronal models including IPSC-derived motor neurons and ALS mouse models will be instrumental in confirming existing observations and testing several new hypotheses proposed in this dissertation.

APPENDIX I – A NOVEL METHOD FOR PURIFICATION OF PFN1

Introduction

Existing methods for purification of profilins utilize the affinity of profilin to poly(L-proline). The procedure entails binding of profilin to poly(L-proline) Sepharose columns, washing with 3 M urea to remove non-specifically bound impurities, eluting the bound PFN1 by denaturation using 8 M urea or DMSO and finally refolding in a suitable buffer (294-296). WT PFN1, purified by this procedure, is functionally active in pyrene-actin polymerization assays or single molecule TIRF microscopy, suggesting that PFN1 refolds successfully (43,255). But the ALS-variants of PFN1 cannot be guaranteed to refold to fully functional forms. Here, we describe a novel method for purifying untagged human WT and ALS-PFN1 variants from the soluble lysates of *E. coli*. The soluble levels of ALS-PFN1 variants varied depending on the mutation in question, but were very low compared to WT or E117G PFN1. They were predominantly present in the inclusion bodies. In particular, the soluble levels of C71G were extremely low and had to be purified from the inclusion bodies. In addition to purifying C71G from soluble lysates, we also purified C71G from inclusion bodies and show that this variant refolds and functions in the same way as its soluble counterpart.

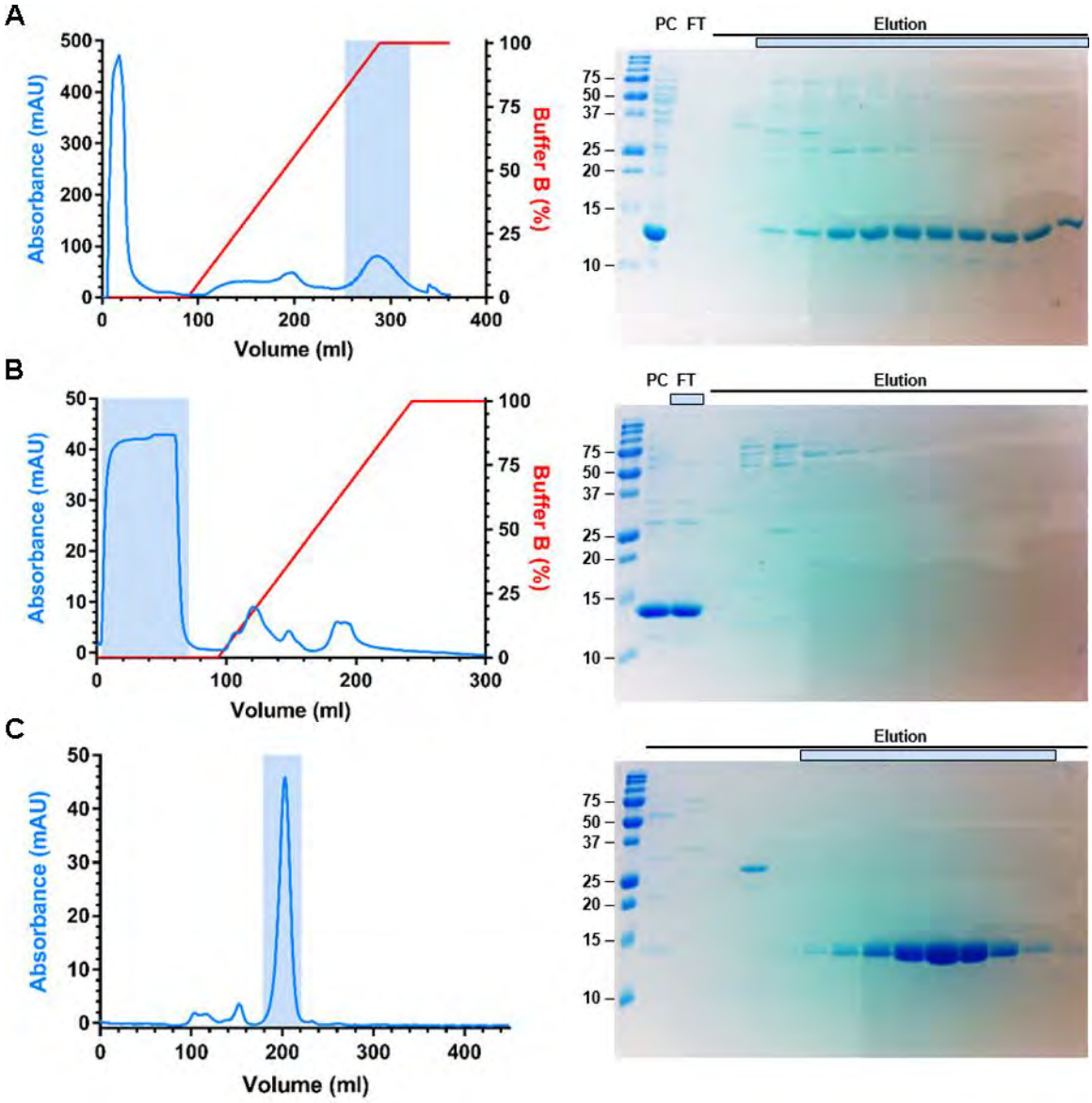

Figure AI-1. Human WT PFN1 purification. (A) Hydrophobic cation exchange chromatography. In this particular case, the lysate was salted out by addition of ammonium sulfate to a final concentration of 1 M and dialyzed in Buffer A. This is not entirely necessary and future PFN1 preparations did not involve this step. PFN1 elutes at 100% Buffer B. (B) Anion exchange chromatography of PFN1 elution fractions from (A) dialyzed in Buffer A. PFN1 does not bind the column and elutes in the flow-through. (C) Size exclusion chromatography of concentrated flow through fractions in (B). In all three panels, PFN1 elution volume is marked blue in the chromatograms and blue bars above the gel. PC –pre-column, FT – flow-through.

Results

Expression conditions

A series of experiments were conducted – (i) expression in three different *E. coli* strains BL21(DE3)pLysS, Rosetta™ 2(DE3), ArcticExpress, (ii) testing different isopropyl β-D-thiogalactopyranoside (IPTG) concentrations, (iii) testing induction temperature and duration – to identify optimum conditions that give the best expression for WT and ALS-PFN1. BL21(DE3)pLysS cells transformed with PFN1 constructs were cultured in Luria Broth (LB) containing 100 μg ml^{-1} ampicillin and 34 μg ml^{-1} chloramphenicol at 37 °C until an OD_{600} of 0.7, at which point PFN1 expression was induced by addition of 1 mM IPTG for either 3 h at 37 °C (for WT and E117G) or 24 h at 18 °C (for C71G, M114T and G118V). Cells were harvested by centrifugation and stored at –80 °C until purification.

Purification of PFN1 from soluble lysate

The purification procedure was developed for WT PFN1 and subsequently applied to the ALS-PFN1 variants. Since human WT PFN1 is basic with an isoelectric point of 8.44, we attempted cation-exchange (S-resin) chromatography. Surprisingly, the human WT PFN1 exhibited poor binding to the column. Next we used a chromatographic technique which employs a mixed-mode resin with both hydrophobic and cation-exchange properties. The harvested cells were lysed by sonication in 10 mM citrate and 10 mM NaCl, pH 5.0 (Buffer A) containing protease inhibitor. The lysate was cleared by centrifugation and applied to the hydrophobic cation exchange column pre-equilibrated with Buffer A. Bound impurities were

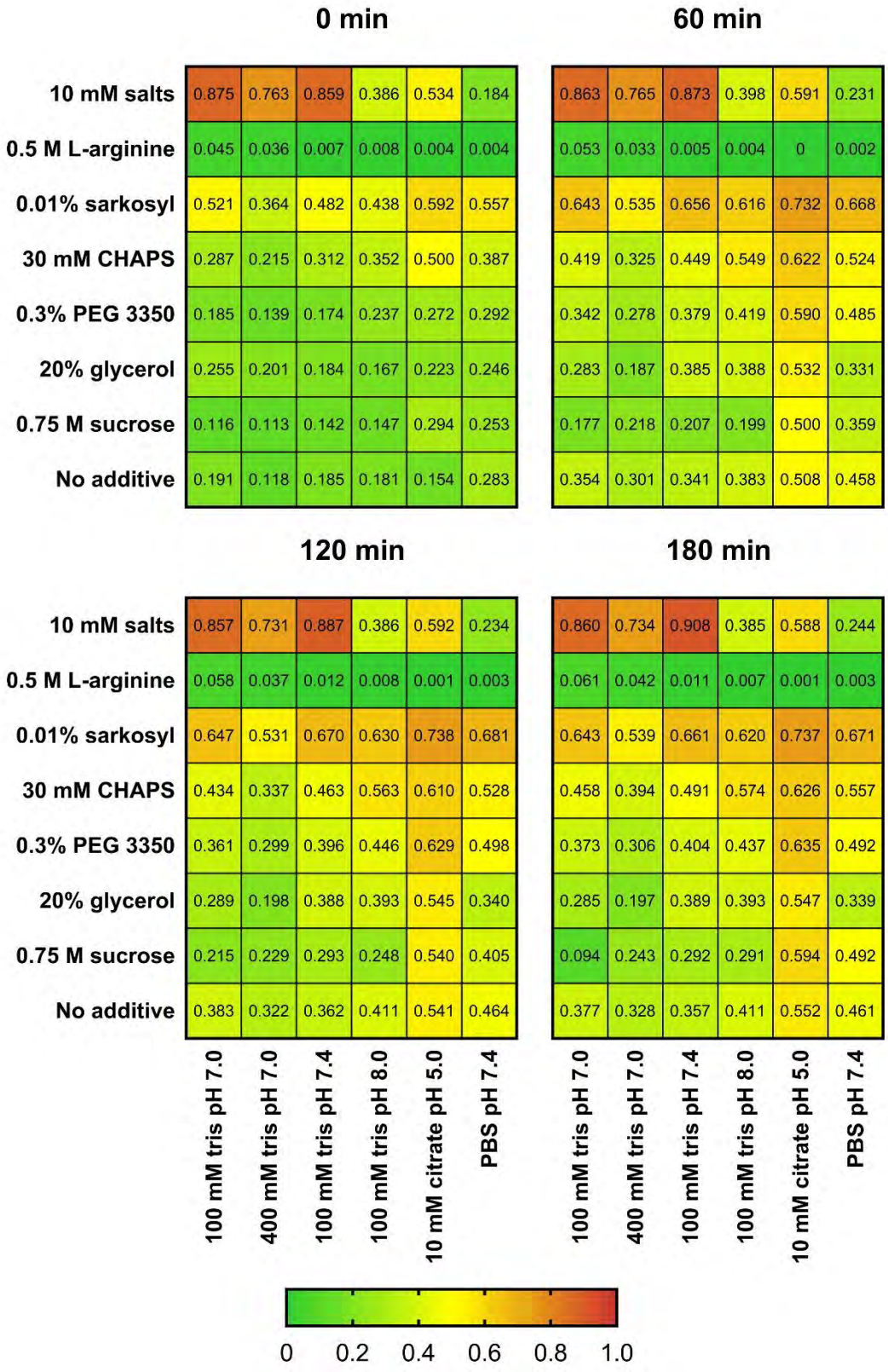
0 min
60 min
120 min
180 min
10 mM salts
0.5 M L-arginine
0.01% sarkosyl
30 mM CHAPS
0.3% PEG 3350
20% glycerol
0.75 M sucrose
No additive
0.875 0.763 0.859 0.386 0.534 0.184
0.045 0.036 0.007 0.008 0.004 0.004
0.521 0.364 0.482 0.438 0.592 0.557
0.287 0.215 0.312 0.352 0.500 0.387
0.185 0.139 0.174 0.237 0.272 0.292
0.255 0.201 0.184 0.167 0.223 0.246
0.116 0.113 0.142 0.147 0.294 0.253
0.191 0.118 0.185 0.181 0.154 0.283
0.863 0.765 0.873 0.398 0.591 0.231
0.053 0.033 0.005 0.004 0 0.002
0.643 0.535 0.656 0.616 0.732 0.668
0.419 0.325 0.449 0.549 0.622 0.524
0.342 0.278 0.379 0.419 0.590 0.485
0.283 0.187 0.385 0.388 0.532 0.331
0.177 0.218 0.207 0.199 0.500 0.359
0.354 0.301 0.341 0.383 0.508 0.458
0.857 0.731 0.887 0.386 0.592 0.234
0.058 0.037 0.012 0.008 0.001 0.003
0.647 0.531 0.670 0.630 0.738 0.681
0.434 0.337 0.463 0.563 0.610 0.528
0.361 0.299 0.396 0.446 0.629 0.498
0.289 0.198 0.388 0.393 0.545 0.340
0.215 0.229 0.293 0.248 0.540 0.405
0.383 0.322 0.362 0.411 0.541 0.464
0.860 0.734 0.908 0.385 0.588 0.244
0.061 0.042 0.011 0.007 0.001 0.003
0.643 0.539 0.661 0.620 0.737 0.671
0.458 0.394 0.491 0.574 0.626 0.557
0.373 0.306 0.404 0.437 0.635 0.492
0.285 0.197 0.389 0.393 0.547 0.339
0.094 0.243 0.292 0.291 0.594 0.492
0.377 0.328 0.357 0.411 0.552 0.461
100 mM tris pH 7.0
400 mM tris pH 7.0
100 mM tris pH 7.4
100 mM tris pH 8.0
10 mM citrate pH 5.0
PBS pH 7.4
0 0.2 0.4 0.6 0.8 1.0

Figure AI-2. Screening additives for C71G PFN1 refolding. The C71G PFN1-containing inclusion bodies was extracted in Buffer D and refolded in a variety of buffer-additive combinations. The salts used as additives (top row in each heat map) consisted of 10 mM each of zinc chloride, calcium chloride and magnesium chloride. The solubility was monitored by measuring OD_{355} over a period of 3 h. Buffers that contained 0.5 M L-arginine invariably maintained the solubility of C71G on dilution of guanidinium hydrochloride, indicated by relatively small values of OD_{355}. The colorbar represents OD_{355}.

eluted with 200 ml linear gradient of 10 mM citrate and 1 M NaCl, pH 5.0 (Buffer B). PFN1 eluted at 100% Buffer B (Figure AI-1A). For large preparations, PFN1 elutes on complete saturation of the column with Buffer B. The PFN1-containing fractions were pooled and dialyzed into Buffer A with 6000-8000 MWCO dialysis tubing prior to being applied to an anion-exchange (Q-resin) column. On account of its high isoelectric point and the low pH of Buffer A, PFN1 is not expected to bind the Q-column. PFN1 eluted in the flow-through (Figure AI-1B) and was concentrated to 1–2 ml using stirred ultrafiltration cells (equipped with 5000 MWCO discs) and then applied to a Sephacryl S-100 HR size exclusion column pre-equilibrated with phosphate buffered saline (PBS). PFN1 proteins eluted at approximately 200 ml and were >95% pure as assessed by SDS PAGE analysis with Coomassie Brilliant Blue stain (Figure AI-1C). The concentration of PFN1 was determined spectrophotometrically at a wavelength of 280 nm using a molar extinction coefficient of 18450 M^{-1} cm^{-1}. Aliquots of PFN1 proteins were stored at –80 °C, typically at concentrations between 60-600 μM.

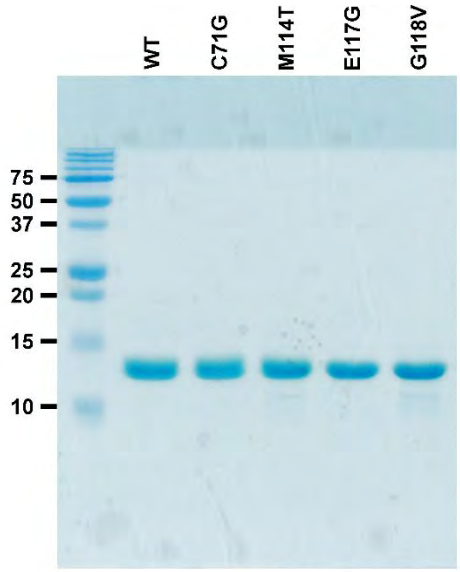

Figure AI-3. PFN1 proteins purified from *E. coli* are > 95% pure. Indicated PFN1 proteins (10 µg) purified using the novel method were subjected to SDS PAGE on a 15% polyacrylamide gel to assess purity. All the PFN1 proteins show greater than 95% purity.

Purification of C71G PFN1 from inclusion bodies

The C71G-containing inclusion bodies were extracted as previously described (297). The cells were lysed by sonication in 100 mM Tris-HCl pH 7.0, 5 mM ethylenediaminetetraacetic acid (EDTA), 5 mM dithiothreitol (DTT) (Buffer C) containing 200 µg ml^{-1} lysozyme and protease inhibitor followed by centrifugation. The resulting pellet was washed (4-8 ml per gram of dry weight of cells) three times with Buffer C containing 2 M urea and 2% Triton X-100 and once with Buffer C. The resulting inclusion body pellet was stored at –80 °C until needed.

At this juncture, a chemical screen was performed to identify the best conditions that promoted C71G refolding. C71G present in the inclusion bodies did not refold as previously described (295) in either Buffer A or PBS. On the other

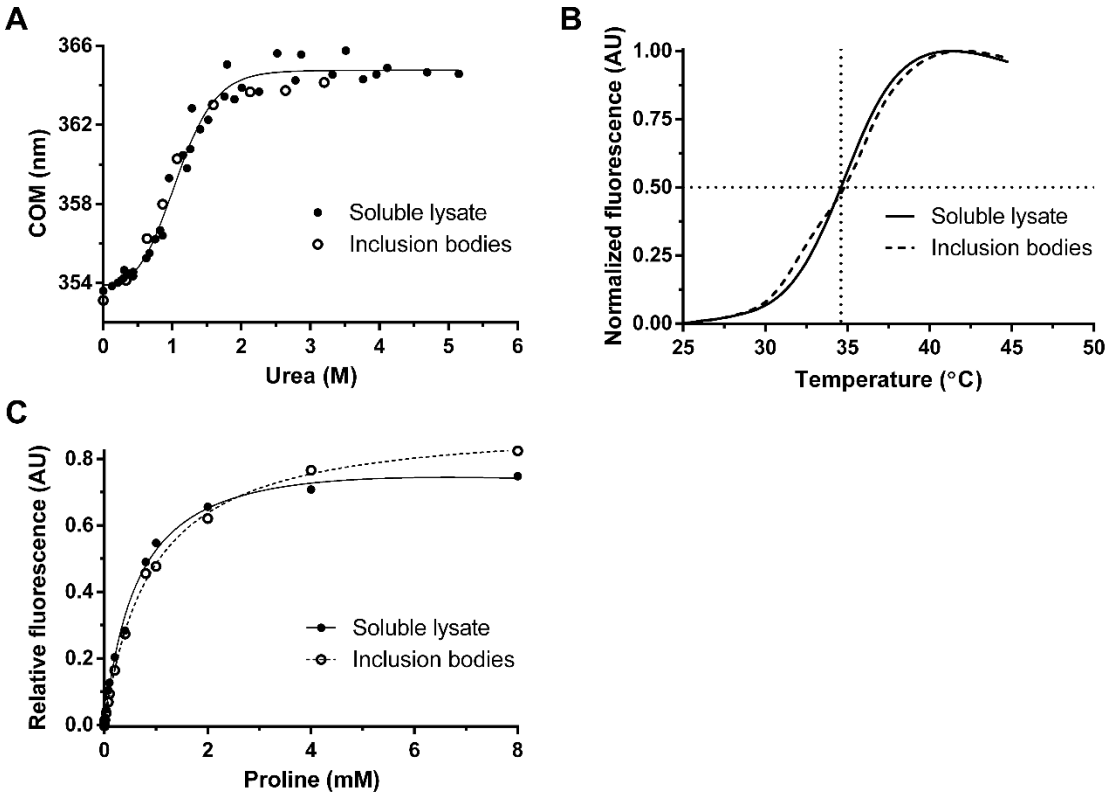

Figure AI-4. A comparison of PFN1 C71G purified from the soluble lysate of *E. coli* vs. from inclusion bodies. (A) Equilibrium unfolding and (B) thermal denaturation curves (described in Figure II-1) for PFN1 C71G purified from the soluble lysate and inclusion bodies. The apparent melting temperature of PFN1 C71G purified from inclusion bodies (34.62 ± 0.05 °C) is the same as that purified from soluble lysate (34.60 ± 0.03 °C). (C) PFN1 C71G has similar affinities to poly(L-proline) as determined by the binding assay described in Figure II-13 irrespective of whether this variant was purified from the soluble lysate or inclusion bodies.

hand, pure C71G refolded in equilibrium refolding experiments (Figure II-2B). This suggests that certain impurities present in the inclusion bodies precluded C71G from refolding. Inclusion bodies were solubilized (0.5-1 ml per gram dry weight of cells) in 50 mM Tris-HCl pH 7.0 containing 5 mM EDTA, 5 mM DTT and 3 M guanidinium hydrochloride (Buffer D) at ambient temperature. The solubilized

Table AI-1. Approximate yields of PFN1 proteins from *E. coli*.

	Soluble lysate (mg l^{-1})	Inclusion bodies (mg l^{-1})
WT	7.0	-
Y7F	5.2	-
C71G	0.16	4.3
M114T	0.3	1.6
E117G	8.0	-
G118V	0.5	-
H120E	1.1	-

inclusion bodies were diluted in Buffer D to a PFN1 C71G concentration of approximately 5 mg ml^{-1}. A 96-well plate was loaded with an array of buffer-additive combinations (190 µl per well) and the inclusion body extract (10 µl) was added to each well, thereby diluting the guanidinium hydrochloride. The scattering at 355 nm (protein molecules are less likely to absorb at 355 nm) was measured periodically. Buffers that contained 0.5 M L-arginine were able to maintain the solubility of C71G over an extended period of time (Figure AI-2). In subsequent large-scale purifications, C71G was refolded by drop-wise addition of the inclusion body extract to rapidly stirring Buffer A containing 0.5 M L-arginine at ambient temperature under conditions where the final concentrations of guanidinium hydrochloride and C71G were below 0.1 M and 0.2 mg ml^{-1}, respectively. The refolded protein was dialyzed in Buffer A at 4 °C and purified using a Sephacryl S-100 HR column as described for PFN1 WT.

Characterization of purified PFN1 proteins

All the purified PFN1 proteins were greater than 95% pure by SDS polyacrylamide gel electrophoresis (Figure AI-3). Further, the identity and purity of the PFN1 proteins were verified by intact mass analysis. The C71G variant purified from inclusions bodies exhibited similar thermodynamic stability, melting temperature, poly(L-proline) binding as its soluble counterpart (Figure AI-4).

Discussion

To summarize, we developed new methods for purifying WT and ALS-PFN1. WT PFN1 purified by the above method had thermodynamic stability comparable to published values (see Table II-1) (29,298), functionally active in pyrene-actin polymerization assays and in single molecule experiments (Figure II-14, Figure III-3). Moreover, C71G purified from soluble lysates and inclusion bodies are structurally and functionally similar (Figure AI-4). While the assessed expression levels of E117G in *E. coli* were close to WT, the mutants had low expression with C71G being the lowest. In fact, their soluble expression levels and yields (Table AI-1) correlate with their thermodynamic stabilities (Figure II-1 and Table II-1) as well as published data on aggregation propensities (7).

Materials and Methods

Materials

The following materials were used for PFN1 protein expression and purification – Rosetta™ 2(DE3) (EMD Millipore, 71400-4), ArcticExpress (DE3) (Agilent Technologies, 230192), BL21(DE3)pLysS (Agilent Technologies, 200132) competent cells, isopropyl β-D-thiogalactopyranoside (IPTG; Amresco, 0487), protease inhibitor (Roche, 11873580001), HiTrap™ SP FF cation-exchange column (GE Healthcare Life Sciences, 17-5157-01), Nuvia cPrime hydrophobic cation exchange column (packed approximately 35 ml of the resin in the column) (BioRAD, 156-3402), anion (Q-resin) exchange column (GE Healthcare, 17-0510-01), Sephacryl S-100 HR (GE Healthcare Life Sciences, 17-1194-01), ÄKTAPurifier FPLC system (GE Healthcare Life Sciences), 6000-8000 MWCO dialysis tubing (Membrane Filtration Products, Inc., 8015-40), stirred ultrafiltration cells (Millipore, 5123 and 5121), 96-well microplates (VWR, 82050-760).

Absorbance measurements

Absorbance at 355 nm was measured using a PerkinElmer 2030 Multilabel Reader.

Mass spectrometry

Mass spectrometry was performed at the UMMS Proteomics and Mass Spectrometry Facility.

Equilibrium unfolding experiment

The equilibrium unfolding experiment was performed as described in Chapter II Materials and Methods section.

Poly(L-proline) binding experiment

The poly(L-proline) binding experiment was performed as described in Chapter II Materials and Methods section.

APPENDIX II – PYTHON CLASS FOR READING THE TCSPC .SDT FILES

Python code

This file uses the numpy module. The class is named “ReadSDT”.

```
# Class to read Becker and Hickl GmbH TCSPC .sdt files
# Note the code is not exception handled
# Feel free to use, simplify or modify code, but remember my name
import struct
import numpy

__file__ = 'readsdt.py'
__author__ = 'siva.kuttiya'

# 32 bit architecture
# byte size
CHAR32 = 1
SHORT32 = 2
INT32 = 2
LONG32 = 4
FLOAT32 = 4
DOUBLE32 = 8
UNSIGNED_SHORT32 = 2
UNSIGNED_LONG32 = 4

TIME_AXIS = 0

# byte order
# @ - native
# = - native
# < - little-endian
# > - big-endian


class ReadSDT:
    # Class initialization
    def __init__(self):
        self.source = ""
        self.destination = ""

        # Initialize "File Header" parameters
        self.revision = 0  # SHORT32, "h"
        self.info_offset = 0  # LONG32, "l"
        self.info_length = 0  # SHORT32, "h"
        self.setup_offs = 0  # LONG32, "l"
        self.setup_length = 0  # SHORT32, "h"
        self.data_block_offset = 0  # LONG32, "l"
        self.no_of_data_blocks = 0  # SHORT32, "h"
        self.data_block_length = 0  # LONG32, "l"
        self.meas_desc_block_offset = 0  # LONG32, "l"
        self.no_of_meas_desc_blocks = 0  # LONG32, "h"
        self.meas_desc_block_length = 0  # LONG32, "h"
        self.header_valid = 0  # UNSIGNED SHORT32, "H"
        self.reserved1 = 0  # UNSIGNED LONG32, "L"
```

```
self.reserved2 = 0  # UNSIGNED SHORT32, "H"
self.chksum = 0  # UNSIGNED SHORT32, "H"

# # Initialize "File Info" parameter
self.file_info = ""  # CHAR[], "s"
#
# # Initialize "Setup" parameter
self.setup = ""  # CHAR[], "s"

# Initialize "Measurement Description Blocks" parameters
self.time = ""  # CHAR32 * 9, "s"
self.date = ""  # CHAR32 * 11, "s"
self.mod_ser_no = ""  # CHAR32 * 16, "s"
self.meas_mode = 0  # SHORT32, "h"
self.cfd_ll = 0.0  # FLOAT32, "f"
self.cfd_lh = 0.0  # FLOAT32, "f"
self.cfd_zc = 0.0  # FLOAT32, "f"
self.cfd_hf = 0.0  # FLOAT32, "f"
self.syn_zc = 0.0  # FLOAT32, "f"
self.syn_fd = 0  # SHORT32, "h"
self.syn_hf = 0.0  # FLOAT32, "f"
self.tac_r = 0.0  # FLOAT32, "f"
self.tac_g = 0  # SHORT32, "h"
self.tac_of = 0.0  # FLOAT32, "f"
self.tac_ll = 0.0  # FLOAT32, "f"
self.tac_lh = 0.0  # FLOAT32, "f"
self.adc_re = 0  # SHORT32, "h"
self.eal_de = 0  # SHORT32, "h"
self.ncx = 0  # SHORT32, "h"
self.ncy = 0  # SHORT32, "h"
self.page = 0  # UNSIGNED SHORT32, "H"
self.col_t = 0.0  # FLOAT32, "f"
self.rep_t = 0.0  # FLOAT32, "f"
self.stopt = 0  # SHORT32, "h"
self.overfl = ""  # CHAR32, "s"
self.use_motor = 0  # SHORT32, "h"
self.steps = 0  # SHORT32, "h"
self.offset = 0.0  # FLOAT32, "f"
self.dither = 0  # SHORT32, "h"
self.incr = 0  # SHORT32, "h"
self.mem_bank = 0  # SHORT32, "h"
self.mod_type = ""  # CHAR32 * 16, "s"
self.syn_th = 0.0  # FLOAT32, "f"
self.dead_time_comp = 0  # SHORT32, "h"
self.polarity_l = 0  # SHORT32, "h"
self.polarity_f = 0  # SHORT32, "h"
self.polarity_p = 0  # SHORT32, "h"
self.linediv = 0  # SHORT32, "h"
self.accumulate = 0  # SHORT32, "h"
self.flbck_y = 0  # INT32, "h"
self.flbck_x = 0  # INT32, "h"
self.bord_u = 0  # INT32, "h"
self.bord_l = 0  # INT32, "h"
self.pix_time = 0.0  # FLOAT32, "f"
self.pix_clk = 0  # SHORT32, "h"
self.trigger = 0  # SHORT32, "h"
self.scan_x = 0  # INT32, "h"
self.scan_y = 0  # INT32, "h"
self.scan_rx = 0  # INT32, "h"
self.scan_ry = 0  # INT32, "h"
```

```
        self.fifo_typ = 0  # SHORT32, "h"
        self.epx_div = 0  # INT32, "h"
        self.mod_type_code = 0  # INT32, "h"

        # Initialize "Data Blocks" parameters
        self.block_no = [0]
        self.data_offs = [0]
        self.next_block_off = [0]
        self.block_type = [0]
        self.meas_desc_block_no = [0]
        self.lblock_no = [0]
        self.block_length = [0]

        # Initialize "Data Points"
        self.data_points = numpy.zeros(0)

    # A function to read the file
    def read_sdt_file(self, filename):
        """
        :param filename: The .sdt file
        :return: The data points are in the form of a numpy array
        """

        self.source = filename
        read_sdt = open(filename, "rb")

        # The return value of "struct.unpack" is always one element tuples
        # struct.unpack is not being used for "s". It doesn't work and haven't
figured out why

        # File Header
        self.revision = struct.unpack("h", read_sdt.read(SHORT32))[0]
        self.info_offset = struct.unpack("l", read_sdt.read(LONG32))[0]
        self.info_length = struct.unpack("h", read_sdt.read(SHORT32))[0]
        self.setup_offs = struct.unpack("l", read_sdt.read(LONG32))[0]
        self.setup_length = struct.unpack("h", read_sdt.read(SHORT32))[0]
        self.data_block_offset = struct.unpack("l", read_sdt.read(LONG32))[0]
        self.no_of_data_blocks = struct.unpack("h", read_sdt.read(SHORT32))[0]
        self.data_block_length = struct.unpack("l", read_sdt.read(LONG32))[0]
        self.meas_desc_block_offset = struct.unpack("l",
read_sdt.read(LONG32))[0]
        self.no_of_meas_desc_blocks = struct.unpack("h",
read_sdt.read(SHORT32))[0]
        self.meas_desc_block_length = struct.unpack("h",
read_sdt.read(SHORT32))[0]
        self.header_valid = struct.unpack("H",
read_sdt.read(UNSIGNED_SHORT32))[0]
        self.reserved1 = struct.unpack("L", read_sdt.read(UNSIGNED_LONG32))[0]
        self.reserved2 = struct.unpack("H", read_sdt.read(UNSIGNED_SHORT32))[0]
        self.chksum = struct.unpack("H", read_sdt.read(UNSIGNED_SHORT32))[0]

        # File Info
        read_sdt.seek(self.info_offset, 0)
        self.file_info = read_sdt.read(self.info_length).decode("ascii",
"ignore")

        # Setup
        read_sdt.seek(self.setup_offs, 0)
        self.setup = read_sdt.read(self.setup_length).decode("ascii", "ignore")
        # This section ends with the sub-section BIN_PARA_BEGIN: binary values
```

```
*END

        # Measurement Description Blocks
        read_sdt.seek(self.meas_desc_block_offset, 0)
        self.time = read_sdt.read(CHAR32 * 9).decode("ascii", "ignore")
        self.date = read_sdt.read(CHAR32 * 11).decode("ascii", "ignore")
        self.mod_ser_no = read_sdt.read(CHAR32 * 16).decode("ascii", "ignore")
        self.meas_mode = struct.unpack("h", read_sdt.read(SHORT32))[0]
        self.cfd_ll = struct.unpack("f", read_sdt.read(FLOAT32))[0]
        self.cfd_lh = struct.unpack("f", read_sdt.read(FLOAT32))[0]
        self.cfd_zc = struct.unpack("f", read_sdt.read(FLOAT32))[0]
        self.cfd_hf = struct.unpack("f", read_sdt.read(FLOAT32))[0]
        self.syn_zc = struct.unpack("f", read_sdt.read(FLOAT32))[0]
        self.syn_fd = struct.unpack("h", read_sdt.read(SHORT32))[0]
        self.syn_hf = struct.unpack("f", read_sdt.read(FLOAT32))[0]
        self.tac_r = struct.unpack("f", read_sdt.read(FLOAT32))[0]
        self.tac_g = struct.unpack("h", read_sdt.read(SHORT32))[0]
        self.tac_of = struct.unpack("f", read_sdt.read(FLOAT32))[0]
        self.tac_ll = struct.unpack("f", read_sdt.read(FLOAT32))[0]
        self.tac_lh = struct.unpack("f", read_sdt.read(FLOAT32))[0]
        self.adc_re = struct.unpack("h", read_sdt.read(SHORT32))[0]
        self.eal_de = struct.unpack("h", read_sdt.read(SHORT32))[0]
        self.ncx = struct.unpack("h", read_sdt.read(SHORT32))[0]
        self.ncy = struct.unpack("h", read_sdt.read(SHORT32))[0]
        self.page = struct.unpack("H", read_sdt.read(UNSIGNED_SHORT32))[0]
        self.col_t = struct.unpack("f", read_sdt.read(FLOAT32))[0]
        self.rep_t = struct.unpack("f", read_sdt.read(FLOAT32))[0]
        self.stopt = struct.unpack("h", read_sdt.read(SHORT32))[0]
        self.overfl = read_sdt.read(CHAR32).decode("ascii", "ignore")
        self.use_motor = struct.unpack("h", read_sdt.read(SHORT32))[0]
        self.steps = struct.unpack("h", read_sdt.read(SHORT32))[0]
        self.offset = struct.unpack("f", read_sdt.read(FLOAT32))[0]
        self.dither = struct.unpack("h", read_sdt.read(SHORT32))[0]
        self.incr = struct.unpack("h", read_sdt.read(SHORT32))[0]
        self.mem_bank = struct.unpack("h", read_sdt.read(SHORT32))[0]
        self.mod_type = read_sdt.read(CHAR32 * 16).decode("ascii", "ignore")
        self.syn_th = struct.unpack("f", read_sdt.read(FLOAT32))[0]
        self.dead_time_comp = struct.unpack("h", read_sdt.read(SHORT32))[0]
        self.polarity_l = struct.unpack("h", read_sdt.read(SHORT32))[0]
        self.polarity_f = struct.unpack("h", read_sdt.read(SHORT32))[0]
        self.polarity_p = struct.unpack("h", read_sdt.read(SHORT32))[0]
        self.linediv = struct.unpack("h", read_sdt.read(SHORT32))[0]
        self.accumulate = struct.unpack("h", read_sdt.read(SHORT32))[0]
        self.flbck_y = struct.unpack("h", read_sdt.read(INT32))[0]
        self.flbck_x = struct.unpack("h", read_sdt.read(INT32))[0]
        self.bord_u = struct.unpack("h", read_sdt.read(INT32))[0]
        self.bord_l = struct.unpack("h", read_sdt.read(INT32))[0]
        self.pix_time = struct.unpack("f", read_sdt.read(FLOAT32))[0]
        self.pix_clk = struct.unpack("h", read_sdt.read(SHORT32))[0]
        self.trigger = struct.unpack("h", read_sdt.read(SHORT32))[0]
        self.scan_x = struct.unpack("h", read_sdt.read(INT32))[0]
        self.scan_y = struct.unpack("h", read_sdt.read(INT32))[0]
        self.scan_rx = struct.unpack("h", read_sdt.read(INT32))[0]
        self.scan_ry = struct.unpack("h", read_sdt.read(INT32))[0]
        self.fifo_typ = struct.unpack("h", read_sdt.read(SHORT32))[0]
        self.epx_div = struct.unpack("h", read_sdt.read(INT32))[0]
        self.mod_type_code = struct.unpack("h", read_sdt.read(INT32))[0]

        # Data Blocks
        read_sdt.seek(self.data_block_offset, 0)
```

```
        # Initialize "Data Blocks" parameters
        self.block_no = [0] * self.no_of_data_blocks  # SHORT32, "h"
        self.data_offs = [0] * self.no_of_data_blocks  # LONG32, "l"
        self.next_block_off = [0] * self.no_of_data_blocks  # LONG32, "l"
        self.block_type = [0] * self.no_of_data_blocks  # UNSIGNED SHORT32, "H"
        self.meas_desc_block_no = [0] * self.no_of_data_blocks  # SHORT32, "h"
        self.lblock_no = [0] * self.no_of_data_blocks  # UNSIGNED LONG32, "L"
        self.block_length = [0] * self.no_of_data_blocks  # UNSIGNED LONG32,
"L"

        # Initialize "Data Points" parameters
        self.data_points = numpy.zeros((self.adc_re, self.no_of_data_blocks +
1))

        for point in range(0, self.adc_re):
            self.data_points[point, TIME_AXIS] = point * (self.tac_r /
float(self.tac_g * self.adc_re)) * 10 ** 9

        for blk_no in range(0, self.no_of_data_blocks):
            # not sure if this should be "no_of_data_blocks" or
"no_of_meas_desc_blocks"
            # To generalize there should be multiple for loops
            self.block_no[blk_no] = struct.unpack("h",
read_sdt.read(SHORT32))[0]
            self.data_offs[blk_no] = struct.unpack("l",
read_sdt.read(LONG32))[0]
            self.next_block_off[blk_no] = struct.unpack("l",
read_sdt.read(LONG32))[0]
            self.block_type[blk_no] = struct.unpack("H",
read_sdt.read(UNSIGNED_SHORT32))[0]
            self.meas_desc_block_no[blk_no] = struct.unpack("h",
read_sdt.read(SHORT32))[0]
            self.lblock_no[blk_no] = struct.unpack("L",
read_sdt.read(UNSIGNED_LONG32))[0]
            # need to break the above further
            # data block/data set number - bits 0 to 23
            # module number (0 to 3) - bits 24 to 25
            self.block_length[blk_no] = struct.unpack("L",
read_sdt.read(UNSIGNED_LONG32))[0]

            # Data Points
            read_sdt.seek(self.data_offs[blk_no], 0)
            for point in range(0, self.adc_re):
                self.data_points[point, blk_no + 1] = struct.unpack("h",
read_sdt.read(SHORT32))[0]

            read_sdt.seek(self.next_block_off[blk_no], 0)

        # Close the file
        read_sdt.close()
```

Usage

```
Python 3.5.2 |Anaconda 4.2.0 (64-bit)| (default, Jul  5 2016, 11:41:13) [MSC
v.1900 64 bit (AMD64)] on win32
In[1]: import readsdt
```

```
In[2]: sdt_object = readsdt.ReadSDT()
In[3]:
sdt_object.read_sdt_file("C:\\Users\\siva.kuttiya\\Desktop\\s37c_c006.sdt")
In[4]: sdt_object.data_points
Out[4]:
array([[  0.00000000e+00,   0.00000000e+00,   0.00000000e+00],
       [  1.46372116e-02,   0.00000000e+00,   0.00000000e+00],
       [  2.92744232e-02,   0.00000000e+00,   0.00000000e+00],
       ...,
       [  5.99101070e+01,   0.00000000e+00,   0.00000000e+00],
       [  5.99247442e+01,   0.00000000e+00,   0.00000000e+00],
       [  5.99393814e+01,   0.00000000e+00,   0.00000000e+00]])
In[5]: sdt_object.data_points[1000]
Out[5]:
array([   14.63721158,  1982.        ,  2179.        ])
```

APPENDIX III – MEASURING AFFINITIES OF PFN1 TO ACTIN AND FORMIN

Introduction

Conventional methods for measuring binding affinities, such as isothermal titration calorimetry, surface plasmon resonance and analytical size exclusion chromatography, require large volumes and high concentrations of substrate and ligand. Actin, purified from rabbit muscles, is difficult to obtain or maintain at high concentrations as it can spontaneously polymerize once the critical concentration of 0.1 μM is exceeded (299). Conditions that inhibit actin polymerization, such as storage at low concentration in G-buffer supplemented with calcium, does not completely prevent polymerization and the purified actin has to be ultracentrifuged to remove polymers before experiments. Further, it has a short shelf-life. On the other hand, the ALS-PFN1 variants, due to their unstable nature, are aggregation prone at high concentrations. Hence, we attempted to use fluorescence anisotropy to measure the affinities of PFN1 to actin and formin. Fluorescence anisotropy is a sensitive technique that requires very low amounts of substrate and ligand (20,300). The approach being adopted is similar to the competition-based binding experiments described previously (20,301-303). The first step involves binding and semi-saturating Alexa Fluor 488 or tetramethylrhodamine-6-maleimide labelled profilin with actin. Profilin, being the smaller molecule of the two, exhibits a much smaller fluorescence anisotropy. Profilin, when bound to actin (43 kDa), results in an increase in anisotropy. Then, the labeled profilin bound to actin can be

competed with unlabeled profilin, such as human WT or ALS-PFN1. This indirect competition-based binding experiment will also help avoid labeling the human PFN1 variants.

Results

Experiments using Cy3-, A488-, TMR-labeled Sc-S36C

Initially, experiments were performed using Cy3-labeled *Saccharomyces cerevisiae* profilin, Cy3-Sc-S36C. Actin-binding experiments using this protein did not give a sufficient change in fluorescence anisotropy (Figure AIII-1). Cy3-Sc-S36C also had a high baseline anisotropy to begin with. This could be because the fluorescence lifetime of Cy3 is very small (0.3 ns) (http://www.iss.com/resources/reference/data_tables/LifetimeDataFluorophores.html). The fluorescence lifetime of a fluorophore is related to the steady state anisotropy by the relation (300),

$$r = \frac{r_0}{1 + \frac{\tau}{\theta}}$$

In this relation, r is the steady state anisotropy, r_o is the limiting anisotropy, τ is the lifetime (property of the fluorophore), and θ is the correlation time (property of the macromolecule). Assuming the fluorescence lifetime of Cy3 is not affected on conjugation to S37C, its small fluorescence lifetime of 0.3 ns could contribute to the high anisotropy according to the above equation. Since the maximum value of the anisotropy is about 0.4 for most fluorophores due to excitation photo-selection

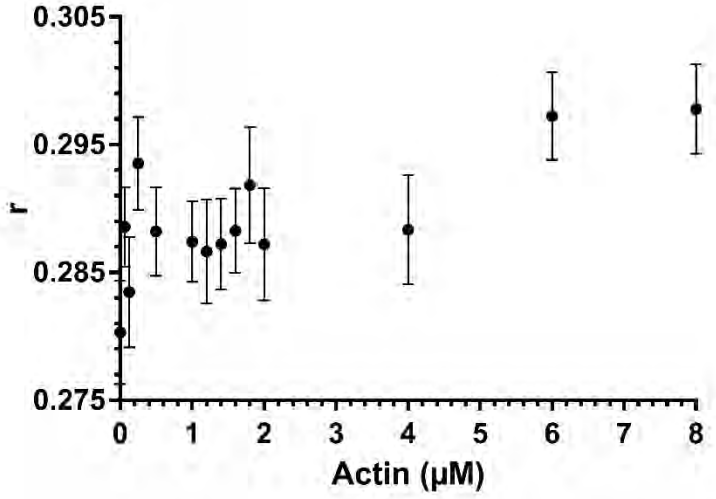

Figure AIII-1. Binding of Cy3-Sc-S36C to actin measured by fluorescence anisotropy. 200 nM Cy3-Sc-S36C was incubated with varying concentrations of actin, excited with vertically polarized light at 530 nm (SW 5 nm) and the polarized emissions, I_{VV} and I_{VH}, from 580 nm to 610 nm (SW 5 nm, integration time 1 s) were measured with 1 nm increments at 25 °C. Emission intensities from three scans were summed, the average of fluorescence anisotropy (r) values from 580 nm to 610 nm was calculated and plotted as shown. The buffer used to prepare the samples was 5 mM Tris-HCl, 0.2 mM $CaCl_2$, 0.2 mM ATP, 0.5 mM DTT, pH 8.0. Error bars represent SD. SW – slit width.

and other factors (300), the observable change for Cy3-Sc-S36C will not exceed 0.12 (i.e. approximately from 0.28 to 0.4). Even this change is possible only when the motions of the Cy-Sc-S36C is completely restricted. Hence, two other fluorophores were chosen for labeling Sc-S36C, (i) Alexa Fluor 488 (A488), lifetime 4.1 ns and, (ii) tetramethyl rhodamine-6-maleimide (TMR), lifetime 3.1 ns.

The steady state anisotropy of 50 nM A488 in 20 mM Tris-HCl, 150 mM KCl, pH 7.4 (room temperature) and the limiting anisotropy in 100% glycerol (–20 °C) was 0.0257 ± 0.0029 and 0.375 ± 0.0064 respectively. The latter agrees with the

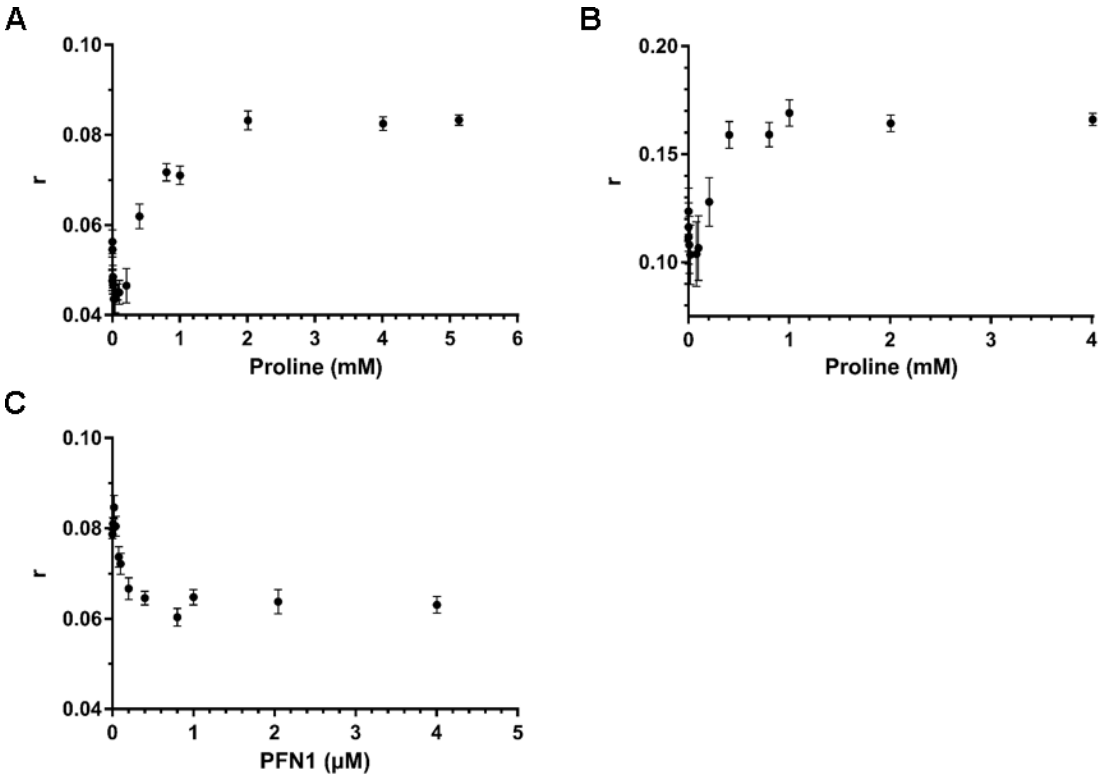

Figure AIII-2. Binding of A488-Sc-S36C and TMR-Sc-S36C to poly(L-proline) measured by fluorescence anisotropy. (A) 200 nM A488-Sc-S36C was titrated with samples of 200 nM A488-Sc-S36C containing poly(L-proline)*, excited with vertically polarized light at 488 nm (SW 5 nm) and the polarized emissions, I_{VV} and I_{VH}, from 510 nm to 550 nm (SW 5 nm, integration time 1 s) were measured with 1 nm increments at 25 °C. Emission intensities from three scans were summed, the average fluorescence anisotropy (r) at each wavelength was calculated and plotted as shown. (B) 400 nM TMR-Sc-S36C was titrated with samples of 400 nM TMR-Sc-S36C containing poly(L-proline)*, excited with vertically polarized light at 553 nm (SW 5 nm) and the polarized emissions, I_{VV} and I_{VH}, were measured at 580 nm (SW 10 nm, integration time 0.1 s) every 0.2 s for 60 s. The plot shows the average fluorescence anisotropy (r). (C) 200 nM A488-Sc-S36C and 0.5 mM proline* was titrated with samples of 200 nM A488-Sc-S36C and 0.5 mM proline* containing unlabeled WT PFN1. Intensity measurements and fluorescence anisotropy (r) calculations were performed as in (A). In all experiments PBS was used to prepare the samples. Error bars represent SD. SW – slit width. *Concentrations were measured in terms of proline residues.

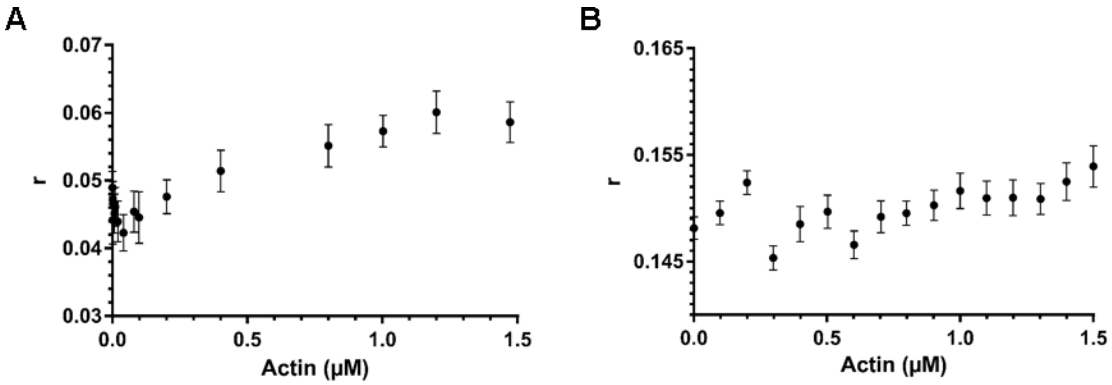

Figure AIII-3. Binding of A488-Sc-S36C and TMR-Sc-S36C to actin. (A) 200 nM A488-Sc-S36C was titrated with samples of 200 nM A488-Sc-S36C containing actin. Intensity measurements and fluorescence anisotropy (r) calculations were performed as described in Figure AIII-2A. The buffer used was 3 mM Tris-HCl, 0.1 mM $MgCl_2$, 0.2 mM ATP, 0.5 mM DTT, 0.01% NaN_3, pH 8.0. (B) 400 nM TMR-Sc-S36C was titrated with samples of 400 nM TMR-Sc-S36C containing actin. Polarized emissions at 580 nm were measured as in Figure AIII-2B, but every 1.5 s for 60 s with an integration time of 1 s. Fluorescence anisotropy (r) calculations were performed as in Figure AIII-2B. The buffer used was 2 mM Tris-HCl, 0.1 mM $MgCl_2$, 0.2 mM ATP, 1 mM DTT, pH 8.0. Error bars represent SD.

published value of 0.376 (304). By this way, we ensured the instrument was in working condition. Next, binding and competition experiments were performed using the poly(L-proline) peptide. The molecular weights of the peptide mixture is expected to be between 1,000 and 10,000 Da. This implies the peptide can possibly bind at least ten PFN1 molecules as about 6 prolines that form a rigid type-II helix are required to bind a single PFN1 molecule (24,25,27). This can lead to an increased anisotropy. Binding of A488-Sc-S36C or TMR-Sc-S36C to poly(L-proline) led to an increase in anisotropy (Figure AIII-2A and B). The very small but significant change in anisotropy upon saturation with poly(L-proline) suggests that the poly(L-proline) peptides loaded with profilin adopts a globular as opposed to

an extended conformation. The Förster resonance energy transfer (FRET) effects between closely situated A488 molecules in such a conformation can depolarize the signal leading to an anisotropy below the value that would be expected for A488-Sc-S36C going from 13.6 kDa in the unbound state to about 150 kDa in the complexed state. In addition, the poly(L-proline) bound A488-Sc-S36C could be competed with human unlabeled WT PFN1 (Figure AIII-2C), although at very high concentrations of WT PFN1, there was again an increase in anisotropy which was reasoned to be due to co-aggregation of A488-Sc-S36C and WT PFN1.

The change in anisotropy of labelled profilin, upon saturation with actin, was poor (Figure AIII-3). Time resolved studies also yielded very small change in anisotropy that were irreproducible and unreliable (the forward and reverse titrations did not agree). In contrast, an appreciable change in anisotropy of TMR-Ac-S38C upon binding actin was reported previously (20). The small anisotropy change in our experiments possibly results from the label being located in the middle of the loop between β-strand 2 and α-helix 2 in Sc-S36C (Figure I-1) (305). If the loop is highly flexible, then it can induce local motions causing the emission from the A488 to be depolarized. Hence, the local motions will dominate over the overall molecular tumbling, of which the latter is needed to measure binding. On examination of the Ac-S38C used in Vinson et al. (20), the label, although present in the same loop, resides next to an alpha helix (305,306). This might stabilize and limit the movement of the fluorophore.

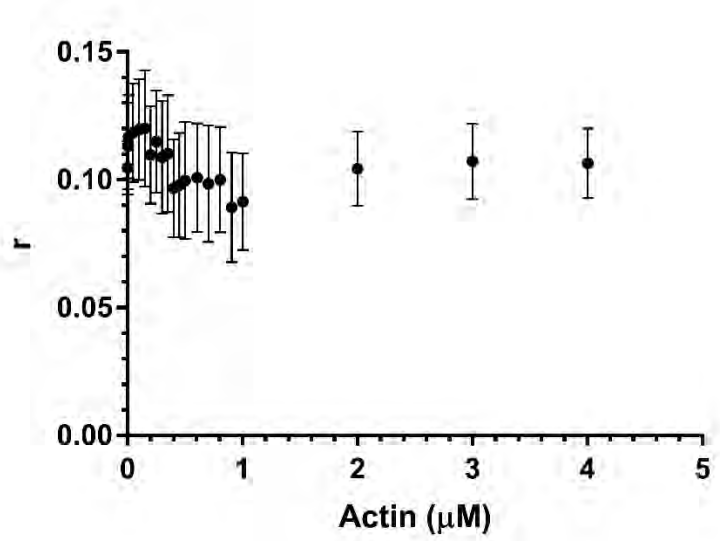

Figure AIII-4. Binding of TMR-Ac-S38C to actin. (A) 200 nM TMR-Ac-S38C was titrated with samples of 200 nM TMR-Ac-S38C containing actin. Intensity measurements and fluorescence anisotropy (r) calculations were performed as described in Figure AIII-3B. The buffer used was 2 mM Tris-HCl, 0.1 mM $MgCl_2$, 0.2 mM ATP, 1 mM DTT, pH 8.0. Error bars represent SD.

Experiments using TMR-labeled Ac-S38C

We synthesized, expressed, purified and labeled the Ac-S38C profilin II with TMR (TMR-Ac-S38C). The activity of TMR-Ac-S38C was verified in single molecule actin assembly experiments using mDia1. The elongation rates of the unlabeled (56.5 ±12.3 sub s^{-1} μm^{-1} actin) and TMR-Ac-S38C (52.3 ± 9.9 sub s^{-1} μm^{-1} actin) were comparable. Actin alone exhibited an elongation rate of 9.3 ± 1.1 sub s^{-1} μm^{-1} actin (Dr. Richa Jaiswal and Dr. Bruce Goode, Brandeis University). Actin-binding experiments performed using TMR-Ac-S38C still yielded little change in anisotropy (Figure AIII-4).

Discussion

The binding experiments were largely unsuccessful. There were a few suggestions from Dr. Thomas Pollard, Yale University. One, to use actin eluting at later volumes in size exclusion chromatography during its purification. There are usually trace amounts of certain actin-binding proteins that elute with actin in the peak fractions, which could potentially interfere with the PFN1-actin binding reactions. Two, in addition to using Mg^{2+}, the use of ethylene glycol-bis(2-aminoethylether)-N,N,N′,N′-tetraacetic acid (EGTA) in the buffer was recommended, to chelate the Ca^{2+} normally bound to the ATP. The same fluorescence anisotropy based competition experiments were also proposed to measure affinities of PFN1 to formins, but were not performed. The method of biolayer interferometry which also requires less substrate and ligand can be considered in the future as an alternative to fluorescence anisotropy for measuring affinities of PFN1 to actin or formins.

Materials and Methods

Plasmids

The plasmid encoding *Saccharomyces cerevisiae* S36C profilin (Sc-S36C) was kindly provided by Dr. Bruce Goode (Brandeis University). The *Acanthamoeba castellanii* S38C profilin II (Ac-S38C) in pET3a vector with NdeI and BamHI cloning sites was synthesized at GenScript.

Protein purification

A modified method based on Dr. Avital Rodal's (Brandeis University) protocol was used for purifying Sc-S36C. BL21(DE3)pLysS cells, expressing Sc-S36C after induction with 1 mM IPTG for 3 h at 37 °C, were harvested by centrifugation and lysed in 20 mM tris-HCl pH 8.0, 1 mM DTT (Buffer A) supplemented with protease inhibitor. The lysate was clarified by centrifugation and injected into an anionic Q-column pre-equilibrated with Buffer A. Elution was achieved using Buffer A containing 1 M NaCl. The fractions containing Sc-S36C were combined, concentrated and subjected to size exclusion chromatography using a Sephacryl S100 column pre-equilibrated with Buffer A containing 150 mM KCl. After combining fractions containing Sc-S36C, NaCl was added to a final concentration of 1 M. In the final step, the sample was subjected to hydrophobic interaction chromatography with Buffer A containing 1 M NaCl as the equilibration/binding buffer and Buffer A as the elution buffer. Pure Sc-S36C in 20 mM Tris-HCl pH 8.0, 150 mM KCl, 1 mM DTT was aliquoted and stored at –80 °C. The method used for purifying Ac-S38C was similar to that of human PFN1 (see Appendix I). Actin in G-buffer (3 mM tris-HCl, 0.5 mM DTT, 0.2 mM ATP, 0.1 mM $CaCl_2$, 0.01% NaN_3) was kindly provided by Dr. Bruce Goode (Brandeis University).

Fluorophore labeling and quantification

Prior to labeling, the Sc-S36C protein sample was dialyzed in 20 mM Tris-HCl, 150 mM KCl, pH 7.0. The protein, at 75 µM concentration, was incubated

overnight at 4 °C with a 10- or 8-fold molar excess of Alexa Fluor® 488 C_5 maleimide (A488, Thermo Fisher Scientific, A10254) or tetramethylrhodamine-6-maleimide (TMR, Thermo Fisher Scientific, T6028), respectively. The reactions were quenched with approximately 48 mM β-mercaptoethanol, dialyzed extensively in 20 mM Tris-HCl, 150 mM, pH 7.4 (A488-Sc-S36C) or 20 mM Tris-HCl pH 7.0, 20 mM KCl (TMR-Sc-S36C), aliquoted and stored at –80 °C. Labeling of Ac-S38C was carried out as above using 80 µM of purified protein and a 10 fold molar excess of TMR. The labeled sample was further purified using size exclusion chromatography using superdex-75. The Cy3-Sc-S36C was kindly provided by Dr. Bruce Goode (Brandeis University).

The A488-Sc-S36C was quantified using the "Proteins and Labels" feature in NanoDrop ND-1000 Spectrophotometer. The concentrations of TMR-Sc-S36C and TMR-Ac-S38C were calculated using the relation,

$$C = \frac{A_{280} - 0.27A_{553}}{\varepsilon l}$$

C is the concentration of the protein, A_{280} and A_{553} are the absorbance values at 280 nm and 553 nm respectively, ε is the molar extinction coefficient of Sc-S36C (19940 M^{-1} cm^{-1} at 280 nm) and l is the path length. Without the right molar extinction coefficient for TMR, it was not possible to calculate its concentration and hence, the labeling efficiency. The labeled proteins were subjected to native and denaturing gel electrophoresis to assess purity, presence of unlabeled protein and free dye. The masses of A488-Sc-S36C and TMR-Ac-S38C were verified by mass spectrometry and the labeling efficiency was estimated to be over 95%.

Native and denaturing gel electrophoresis

Native and denaturing gel electrophoresis were done as previously described (232). Briefly, samples were subjected to electrophoresis on 7.5% resolving and 5% stacking polyacrylamide (29:1 acrylamide-bisacrylamide, Fisher Scientific, BP1408-1) gels at ice-cold conditions and subsequently stained with Coomassie Brilliant Blue stain.

Fluorescence spectroscopy

Steady state fluorescence measurements were done using a T-format Horiba Fluorolog fluorimeter. Fluorophore-labeled samples were excited with vertically polarized light and the vertical (I_{VV}) and horizontal emissions (I_{VH}) were measured. The G-factor was measured by exciting the samples with horizontally polarized light. The fluorescence anisotropy was calculated using the formula,

$$r = (I_{VV} - GI_{VH})/(I_{VV} + 2GI_{VH})$$

The time resolved data were collected using a Becker and Hickl based custom TCSPC equipment (245,246).

APPENDIX IV – RESOURCES FOR THE ANALYSIS OF MICROSCOPY DATA

ImageJ macro for maximum projection of Z-stacks

```
/*
 * Macro to z-project the z-stack and save with the default name
 */

input = getDirectory("Input directory");
output = input

processFolder(input);

function processFolder(input) {
	list = getFileList(input);
	for (i = 0; i < list.length; i++) {
		if(File.isDirectory(input + list[i]))
			processFolder("" + input + list[i]);
		if(endsWith(list[i], "_z00_ch00.tif")) // Choose appropriate
suffix
			{
				processFile(input, output, list[i]);
				i = 10000; // An aribitrary high number, equivalent
to "break"
			}
	}
}

function processFile(input, output, file) {
	run("Image Sequence...", "open=[input] starting=2 increment=4 sort");
	run("Z Project...", "projection=[Max Intensity]");
	save_name = output + getTitle() + ".tif";
	run("Save", "save=save_name");
	close();
	close();
}
```

ImageJ macro for particle counting

```
/*
 * Macro for counting particles and save the overlaid masks and counts roi as
zip
 * This assumes there are only three channels and the second channel is the
EGFP channel
 * You need to change this if the above condition changes
 */

// Enter the right folder
output_directory = "C:\\Users\\siva.kuttiya\\Desktop\\mDia2_analysis\\";

// Get the image title name and id
original_image = getTitle();
original_image_id = getImageID();
```

```
// Duplicate the image, Gaussian blur the duplicated image
// Subtract the duplicated blurred image from the original image and create the
result in a new window
run("Duplicate...", "title=Duplicate.tif");
run("Gaussian Blur...", "sigma=5");
imageCalculator("Subtract create", original_image, "Duplicate.tif");

// Get the title and id of the subtracted image, rename
subtracted_image = getTitle();
subtracted_image_id = getImageID();
rename("Subtracted.tif");

// Threshold. Change the parameters as you see fit
run("8-bit");
setAutoThreshold("Default");
run("Threshold...");
setThreshold(10, 100);
setOption("BlackBackground", false);
run("Convert to Mask");

// Analyze particles. Change the parameters as you see fit
run("Set Scale...", "distance=1 known=0.0928 pixel=1 unit=um");
run("Analyze Particles...", "size=0.02-0.40 circularity=0.75-1.00 show=Outlines
display clear record add");

// Get the title of the active window which is the results of the particle
analysis
// Modify the image and overlay into the original image
analyzed_image = getTitle();
analyzed_image_id = getImageID();
run("Invert LUT");
run("Red");
run("Invert LUT");
run("RGB Color");
imageCalculator("Add create", original_image, analyzed_image);

added_image = getTitle();
added_image_id = getImageID();
rename("Overlaid.tif");

// Prepare filenames for the anlayzed and overlaid file and the ROI information
analyzed_file = output_directory + original_image + "(overlaid).tif";
roi_counts_file = output_directory + original_image + "(counts).zip";

// Save files
run("Save", "save=analyzed_file");
if(roiManager("count") > 0)
	{
		roiManager("Save", roi_counts_file);
		selectWindow("Results");
		run("Close");
	}

//Print the filename and counts in the log window
print(original_image + ":\t" + roiManager("count"));

// Close windows one by one
selectWindow("ROI Manager");
run("Close");
```

```
selectImage(added_image_id);
close();

selectImage("Drawing of Subtracted.tif");
close();

selectWindow("Threshold");
run("Close");

selectImage(subtracted_image_id);
close();

selectImage("Duplicate.tif");
close();

selectImage(original_image_id);
close();
```

MATLAB code for selecting linear filopodia trajectories

```
function tracks_info = analyzetrajectories(tracks_xml_file)
%analyzetrajectories Plots trajectories and displacement autocorrelation.
%   This function reads the tracks from the tracks_xml_file and plots the
%   filopodia trajectory and the displacement autocorrelation as well as
%   the linear segments within the trajectory. This is useful to see if
%   there are segments where the motion is in a near straight line. Feel
%   free to use, modify or simplify this code, but remember my name.
%
%   Argument:   tracks xml file generated by TrackMate plugin
%   Returns:    tracks_info consisting of rms_speed, effective_speed etc.

    % The below function was provided by Jean-Yves Tinevez as part of the
    % publication...
    % "Nadine Tarantino, Jean-Yves Tinevez, Elizabeth Faris Crowell,
    % Bertrand Boisson, Ricardo Henriques, Musa Mhlanga, Fabrice Agou,
    % Alain Israël, and Emmanuel Laplantine. TNF and IL-1 exhibit distinct
    % ubiquitin requirements for inducing NEMO-IKK supramolecular
    % structures. J Cell Biol (2014) vol. 204 (2) pp. 231-45".
    [tracks, md] = importTrackMateTracks(tracks_xml_file, true, true);
    no_of_tracks = numel(tracks);

    TIME = 1;
    X_COORD = 2;
    Y_COORD = 3;
    SEGMENT_CORR = 4;

    linear_segments = {};

    % Initialize the plots. You can comment the below section if you do not
    % want the plots
    %%%%%%%%%%%%%%%%%%%%%%%%%%%%%%%%%%%%%%%%%%%%%%%%%%%%%%%%%%%%%%%%%%%%%%%%%%%%
    %%%%%%%%%%%%%%%%%%%%%%%%%%%%%%%%%%%%%%%%%%%%%%%%%%%%%%%%%%%%%%%%%%%%%%%%%%%%
    ax1 = subplot(2, 2, 1);
    daspect([1 1 1])
    xlabel('x (\mum)');
    ylabel('y (\mum)');
```

```
ax2 = subplot(2, 2, 2);
xlim([0 180]);
ylim([-1 1]);
xlabel('t (s)');
ylabel('dcorr');

ax3 = subplot(2, 2, 3);
daspect([1 1 1])
xlabel('x (\mum)');
ylabel('y (\mum)');
title('Linear segments');

ax4 = subplot(2, 2, 4);
xlim([0 180]);
ylim([0.75 1]);
xlabel('t (s)');
ylabel('dcorr');
title('Autocorrelation of segments');
%%%%%%%%%%%%%%%%%%%%%%%%%%%%%%%%%%%%%%%%%%%%%%%%%%%%%%%%%%%%%%%%%%%%%%%%%%%%
%%%%%%%%%%%%%%%%%%%%%%%%%%%%%%%%%%%%%%%%%%%%%%%%%%%%%%%%%%%%%%%%%%%%%%%%%%%%

% Iterate through the tracks
for track_no = 1 : no_of_tracks

    current_track = tracks{track_no};
    corr_values = computeautocorrelation(current_track);
    segments = identifylinearsegments(current_track);
    segments = discardshortsegments(segments);
    linear_segments = [linear_segments, segments];

    % Plot filopodia trajectory and autocorrelation. You can comment
    % the below section if you do not want the plots
    %%%%%%%%%%%%%%%%%%%%%%%%%%%%%%%%%%%%%%%%%%%%%%%%%%%%%%%%%%%%%%%%%%%%%%%%%%%%
    %%%%%%%%%%%%%%%%%%%%%%%%%%%%%%%%%%%%%%%%%%%%%%%%%%%%%%%%%%%%%%%%%%%%%%%%%%%%
    % Top left plot will be the trajectory
    subplot(2, 2, 1)
    cla(ax1)
    title(strcat('Trajectory of track ', num2str(track_no)));
    hold on
    xlim([min(current_track(:, X_COORD)),...
        max(current_track(:, X_COORD))]);
    ylim([min(current_track(:, Y_COORD)),...
        max(current_track(:, Y_COORD))]);
    plot(current_track(:, X_COORD), current_track(:, Y_COORD), '-x')
    text(current_track(1, X_COORD), current_track(1, Y_COORD),...
        '\leftarrow t1')
    hold off

    % Top right plot will be the autocorrelation of the track
    subplot(2, 2, 2)
    cla(ax2)
    title(strcat('Autocorrelation of track ', num2str(track_no)));
    hold on
    plot(current_track(:, TIME), corr_values, '-x')
    hold off

    % Bottom left plot will display only the linear segments of the
    % track
    subplot(2, 2, 3)
```

```
        cla(ax3)
        xlim([min(current_track(:, X_COORD)),...
            max(current_track(:, X_COORD))]);
        ylim([min(current_track(:, Y_COORD)),...
            max(current_track(:, Y_COORD))]);
        hold on
        if numel(segments) > 0
            for segment = 1 : numel(segments)
                plot(segments{segment}(:, X_COORD),...
                    segments{segment}(:, Y_COORD), '-x')
            end
        end
        hold off

        % Bottom right plot will display the auttocorrelation of segments
        subplot(2, 2, 4)
        cla(ax4)
        hold on
        if numel(segments) > 0
            for segment = 1 : numel(segments)
                plot(segments{segment}(:, TIME),...
                    segments{segment}(:, SEGMENT_CORR), '-x')
            end
        end
        hold off

        waitforbuttonpress;
        %%%%%%%%%%%%%%%%%%%%%%%%%%%%%%%%%%%%%%%%%%%%%%%%%%%%%%%%%%%%%%%%%%%%%%%%%%%%
        %%%%%%%%%%%%%%%%%%%%%%%%%%%%%%%%%%%%%%%%%%%%%%%%%%%%%%%%%%%%%%%%%%%%%%%%%%%%

    end

    % For all the identified linear segments collect the tracks_info which
    % includes duration, rms_speed, effective_speed etc.
    no_of_linear_segments = numel(linear_segments);
    tracks_info = zeros(no_of_linear_segments, 12);
    for linear_track_no = 1 : no_of_linear_segments
        % The function processtrack calculates all the quantities and
        % assigns them in the row of tracks_info
        tracks_info(linear_track_no, :) = ...
            processtrack(linear_segments{linear_track_no});
    end

end



function corr_values = computeautocorrelation(track)
%computeautocorrelation Computes displacment autocorrelation of the track
%   This function takes the track co-ordinates as input and computes the
%   displacement autocorrelation as a function of time. Feel free to use,
%   modify or simplify this code, but remember my name.
%
%   t1       t2       t3       t4       t5  - time-points
%   x1       x2       x3       x4       x5  - x-coordinates
%   y1       y2       y3       y4       y5  - y-coordinates
%   --      d21      d31      d41      d51  - unit displacement at time tn
%    1  d21.d21  d31.d21  d41.d21  d51.d21  - autocorrelation from t1
%
%   Argument:   track, an n x 3 matrix [t x_coord y_coord]
```

```
%   Returns:    corr_values

    % track is a n x 3 matrix, and the columns are time (s), x-coordinate
    % and y-coordinate
    X_COORD = 2;
    Y_COORD = 3;

    t1 = 1; t2 = 2;

    % Calculate the d21 displacement
    d21 = [track(t2, X_COORD) - track(t1, X_COORD),...
        track(t2, Y_COORD) - track(t1, Y_COORD)];

    % Convert to unit vector
    d21 = d21 / norm(d21);

    % Obtain the number of nodes in the track
    nodes = length(track);

    % Calculate the correlations
    corr_values = transpose(zeros(nodes, 1));
    corr_values(t1) = 1;

    for tn = 2 : nodes
        % Calculate the dn1 displacement
        dn1 = [track(tn, X_COORD) - track(t1, X_COORD),...
            track(tn, Y_COORD) - track(t1, Y_COORD)];

        % Convert to unit vector
        dn1 = dn1 / norm(dn1);

        % Calculate the dot product
        corr_values(tn) = dot(dn1, d21);
    end

end



function segments = identifylinearsegments(track)
%identifylinearsegments Identifies linear segments of filopodia tracks.
%   This function is similar to "computeautocorrelation" but does the extra
%   task of checking whether the autocorrelation values conform to a set of
%   conditions. It restricts the autocorrelation values (constricts the
%   "cone" angle) as time increases, thereby picking linear segments. Then
%   it traverses to the point where there is a break in correlation occurs
%   and repeats the process and so on. In the end it picks up several
%   linear segments within the trajectory and returns those segments as a
%   cell array. Feel free to use, modify or simplify this code, but
%   remember by name.
%
%   t1       t2       t3       t4       t5  - time-points
%   x1       x2       x3       x4       x5  - x-coordinates
%   y1       y2       y3       y4       y5  - y-coordinates
%   --      d21      d31      d41      d51  - unit displacement at time tn
%    1  d21.d21  d31.d21  d41.d21  d51.d21  - autocorrelation from t1
%   --        1  d32.d32  d42.d32  d52.d32  - autocorrelation from t2
%   --       --        1  d43.d43  d53.d43  - autocorrelation from t3
%
%   Argument:   track, an n x 3 matrix [t x_coord y_coord]
```

```
%   Returns:    near linear segments above 20 s duration with corr_values

    % Obtain the number of nodes in the track
    nodes = length(track);

    % track is a n x 3 matrix, and the columns are time (s), x-coordinate
    % and y-coordinate
    X_COORD = 2;
    Y_COORD = 3;

    segment_no = 1;
    segments{segment_no} = 0;

    ti = 2; % start from the second time point

    while (ti < nodes)

        tj = ti - 1;

        % Calculate the d21 displacement
        dij = [track(ti, X_COORD) - track(tj, X_COORD),...
            track(ti, Y_COORD) - track(tj, Y_COORD)];

        % Convert to unit vector
        dij = dij / norm(dij);

        % Calculate the correlations
        corr_values = zeros(nodes, 1);
        corr_values(tj) = 1;

        for tn = ti : nodes

            % Calculate the dnj displacement
            dnj = [track(tn, X_COORD) - track(tj, X_COORD),...
                track(tn, Y_COORD) - track(tj, Y_COORD)];

            % Convert to unit vector
            dnj = dnj / norm(dnj);

            % Calculate the dot product
            corr_values(tn) = dot(dnj, dij);

            % Increase stringency with time (Here tmax = 90)
            % Start with 0.98 and then over time increase the stringency
            % linearly (0.02 comes from 1.00 - 0.98)
            stringency = 0.98 + (((tn - tj) * 0.02) / 90);
            if (corr_values(tn) < stringency) || (tn == nodes)
                segments{segment_no} = [track(tj : tn - 1, :),...
                    corr_values(tj : tn - 1)];
                segment_no = segment_no + 1;
                ti = tn;
                break;
            else
                continue;
            end

        end

    end
```

```
end


function segments = discardshortsegments(segments)
%discardshortsegments Discards filopodia track segments below 20 s
%   This function looks at the segments within a track and discards those
%   that are below 20 s
%
%   Argument:   segments, an n x 4 matrix [t x_coord y_coord corr_values]
%   Returns:    segments, with short segments discarded

    for segment_no = 1 : numel(segments)

        if length(segments{segment_no}) < 20
            % empty the cell if less than 20 s
            segments{segment_no} = [];
        else
            continue;
        end

    end
    % remove the empty cell
    segments = segments(~cellfun('isempty', segments));

end



function track_info = processtrack(track)
%processtrack Collects track parameters
%   This function takes each track or track segment and caluclates
%   no_of_steps, track_duration, mean_distance, rms_distance,
%   effective_displacement_xy, effective_distance, mean_speed, rms_speed,
%   effective_velocity_xy, effective speed.
%
%   Argument:   track, an n x 3 matrix [t x_coord y_coord]
%   Returns:    track_info containing the above parameters

    % The track is n x 3 matrix, and the columns are time (s), x-coordinate
    % and y-coordinate

    % Obtain the number of nodes in the track
    nodes = length(track);

    % Initialize the return variables
    no_of_steps = nodes - 1;
    track_duration = track(nodes, 1) - track(1, 1);
    mean_distance = 0; rms_distance = 0;
    effective_displacement_xy = [track(nodes, 2) - track(1, 2),...
        track(nodes, 3) - track(1, 3)];
    effective_distance = norm(effective_displacement_xy);
    mean_speed = 0; rms_speed = 0;
    effective_velocity_xy = effective_displacement_xy / (track(nodes, 1) -
track(1, 1));
    effective_speed = norm(effective_velocity_xy);

    % Iterate through the nodes starting with the second node (second node
    % because for a track of length n, there will be n-1 displacements and
    % hence n-1 velocities
```

```
    for node = 2 : nodes
        % displacement
        displacement = [track(node, 2) - track(node - 1, 2),...
            track(node, 3) - track(node - 1, 3)];
        mean_distance = mean_distance + norm(displacement);
        rms_distance = rms_distance + (norm(displacement))^2;

        % velocity
        velocity = displacement / (track(node, 1) - track(node - 1, 1));
        mean_speed = mean_speed + norm(velocity);
        rms_speed = rms_speed + (norm(velocity))^2;
    end

    % calculate mean and rms values
    mean_distance = mean_distance / (nodes - 1);
    rms_distance = sqrt(rms_distance / (nodes - 1));

    mean_speed = mean_speed / (nodes - 1);
    rms_speed = sqrt(rms_speed / (nodes - 1));

    track_info = [...
        no_of_steps,...                 % 1
        track_duration,...              % 2
        mean_distance,...               % 3
        rms_distance,...                % 4
        effective_displacement_xy,...   % 5, 6
        effective_distance,...          % 7
        mean_speed,...                  % 8
        rms_speed,...                   % 9
        effective_velocity_xy,...       % 10, 11
        effective_speed];               % 12
end
```

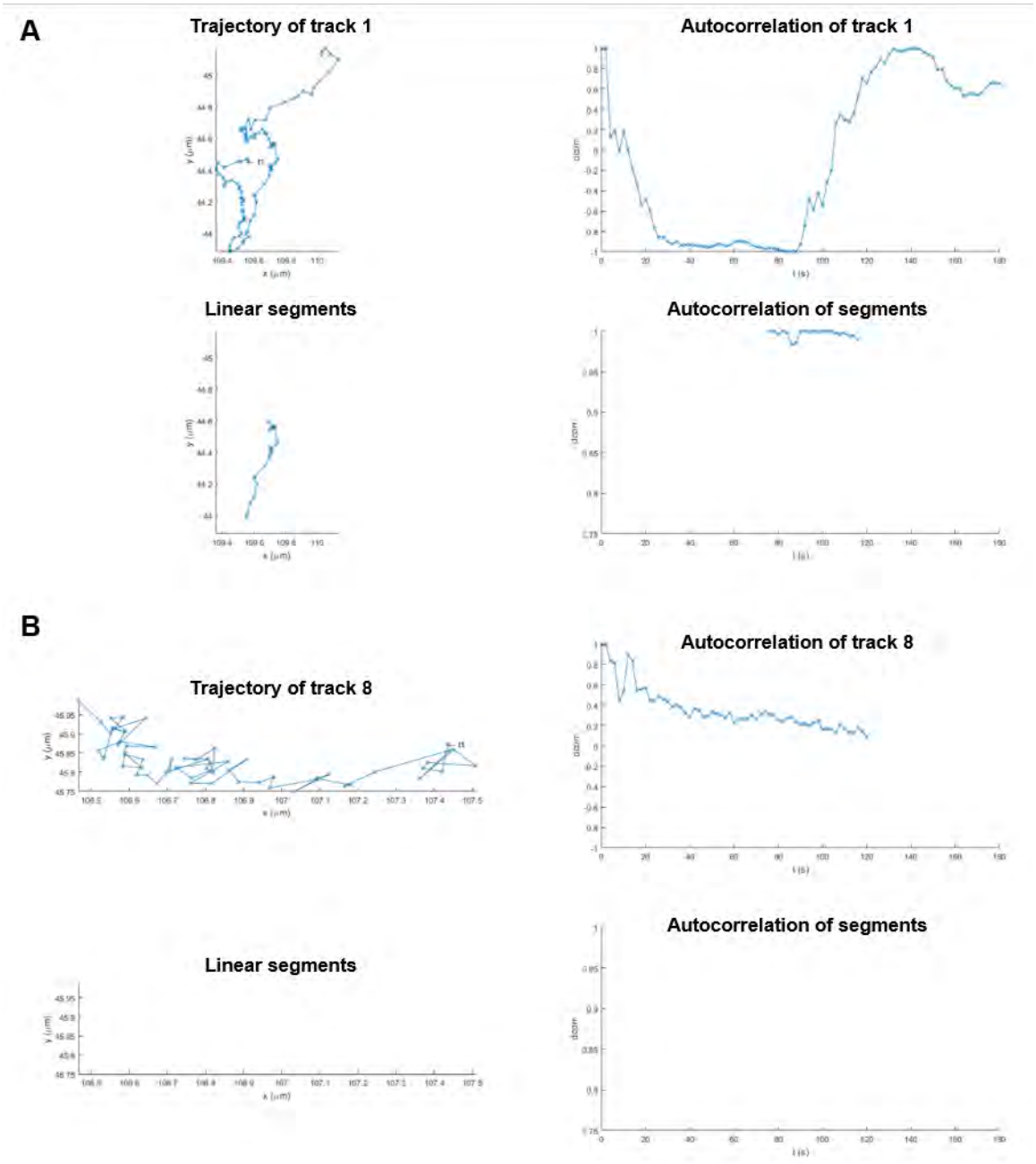

Figure AIV-1. Identification of linear segments from the filopodia trajectories. (A) An example track whose trajectory (top left), position autocorrelation (top right), the linear segment within the trajectory (bottom left) and its corresponding autocorrelation values (bottom right) are plotted. The algorithm identifies a linear segment in this track. (B) An example of a track (plots same as in (A)) that exhibits random motion with no linear segments.

APPENDIX V – ARTIFICIAL PFN1 MICRO RNA SEQUENCES

U6 promoter: Green letters
miR155 flanking sequences: highlighted in blue
mature miR: underlined
Passenger strand: blue letters

PFN1-1169
Guide strand: TTGTATGGGGAGGAAAGGGGT

Artificial miR-PFN1-1169
AAGGTCGGGCAGGAAGAGGGCCTATTTCCCATGATTCCTTCATATTTGCATATACGATACAAGGCTGTTAG
AGAGATAATTGGAATTAATTTGACTGTAAACACAAAGATATTAGTACAAAATACGTGACGTAGAAAGTAAT
AATTTCTTGGGTAGTTTGCAGTTTTAAAATTATGTTTTAAAATGGACTATCATATGCTTACCGTAACTTGA
AAGTATTTCGATTTCTTGGCTTTATATATCTTGTGGAAAGGACGAAACACCGCTGGAGGCTTGCTGAAGGC
TGTATGCTGTTGTATGGGGAGGAAAGGGGTGTTTTGGCCACTGACTGACACCCCTTTTCCCCATACAACAG
GACACAAGGCCTGTTACTAGCACTCACATGGAACAAATGGCCCTTTTTT

PFN1-1171
Guide strand: TAATGGTTTGTGTGTGTATGG

Artificial miR-PFN1-1107
AAGGTCGGGCAGGAAGAGGGCCTATTTCCCATGATTCCTTCATATTTGCATATACGATACAAGGCTGTTAG
AGAGATAATTGGAATTAATTTGACTGTAAACACAAAGATATTAGTACAAAATACGTGACGTAGAAAGTAAT
AATTTCTTGGGTAGTTTGCAGTTTTAAAATTATGTTTTAAAATGGACTATCATATGCTTACCGTAACTTGA
AAGTATTTCGATTTCTTGGCTTTATATATCTTGTGGAAAGGACGAAACACCGCTGGAGGCTTGCTGAAGGC
TGTATGCTGTAATGGTTTGTGTGTGTATGGGTTTTGGCCACTGACTGACCCATACACACAAACCATTACAG
GACACAAGGCCTGTTACTAGCACTCACATGGAACAAATGGCCCTTTTTT

PFN1-1198
Guide Strand: TGGTATGGGGTAATGGCCCAA

Artificial miR-PFN1-1169
AAGGTCGGGCAGGAAGAGGGCCTATTTCCCATGATTCCTTCATATTTGCATATACGATACAAGGCTGTTAG
AGAGATAATTGGAATTAATTTGACTGTAAACACAAAGATATTAGTACAAAATACGTGACGTAGAAAGTAAT
AATTTCTTGGGTAGTTTGCAGTTTTAAAATTATGTTTTAAAATGGACTATCATATGCTTACCGTAACTTGA
AAGTATTTCGATTTCTTGGCTTTATATATCTTGTGGAAAGGACGAAACACCGCTGGAGGCTTGCTGAAGGC
TGTATGCTGTGGTATGGGGTAATGGCCCAAGTTTTGGCCACTGACTGACTTGGGCCAACCCCATACCACAG
GACACAAGGCCTGTTACTAGCACTCACATGGAACAAATGGCCCTTTTTT

PFN1-1207
Guide strand: TGCAATAAGGGGTATGGGGTA

Artificial miR-PFN1-1207
AAGGTCGGGCAGGAAGAGGGCCTATTTCCCATGATTCCTTCATATTTGCATATACGATACAAGGCTGTTAG
AGAGATAATTGGAATTAATTTGACTGTAAACACAAAGATATTAGTACAAAATACGTGACGTAGAAAGTAAT
AATTTCTTGGGTAGTTTGCAGTTTTAAAATTATGTTTTAAAATGGACTATCATATGCTTACCGTAACTTGA

AAGTATTTCGATTTCTTGGCTTTATATATCTTGTGGAAAGGACGAAACACCGCTGGAGGCTTGCTGAAGGC
TGTATGCTGTGCAATAAGGGGTATGGGGTAGTTTTGGCCACTGACTGACTACCCCATCCCTTATTGCACAG
GACACAAGGCCTGTTACTAGCACTCACATGGAACAAATGGCCCTTTTTT

PFN1-1217
Guide strand: TGGTTTTGGCAGCAATAAGGG

Artificial miR-PFN1-1217
AAGGTCGGGCAGGAAGAGGGCCTATTTCCCATGATTCCTTCATATTTGCATATACGATACAAGGCTGTTAG
AGAGATAATTGGAATTAATTTGACTGTAAACACAAAGATATTAGTACAAAATACGTGACGTAGAAAGTAAT
AATTTCTTGGGTAGTTTGCAGTTTTAAAATTATGTTTTAAAATGGACTATCATATGCTTACCGTAACTTGA
AAGTATTTCGATTTCTTGGCTTTATATATCTTGTGGAAAGGACGAAACACCGCTGGAGGCTTGCTGAAGGC
TGTATGCTGTGGTTTTGGCAGCAATAAGGGGTTTTGGCCACTGACTGACCCCTTATTTGCCAAAACCACAG
GACACAAGGCCTGTTACTAGCACTCACATGGAACAAATGGCCCTTTTTT

BIBILIOGRAPHY

1. Brown, R. H., and Al-Chalabi, A. (2017) Amyotrophic Lateral Sclerosis. *N Engl J Med* **377**, 162-172
2. Taylor, J. P., Brown, R. H., Jr., and Cleveland, D. W. (2016) Decoding ALS: from genes to mechanism. *Nature* **539**, 197-206
3. Rosen, D. R., Siddique, T., Patterson, D., Figlewicz, D. A., Sapp, P., Hentati, A., Donaldson, D., Goto, J., O'Regan, J. P., Deng, H. X., and et al. (1993) Mutations in Cu/Zn superoxide dismutase gene are associated with familial amyotrophic lateral sclerosis. *Nature* **362**, 59-62
4. Ghasemi, M., and Brown, R. H., Jr. (2017) Genetics of Amyotrophic Lateral Sclerosis. *Cold Spring Harb Perspect Med* doi: 10.1101/cshperspect.a024125
5. Pollard, T. D., and Quirk, S. (1994) Profilins, ancient actin binding proteins with highly divergent primary structures. *Soc Gen Physiol Ser* **49**, 117-128
6. Smith, B. N., Vance, C., Scotter, E. L., Troakes, C., Wong, C. H., Topp, S., Maekawa, S., King, A., Mitchell, J. C., Lund, K., Al-Chalabi, A., Ticozzi, N., Silani, V., Sapp, P., Brown, R. H., Jr., Landers, J. E., Al-Sarraj, S., and Shaw, C. E. (2015) Novel mutations support a role for Profilin 1 in the pathogenesis of ALS. *Neurobiology of aging* **36**, 1602 e1617-1627
7. Wu, C. H., Fallini, C., Ticozzi, N., Keagle, P. J., Sapp, P. C., Piotrowska, K., Lowe, P., Koppers, M., McKenna-Yasek, D., Baron, D. M., Kost, J. E., Gonzalez-Perez, P., Fox, A. D., Adams, J., Taroni, F., Tiloca, C., Leclerc, A. L., Chafe, S. C., Mangroo, D., Moore, M. J., Zitzewitz, J. A., Xu, Z. S., van den Berg, L. H., Glass, J. D., Siciliano, G., Cirulli, E. T., Goldstein, D. B., Salachas, F., Meininger, V., Rossoll, W., Ratti, A., Gellera, C., Bosco, D. A., Bassell, G. J., Silani, V., Drory, V. E., Brown, R. H., Jr., and Landers, J. E. (2012) Mutations in the profilin 1 gene cause familial amyotrophic lateral sclerosis. *Nature* **488**, 499-503
8. Krishnan, K., and Moens, P. D. J. (2009) Structure and functions of profilins. *Biophys Rev* **1**, 71-81
9. Jockusch, B. M., Murk, K., and Rothkegel, M. (2007) The profile of profilins. *Rev Physiol Biochem Pharmacol* **159**, 131-149
10. Metzler, W. J., Farmer, B. T., 2nd, Constantine, K. L., Friedrichs, M. S., Lavoie, T., and Mueller, L. (1995) Refined solution structure of human profilin I. *Protein science : a publication of the Protein Society* **4**, 450-459
11. Babich, M., Foti, L. R., Sykaluk, L. L., and Clark, C. R. (1996) Profilin forms tetramers that bind to G-actin. *Biochem Biophys Res Commun* **218**, 125-131
12. Korupolu, R. V., Achary, M. S., Aneesa, F., Sathish, K., Wasia, R., Sairam, M., Nagarajaram, H. A., and Singh, S. S. (2009) Profilin

oligomerization and its effect on poly (L-proline) binding and phosphorylation. *Int J Biol Macromol* **45**, 265-273
13. Rennella, E., Sekhar, A., and Kay, L. E. (2017) Self-Assembly of Human Profilin-1 Detected by Carr-Purcell-Meiboom-Gill Nuclear Magnetic Resonance (CPMG NMR) Spectroscopy. *Biochemistry* **56**, 692-703
14. Carlsson, L., Nystrom, L. E., Lindberg, U., Kannan, K. K., Cid-Dresdner, H., and Lovgren, S. (1976) Crystallization of a non-muscle actin. *J Mol Biol* **105**, 353-366
15. Witke, W. (2004) The role of profilin complexes in cell motility and other cellular processes. *Trends Cell Biol* **14**, 461-469
16. Schluter, K., Jockusch, B. M., and Rothkegel, M. (1997) Profilins as regulators of actin dynamics. *Biochim Biophys Acta* **1359**, 97-109
17. Schutt, C. E., Myslik, J. C., Rozycki, M. D., Goonesekere, N. C., and Lindberg, U. (1993) The structure of crystalline profilin-beta-actin. *Nature* **365**, 810-816
18. Courtemanche, N., and Pollard, T. D. (2013) Interaction of profilin with the barbed end of actin filaments. *Biochemistry* **52**, 6456-6466
19. Pernier, J., Shekhar, S., Jegou, A., Guichard, B., and Carlier, M. F. (2016) Profilin Interaction with Actin Filament Barbed End Controls Dynamic Instability, Capping, Branching, and Motility. *Developmental cell* **36**, 201-214
20. Vinson, V. K., De La Cruz, E. M., Higgs, H. N., and Pollard, T. D. (1998) Interactions of Acanthamoeba profilin with actin and nucleotides bound to actin. *Biochemistry* **37**, 10871-10880
21. Lu, J., and Pollard, T. D. (2001) Profilin binding to poly-L-proline and actin monomers along with ability to catalyze actin nucleotide exchange is required for viability of fission yeast. *Mol Biol Cell* **12**, 1161-1175
22. Bjorkegren, C., Rozycki, M., Schutt, C. E., Lindberg, U., and Karlsson, R. (1993) Mutagenesis of human profilin locates its poly(L-proline)-binding site to a hydrophobic patch of aromatic amino acids. *FEBS Lett* **333**, 123-126
23. Bjorkegren-Sjogren, C., Korenbaum, E., Nordberg, P., Lindberg, U., and Karlsson, R. (1997) Isolation and characterization of two mutants of human profilin I that do not bind poly(L-proline). *FEBS Lett* **418**, 258-264
24. Mahoney, N. M., Janmey, P. A., and Almo, S. C. (1997) Structure of the profilin-poly-L-proline complex involved in morphogenesis and cytoskeletal regulation. *Nat Struct Biol* **4**, 953-960
25. Mahoney, N. M., Rozwarski, D. A., Fedorov, E., Fedorov, A. A., and Almo, S. C. (1999) Profilin binds proline-rich ligands in two distinct amide backbone orientations. *Nat Struct Biol* **6**, 666-671
26. Metzler, W. J., Bell, A. J., Ernst, E., Lavoie, T. B., and Mueller, L. (1994) Identification of the poly-L-proline-binding site on human profilin. *J Biol Chem* **269**, 4620-4625

27. Petrella, E. C., Machesky, L. M., Kaiser, D. A., and Pollard, T. D. (1996) Structural requirements and thermodynamics of the interaction of proline peptides with profilin. *Biochemistry* **35**, 16535-16543
28. Chaudhary, A., Chen, J., Gu, Q. M., Witke, W., Kwiatkowski, D. J., and Prestwich, G. D. (1998) Probing the phosphoinositide 4,5-bisphosphate binding site of human profilin I. *Chem Biol* **5**, 273-281
29. Lambrechts, A., Jonckheere, V., Dewitte, D., Vandekerckhove, J., and Ampe, C. (2002) Mutational analysis of human profilin I reveals a second PI(4,5)-P2 binding site neighbouring the poly(L-proline) binding site. *BMC Biochem* **3**, 12
30. Skare, P., and Karlsson, R. (2002) Evidence for two interaction regions for phosphatidylinositol(4,5)-bisphosphate on mammalian profilin I. *FEBS Lett* **522**, 119-124
31. Sohn, R. H., Chen, J., Koblan, K. S., Bray, P. F., and Goldschmidt-Clermont, P. J. (1995) Localization of a binding site for phosphatidylinositol 4,5-bisphosphate on human profilin. *J Biol Chem* **270**, 21114-21120
32. Lambrechts, A., Verschelde, J. L., Jonckheere, V., Goethals, M., Vandekerckhove, J., and Ampe, C. (1997) The mammalian profilin isoforms display complementary affinities for PIP2 and proline-rich sequences. *EMBO J* **16**, 484-494
33. Lassing, I., and Lindberg, U. (1985) Specific interaction between phosphatidylinositol 4,5-bisphosphate and profilactin. *Nature* **314**, 472-474
34. Lassing, I., and Lindberg, U. (1988) Specificity of the interaction between phosphatidylinositol 4,5-bisphosphate and the profilin:actin complex. *J Cell Biochem* **37**, 255-267
35. Goldschmidt-Clermont, P. J., Kim, J. W., Machesky, L. M., Rhee, S. G., and Pollard, T. D. (1991) Regulation of phospholipase C-gamma 1 by profilin and tyrosine phosphorylation. *Science* **251**, 1231-1233
36. Goldschmidt-Clermont, P. J., Machesky, L. M., Baldassare, J. J., and Pollard, T. D. (1990) The actin-binding protein profilin binds to PIP2 and inhibits its hydrolysis by phospholipase C. *Science* **247**, 1575-1578
37. Moens, P. D., and Bagatolli, L. A. (2007) Profilin binding to sub-micellar concentrations of phosphatidylinositol (4,5) bisphosphate and phosphatidylinositol (3,4,5) trisphosphate. *Biochim Biophys Acta* **1768**, 439-449
38. Richer, S. M., Stewart, N. K., Webb, S. A., Tomaszewski, J. W., and Oakley, M. G. (2009) High affinity binding to profilin by a covalently constrained, soluble mimic of phosphatidylinositol-4,5-bisphosphate micelles. *ACS Chem Biol* **4**, 733-739
39. Lu, P. J., Shieh, W. R., Rhee, S. G., Yin, H. L., and Chen, C. S. (1996) Lipid products of phosphoinositide 3-kinase bind human profilin with high affinity. *Biochemistry* **35**, 14027-14034

40. Raghunathan, V., Mowery, P., Rozycki, M., Lindberg, U., and Schutt, C. (1992) Structural changes in profilin accompany its binding to phosphatidylinositol, 4,5-bisphosphate. *FEBS Lett* **297**, 46-50
41. Goode, B. L., and Eck, M. J. (2007) Mechanism and function of formins in the control of actin assembly. *Annu Rev Biochem* **76**, 593-627
42. Bubb, M. R., Yarmola, E. G., Gibson, B. G., and Southwick, F. S. (2003) Depolymerization of actin filaments by profilin. Effects of profilin on capping protein function. *J Biol Chem* **278**, 24629-24635
43. Gieselmann, R., Kwiatkowski, D. J., Janmey, P. A., and Witke, W. (1995) Distinct biochemical characteristics of the two human profilin isoforms. *Eur J Biochem* **229**, 621-628
44. Shekhar, S., Pernier, J., and Carlier, M. F. (2016) Regulators of actin filament barbed ends at a glance. *J Cell Sci* **129**, 1085-1091
45. Yarmola, E. G., and Bubb, M. R. (2006) Profilin: emerging concepts and lingering misconceptions. *Trends Biochem Sci* **31**, 197-205
46. Yarmola, E. G., and Bubb, M. R. (2009) How depolymerization can promote polymerization: the case of actin and profilin. *Bioessays* **31**, 1150-1160
47. Korenbaum, E., Nordberg, P., Bjorkegren-Sjogren, C., Schutt, C. E., Lindberg, U., and Karlsson, R. (1998) The role of profilin in actin polymerization and nucleotide exchange. *Biochemistry* **37**, 9274-9283
48. Mockrin, S. C., and Korn, E. D. (1980) Acanthamoeba profilin interacts with G-actin to increase the rate of exchange of actin-bound adenosine 5'-triphosphate. *Biochemistry* **19**, 5359-5362
49. Balcer, H. I., Goodman, A. L., Rodal, A. A., Smith, E., Kugler, J., Heuser, J. E., and Goode, B. L. (2003) Coordinated regulation of actin filament turnover by a high-molecular-weight Srv2/CAP complex, cofilin, profilin, and Aip1. *Curr Biol* **13**, 2159-2169
50. Johnston, A. B., Collins, A., and Goode, B. L. (2015) High-speed depolymerization at actin filament ends jointly catalysed by Twinfilin and Srv2/CAP. *Nat Cell Biol* **17**, 1504-1511
51. Goley, E. D., and Welch, M. D. (2006) The ARP2/3 complex: an actin nucleator comes of age. *Nature reviews. Molecular cell biology* **7**, 713-726
52. Pollard, T. D. (2007) Regulation of actin filament assembly by Arp2/3 complex and formins. *Annu Rev Biophys Biomol Struct* **36**, 451-477
53. Chesarone, M. A., DuPage, A. G., and Goode, B. L. (2010) Unleashing formins to remodel the actin and microtubule cytoskeletons. *Nature reviews. Molecular cell biology* **11**, 62-74
54. Bear, J. E., and Gertler, F. B. (2009) Ena/VASP: towards resolving a pointed controversy at the barbed end. *J Cell Sci* **122**, 1947-1953
55. Krause, M., Dent, E. W., Bear, J. E., Loureiro, J. J., and Gertler, F. B. (2003) Ena/VASP proteins: regulators of the actin cytoskeleton and cell migration. *Annu Rev Cell Dev Biol* **19**, 541-564

56. Sechi, A. S., and Wehland, J. (2004) ENA/VASP proteins: multifunctional regulators of actin cytoskeleton dynamics. *Front Biosci* **9**, 1294-1310
57. Suetsugu, S., Miki, H., and Takenawa, T. (1998) The essential role of profilin in the assembly of actin for microspike formation. *EMBO J* **17**, 6516-6526
58. Machesky, L. M., Mullins, R. D., Higgs, H. N., Kaiser, D. A., Blanchoin, L., May, R. C., Hall, M. E., and Pollard, T. D. (1999) Scar, a WASp-related protein, activates nucleation of actin filaments by the Arp2/3 complex. *Proc Natl Acad Sci U S A* **96**, 3739-3744
59. Rotty, J. D., Wu, C., Haynes, E. M., Suarez, C., Winkelman, J. D., Johnson, H. E., Haugh, J. M., Kovar, D. R., and Bear, J. E. (2015) Profilin-1 serves as a gatekeeper for actin assembly by Arp2/3-dependent and -independent pathways. *Developmental cell* **32**, 54-67
60. Suarez, C., Carroll, R. T., Burke, T. A., Christensen, J. R., Bestul, A. J., Sees, J. A., James, M. L., Sirotkin, V., and Kovar, D. R. (2015) Profilin regulates F-actin network homeostasis by favoring formin over Arp2/3 complex. *Developmental cell* **32**, 43-53
61. Higgs, H. N. (2005) Formin proteins: a domain-based approach. *Trends Biochem Sci* **30**, 342-353
62. Mizuno, H., Higashida, C., Yuan, Y., Ishizaki, T., Narumiya, S., and Watanabe, N. (2011) Rotational movement of the formin mDia1 along the double helical strand of an actin filament. *Science* **331**, 80-83
63. Mizuno, H., and Watanabe, N. (2012) mDia1 and formins: screw cap of the actin filament. *Biophysics (Nagoya-shi)* **8**, 95-102
64. Paul, A. S., and Pollard, T. D. (2009) Review of the mechanism of processive actin filament elongation by formins. *Cell motility and the cytoskeleton* **66**, 606-617
65. Paul, A. S., and Pollard, T. D. (2009) Energetic requirements for processive elongation of actin filaments by FH1FH2-formins. *J Biol Chem* **284**, 12533-12540
66. Paul, A. S., and Pollard, T. D. (2008) The role of the FH1 domain and profilin in formin-mediated actin-filament elongation and nucleation. *Curr Biol* **18**, 9-19
67. Ferron, F., Rebowski, G., Lee, S. H., and Dominguez, R. (2007) Structural basis for the recruitment of profilin-actin complexes during filament elongation by Ena/VASP. *EMBO J* **26**, 4597-4606
68. Le Clainche, C., and Carlier, M. F. (2004) Actin-based motility assay. *Curr Protoc Cell Biol* **Chapter 12**, Unit 12 17
69. Wiesner, S., Helfer, E., Didry, D., Ducouret, G., Lafuma, F., Carlier, M. F., and Pantaloni, D. (2003) A biomimetic motility assay provides insight into the mechanism of actin-based motility. *J Cell Biol* **160**, 387-398
70. Cao, L. G., Babcock, G. G., Rubenstein, P. A., and Wang, Y. L. (1992) Effects of profilin and profilactin on actin structure and function in living cells. *J Cell Biol* **117**, 1023-1029

71. Ostrander, D. B., Gorman, J. A., and Carman, G. M. (1995) Regulation of profilin localization in Saccharomyces cerevisiae by phosphoinositide metabolism. *J Biol Chem* **270**, 27045-27050
72. Fan, Y., Potdar, A. A., Gong, Y., Eswarappa, S. M., Donnola, S., Lathia, J. D., Hambardzumyan, D., Rich, J. N., and Fox, P. L. (2014) Profilin-1 phosphorylation directs angiocrine expression and glioblastoma progression through HIF-1alpha accumulation. *Nat Cell Biol* **16**, 445-456
73. Gau, D., Veon, W., Zeng, X., Yates, N., Shroff, S. G., Koes, D. R., and Roy, P. (2016) Threonine 89 Is an Important Residue of Profilin-1 That Is Phosphorylatable by Protein Kinase A. *PloS one* **11**, e0156313
74. Ingre, C., Landers, J. E., Rizik, N., Volk, A. E., Akimoto, C., Birve, A., Hubers, A., Keagle, P. J., Piotrowska, K., Press, R., Andersen, P. M., Ludolph, A. C., and Weishaupt, J. H. (2013) A novel phosphorylation site mutation in profilin 1 revealed in a large screen of US, Nordic, and German amyotrophic lateral sclerosis/frontotemporal dementia cohorts. *Neurobiology of aging* **34**, 1708 e1701-1706
75. Shao, J., Welch, W. J., Diprospero, N. A., and Diamond, M. I. (2008) Phosphorylation of profilin by ROCK1 regulates polyglutamine aggregation. *Mol Cell Biol* **28**, 5196-5208
76. Sathish, K., Padma, B., Munugalavadla, V., Bhargavi, V., Radhika, K. V., Wasia, R., Sairam, M., and Singh, S. S. (2004) Phosphorylation of profilin regulates its interaction with actin and poly (L-proline). *Cell Signal* **16**, 589-596
77. Schonichen, A., and Geyer, M. (2010) Fifteen formins for an actin filament: a molecular view on the regulation of human formins. *Biochim Biophys Acta* **1803**, 152-163
78. Giesemann, T., Rathke-Hartlieb, S., Rothkegel, M., Bartsch, J. W., Buchmeier, S., Jockusch, B. M., and Jockusch, H. (1999) A role for polyproline motifs in the spinal muscular atrophy protein SMN. Profilins bind to and colocalize with smn in nuclear gems. *J Biol Chem* **274**, 37908-37914
79. Skare, P., Kreivi, J. P., Bergstrom, A., and Karlsson, R. (2003) Profilin I colocalizes with speckles and Cajal bodies: a possible role in pre-mRNA splicing. *Exp Cell Res* **286**, 12-21
80. Stuven, T., Hartmann, E., and Gorlich, D. (2003) Exportin 6: a novel nuclear export receptor that is specific for profilin.actin complexes. *EMBO J* **22**, 5928-5940
81. de Lanerolle, P., and Serebryannyy, L. (2011) Nuclear actin and myosins: life without filaments. *Nat Cell Biol* **13**, 1282-1288
82. Kapoor, P., and Shen, X. (2014) Mechanisms of nuclear actin in chromatin-remodeling complexes. *Trends Cell Biol* **24**, 238-246
83. Wesolowska, N., and Lenart, P. (2015) Nuclear roles for actin. *Chromosoma* **124**, 481-489

84. Belin, B. J., Lee, T., and Mullins, R. D. (2015) DNA damage induces nuclear actin filament assembly by Formin -2 and Spire-(1/2) that promotes efficient DNA repair. [corrected]. *Elife* **4**, e07735
85. Isogai, T., and Innocenti, M. (2016) New nuclear and perinuclear functions of formins. *Biochem Soc Trans* **44**, 1701-1708
86. Miki, T., Okawa, K., Sekimoto, T., Yoneda, Y., Watanabe, S., Ishizaki, T., and Narumiya, S. (2009) mDia2 shuttles between the nucleus and the cytoplasm through the importin-{alpha}/{beta}- and CRM1-mediated nuclear transport mechanism. *J Biol Chem* **284**, 5753-5762
87. Murk, K., Wittenmayer, N., Michaelsen-Preusse, K., Dresbach, T., Schoenenberger, C. A., Korte, M., Jockusch, B. M., and Rothkegel, M. (2012) Neuronal profilin isoforms are addressed by different signalling pathways. *PloS one* **7**, e34167
88. Doussau, F., and Augustine, G. J. (2000) The actin cytoskeleton and neurotransmitter release: an overview. *Biochimie* **82**, 353-363
89. Wang, X., Kibschull, M., Laue, M. M., Lichte, B., Petrasch-Parwez, E., and Kilimann, M. W. (1999) Aczonin, a 550-kD putative scaffolding protein of presynaptic active zones, shares homology regions with Rim and Bassoon and binds profilin. *J Cell Biol* **147**, 151-162
90. Ackermann, M., and Matus, A. (2003) Activity-induced targeting of profilin and stabilization of dendritic spine morphology. *Nat Neurosci* **6**, 1194-1200
91. Neuhoff, H., Sassoe-Pognetto, M., Panzanelli, P., Maas, C., Witke, W., and Kneussel, M. (2005) The actin-binding protein profilin I is localized at synaptic sites in an activity-regulated manner. *Eur J Neurosci* **21**, 15-25
92. Witke, W., Podtelejnikov, A. V., Di Nardo, A., Sutherland, J. D., Gurniak, C. B., Dotti, C., and Mann, M. (1998) In mouse brain profilin I and profilin II associate with regulators of the endocytic pathway and actin assembly. *EMBO J* **17**, 967-976
93. Witke, W., Sutherland, J. D., Sharpe, A., Arai, M., and Kwiatkowski, D. J. (2001) Profilin I is essential for cell survival and cell division in early mouse development. *Proc Natl Acad Sci U S A* **98**, 3832-3836
94. Schweinhuber, S. K., Messerschmidt, T., Hansch, R., Korte, M., and Rothkegel, M. (2015) Profilin isoforms modulate astrocytic morphology and the motility of astrocytic processes. *PloS one* **10**, e0117244
95. Molotkov, D., Zobova, S., Arcas, J. M., and Khiroug, L. (2013) Calcium-induced outgrowth of astrocytic peripheral processes requires actin binding by Profilin-1. *Cell Calcium* **53**, 338-348
96. Birbach, A. (2008) Profilin, a multi-modal regulator of neuronal plasticity. *BioEssays : news and reviews in molecular, cellular and developmental biology* **30**, 994-1002
97. Lambrechts, A., Jonckheere, V., Peleman, C., Polet, D., De Vos, W., Vandekerckhove, J., and Ampe, C. (2006) Profilin-I-ligand interactions

influence various aspects of neuronal differentiation. *J Cell Sci* **119**, 1570-1578
98. Dong, J. H., Ying, G. X., and Zhou, C. F. (2004) Entorhinal deafferentation induces the expression of profilin mRNA in the reactive microglial cells in the hippocampus. *Glia* **47**, 102-108
99. Kullmann, J. A., Neumeyer, A., Gurniak, C. B., Friauf, E., Witke, W., and Rust, M. B. (2011) Profilin1 is required for glial cell adhesion and radial migration of cerebellar granule neurons. *EMBO Rep* **13**, 75-82
100. Kullmann, J. A., Neumeyer, A., Wickertsheim, I., Bottcher, R. T., Costell, M., Deitmer, J. W., Witke, W., Friauf, E., and Rust, M. B. (2012) Purkinje cell loss and motor coordination defects in profilin1 mutant mice. *Neuroscience* **223**, 355-364
101. Kullmann, J. A., Wickertsheim, I., Minnerup, L., Costell, M., Friauf, E., and Rust, M. B. (2015) Profilin1 activity in cerebellar granule neurons is required for radial migration in vivo. *Cell Adh Migr* **9**, 247-253
102. Rust, M. B., Kullmann, J. A., and Witke, W. (2012) Role of the actin-binding protein profilin1 in radial migration and glial cell adhesion of granule neurons in the cerebellum. *Cell Adh Migr* **6**, 13-17
103. Montani, L., Buerki-Thurnherr, T., de Faria, J. P., Pereira, J. A., Dias, N. G., Fernandes, R., Goncalves, A. F., Braun, A., Benninger, Y., Bottcher, R. T., Costell, M., Nave, K. A., Franklin, R. J., Meijer, D., Suter, U., and Relvas, J. B. (2014) Profilin 1 is required for peripheral nervous system myelination. *Development* **141**, 1553-1561
104. Michaelsen-Preusse, K., Zessin, S., Grigoryan, G., Scharkowski, F., Feuge, J., Remus, A., and Korte, M. (2016) Neuronal profilins in health and disease: Relevance for spine plasticity and Fragile X syndrome. *Proc Natl Acad Sci U S A* **113**, 3365-3370
105. Pilo Boyl, P., Di Nardo, A., Mulle, C., Sassoe-Pognetto, M., Panzanelli, P., Mele, A., Kneussel, M., Costantini, V., Perlas, E., Massimi, M., Vara, H., Giustetto, M., and Witke, W. (2007) Profilin2 contributes to synaptic vesicle exocytosis, neuronal excitability, and novelty-seeking behavior. *EMBO J* **26**, 2991-3002
106. Michaelsen, K., Murk, K., Zagrebelsky, M., Dreznjak, A., Jockusch, B. M., Rothkegel, M., and Korte, M. (2010) Fine-tuning of neuronal architecture requires two profilin isoforms. *Proc Natl Acad Sci U S A* **107**, 15780-15785
107. Gorlich, A., Zimmermann, A. M., Schober, D., Bottcher, R. T., Sassoe-Pognetto, M., Friauf, E., Witke, W., and Rust, M. B. (2012) Preserved morphology and physiology of excitatory synapses in profilin1-deficient mice. *PloS one* **7**, e30068
108. Burnett, B. G., Andrews, J., Ranganathan, S., Fischbeck, K. H., and Di Prospero, N. A. (2008) Expression of expanded polyglutamine targets profilin for degradation and alters actin dynamics. *Neurobiol Dis* **30**, 365-374

109. Narayanan, K. L., Chopra, V., Rosas, H. D., Malarick, K., and Hersch, S. (2016) Rho Kinase Pathway Alterations in the Brain and Leukocytes in Huntington's Disease. *Mol Neurobiol* **53**, 2132-2140
110. Ridley, A. J., and Hall, A. (1992) The small GTP-binding protein rho regulates the assembly of focal adhesions and actin stress fibers in response to growth factors. *Cell* **70**, 389-399
111. Nobes, C. D., and Hall, A. (1995) Rho, rac, and cdc42 GTPases regulate the assembly of multimolecular focal complexes associated with actin stress fibers, lamellipodia, and filopodia. *Cell* **81**, 53-62
112. Sadok, A., and Marshall, C. J. (2014) Rho GTPases: masters of cell migration. *Small GTPases* **5**, e29710
113. van Buul, J. D., Geerts, D., and Huveneers, S. (2014) Rho GAPs and GEFs: controling switches in endothelial cell adhesion. *Cell Adh Migr* **8**, 108-124
114. Zegers, M. M., and Friedl, P. (2014) Rho GTPases in collective cell migration. *Small GTPases* **5**, e28997
115. Julian, L., and Olson, M. F. (2014) Rho-associated coiled-coil containing kinases (ROCK): structure, regulation, and functions. *Small GTPases* **5**, e29846
116. Schofield, A. V., and Bernard, O. (2013) Rho-associated coiled-coil kinase (ROCK) signaling and disease. *Crit Rev Biochem Mol Biol* **48**, 301-316
117. Mueller, B. K., Mack, H., and Teusch, N. (2005) Rho kinase, a promising drug target for neurological disorders. *Nat Rev Drug Discov* **4**, 387-398
118. Roser, A. E., Tonges, L., and Lingor, P. (2017) Modulation of Microglial Activity by Rho-Kinase (ROCK) Inhibition as Therapeutic Strategy in Parkinson's Disease and Amyotrophic Lateral Sclerosis. *Front Aging Neurosci* **9**, 94
119. Bauer, P. O., Wong, H. K., Oyama, F., Goswami, A., Okuno, M., Kino, Y., Miyazaki, H., and Nukina, N. (2009) Inhibition of Rho kinases enhances the degradation of mutant huntingtin. *J Biol Chem* **284**, 13153-13164
120. Li, M., Yasumura, D., Ma, A. A., Matthes, M. T., Yang, H., Nielson, G., Huang, Y., Szoka, F. C., Lavail, M. M., and Diamond, M. I. (2013) Intravitreal administration of HA-1077, a ROCK inhibitor, improves retinal function in a mouse model of huntington disease. *PloS one* **8**, e56026
121. Angeli, S., Shao, J., and Diamond, M. I. (2010) F-actin binding regions on the androgen receptor and huntingtin increase aggregation and alter aggregate characteristics. *PloS one* **5**, e9053
122. Sharma, A., Lambrechts, A., Hao le, T., Le, T. T., Sewry, C. A., Ampe, C., Burghes, A. H., and Morris, G. E. (2005) A role for complexes of survival of motor neurons (SMN) protein with gemins and profilin in neurite-like cytoplasmic extensions of cultured nerve cells. *Exp Cell Res* **309**, 185-197
123. Nolle, A., Zeug, A., van Bergeijk, J., Tonges, L., Gerhard, R., Brinkmann, H., Al Rayes, S., Hensel, N., Schill, Y., Apkhazava, D., Jablonka, S., O'Mer, J., Srivastav, R. K., Baasner, A., Lingor, P., Wirth, B., Ponimaskin,

E., Niedenthal, R., Grothe, C., and Claus, P. (2011) The spinal muscular atrophy disease protein SMN is linked to the Rho-kinase pathway via profilin. *Human molecular genetics* **20**, 4865-4878

124. Bowerman, M., Shafey, D., and Kothary, R. (2007) Smn depletion alters profilin II expression and leads to upregulation of the RhoA/ROCK pathway and defects in neuronal integrity. *J Mol Neurosci* **32**, 120-131
125. Bowerman, M., Anderson, C. L., Beauvais, A., Boyl, P. P., Witke, W., and Kothary, R. (2009) SMN, profilin IIa and plastin 3: a link between the deregulation of actin dynamics and SMA pathogenesis. *Mol Cell Neurosci* **42**, 66-74
126. Caraballo-Miralles, V., Cardona-Rossinyol, A., Garcera, A., Villalonga, P., Soler, R. M., Olmos, G., and Llado, J. (2012) SMN deficiency attenuates migration of U87MG astroglioma cells through the activation of RhoA. *Mol Cell Neurosci* **49**, 282-289
127. Reeve, S. P., Bassetto, L., Genova, G. K., Kleyner, Y., Leyssen, M., Jackson, F. R., and Hassan, B. A. (2005) The Drosophila fragile X mental retardation protein controls actin dynamics by directly regulating profilin in the brain. *Curr Biol* **15**, 1156-1163
128. Estes, P. S., O'Shea, M., Clasen, S., and Zarnescu, D. C. (2008) Fragile X protein controls the efficacy of mRNA transport in Drosophila neurons. *Mol Cell Neurosci* **39**, 170-179
129. Alkam, D., Feldman, E. Z., Singh, A., and Kiaei, M. (2017) Profilin1 biology and its mutation, actin(g) in disease. *Cell Mol Life Sci* **74**, 967-981
130. Ding, Z., Bae, Y. H., and Roy, P. (2012) Molecular insights on context-specific role of profilin-1 in cell migration. *Cell Adh Migr* **6**, 442-449
131. Jiang, C., Ding, Z., Joy, M., Chakraborty, S., Kim, S. H., Bottcher, R., Condeelis, J., Singh, S., and Roy, P. (2017) A balanced level of profilin-1 promotes stemness and tumor-initiating potential of breast cancer cells. *Cell Cycle* doi: 10.1080/15384101.2017.1346759
132. Lu, Q., Lu, L., Chen, W., Chen, H., Xu, X., and Zheng, Z. (2015) RhoA/mDia-1/profilin-1 signaling targets microvascular endothelial dysfunction in diabetic retinopathy. *Graefes Arch Clin Exp Ophthalmol* **253**, 669-680
133. Pae, M., and Romeo, G. R. (2014) The multifaceted role of profilin-1 in adipose tissue inflammation and glucose homeostasis. *Adipocyte* **3**, 69-74
134. Tiloca, C., Ticozzi, N., Pensato, V., Corrado, L., Del Bo, R., Bertolin, C., Fenoglio, C., Gagliardi, S., Calini, D., Lauria, G., Castellotti, B., Bagarotti, A., Corti, S., Galimberti, D., Cagnin, A., Gabelli, C., Ranieri, M., Ceroni, M., Siciliano, G., Mazzini, L., Cereda, C., Scarpini, E., Soraru, G., Comi, G. P., D'Alfonso, S., Gellera, C., Ratti, A., Landers, J. E., Silani, V., and Consortium, S. (2013) Screening of the PFN1 gene in sporadic amyotrophic lateral sclerosis and in frontotemporal dementia. *Neurobiology of aging* **34**, 1517 e1519-1510

135. Chen, Y., Zheng, Z. Z., Huang, R., Chen, K., Song, W., Zhao, B., Chen, X., Yang, Y., Yuan, L., and Shang, H. F. (2013) PFN1 mutations are rare in Han Chinese populations with amyotrophic lateral sclerosis. *Neurobiology of aging* **34**, 1922 e1921-1925
136. Yang, S., Fifita, J. A., Williams, K. L., Warraich, S. T., Pamphlett, R., Nicholson, G. A., and Blair, I. P. (2013) Mutation analysis and immunopathological studies of PFN1 in familial and sporadic amyotrophic lateral sclerosis. *Neurobiology of aging* **34**, 2235 e2237-2210
137. Syriani, E., Salvans, C., Salvado, M., Morales, M., Lorenzo, L., Cazorla, S., and Gamez, J. (2014) PFN1 mutations are also rare in the Catalan population with amyotrophic lateral sclerosis. *J Neurol* **261**, 2387-2392
138. Daoud, H., Dobrzeniecka, S., Camu, W., Meininger, V., Dupre, N., Dion, P. A., and Rouleau, G. A. (2013) Mutation analysis of PFN1 in familial amyotrophic lateral sclerosis patients. *Neurobiology of aging* **34**, 1311 e1311-1312
139. Lattante, S., Le Ber, I., Camuzat, A., Brice, A., and Kabashi, E. (2013) Mutations in the PFN1 gene are not a common cause in patients with amyotrophic lateral sclerosis and frontotemporal lobar degeneration in France. *Neurobiology of aging* **34**, 1709 e1701-1702
140. Zou, Z. Y., Sun, Q., Liu, M. S., Li, X. G., and Cui, L. Y. (2013) Mutations in the profilin 1 gene are not common in amyotrophic lateral sclerosis of Chinese origin. *Neurobiology of aging* **34**, 1713 e1715-1716
141. Dillen, L., Van Langenhove, T., Engelborghs, S., Vandenbulcke, M., Sarafov, S., Tournev, I., Merlin, C., Cras, P., Vandenberghe, R., De Deyn, P. P., Jordanova, A., Cruts, M., Van Broeckhoven, C., and van der Zee, J. (2013) Explorative genetic study of UBQLN2 and PFN1 in an extended Flanders-Belgian cohort of frontotemporal lobar degeneration patients. *Neurobiology of aging* **34**, 1711 e1711-1715
142. van Blitterswijk, M., Baker, M. C., Bieniek, K. F., Knopman, D. S., Josephs, K. A., Boeve, B., Caselli, R., Wszolek, Z. K., Petersen, R., Graff-Radford, N. R., Boylan, K. B., Dickson, D. W., and Rademakers, R. (2013) Profilin-1 mutations are rare in patients with amyotrophic lateral sclerosis and frontotemporal dementia. *Amyotroph Lateral Scler Frontotemporal Degener* **14**, 463-469
143. Fratta, P., Charnock, J., Collins, T., Devoy, A., Howard, R., Malaspina, A., Orrell, R., Sidle, K., Clarke, J., Shoai, M., Lu, C. H., Hardy, J., Plagnol, V., and Fisher, E. M. (2014) Profilin1 E117G is a moderate risk factor for amyotrophic lateral sclerosis. *Journal of neurology, neurosurgery, and psychiatry* **85**, 506-508
144. Figley, M. D., Bieri, G., Kolaitis, R. M., Taylor, J. P., and Gitler, A. D. (2014) Profilin 1 associates with stress granules and ALS-linked mutations alter stress granule dynamics. *J Neurosci* **34**, 8083-8097
145. Tanaka, Y., Nonaka, T., Suzuki, G., Kametani, F., and Hasegawa, M. (2016) Gain-of-function profilin 1 mutations linked to familial amyotrophic

lateral sclerosis cause seed-dependent intracellular TDP-43 aggregation. *Human molecular genetics* **25**, 1420-1433
146. Brettle, M., Suchowerska, A. K., Chua, S. W., Ittner, L. M., and Fath, T. (2015) Amyotrophic lateral sclerosis-associated mutant profilin 1 increases dendritic arborisation and spine formation in primary hippocampal neurons. *Neurosci Lett* **609**, 223-228
147. Wu, C. H., Giampetruzzi, A., Tran, H., Fallini, C., Gao, F. B., and Landers, J. E. (2017) A Drosophila model of ALS reveals a partial loss of function of causative human PFN1 mutants. *Human molecular genetics* **26**, 2146-2155
148. Freischmidt, A., Schopflin, M., Feiler, M. S., Fleck, A. K., Ludolph, A. C., and Weishaupt, J. H. (2015) Profilin 1 with the amyotrophic lateral sclerosis associated mutation T109M displays unaltered actin binding and does not affect the actin cytoskeleton. *BMC neuroscience* **16**, 77
149. Matsukawa, K., Hashimoto, T., Matsumoto, T., Ihara, R., Chihara, T., Miura, M., Wakabayashi, T., and Iwatsubo, T. (2016) Familial Amyotrophic Lateral Sclerosis-linked Mutations in Profilin 1 Exacerbate TDP-43-induced Degeneration in the Retina of Drosophila melanogaster through an Increase in the Cytoplasmic Localization of TDP-43. *J Biol Chem* **291**, 23464-23476
150. Fil, D., DeLoach, A., Yadav, S., Alkam, D., MacNicol, M., Singh, A., Compadre, C. M., Goellner, J. J., O'Brien, C. A., Fahmi, T., Basnakian, A. G., Calingasan, N. Y., Klessner, J. L., Beal, F. M., Peters, O. M., Metterville, J., Brown, R. H., Jr., Ling, K. K. Y., Rigo, F., Ozdinler, P. H., and Kiaei, M. (2017) Mutant Profilin1 transgenic mice recapitulate cardinal features of motor neuron disease. *Human molecular genetics* **26**, 686-701
151. Yang, C., Danielson, E. W., Qiao, T., Metterville, J., Brown, R. H., Jr., Landers, J. E., and Xu, Z. (2016) Mutant PFN1 causes ALS phenotypes and progressive motor neuron degeneration in mice by a gain of toxicity. *Proc Natl Acad Sci U S A* **113**, E6209-E6218
152. Mackness, B. C., Tran, M. T., McClain, S. P., Matthews, C. R., and Zitzewitz, J. A. (2014) Folding of the RNA recognition motif (RRM) domains of the amyotrophic lateral sclerosis (ALS)-linked protein TDP-43 reveals an intermediate state. *J Biol Chem* **289**, 8264-8276
153. Atkins, P. W., and De Paula, J. (2017) *Elements of physical chemistry*, 7th edition. ed., Oxford University Press, Oxford, United Kingdom
154. Lehninger, A. L., Nelson, D. L., and Cox, M. M. (2013) *Lehninger principles of biochemistry*, 6th ed., W.H. Freeman, New York
155. Lindberg, I., Shorter, J., Wiseman, R. L., Chiti, F., Dickey, C. A., and McLean, P. J. (2015) Chaperones in Neurodegeneration. *J Neurosci* **35**, 13853-13859
156. Smith, H. L., Li, W., and Cheetham, M. E. (2015) Molecular chaperones and neuronal proteostasis. *Semin Cell Dev Biol* **40**, 142-152

157. Hardy, J. A., and Higgins, G. A. (1992) Alzheimer's disease: the amyloid cascade hypothesis. *Science* **256**, 184-185
158. Musiek, E. S., and Holtzman, D. M. (2015) Three dimensions of the amyloid hypothesis: time, space and 'wingmen'. *Nat Neurosci* **18**, 800-806
159. Maziuk, B., Ballance, H. I., and Wolozin, B. (2017) Dysregulation of RNA Binding Protein Aggregation in Neurodegenerative Disorders. *Front Mol Neurosci* **10**, 89
160. Tan, L., Yu, J. T., and Tan, L. (2015) Causes and Consequences of MicroRNA Dysregulation in Neurodegenerative Diseases. *Mol Neurobiol* **51**, 1249-1262
161. Vanderweyde, T., Youmans, K., Liu-Yesucevitz, L., and Wolozin, B. (2013) Role of stress granules and RNA-binding proteins in neurodegeneration: a mini-review. *Gerontology* **59**, 524-533
162. Chiti, F., and Dobson, C. M. (2017) Protein Misfolding, Amyloid Formation, and Human Disease: A Summary of Progress Over the Last Decade. *Annu Rev Biochem* **86**, 27-68
163. Sontag, E. M., Samant, R. S., and Frydman, J. (2017) Mechanisms and Functions of Spatial Protein Quality Control. *Annu Rev Biochem* **86**, 97-122
164. Arrasate, M., and Finkbeiner, S. (2012) Protein aggregates in Huntington's disease. *Exp Neurol* **238**, 1-11
165. Kalia, L. V., and Kalia, S. K. (2015) alpha-Synuclein and Lewy pathology in Parkinson's disease. *Curr Opin Neurol* **28**, 375-381
166. Parakh, S., and Atkin, J. D. (2016) Protein folding alterations in amyotrophic lateral sclerosis. *Brain Res* **1648**, 633-649
167. Van Damme, P., Robberecht, W., and Van Den Bosch, L. (2017) Modelling amyotrophic lateral sclerosis: progress and possibilities. *Dis Model Mech* **10**, 537-549
168. Molliex, A., Temirov, J., Lee, J., Coughlin, M., Kanagaraj, A. P., Kim, H. J., Mittag, T., and Taylor, J. P. (2015) Phase separation by low complexity domains promotes stress granule assembly and drives pathological fibrillization. *Cell* **163**, 123-133
169. Murakami, T., Qamar, S., Lin, J. Q., Schierle, G. S., Rees, E., Miyashita, A., Costa, A. R., Dodd, R. B., Chan, F. T., Michel, C. H., Kronenberg-Versteeg, D., Li, Y., Yang, S. P., Wakutani, Y., Meadows, W., Ferry, R. R., Dong, L., Tartaglia, G. G., Favrin, G., Lin, W. L., Dickson, D. W., Zhen, M., Ron, D., Schmitt-Ulms, G., Fraser, P. E., Shneider, N. A., Holt, C., Vendruscolo, M., Kaminski, C. F., and St George-Hyslop, P. (2015) ALS/FTD Mutation-Induced Phase Transition of FUS Liquid Droplets and Reversible Hydrogels into Irreversible Hydrogels Impairs RNP Granule Function. *Neuron* **88**, 678-690
170. Liu, E. Y., Cali, C. P., and Lee, E. B. (2017) RNA metabolism in neurodegenerative disease. *Dis Model Mech* **10**, 509-518

171. Eisenberg, D. S., and Sawaya, M. R. (2017) Structural Studies of Amyloid Proteins at the Molecular Level. *Annu Rev Biochem* **86**, 69-95
172. Hetz, C., and Saxena, S. (2017) ER stress and the unfolded protein response in neurodegeneration. *Nat Rev Neurol* **13**, 477-491
173. Brehme, M., Voisine, C., Rolland, T., Wachi, S., Soper, J. H., Zhu, Y., Orton, K., Villella, A., Garza, D., Vidal, M., Ge, H., and Morimoto, R. I. (2014) A chaperome subnetwork safeguards proteostasis in aging and neurodegenerative disease. *Cell reports* **9**, 1135-1150
174. McKinnon, C., and Tabrizi, S. J. (2014) The ubiquitin-proteasome system in neurodegeneration. *Antioxid Redox Signal* **21**, 2302-2321
175. Martinez-Lopez, N., Athonvarangkul, D., and Singh, R. (2015) Autophagy and aging. *Adv Exp Med Biol* **847**, 73-87
176. Balch, W. E., Morimoto, R. I., Dillin, A., and Kelly, J. W. (2008) Adapting proteostasis for disease intervention. *Science* **319**, 916-919
177. Powers, E. T., Morimoto, R. I., Dillin, A., Kelly, J. W., and Balch, W. E. (2009) Biological and Chemical Approaches to Diseases of Proteostasis Deficiency. *Annu Rev Biochem* **78**, 959-991
178. Eira, J., Silva, C. S., Sousa, M. M., and Liz, M. A. (2016) The cytoskeleton as a novel therapeutic target for old neurodegenerative disorders. *Prog Neurobiol* **141**, 61-82
179. Brandt, R., and Bakota, L. (2017) Microtubule dynamics and the neurodegenerative triad of Alzheimer's disease: The hidden connection. *J Neurochem* doi: 10.1111/jnc.14011
180. Dent, E. W., Gupton, S. L., and Gertler, F. B. (2011) The growth cone cytoskeleton in axon outgrowth and guidance. *Cold Spring Harb Perspect Biol* **3**, a001800
181. Coles, C. H., and Bradke, F. (2015) Coordinating neuronal actin-microtubule dynamics. *Curr Biol* **25**, R677-691
182. Watanabe, K., Al-Bassam, S., Miyazaki, Y., Wandless, T. J., Webster, P., and Arnold, D. B. (2012) Networks of polarized actin filaments in the axon initial segment provide a mechanism for sorting axonal and dendritic proteins. *Cell reports* **2**, 1546-1553
183. Xu, K., Zhong, G., and Zhuang, X. (2013) Actin, spectrin, and associated proteins form a periodic cytoskeletal structure in axons. *Science* **339**, 452-456
184. He, J., Zhou, R., Wu, Z., Carrasco, M. A., Kurshan, P. T., Farley, J. E., Simon, D. J., Wang, G., Han, B., Hao, J., Heller, E., Freeman, M. R., Shen, K., Maniatis, T., Tessier-Lavigne, M., and Zhuang, X. (2016) Prevalent presence of periodic actin-spectrin-based membrane skeleton in a broad range of neuronal cell types and animal species. *Proc Natl Acad Sci U S A* **113**, 6029-6034
185. Ganguly, A., Tang, Y., Wang, L., Ladt, K., Loi, J., Dargent, B., Leterrier, C., and Roy, S. (2015) A dynamic formin-dependent deep F-actin network in axons. *J Cell Biol* **210**, 401-417

186. Nelson, J. C., Stavoe, A. K., and Colon-Ramos, D. A. (2013) The actin cytoskeleton in presynaptic assembly. *Cell Adh Migr* **7**, 379-387
187. Kim, C. H., and Lisman, J. E. (1999) A role of actin filament in synaptic transmission and long-term potentiation. *J Neurosci* **19**, 4314-4324
188. Lin, W. H., and Webb, D. J. (2009) Actin and Actin-Binding Proteins: Masters of Dendritic Spine Formation, Morphology, and Function. *Open Neurosci J* **3**, 54-66
189. Stefen, H., Chaichim, C., Power, J., and Fath, T. (2016) Regulation of the Postsynaptic Compartment of Excitatory Synapses by the Actin Cytoskeleton in Health and Its Disruption in Disease. *Neural Plast* **2016**, 2371970
190. Spence, E. F., and Soderling, S. H. (2015) Actin Out: Regulation of the Synaptic Cytoskeleton. *J Biol Chem* **290**, 28613-28622
191. Yuan, A., Rao, M. V., Veeranna, and Nixon, R. A. (2017) Neurofilaments and Neurofilament Proteins in Health and Disease. *Cold Spring Harb Perspect Biol* **9**, a018309
192. Brunden, K. R., Lee, V. M., Smith, A. B., 3rd, Trojanowski, J. Q., and Ballatore, C. (2017) Altered microtubule dynamics in neurodegenerative disease: Therapeutic potential of microtubule-stabilizing drugs. *Neurobiol Dis* **105**, 328-335
193. Cartelli, D., and Cappelletti, G. (2017) Microtubule Destabilization Paves the Way to Parkinson's Disease. *Mol Neurobiol* **54**, 6762
194. Dubey, J., Ratnakaran, N., and Koushika, S. P. (2015) Neurodegeneration and microtubule dynamics: death by a thousand cuts. *Front Cell Neurosci* **9**, 343
195. Matamoros, A. J., and Baas, P. W. (2016) Microtubules in health and degenerative disease of the nervous system. *Brain Res Bull* **126**, 217-225
196. Chevalier-Larsen, E., and Holzbaur, E. L. (2006) Axonal transport and neurodegenerative disease. *Biochim Biophys Acta* **1762**, 1094-1108
197. De Vos, K. J., and Hafezparast, M. (2017) Neurobiology of axonal transport defects in motor neuron diseases: Opportunities for translational research? *Neurobiol Dis* **105**, 283-299
198. Fallini, C., Zhang, H., Su, Y., Silani, V., Singer, R. H., Rossoll, W., and Bassell, G. J. (2011) The survival of motor neuron (SMN) protein interacts with the mRNA-binding protein HuD and regulates localization of poly(A) mRNA in primary motor neuron axons. *J Neurosci* **31**, 3914-3925
199. Perlson, E., Maday, S., Fu, M. M., Moughamian, A. J., and Holzbaur, E. L. (2010) Retrograde axonal transport: pathways to cell death? *Trends Neurosci* **33**, 335-344
200. Bosco, D. A., Morfini, G., Karabacak, N. M., Song, Y., Gros-Louis, F., Pasinelli, P., Goolsby, H., Fontaine, B. A., Lemay, N., McKenna-Yasek, D., Frosch, M. P., Agar, J. N., Julien, J. P., Brady, S. T., and Brown, R. H., Jr. (2010) Wild-type and mutant SOD1 share an aberrant conformation and a common pathogenic pathway in ALS. *Nat Neurosci* **13**, 1396-1403

201. Sama, R. R., Fallini, C., Gatto, R., McKeon, J. E., Song, Y., Rotunno, M. S., Penaranda, S., Abdurakhmanov, I., Landers, J. E., Morfini, G., Brady, S. T., and Bosco, D. A. (2017) ALS-linked FUS exerts a gain of toxic function involving aberrant p38 MAPK activation. *Scientific reports* **7**, 115
202. Smith, B. N., Ticozzi, N., Fallini, C., Gkazi, A. S., Topp, S., Kenna, K. P., Scotter, E. L., Kost, J., Keagle, P., Miller, J. W., Calini, D., Vance, C., Danielson, E. W., Troakes, C., Tiloca, C., Al-Sarraj, S., Lewis, E. A., King, A., Colombrita, C., Pensato, V., Castellotti, B., de Belleroche, J., Baas, F., Ten Asbroek, A. L., Sapp, P. C., McKenna-Yasek, D., McLaughlin, R. L., Polak, M., Asress, S., Esteban-Perez, J., Munoz-Blanco, J. L., Simpson, M., Consortium, S., van Rheenen, W., Diekstra, F. P., Lauria, G., Duga, S., Corti, S., Cereda, C., Corrado, L., Soraru, G., Morrison, K. E., Williams, K. L., Nicholson, G. A., Blair, I. P., Dion, P. A., Leblond, C. S., Rouleau, G. A., Hardiman, O., Veldink, J. H., van den Berg, L. H., Al-Chalabi, A., Pall, H., Shaw, P. J., Turner, M. R., Talbot, K., Taroni, F., Garcia-Redondo, A., Wu, Z., Glass, J. D., Gellera, C., Ratti, A., Brown, R. H., Jr., Silani, V., Shaw, C. E., Landers, J. E., and Consortium, S. (2014) Exome-wide Rare Variant Analysis Identifies TUBA4A Mutations Associated with Familial ALS. *Neuron* **84**, 324-331
203. Duan, W., Guo, Y., Jiang, H., Yu, X., and Li, C. (2011) MG132 enhances neurite outgrowth in neurons overexpressing mutant TAR DNA-binding protein-43 via increase of HO-1. *Brain Res* **1397**, 1-9
204. Takeuchi, H., Kobayashi, Y., Yoshihara, T., Niwa, J., Doyu, M., Ohtsuka, K., and Sobue, G. (2002) Hsp70 and Hsp40 improve neurite outgrowth and suppress intracytoplasmic aggregate formation in cultured neuronal cells expressing mutant SOD1. *Brain Res* **949**, 11-22
205. Minamide, L. S., Striegl, A. M., Boyle, J. A., Meberg, P. J., and Bamburg, J. R. (2000) Neurodegenerative stimuli induce persistent ADF/cofilin-actin rods that disrupt distal neurite function. *Nat Cell Biol* **2**, 628-636
206. Rahman, T., Davies, D. S., Tannenberg, R. K., Fok, S., Shepherd, C., Dodd, P. R., Cullen, K. M., and Goldsbury, C. (2014) Cofilin rods and aggregates concur with tau pathology and the development of Alzheimer's disease. *J Alzheimers Dis* **42**, 1443-1460
207. Bamburg, J. R., and Bernstein, B. W. (2016) Actin dynamics and cofilin-actin rods in alzheimer disease. *Cytoskeleton (Hoboken)* **73**, 477-497
208. Bamburg, J. R., Bernstein, B. W., Davis, R. C., Flynn, K. C., Goldsbury, C., Jensen, J. R., Maloney, M. T., Marsden, I. T., Minamide, L. S., Pak, C. W., Shaw, A. E., Whiteman, I., and Wiggan, O. (2010) ADF/Cofilin-actin rods in neurodegenerative diseases. *Curr Alzheimer Res* **7**, 241-250
209. Munsie, L. N., and Truant, R. (2012) The role of the cofilin-actin rod stress response in neurodegenerative diseases uncovers potential new drug targets. *Bioarchitecture* **2**, 204-208
210. Schonhofen, P., de Medeiros, L. M., Chatain, C. P., Bristot, I. J., and Klamt, F. (2014) Cofilin/actin rod formation by dysregulation of cofilin-1

activity as a central initial step in neurodegeneration. *Mini Rev Med Chem* **14**, 393-400
211. Cichon, J., Sun, C., Chen, B., Jiang, M., Chen, X. A., Sun, Y., Wang, Y., and Chen, G. (2012) Cofilin aggregation blocks intracellular trafficking and induces synaptic loss in hippocampal neurons. *J Biol Chem* **287**, 3919-3929
212. Ha, S., Furukawa, R., Stramiello, M., Wagner, J. J., and Fechheimer, M. (2011) Transgenic mouse model for the formation of Hirano bodies. *BMC neuroscience* **12**, 97
213. Fechheimer, M., Furukawa, R., Maselli, A., and Davis, R. C. (2002) Hirano bodies in health and disease. *Trends Mol Med* **8**, 590-591
214. Mitake, S., Ojika, K., and Hirano, A. (1997) Hirano bodies and Alzheimer's disease. *Kaohsiung J Med Sci* **13**, 10-18
215. Munsie, L., Caron, N., Atwal, R. S., Marsden, I., Wild, E. J., Bamburg, J. R., Tabrizi, S. J., and Truant, R. (2011) Mutant huntingtin causes defective actin remodeling during stress: defining a new role for transglutaminase 2 in neurodegenerative disease. *Human molecular genetics* **20**, 1937-1951
216. Domazetovska, A., Ilkovski, B., Cooper, S. T., Ghoddusi, M., Hardeman, E. C., Minamide, L. S., Gunning, P. W., Bamburg, J. R., and North, K. N. (2007) Mechanisms underlying intranuclear rod formation. *Brain* **130**, 3275-3284
217. Domazetovska, A., Ilkovski, B., Kumar, V., Valova, V. A., Vandebrouck, A., Hutchinson, D. O., Robinson, P. J., Cooper, S. T., Sparrow, J. C., Peckham, M., and North, K. N. (2007) Intranuclear rod myopathy: molecular pathogenesis and mechanisms of weakness. *Ann Neurol* **62**, 597-608
218. Ilkovski, B., Nowak, K. J., Domazetovska, A., Maxwell, A. L., Clement, S., Davies, K. E., Laing, N. G., North, K. N., and Cooper, S. T. (2004) Evidence for a dominant-negative effect in ACTA1 nemaline myopathy caused by abnormal folding, aggregation and altered polymerization of mutant actin isoforms. *Human molecular genetics* **13**, 1727-1743
219. Serebryannyy, L. A., Yuen, M., Parilla, M., Cooper, S. T., and de Lanerolle, P. (2016) The Effects of Disease Models of Nuclear Actin Polymerization on the Nucleus. *Front Physiol* **7**, 454
220. Bosco, D. A., LaVoie, M. J., Petsko, G. A., and Ringe, D. (2011) Proteostasis and movement disorders: Parkinson's disease and amyotrophic lateral sclerosis. *Cold Spring Harb Perspect Biol* **3**, a007500
221. Winklhofer, K. F., Tatzelt, J., and Haass, C. (2008) The two faces of protein misfolding: gain- and loss-of-function in neurodegenerative diseases. *EMBO J* **27**, 336-349
222. Austin, J. A., Wright, G. S., Watanabe, S., Grossmann, J. G., Antonyuk, S. V., Yamanaka, K., and Hasnain, S. S. (2014) Disease causing mutants of TDP-43 nucleic acid binding domains are resistant to aggregation and

have increased stability and half-life. *Proc Natl Acad Sci U S A* **111**, 4309-4314
223. Rotunno, M. S., and Bosco, D. A. (2013) An emerging role for misfolded wild-type SOD1 in sporadic ALS pathogenesis. *Front Cell Neurosci* **7**, 253
224. Watanabe, S., Kaneko, K., and Yamanaka, K. (2013) Accelerated disease onset with stabilized familial amyotrophic lateral sclerosis (ALS)-linked mutant TDP-43 proteins. *J Biol Chem* **288**, 3641-3654
225. Eriksson, A. E., Baase, W. A., Zhang, X. J., Heinz, D. W., Blaber, M., Baldwin, E. P., and Matthews, B. W. (1992) Response of a protein structure to cavity-creating mutations and its relation to the hydrophobic effect. *Science* **255**, 178-183
226. Joerger, A. C., Ang, H. C., and Fersht, A. R. (2006) Structural basis for understanding oncogenic p53 mutations and designing rescue drugs. *Proc Natl Acad Sci U S A* **103**, 15056-15061
227. Yue, P., Li, Z., and Moult, J. (2005) Loss of protein structure stability as a major causative factor in monogenic disease. *J Mol Biol* **353**, 459-473
228. Vedadi, M., Niesen, F. H., Allali-Hassani, A., Fedorov, O. Y., Finerty, P. J., Jr., Wasney, G. A., Yeung, R., Arrowsmith, C., Ball, L. J., Berglund, H., Hui, R., Marsden, B. D., Nordlund, P., Sundstrom, M., Weigelt, J., and Edwards, A. M. (2006) Chemical screening methods to identify ligands that promote protein stability, protein crystallization, and structure determination. *Proc Natl Acad Sci U S A* **103**, 15835-15840
229. Ringe, D., and Petsko, G. A. (2009) What are pharmacological chaperones and why are they interesting? *Journal of biology* **8**, 80
230. Verhoef, L. G., Lindsten, K., Masucci, M. G., and Dantuma, N. P. (2002) Aggregate formation inhibits proteasomal degradation of polyglutamine proteins. *Human molecular genetics* **11**, 2689-2700
231. Myers, J. K., Pace, C. N., and Scholtz, J. M. (1995) Denaturant m values and heat capacity changes: relation to changes in accessible surface areas of protein unfolding. *Protein science : a publication of the Protein Society* **4**, 2138-2148
232. Rotunno, M. S., Auclair, J. R., Maniatis, S., Shaffer, S. A., Agar, J., and Bosco, D. A. (2014) Identification of a Misfolded Region in Superoxide Dismutase 1 that is Exposed in Amyotrophic Lateral Sclerosis. *J Biol Chem* **289**, 28527-28538
233. Fedorov, A. A., Pollard, T. D., and Almo, S. C. (1994) Purification, characterization and crystallization of human platelet profilin expressed in Escherichia coli. *Journal of molecular biology* **241**, 480-482
234. Prabu-Jeyabalan, M., Nalivaika, E. A., Romano, K., and Schiffer, C. A. (2006) Mechanism of substrate recognition by drug-resistant human immunodeficiency virus type 1 protease variants revealed by a novel structural intermediate. *Journal of virology* **80**, 3607-3616
235. Cedergren-Zeppezauer, E. S., Goonesekere, N. C., Rozycki, M. D., Myslik, J. C., Dauter, Z., Lindberg, U., and Schutt, C. E. (1994)

Crystallization and structure determination of bovine profilin at 2.0 A resolution. *J Mol Biol* **240**, 459-475
236. Chik, J. K., Lindberg, U., and Schutt, C. E. (1996) The structure of an open state of beta-actin at 2.65 A resolution. *Journal of molecular biology* **263**, 607-623
237. Hajkova, L., Bjorkegren Sjogren, C., Korenbaum, E., Nordberg, P., and Karlsson, R. (1997) Characterization of a mutant profilin with reduced actin-binding capacity: effects in vitro and in vivo. *Exp Cell Res* **234**, 66-77
238. Porta, J. C., and Borgstahl, G. E. (2012) Structural basis for profilin-mediated actin nucleotide exchange. *J Mol Biol* **418**, 103-116
239. Ostrander, D. B., Ernst, E. G., Lavoie, T. B., and Gorman, J. A. (1999) Polyproline binding is an essential function of human profilin in yeast. *Eur J Biochem* **262**, 26-35
240. Pollard, T. D., and Cooper, J. A. (1984) Quantitative analysis of the effect of Acanthamoeba profilin on actin filament nucleation and elongation. *Biochemistry* **23**, 6631-6641
241. Eriksson, A. E., Baase, W. A., Wozniak, J. A., and Matthews, B. W. (1992) A cavity-containing mutant of T4 lysozyme is stabilized by buried benzene. *Nature* **355**, 371-373
242. Ling, S. C., Albuquerque, C. P., Han, J. S., Lagier-Tourenne, C., Tokunaga, S., Zhou, H., and Cleveland, D. W. (2010) ALS-associated mutations in TDP-43 increase its stability and promote TDP-43 complexes with FUS/TLS. *Proc Natl Acad Sci U S A* **107**, 13318-13323
243. Bilsel, O., Yang, L., Zitzewitz, J. A., Beechem, J. M., and Matthews, C. R. (1999) Time-resolved fluorescence anisotropy study of the refolding reaction of the alpha-subunit of tryptophan synthase reveals nonmonotonic behavior of the rotational correlation time. *Biochemistry* **38**, 4177-4187
244. Greene, R. F., Jr., and Pace, C. N. (1974) Urea and guanidine hydrochloride denaturation of ribonuclease, lysozyme, alpha-chymotrypsin, and beta-lactoglobulin. *J Biol Chem* **249**, 5388-5393
245. Kathuria, S. V., Kayatekin, C., Barrea, R., Kondrashkina, E., Graceffa, R., Guo, L., Nobrega, R. P., Chakravarthy, S., Matthews, C. R., Irving, T. C., and Bilsel, O. (2014) Microsecond barrier-limited chain collapse observed by time-resolved FRET and SAXS. *J Mol Biol* **426**, 1980-1994
246. Wu, Y., Kondrashkina, E., Kayatekin, C., Matthews, C. R., and Bilsel, O. (2008) Microsecond acquisition of heterogeneous structure in the folding of a TIM barrel protein. *Proc Natl Acad Sci U S A* **105**, 13367-13372
247. Winter, G. (2010) xia2: an expert system for macromolecular crystallography data reduction. *Journal of applied crystallography* **43**, 186-190
248. Kabsch, W. (2010) Xds. *Acta crystallographica. Section D, Biological crystallography* **66**, 125-132

249. McCoy, A. J., Grosse-Kunstleve, R. W., Adams, P. D., Winn, M. D., Storoni, L. C., and Read, R. J. (2007) Phaser crystallographic software. *Journal of applied crystallography* **40**, 658-674
250. Emsley, P., and Cowtan, K. (2004) Coot: model-building tools for molecular graphics. *Acta crystallographica. Section D, Biological crystallography* **60**, 2126-2132
251. Adams, P. D., Afonine, P. V., Bunkoczi, G., Chen, V. B., Davis, I. W., Echols, N., Headd, J. J., Hung, L. W., Kapral, G. J., Grosse-Kunstleve, R. W., McCoy, A. J., Moriarty, N. W., Oeffner, R., Read, R. J., Richardson, D. C., Richardson, J. S., Terwilliger, T. C., and Zwart, P. H. (2010) PHENIX: a comprehensive Python-based system for macromolecular structure solution. *Acta crystallographica. Section D, Biological crystallography* **66**, 213-221
252. Murshudov, G. N., Vagin, A. A., and Dodson, E. J. (1997) Refinement of macromolecular structures by the maximum-likelihood method. *Acta crystallographica. Section D, Biological crystallography* **53**, 240-255
253. dos Remedios, C. G., Chhabra, D., Kekic, M., Dedova, I. V., Tsubakihara, M., Berry, D. A., and Nosworthy, N. J. (2003) Actin binding proteins: regulation of cytoskeletal microfilaments. *Physiol Rev* **83**, 433-473
254. Harris, E. S., Gauvin, T. J., Heimsath, E. G., and Higgs, H. N. (2010) Assembly of filopodia by the formin FRL2 (FMNL3). *Cytoskeleton (Hoboken)* **67**, 755-772
255. Kovar, D. R., Harris, E. S., Mahaffy, R., Higgs, H. N., and Pollard, T. D. (2006) Control of the assembly of ATP- and ADP-actin by formins and profilin. *Cell* **124**, 423-435
256. Goh, W. I., and Ahmed, S. (2012) mDia1-3 in mammalian filopodia. *Communicative & integrative biology* **5**, 340-344
257. Mellor, H. (2010) The role of formins in filopodia formation. *Biochim Biophys Acta* **1803**, 191-200
258. Harris, E. S., Rouiller, I., Hanein, D., and Higgs, H. N. (2006) Mechanistic differences in actin bundling activity of two mammalian formins, FRL1 and mDia2. *J Biol Chem* **281**, 14383-14392
259. Breitsprecher, D., Jaiswal, R., Bombardier, J. P., Gould, C. J., Gelles, J., and Goode, B. L. (2012) Rocket launcher mechanism of collaborative actin assembly defined by single-molecule imaging. *Science* **336**, 1164-1168
260. Courtemanche, N., Pollard, T. D., and Chen, Q. (2016) Avoiding artefacts when counting polymerized actin in live cells with LifeAct fused to fluorescent proteins. *Nat Cell Biol* **18**, 676-683
261. Deibler, M., Spatz, J. P., and Kemkemer, R. (2011) Actin fusion proteins alter the dynamics of mechanically induced cytoskeleton rearrangement. *PloS one* **6**, e22941

262. Du, J., Fan, Y. L., Chen, T. L., and Feng, X. Q. (2015) Lifeact and Utr230 induce distinct actin assemblies in cell nuclei. *Cytoskeleton (Hoboken)* **72**, 570-575
263. Lemieux, M. G., Janzen, D., Hwang, R., Roldan, J., Jarchum, I., and Knecht, D. A. (2014) Visualization of the actin cytoskeleton: different F-actin-binding probes tell different stories. *Cytoskeleton (Hoboken)* **71**, 157-169
264. Melak, M., Plessner, M., and Grosse, R. (2017) Actin visualization at a glance. *J Cell Sci* **130**, 525-530
265. Riedl, J., Crevenna, A. H., Kessenbrock, K., Yu, J. H., Neukirchen, D., Bista, M., Bradke, F., Jenne, D., Holak, T. A., Werb, Z., Sixt, M., and Wedlich-Soldner, R. (2008) Lifeact: a versatile marker to visualize F-actin. *Nat Methods* **5**, 605-607
266. Higashida, C., Miyoshi, T., Fujita, A., Oceguera-Yanez, F., Monypenny, J., Andou, Y., Narumiya, S., and Watanabe, N. (2004) Actin polymerization-driven molecular movement of mDia1 in living cells. *Science* **303**, 2007-2010
267. Barzik, M., McClain, L. M., Gupton, S. L., and Gertler, F. B. (2014) Ena/VASP regulates mDia2-initiated filopodial length, dynamics, and function. *Mol Biol Cell* **25**, 2604-2619
268. Ishizaki, T., Morishima, Y., Okamoto, M., Furuyashiki, T., Kato, T., and Narumiya, S. (2001) Coordination of microtubules and the actin cytoskeleton by the Rho effector mDia1. *Nat Cell Biol* **3**, 8-14
269. Watanabe, N., Kato, T., Fujita, A., Ishizaki, T., and Narumiya, S. (1999) Cooperation between mDia1 and ROCK in Rho-induced actin reorganization. *Nat Cell Biol* **1**, 136-143
270. Sivadasan, R., Hornburg, D., Drepper, C., Frank, N., Jablonka, S., Hansel, A., Lojewski, X., Sterneckert, J., Hermann, A., Shaw, P. J., Ince, P. G., Mann, M., Meissner, F., and Sendtner, M. (2016) C9ORF72 interaction with cofilin modulates actin dynamics in motor neurons. *Nat Neurosci* **19**, 1610-1618
271. Zacharias, D. A., Violin, J. D., Newton, A. C., and Tsien, R. Y. (2002) Partitioning of lipid-modified monomeric GFPs into membrane microdomains of live cells. *Science* **296**, 913-916
272. Smith, B. A., Gelles, J., and Goode, B. L. (2014) Single-molecule studies of actin assembly and disassembly factors. *Methods in enzymology* **540**, 95-117
273. Ward, C. L., Boggio, K. J., Johnson, B. N., Boyd, J. B., Douthwright, S., Shaffer, S. A., Landers, J. E., Glicksman, M. A., and Bosco, D. A. (2014) A loss of FUS/TLS function leads to impaired cellular proliferation. *Cell death & disease* **5**, e1572
274. Tarantino, N., Tinevez, J. Y., Crowell, E. F., Boisson, B., Henriques, R., Mhlanga, M., Agou, F., Israel, A., and Laplantine, E. (2014) TNF and IL-1

exhibit distinct ubiquitin requirements for inducing NEMO-IKK supramolecular structures. *J Cell Biol* **204**, 231-245
275. Qian, H., Sheetz, M. P., and Elson, E. L. (1991) Single particle tracking. Analysis of diffusion and flow in two-dimensional systems. *Biophys J* **60**, 910-921
276. Peters, O. M., Ghasemi, M., and Brown, R. H., Jr. (2015) Emerging mechanisms of molecular pathology in ALS. *J Clin Invest* **125**, 2548
277. Selkoe, D. J. (2011) Alzheimer's disease. *Cold Spring Harb Perspect Biol* **3**, a004457
278. Kalia, L. V., and Lang, A. E. (2015) Parkinson's disease. *Lancet* **386**, 896-912
279. Finkbeiner, S. (2011) Huntington's Disease. *Cold Spring Harb Perspect Biol* **3**, a007476
280. Shahheydari, H., Ragagnin, A., Walker, A. K., Toth, R. P., Vidal, M., Jagaraj, C. J., Perri, E. R., Konopka, A., Sultana, J. M., and Atkin, J. D. (2017) Protein Quality Control and the Amyotrophic Lateral Sclerosis/Frontotemporal Dementia Continuum. *Front Mol Neurosci* **10**, 119
281. Del Poggetto, E., Bemporad, F., Tatini, F., and Chiti, F. (2015) Mutations of Profilin-1 Associated with Amyotrophic Lateral Sclerosis Promote Aggregation Due to Structural Changes of Its Native State. *ACS Chem Biol* **10**, 2553-2563
282. Del Poggetto, E., Chiti, F., and Bemporad, F. (2015) The Folding process of Human Profilin-1, a novel protein associated with familial amyotrophic lateral sclerosis. *Scientific reports* **5**, 12332
283. Del Poggetto, E., Gori, L., and Chiti, F. (2016) Biophysical analysis of three novel profilin-1 variants associated with amyotrophic lateral sclerosis indicates a correlation between their aggregation propensity and the structural features of their globular state. *Biol Chem* **397**, 927-937
284. Metzler, W. J., Constantine, K. L., Friedrichs, M. S., Bell, A. J., Ernst, E. G., Lavoie, T. B., and Mueller, L. (1993) Characterization of the three-dimensional solution structure of human profilin: 1H, 13C, and 15N NMR assignments and global folding pattern. *Biochemistry* **32**, 13818-13829
285. Abdiche, Y., Malashock, D., Pinkerton, A., and Pons, J. (2008) Determining kinetics and affinities of protein interactions using a parallel real-time label-free biosensor, the Octet. *Anal Biochem* **377**, 209-217
286. Minehardt, T. J., Kollman, P. A., Cooke, R., and Pate, E. (2006) The open nucleotide pocket of the profilin/actin x-ray structure is unstable and closes in the absence of profilin. *Biophys J* **90**, 2445-2449
287. Schutt, C. E., Rozycki, M. D., Chik, J. K., and Lindberg, U. (1995) Structural studies on the ribbon-to-helix transition in profilin: actin crystals. *Biophys J* **68**, 12S-17S; discussion 17S-18S
288. Berman, D. E., Dall'Armi, C., Voronov, S. V., McIntire, L. B., Zhang, H., Moore, A. Z., Staniszewski, A., Arancio, O., Kim, T. W., and Di Paolo, G.

(2008) Oligomeric amyloid-beta peptide disrupts phosphatidylinositol-4,5-bisphosphate metabolism. *Nat Neurosci* **11**, 547-554

289. Woerner, A. C., Frottin, F., Hornburg, D., Feng, L. R., Meissner, F., Patra, M., Tatzelt, J., Mann, M., Winklhofer, K. F., Hartl, F. U., and Hipp, M. S. (2016) Cytoplasmic protein aggregates interfere with nucleocytoplasmic transport of protein and RNA. *Science* **351**, 173-176
290. Zhang, K., Donnelly, C. J., Haeusler, A. R., Grima, J. C., Machamer, J. B., Steinwald, P., Daley, E. L., Miller, S. J., Cunningham, K. M., Vidensky, S., Gupta, S., Thomas, M. A., Hong, I., Chiu, S. L., Huganir, R. L., Ostrow, L. W., Matunis, M. J., Wang, J., Sattler, R., Lloyd, T. E., and Rothstein, J. D. (2015) The C9orf72 repeat expansion disrupts nucleocytoplasmic transport. *Nature* **525**, 56-61
291. Rodriguez Del Rio, P., Diaz-Perales, A., Sanchez-Garcia, S., Escudero, C., Ibanez, M. D., Mendez-Brea, P., and Barber, D. (2017) Profilin, a change in the paradigm. *J Investig Allergol Clin Immunol* **28**, doi: 10.18176/jiaci.0193
292. Santos, A., and Van Ree, R. (2011) Profilins: mimickers of allergy or relevant allergens? *Int Arch Allergy Immunol* **155**, 191-204
293. Sudakov, N. P., Klimenkov, I. V., Byvaltsev, V. A., Nikiforov, S. B., and Konstantinov, Y. M. (2017) Extracellular Actin in Health and Disease. *Biochemistry (Mosc)* **82**, 1-12
294. Aspenstrom, P., Lassing, I., and Karlsson, R. (1991) Production, isolation and characterization of human profilin from Saccharomyces cerevisiae. *J Muscle Res Cell Motil* **12**, 201-207
295. Kaiser, D. A., Goldschmidt-Clermont, P. J., Levine, B. A., and Pollard, T. D. (1989) Characterization of renatured profilin purified by urea elution from poly-L-proline agarose columns. *Cell motility and the cytoskeleton* **14**, 251-262
296. Lindberg, U., Schutt, C. E., Hellsten, E., Tjader, A. C., and Hult, T. (1988) The use of poly(L-proline)-Sepharose in the isolation of profilin and profilactin complexes. *Biochim Biophys Acta* **967**, 391-400
297. Palmer, I., and Wingfield, P. T. (2012) Preparation and extraction of insoluble (inclusion-body) proteins from Escherichia coli. *Current protocols in protein science / editorial board, John E. Coligan ... [et al.]* **Chapter 6**, Unit6 3
298. McLachlan, G. D., Cahill, S. M., Girvin, M. E., and Almo, S. C. (2007) Acid-induced equilibrium folding intermediate of human platelet profilin. *Biochemistry* **46**, 6931-6943
299. Machesky, L. M., and Poland, T. D. (1993) Profilin as a potential mediator of membrane-cytoskeleton communication. *Trends Cell Biol* **3**, 381-385
300. Lakowicz, J. R. (2006) *Principles of fluorescence spectroscopy*, 3rd ed., Springer, New York

301. Blanchoin, L., and Pollard, T. D. (1998) Interaction of actin monomers with Acanthamoeba actophorin (ADF/cofilin) and profilin. *J Biol Chem* **273**, 25106-25111
302. Yarmola, E. G., and Bubb, M. R. (2004) Effects of profilin and thymosin beta4 on the critical concentration of actin demonstrated in vitro and in cell extracts with a novel direct assay. *J Biol Chem* **279**, 33519-33527
303. Yarmola, E. G., Parikh, S., and Bubb, M. R. (2001) Formation and implications of a ternary complex of profilin, thymosin beta 4, and actin. *J Biol Chem* **276**, 45555-45563
304. Rusinova, E., Tretyachenko-Ladokhina, V., Vele, O. E., Senear, D. F., and Alexander Ross, J. B. (2002) Alexa and Oregon Green dyes as fluorescence anisotropy probes for measuring protein-protein and protein-nucleic acid interactions. *Anal Biochem* **308**, 18-25
305. Eads, J. C., Mahoney, N. M., Vorobiev, S., Bresnick, A. R., Wen, K. K., Rubenstein, P. A., Haarer, B. K., and Almo, S. C. (1998) Structure determination and characterization of Saccharomyces cerevisiae profilin. *Biochemistry* **37**, 11171-11181
306. Fedorov, A. A., Magnus, K. A., Graupe, M. H., Lattman, E. E., Pollard, T. D., and Almo, S. C. (1994) X-ray structures of isoforms of the actin-binding protein profilin that differ in their affinity for phosphatidylinositol phosphates. *Proc Natl Acad Sci U S A* **91**, 8636-8640